Real-time Feedback of B_0 Shimming at Ultra High Field MRI

Dissertation

zur Erlangung des Grades eines
Doktors der Naturwissenschaften

der Mathematisch-Naturwissenschaftlichen Fakultät
und
der Medizinischen Fakultät
der Eberhard-Karls-Universität Tübingen

vorgelegt
von

Yu-Chun (Paul) Chang
aus Stadt (*Taichung*), Land (*Taiwan*)

Jul - 2018

Tag der mündlichen Prüfung: 5th July 2018

Dekan der Math.-Nat. Fakultät: Prof. Dr. W. Rosenstiel
Dekan der Medizinischen Fakultät: Prof. Dr. I. B. Autenrieth

1. Berichterstatter: Dr. Anke Henning

2. Berichterstatter: Prof. Dr. Uwe Klose

Prüfungskommission: Dr. Anke Henning

Prof. Dr. Uwe Klose

Prof. Dr. Klaus Scheffler

Prof. Dr. Sebastian Kozerke

Erklärung / Declaration:

Ich erkläre, dass ich die zur Promotion eingereichte Arbeit mit dem Titel:

„Real-time Feedback of B_0 Shimming at Ultra High Field MRI“

selbständig verfasst, nur die angegebenen Quellen und Hilfsmittel benutzt und wörtlich oder inhaltlich übernommene Stellen als solche gekennzeichnet habe. Ich versichere an Eides statt, dass diese Angaben wahr sind und dass ich nichts verschwiegen habe. Mir ist bekannt, dass die falsche Abgabe einer Versicherung an Eides statt mit Freiheitsstrafe bis zu drei Jahren oder mit Geldstrafe bestraft wird.

I hereby declare that I have produced the work entitled "……", submitted for the award of a doctorate, on my own (without external help), have used only the sources and aids indicated and have marked passages included from other works, whether verbatim or in content, as such. I swear upon oath that these statements are true and that I have not concealed anything. I am aware that making a false declaration under oath is punishable by a term of imprisonment of up to three years or by a fine.

Tübingen, den ....

Datum / Date Unterschrift /Signature

Abstract

Magnetic resonance imaging (MRI) is moving towards higher and higher field strengths. After 1.5T MRI scanners became commonplace, 3T scanners were introduced and once 3T scanners became commonplace, ultra high field (UHF) scanners were introduced. UHF scanners typically refer to scanners with a field strength of 7T or higher. The number of sites that utilise UHF scanners is slowly growing and the first 7T MRI scanners were recently CE certified for clinical use.

Although UHF scanners have the benefit of higher signal-to-noise ratio (SNR), they come with their own challenges. One of the many challenges is the problem of inhomogeneity of the main static magnetic field (B_0 field). This thesis addresses multiple aspects associated with the problem of B_0 inhomogeneity. The process of homogenising the field is called "shimming". The focus of this thesis is on active shimming where extra shim coils drive DC currents to generate extra magnetic fields superimposed on the main magnetic field to correct for inhomogeneities. In particular, we looked at the following issues: algorithms for calculating optimal shim currents; global static shimming using very high order/degree spherical harmonic-based (VHOS) coils; dynamic slice-wise shimming using VHOS coils compared to a localised multi-coil array shim system; B_0 field monitoring using an NMR field camera; characterisation of the shim system using a field camera; and designing a controller based on the shim system model for real-time feedback.

We hope that, after reading this thesis, the reader will become well-informed in the practical implementation and limitations of B_0 shimming at 9.4T in the human brain.

Contents

List of Figures

1 Synopsis

It can be argued with some vehemence that the biggest bane of a high-resolution NMR spectroscopist's existence is the ritual of "magnet shimming".

- Chmurny and Hoult

"The Ancient and Honourable Art of Shimming"

Concepts in Magnetic Resonance 2;131-149 (1990)

1.1 Introduction

A particle with a n.onzero nuclear spin in the presence of an external magnetic field will precess at a certain frequency. This is the core principle that allows magnetic resonance imaging (MRI) to exist. The frequency at which the particle precesses is dependent on the strength of the magnetic field (B_0 field) and the gyromagnetic ratio of that particle, given by:

$$f = \frac{\gamma}{2\pi} \cdot B_0 \tag{1}$$

This is called the Larmor frequency.

Therefore, MRI relies on an external magnetic B_0 field to form images. This magnetic field should be homogeneous. Nevertheless, despite the efforts of even the most rigorous and precise manufacturers, the magnetic field will always have some inhomogeneity. Even if the magnetic field is perfectly homogeneous, the introduction of an object into the magnetic field would disrupt the homogeneity. The way in which the field is distorted is dependent on the geometry and magnetic (or B_0) susceptibility of the object. This means that the magnetic field distorts differently for different objects, people, body parts, positions and orientations of whatever is being scanned in the MRI machine. In fact, the magnetic susceptibility χ is constant and relates the magnetic flux density B to the external field H of the material by the equation:

$$B = \chi H \tag{2}$$

There is no lack of adverse effects of inhomogeneous B_0 fields on MRI data. If B_0 is shifted, from Eqn. 1 it can be seen that the frequency is also shifted. Since MRI is based on resonance, artifacts will result if the frequency is shifted too far from the resonance frequency. Poor B_0 homogeneity can lead to geometric distortions and signal dropout for MRI imaging. For MR spectroscopy (MRS), poor B_0 homogeneity leads to line broadening which results in less accurate quantification and fewer detectable metabolites. For single voxel spectroscopy (SVS), poor B_0 homogeneity can also lead to inaccurate localization of the voxel. Furthermore, any MRI sequence that uses frequency selective pulses will be affected by the B_0 homogeneity. For example, if the frequency of the water peak is shifted as a result of an inhomogeneous B_0 field, the water suppression quality for typical MRS studies will be affected.

In pursuit of more SNR, there is a trend in the MRI community to go to higher and higher field strengths. In other words, the B_0 strength of MRI scanners is increasing. However, this means that the problem of B_0 inhomogeneity also gets worse. This can be seen from Eqn. 2 where the difference between B fields within different materials is larger if the H field is larger. New methods to ensure a homogeneous B_0 field need to be developed for the advantages of higher field strengths to be fully realised.

The goal of magnetic or B_0 shimming, is to ensure that the field is sufficiently homogeneous. This can be done using passive elements to adjust the magnetic field. Passive shimming is usually done with ferromagnetic materials ($\chi > 10,000$), however, diamagnetic materials have also been used successfully [32]. What is more commonly done now, is to use active elements to generate extra magnetic fields superimposed on the main B_0 field that correct for the inhomogeneities. These extra magnetic fields are generated by inductive coils, or shim coils, and can be controlled by the amount of current driving the coils. This, thereby, allows the magnetic field to be actively shimmed and allows more flexibility and adaptability to different applications.

The question then becomes: how do we design the shim coils? The design of gradient coils is obvious since the desired magnetic field that these coils should generate is known *a priori*. For shim coils, the desired magnetic field depends on the application and is hence less straight-forward. The earlier designs of shim coils can be seen as a generalisation of the gradient coils and were based on spherical harmonic functions

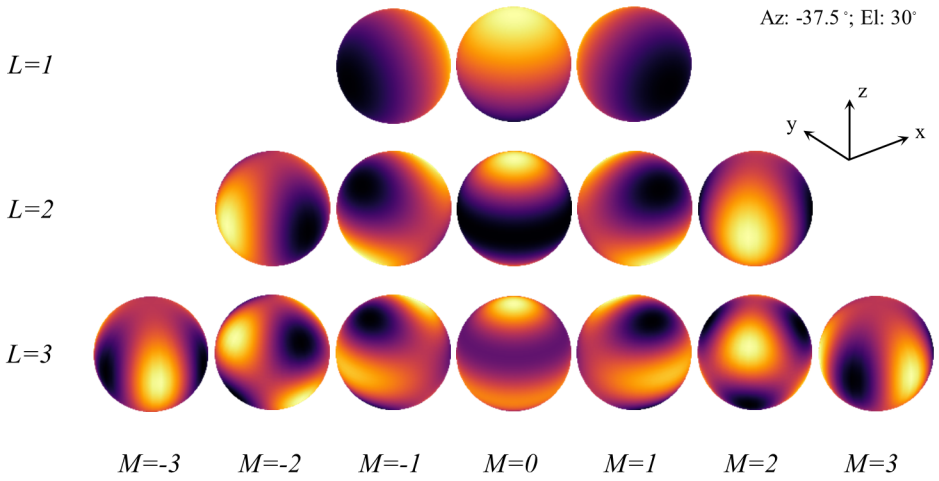

Figure 1: Spherical harmonic functions visualised on the surface of a unit sphere. From first to third degree terms (*L=1* to *L=3*) and corresponding orders *M*. The orientation is shown at an azimuth angle of -37.5° and an elevation angle of 30°.

[23, 6]. Spherical harmonic functions span a 3D space, are orthogonal and are radially invariant. The magnetic fields generated by the spherical harmonic functions are shown in Figure 1[1] (more discussion of very high order/degree spherical harmonic shimming can be found in section 1.3). It can be seen that the first degree terms of the spherial harmonic functions correspond directly to the gradient terms x, y, and z.

However, in recent years, the design of shim coils has moved towards small, localized coils [17, 18]. Orthogonality is not a necessity for the shim fields and smaller coils reduces the amount of unwanted eddy currents and coupling between the coils. Furthermore, since the coils are smaller they need to be closer to the object being scanned and it is therefore possible to combine the RF coil with the shim coils [25]. A downside of this design is that it typically requires more current than the spherical harmonic coil design since the coils are smaller and have less inductance (i.e. less sensitivity). Furthermore, the design of these coils cannot compensate for local inhomogeneities in the magnetic field due to the lack of degrees of freedom for generating local magnetic fields.

[1] The formal equations for the spherical harmonic functions are given in the Appended Publications

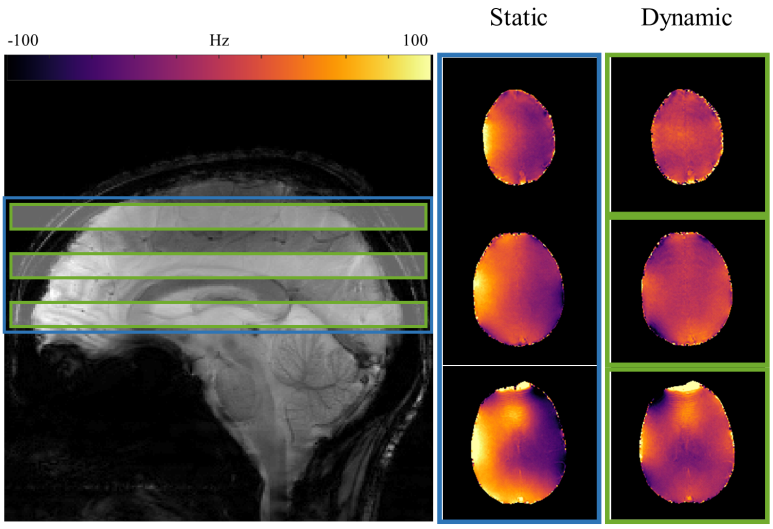

Figure 2: Individually shimming each 2D slice (in green) in a volume results in better B_0 homogeneity than shimming the entire 3D volume (in blue). In trying to compensate for the B_0 inhomogeneity pattern resulting from the air cavities in the bottom slices, strong remaining field inhomogeneities in the left to right direction can be observed in all other slices when the entire 3D volume is shimmed.

Besides hardware modifications, B_0 homogeneity can be improved for 2D sequences using slice-wise shimming [21, 16, 10]. 3D sequences excite the entire volume and read out the data, however, 2D sequences acquire the data from a single slice at a time. This allows us to only shim the slice that is currently excited (Figure 2). More details on dynamic slice-wise B0 shimming can be found in section 1.4.

The B_0 field can also have temporal changes. This means that the B_0 field is not independent of time but can vary and fluctuate with respect to time. Temporal changes can occur due to physiological causes such as motion and breathing or due to fluctuations in the currents in the shim coils. To maintain a stable magnetic field, these temporal fluctuations should be corrected.

However, temporal fluctuations of the magnetic field cannot be corrected unless we can measure or monitor the field. Short modules can be inserted into an MRI sequence to quickly read out an estimate of the B_0 field [30, 19]. These methods require modifications to the sequence and can increase the overall scan duration. Recently, another method for magnetic field monitoring has emerged. Field probes can be used

as sensors to measure the magnetic field at a single position [4]. These field probes utilise the principle of magnetic resonance and generate free induction decay (FID) signals that can be used to calculate the magnetic field using Eqn 1. An array of field probes, or a field camera, can then be used to measure the magnetic field at multiple spatial positions. Since, field cameras can be used simultaneously while the MRI scanner is running a sequence, the magnetic field can be measured in real-time and without increasing the scan duration. Figure 3 depicts the field camera (that was built within the scope of the thesis) and one of the field probes that was mounted on the field camera. Section 1.5 further describes the use of a field camera and how field cameras compare to B_0 mapping sequences.

Suppose now, that we have the good fortune to have available to us a system or method that can allow us to measure the temporal dynamics of the magnetic field such as the field camera formerly described. The system dynamics of our shim system in question can then be measured. That is, we can measure how the magnetic field changes when individual shim currents change. Indeed, no system is perfect and will have certain time responses and surely such a system with so many electrical conductors and changes in current (in the presence of a magnetic field) must generate eddy currents and cross-coupling effects. Only once this is measured, can we hope to control such a system.

A shim system with more than one coil element is, by nature, a multivariable system. Once the system dynamics have been measured and modelled, a controller can be designed to control the system. Details of what a control system is and how to design controllers is given in section 1.6.

This thesis addresses multiple issues regarding B_0 homogeneity: how we can achieve it and how we can keep it stable. Thus, we delve into topics that touch on algorithms, sequence programming, spatial/temporal modelling, instrumentation, electronics and controller design.

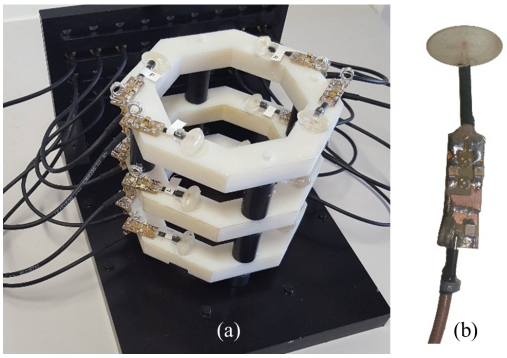

Figure 3: (a) NMR field camera with 12 field probes and (b) one of the field probes.

1.2 Algorithms

The B_0 shimming is, at the core, an inversion problem. That is, the inhomogeneities can be counteracted by applying the inverse. In order to calculate the optimal shim currents that cancel out the inhomogeneities, the B_0 field first needs to be measured. There are different ways the B_0 field can be measured. Either a full image-based B_0 mapping based on dual-echo [15] or multi-echo gradient echo sequences [13] can be used or fast projection-based methods such as FASTMAP (or FASTERMAP) can be used [11, 24]. In any case, the scope of this thesis was not to develop a new B_0 mapping method but rather, is focused on how the B_0 map can be used for shimming.

Calculation of the currents that need to be applied to the shim coils varies across literature and, in some instances, is not even mentioned. However, the hardware limitations of the shim amplifiers are sometimes not properly handled or sometimes not considered at all. Exceeding the hardware limitations usually does not happen for large volumes of interest (VOIs) but for smaller volumes such as single voxel spectroscopy (SVS), the required shim currents can be high and exceed the current limits of the amplifiers. This can also happen for single-slice shimming. Furthermore, the more the shim coils overlap, the more likely this will happen.

Therefore, there is a need for a B_0 shimming algorithm that can account for hardware limitations regardless of the size and nature of the VOI. This inversion problem is typically cast as a linear least squares problem. If the shim currents are constrained due to hardware limitations, this can be described as box constraints in

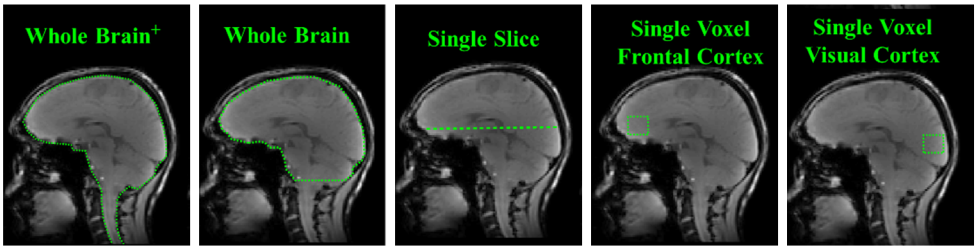

Figure 4: Regions of interest (ROIs) that were used to test the B_0 shimming algorithms.

this optimisation problem. The B_0 shimming optimisation problem is then:

$$\begin{aligned} &\min_x \|Ax - b\|^2 \\ &lb \leq x \leq ub \end{aligned} \tag{3}$$

where b is a $n \times 1$ vector (n is the number of voxels in the ROI) of unshimmed B_0 field map voxels stacked column-wise; A is a $n \times c$ matrix (c is the number of shim coils) of the shim fields generated by each shim coil; and lb and ub are the lower and upper bounds, respectively. Subsequently, the shim fields that need to be generated by the coils is given by $-x$.

As with any linear least-squares problem, this optimisation problem can be rewritten in the following quadratic form:

$$\min_x \left(\frac{1}{2} \cdot x^T Q x - c^T x \right) \tag{4}$$

where $Q = A^T \cdot A$ and $c^T = A^T \cdot b$. Since $Q = A^T \cdot A$ is always positive (semi-)definite. This is a quadratic problem and hence (semi-)convex. Therefore, any solution to this problem is a global minimum. If it is strictly positive definite then the solution to this problem is unique. However, even when the matrix is only positive semi-definite, even though there are multiple solutions, they all yield the same global minimum regardless of the box constraints (i.e. hardware constraints)[2]. It should always converge to the same global minimum.

[2]This means that the algorithm does not have "local" minima and hence does not depend on a starting value as is sometimes misconstrued in the literature [13, 9].

In `Publication 1`, a plethora of different algorithms were considered. Algorithms that were found in the literature such as the linear least squares and Levenberg-Marquardt algorithms were included. Additional optimization algorithms were also compared, including nonlinear solvers and quadratic solvers. Finally, a regularised algorithm that was developed to account for hardware constraints, called *ConsTru,* was compared. The analysis of the algorithms were tested on multiple VOIs (Figure 4):

- whole brain covering the entire cerebrum, cerebellum and brain stem (denoted as whole-brain^{+});
- whole brain without the medulla and cervical spine;
- single slice through the frontal sinus air cavity;
- single voxel (2x2x2 cm^3) in the frontal cortex; and
- in the visual cortex

Multiple performance metrics were used:

1. sensitivity to starting values (if starting values are required),
2. numerical stability (to noise and perturbations in the b vector,
3. speed of convergence/calculation,
4. required total current $\sum abs(x_i)$
5. the objective function value (i.e. the residual error).

In the publication, we showed that our proposed algorithm *ConsTru* outperformed the other algorithms. Although this method was similar to other regularisation methods such as in [20], we provide a systemic method of regularisation that is tailored to the specific MRI shim hardware constraints. Furthermore, we showed that *ConsTru* gave optimal results for multiple different VOIs, which previously had not been thoroughly investigated. In Fig. 5, we also showed that the algorithm works for 7T and

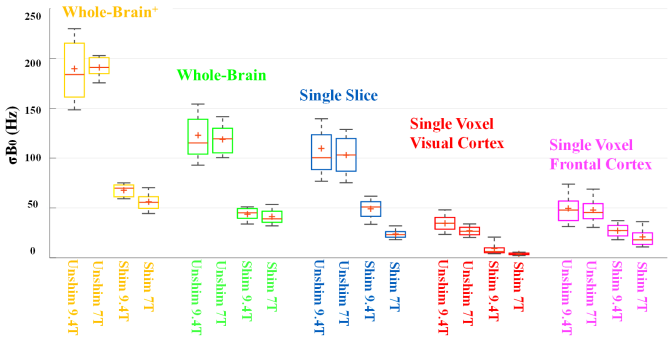

	Unshimmed 9.4 T	Unshimmed 7T	Shimmed (w/ *ConsTru*) 9.4 T	Shimmed (w/ *ConsTru*) 7 T
Whole brain +	189.56 ± 29.93	189.90 ± 10.92	67.86 ± 7.72	54.71 ± 8.81
Whole-Brain	122.86 ± 28.71	118.53 ± 14.87	43.85±6.98	38.33 ± 7.33
Single slice	110.74 ± 35.69	102.99 ± 19.87	49.25 ± 10.62	20.03 ± 4.28
Single voxel (visual cortex)	34.67 ± 9.60	26.90 ± 5.09	9.33 ± 6.98	3.79 ± 1.15
Single voxel (frontal cortex)	50.70 ± 30.69	48.0 ± 13.59	25.20 ± 10.62	15.01 ± 6.90

Figure 5: Achievable shim quality using the proposed ConsTru algorithm for the different ROIs (shown in Fig. 4) at 7T and 9.4T. The standard deviation of the reference field maps (measured with all shim currents set to zero, denoted as "unshimmed" in the plot) are also shown for comparison. Results are shown for a total of 33 volunteers at each field strength.

9.4T field strengths and how beneficial this algorithm is especially for the single voxel case.

Using an optimal algorithm to calculate B_0 shim currents is necessary because improving the B_0 field homogeneities through different methods such as different coil designs or slice-wise updates should not be biased or affected by a poorly chosen algorithm.

1.3 Spherical Harmonic Shimming

Much like the Fourier series for 1D signals, spherical harmonics form an orthogonal basis set for 3D signals. Spherical harmonic functions are, hence, a common method of decomposing and characterising 3D functions. A 3D scalar field can be approximated by spherical harmonic functions as follows:

$$B_0(\mathbf{r}) \approx \sum_{l=0}^{L} \sum_{m=-l}^{l} b_{l,m} \cdot A_{l,m}(\mathbf{r}) \tag{5}$$

where the spherical harmonic functions are $A_{l,m}(\mathbf{r})$, the $b_{l,m}$ are constant coefficients, l is the degree of the spherical harmonic function and m is the order[3]. The degree of the approximation is given by L. An illustration of the first, second and third degree spherical harmonic functions are depicted in Figure 1. In relation to the optimisation problem described in Eqn. 3, $A_{l,m}(\mathbf{r})$ becomes the matrix A, $B_0(\mathbf{r})$ becomes the vector b and the vector of coefficients $b_{l,m}$ form the vector x.

`Publication 2` demonstrates how very high degree (and order) spherical harmonic shimming can be used for B_0 shimming at ultra high field strengths. Most MRI scanners have up to 2^{nd} order shim coils and on some occasions may even have 3^{rd} order shim coils. In this case, very high order B_0 shimming refers to more than 3^{rd} order shim coils. This study was made possible due to the availability of an insert shim system from Resonance Research Inc. (Billerica, MA) that had up to full 4^{th} degree and partial 5^{th} and 6^{th} degree shim terms.

However, it is important to note that the shim coils do not necessarily generate the spherical harmonic shim field that they were designed to. Instead of generating the spherical harmonic shim field $A_{l,m}(\mathbf{r})$, imperfections in the manufacturing of the shim coils may lead to deviations $A_{l,m}(\mathbf{r}) + \varepsilon(\mathbf{r})$. This can be accounted for by measuring the actual (or real) shim fields using a B_0 mapping sequence. Indeed, very high degree B_0 shimming has previously been shown to be advantageous for B_0 homogenisation using this method with a similar shim system [13, 22]. Figure 6 shows the results of B_0

[3]The use of the terminology "order" for spherical harmonics is somewhat confused in the literature and usually refers to the degree. Out of convention, in this thesis, the use of the term "order" refers to the degree, unless otherwise stated.

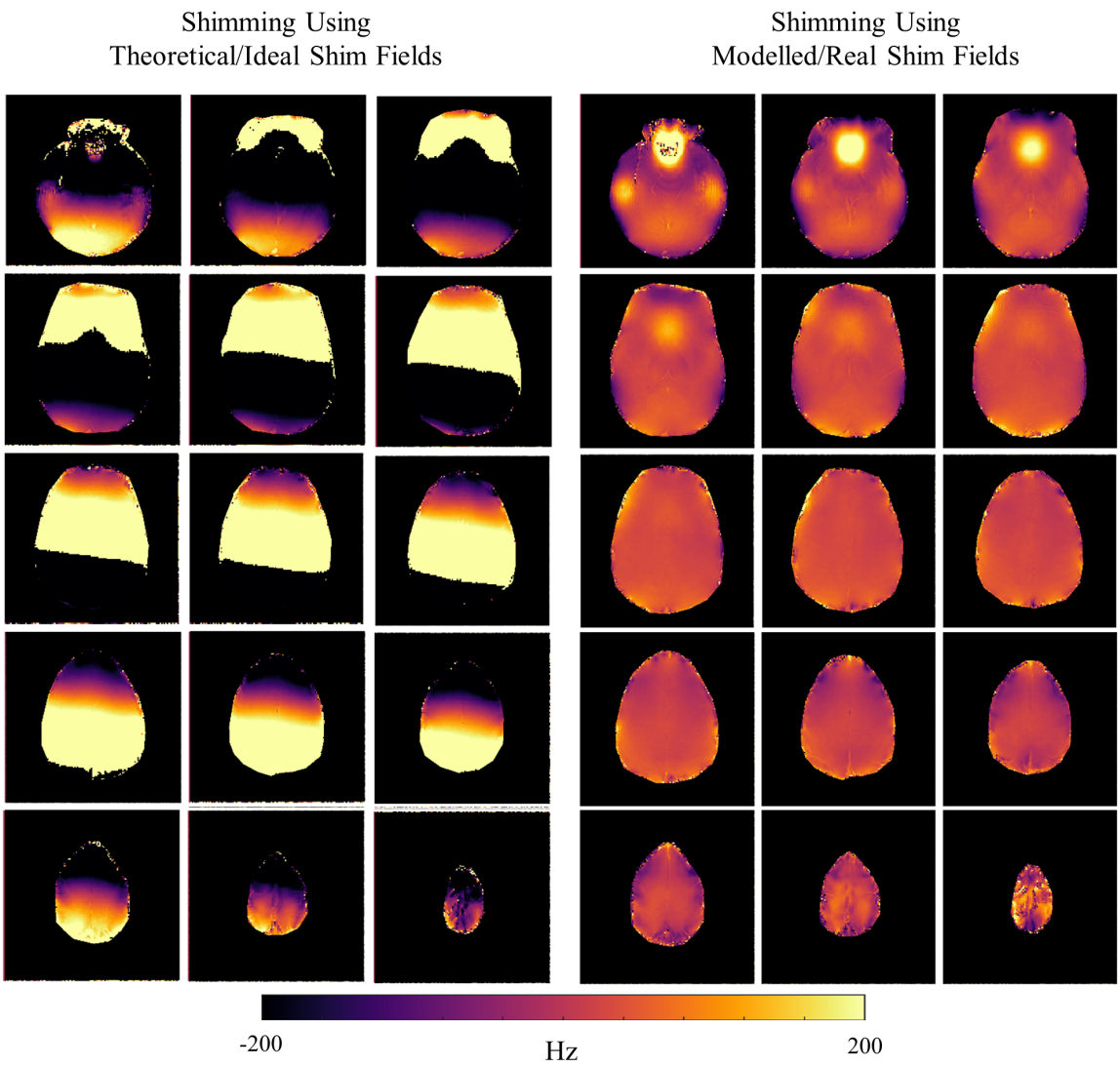

Figure 6: B_0 maps using real shim fields (considering the deviations) and using ideal shim fields (without considering the deviations) for B_0 shimming using all channels of the insert shim (i.e. full 4^{th} degree and partial $5^{th}/6^{th}$ degree spherical harmonics) from Resonance Research Inc. (Billerica, MA, USA).

shimming with and without considering the deviations. It is obvious from the figure that if the imperfections of the system are not accounted for, B_0 shimming completely fails.

In `Publication` 2, we took a slightly different approach by measuring the real shim fields $A_{l,m}(\mathbf{r}) + \varepsilon(\mathbf{r})$ and modelling the fields using spherical harmonic decomposition. The advantage of using a model instead of reference field maps is that they are easier to use since no interpolation is required (between the B_0 maps and the reference maps) and the reference field maps do not need to be stored. Furthermore, using a model allowed us to have amplitude models for the shim coils. A linear amplitude model, nearest-neighbour model and piece-wise linear model were investigated and compared. The process has been described in the publication.

Another aspect of B_0 shimming was also investigated and reported in the publication; that is, the problem of geometric distortion. B_0 inhomogeneities cause geometric distortions in the images (and subsequently the B_0 maps). However, decomposing the B_0 maps using spherical harmonics assumes that the positions are known and correct. Since we need to measure the shim fields, which intrinsically result in B_0 inhomogeneities, the B_0 maps of the shim fields are distorted. We, therefore, studied prospective and retrospective means to minimise the effects of geometric distortion.

In summary, we showed the necessity of considering the imperfections in shim systems. We also showed that using a modelling approach, very high order B_0 shimming can be successfully used for whole brain, single slice and single voxel applications. Additionally, we also showed that although there is advantage of going to higher and higher degree shim terms, the marginal improvement diminishes. In particular, going above more than 6^{th} degree spherical harmonics does not further improve the homogeneity. Similar results have been shown in [22].

1.4 Dynamic Slice-wise Shimming

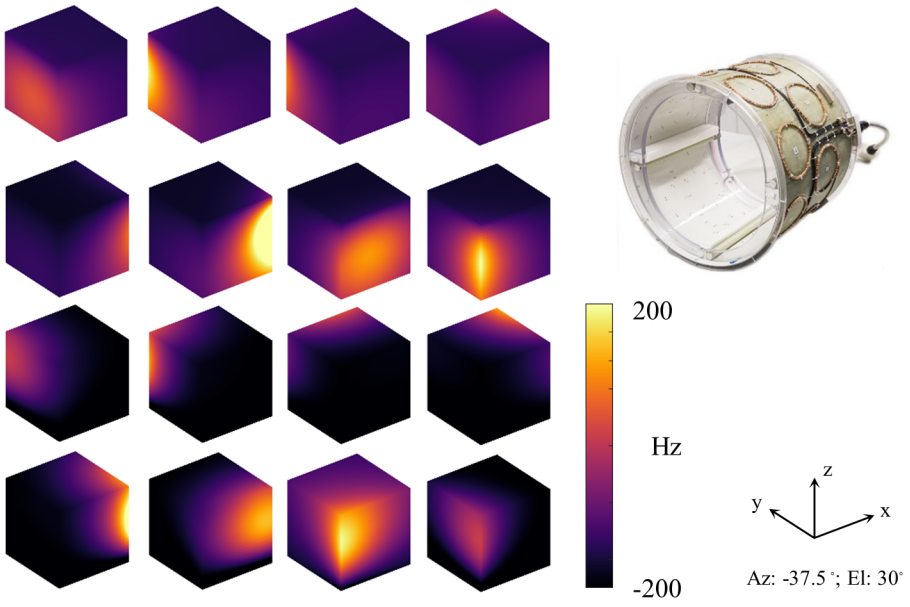

Figure 7: Multi-coil localised shim coil array and measured shim fields generated for each coil element of the array (for a current of 1.0A). The orientation is shown at an azimuth angle of -37.5° and an elevation angle of 30°.

For multi-slice 2D sequences, it is possible to perform slice-wise B_0 shimming. For each slice in the acquisition, different shim currents can be applied to the shim coils to produce a more homogeneous magnetic field for the slice currently being acquired.

Dynamic slice-wise shimming has previously been done using up to 3^{rd} order shim coils [16, 10]. It can also be done using localised shim coils [17]. In `Publication 3`, we extended the number of spherical harmonic shim channels and performed 4^{th}order dynamic slice-wise shimming. Furthermore, we also compared this very high order B_0 shim (VHOS) system to a localised shim coil array system. Even though there is research being done on the localised shim arrays, there is currently no comprehensive and consistent comparison between the two systems. In `Publication 3`, we attempted to compare the two shim systems as fairly as possible for slice-wise shimming. Since the 3^{rd} + 4^{th} order shim coils have 16 shim channels, we compared this to a localised shim array of 16 channels (two rows of 8 channel elements). Therefore, the number of channels was the same and both systems used the 2^{nd} order shim terms in conjunction

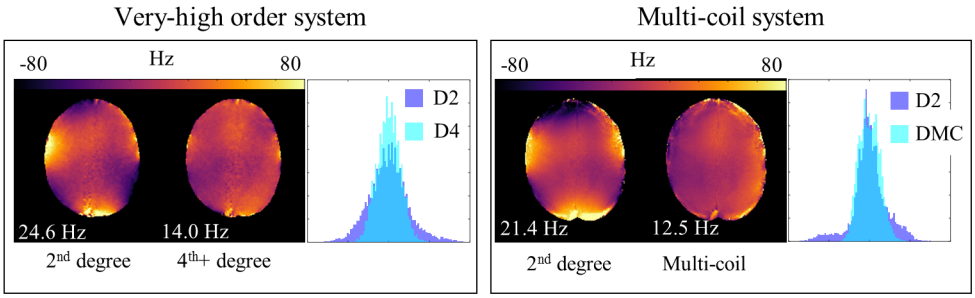

Figure 8: B_0 field maps using different shim systems on the same volunteer. A single transversal slice in the centre of the cerebrum is shown using a 2^{nd} degree shim and a $4^{th}+$ degree shim (for a very-high order shim system) and a 2^{nd} degree shim and a multi-coil shim system. Corresponding histograms are also shown for comparison.

with 16 extra coils. Furthermore, the same current constraints were used on both shim coil configurations. The multi-coil localised shim array that was used is shown in Figure 7.

Dynamic slice-wise shimming was found to have an advantage over static whole volume shimming. The homogeneity of the slices improved by 10 to 20 Hz at 9.4T, depending on the slice position. Slices closer to the top of the head tended to have less improvement. Our findings also showed that the advantage in B_0 homogeneity was very similar for both the VHOS system and the localised shim array. Fig. 8 shows B_0 field maps and the corresponding histograms using the different shim systems. The improvement that the higher degree shim channels offers is very similar to the improvement achieved by the multi-coil system. More results and analyses can be found in `Publication 3`.

In our publication, we showed the advantage of dynamic slice-wise shimming for mapping metabolites in the human brain using spectroscopic imaging. A brief review of the literature showed that Juchem et al. showed the advantage of dynamic slice-wise shimming [16, 17] but did not show any applications. Fillmer et al. showed the advantage for echo-planar imaging (EPI) [10]. We show that better B_0 shimming not only improves the reliability of detecting metabolites (indicated by the lower FWHM of the spectra and lower CRLBs of the fits for the more homogeneous fields), in addition, we show that the resulting metabolite maps differ in their structure. This means that

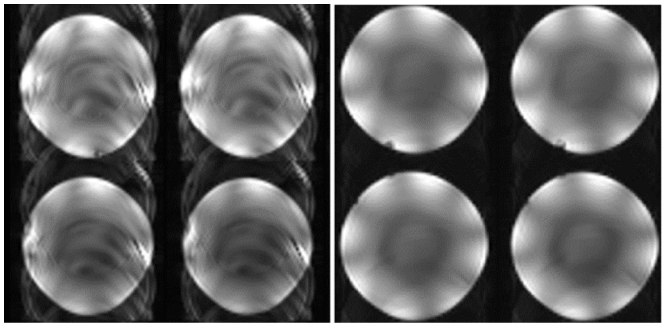

Figure 9: EPI image of the spherical phantom (a) with the insert shim inside the bore and (b) without the insert shim. No current was applied to any of the shim coils.

metabolite maps can change due to poor B_0 shimming and metabolite maps acquired with poor B_0 shimming do not accurately represent the underlying physiological state.

Although dynamically shimming with the VHOS was comparable to the dynamically shimming with the 16 channel multi-coil localised shim array setup, the design of the shim coils of the VHOS system are more susceptible to eddy currents caused by switching the shim and gradient currents (Figure 9). Therefore, the eddy currents need to be corrected for the VHOS system for fast switching, strong shim/gradient currents. This can be done using pre-emphasis as demonstrated in [10, 28].

1.5 Field Monitoring

As mentioned in the introduction, correcting for temporal fluctuations that may result from several effects (such as eddy currents and/or subject breathing and motion) requires a fast method to measure the B_0 fields. Conventional B_0 mapping has higher spatial resolution but low temporal resolution, while NMR field cameras have lower spatial resolution and higher temporal resolution.

The accuracy of NMR field cameras has previously not been thoroughly investigated. While NMR field cameras are likely to be sufficient for monitoring gradient trajectories, for higher order shim terms the accuracy of the NMR field camera becomes more limited. Particularly for shim terms 3^{rd} order and higher, the typical 16-probe field camera is insufficient [1]. We investigated the accuracy of the NMR field camera by comparing it to B_0 mapping sequences which have higher spatial resolution. We mitigated the problem of the insufficient number of field probes by moving the field camera to multiple positions and acquiring the data. We tested the NMR field camera's ability to measure the shim fields for shim terms up to the 4^{th} order.

Prior to the comparison of the NMR field camera and B_0 mapping, we first improved the position calibration of the field probes. The use of a NMR field camera requires the positions of the probes to be known. This is typically done using the gradient fields of the scanner and the change in the FID phase signal can be used to estimate the position [4, 3, 29, 28]. The x-,y-,z-gradients can be used to estimate the respective x-,y-,z-positions. However, this method does not account for any imperfections that may be present in the gradient fields. The gradient fields should be linear but small nonlinearities in the field result in inaccurate position estimates of the field probes. In `Publication 4`, we measured the gradient fields for more accurate estimation of the positions. Secondly, we also constrained the positions of the field probes relative to each other since these are physically fixed. We showed that the accuracy of estimating the positions of the field probes was improved by using the measured gradient fields and the relative position constraints of the field probes. Furthermore, we showed how errors in the position estimation of the field probes change the B_0 field measured using the NMR field camera. The 2^{nd} order shim fields measured using different position estimation methods is shown in Figure 10. The proposed method

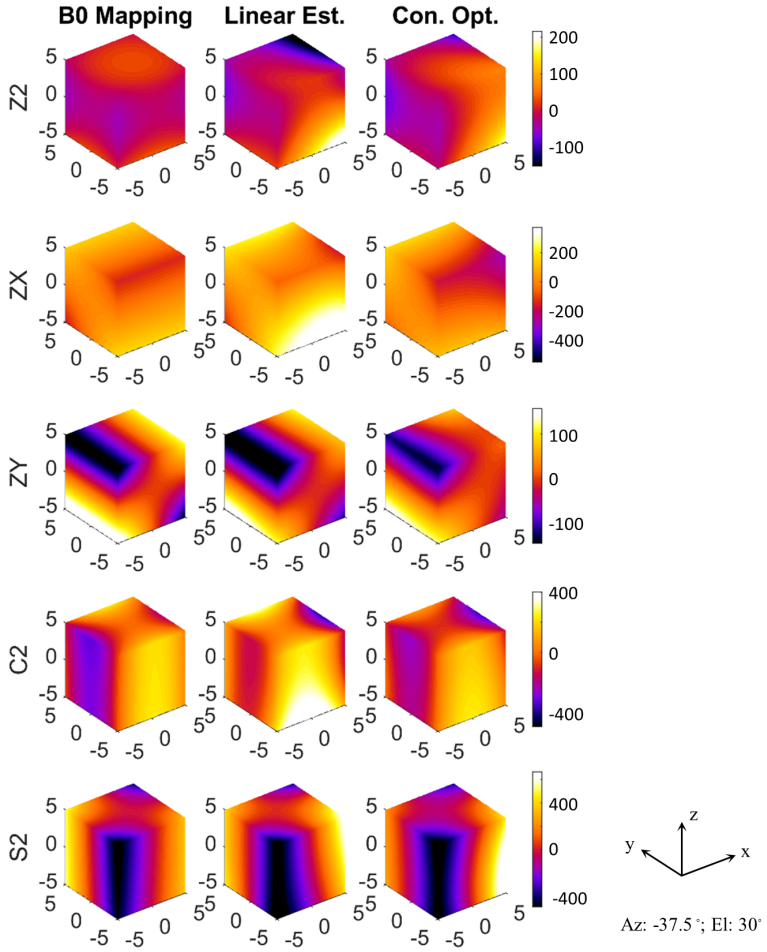

Figure 10: Shim fields measured using B_0 mapping and using a NMR field camera (with linear gradient position estimation and constrained optimised gradient position estimation). The orientation is shown at an azimuth angle of -37.5° and an elevation angle of 30°.

resulted in more robust measurements of the shim fields. The complete analysis of all shim terms up to the 4^{th} degree can be found in the publication.

Therefore, in `Publication 4`, we showed that the position estimation of the field probes can be improved by accounting for the nonlinearities in the gradient fields and also by constraining the relative positions of the field probes. We also showed a comparison of shim fields measured using an NMR field camera compared to B_0 mapping. The low spatial resolution of the NMR field camera proved to have a significant impact on the accuracy of measuring B_0 fields even when 50 probes are used.

1.6 Feedback

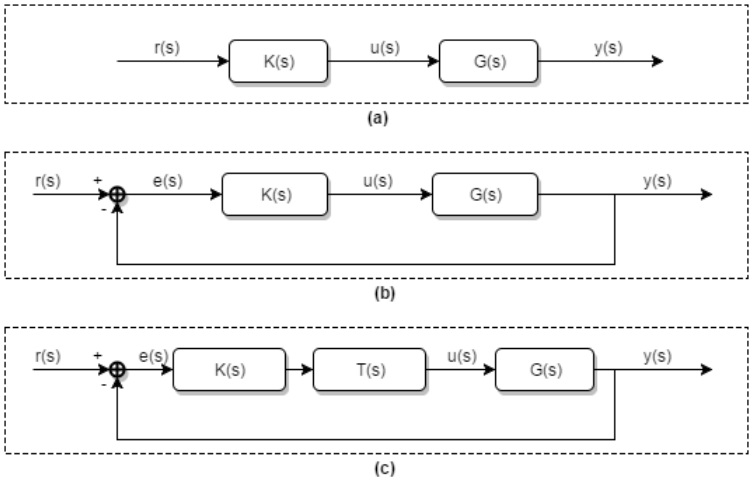

Figure 11: Schematics of (a) an open-loop controller where $G(s)$ is the system, $K(s)$ is the controller (or filter), $r(s)$ is the set-point signal, $u(s)$ is the input signal and $y(s)$ is the output signal, (b) a closed-loop control system where $e(s)$ is the error signal, and (c) a decoupled closed-loop controller where $T(s)$ is the decoupling filter.

If the magnetic field can be measured during the scan, this information can be used to correct for time-varying changes in the magnetic field. For example, one can use navigators interleaved in the sequence to estimate the magnetic field throughout the sequence. This can be used to correct for motion or update the shim currents [12, 19, 27]. However, including navigators or short B_0 read-outs in a sequence can increase the scan duration. Alternatively, if a field camera is available (such as the one described in the previous section), these measurements can be used to correct for the time-varying B_0 inhomogeneities. To date, this has been applied for slower time-varying effects such as breathing and motion correction [31, 5, 8].

If the shim currents are updated at a faster rate, the transient dynamics of the system come into play. Hence, design of a controller is necessary to ensure stability, robustness and good performance. Current implementations of feedback controllers in shim systems use proportional-integral-derivative (PID) controllers or proportional-integral (PI) controllers tuned using the Ziegler-Nichols method [31]. However, this tuning method has been shown to have large overshoot and hence is less robust [2, 7].

The design of controllers often makes the assumption that the system that needs to be controlled is linear time-invariant (LTI). Although there are studies investigating nonlinear systems, such as using input-output linearisation, state linearisation or phase portraits for design, the focus of this study was on linear systems. This is due to the fact that eddy currents can be modelled quite accurately using exponentially decaying functions [14] where the assumption of linear time-invariance holds true. A LTI system can be represented as a transfer function. This means that a n^{th}-order ordinary differential equation:

$$a_n \left(\frac{d}{dt}\right)^n \cdot y(t) + ... + a_1 \frac{d}{dt} \cdot y(t) + a_0 y(t) = b_n \left(\frac{d}{dt}\right)^n \cdot x(t) + ... + b_1 \frac{d}{dt} \cdot x(t) + b_0 x(t)$$

can be written as:

$$\begin{gathered} a_n s^n Y(s) + ... + a_1 s Y(s) + a_0 Y(s) = b_m s^m X(s) + ... + b_1 s X(s) + b_0 X(s) \\ (a_n s^n + ... + a_1 s + a_0) \cdot Y(s) = (b_m s^m + ... + b_1 s + b_0) \cdot X(s) \\ G(s) = \frac{Y(s)}{X(s)} = \frac{b_m s^m + ... + b_1 s + b_0}{a_n s^n + ... + a_1 s + a_0} \end{gathered}$$

where $Y(s)$ and $X(s)$ are the Laplace transforms of the signals $y(t)$ and $x(t)$, respectively (assuming zero initial conditions). Transfer functions can also be represented in the frequency domain by replacing $s = j\omega$.

An open-loop controller (Fig. 11a) such as using pre-emphasis compensation simply includes another transfer function $K(s)$ before the system $G(s)$ such that $K(s) \approx G^{-1}(s)$. Therefore, the whole system would then become:

$$H(s) = K(s) \cdot G(s) \approx I(s)$$

and hence the output $Y(s) \approx I(s) \cdot X(s) = X(s)$.

However, in a closed-loop system (Fig. 11b), the system would become:

$$H(s) = \frac{G(s)}{1 + K(s) \cdot G(s)}$$

and therefore the design of $K(s)$ is less obvious than in the open-loop case.

Now, a single-input single-output (SISO) system can be extended to a multiple-

input multiple-output (MIMO) system intuitively, by creating an array of transfer functions (since linearity is assumed). Although there are multiple design methods for designing such MIMO controllers, many of these methods are not easily scalable to larger systems. The simplest and most practical approach to larger systems is to decouple the MIMO system into a system of multiple SISO systems. That is, to try and form a diagonal transfer function matrix as such:

$$G(s) = \begin{bmatrix} G_{1,1}(s) & \cdots & G_{1,Q}(s) \\ \vdots & \ddots & \vdots \\ G_{P,1}(s) & \cdots & G_{P,Q}(s) \end{bmatrix}$$

$$\Rightarrow G^*(s) = G(s) \cdot T(s) = \begin{bmatrix} G^*_{1,1}(s) & \cdots & 0 \\ \vdots & \ddots & \vdots \\ 0 & \cdots & G^*_{P,Q}(s) \end{bmatrix}$$

where $G^*(s)$ is the decoupled system (so all the off-diagonal transfer functions are zero for the frequency range of interest) and where P and Q are the number of outputs and inputs, respectively.

After the system has been sufficiently well decoupled, the system can be treated as multiple SISO controllers.

Currently, PID controllers are prevalent in industry due to their simplicity of implementation. PID controllers can be presented in the s-domain as such:

$$K(s) = K_P + {}^{K_I}/_{s} + K_D s$$

Even though the structure of PID controllers is simple, the design and tuning of such controllers is still often based on rule-of-thumb and emperically done. Design of optimal PID controllers is still, even to this day, under investigation. The reason for this is that controller design has multiple objectives that need to be satisfied, including their performance and robustness against disturbances. Furthermore, the objectives are highly non-linear and require large amounts of computation.

In light of this, in this thesis two steps for designing controllers for shim systems were proprosed: firstly, the decoupling of the shim system was investigated; secondly,

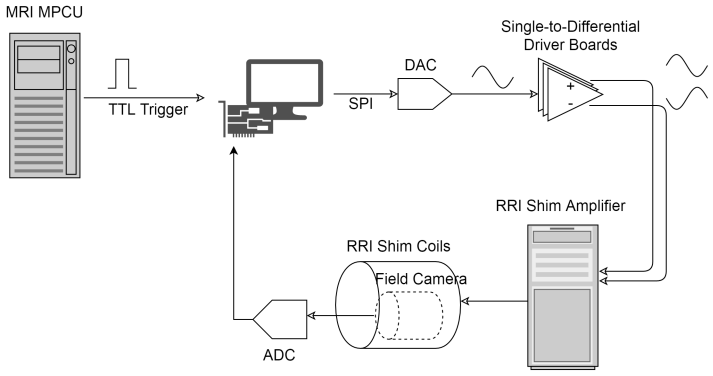

Figure 12: Schematic of a closed-loop system for a B_0 shim system using a field camera and digital controllers.

the design of PI controllers were investigated to find more robust controllers that gave good performance. In `Publication 5`, we investigated different decoupling strategies for a spherical harmonic based shim coil system. Since, the shim coils were based on spherical harmonic functions, the generated fields should be approximately orthogonal. This means that decoupling the system comes intuitively. Each shim field can be decomposed into the theoretical spherical harmonic functions.

Static and dynamic decoupling strategies were compared. For static decoupling, two methods were investigated: a standard static decoupling of the steady state (i.e. at a frequency of 0Hz) and an optimised static decoupling method. The Vaes method [26] was used for the optimised static decoupling that optimises the elements in the decoupling matrices over a range of frequencies using the μ-interaction as an objective function.

Although the dynamic decoupling (analogous to pre-emphasis or compensation) gave better decoupling results when evaluated with the μ-interaction term, in the closed-loop design, the static decoupling gave more robust results. In this case, static decoupling was a better solution as it was more robust and had a similar performance to the dynamically decoupled system. A schematic of the closed-loop system is shown in Fig. 12.

Finally, different methods for optimising and tuning PI controllers were investigated. In `Publication 6`, the optimisation problem was cast as a multi-objective problem where the settling time, sensitivity, complementary sensitivity and control

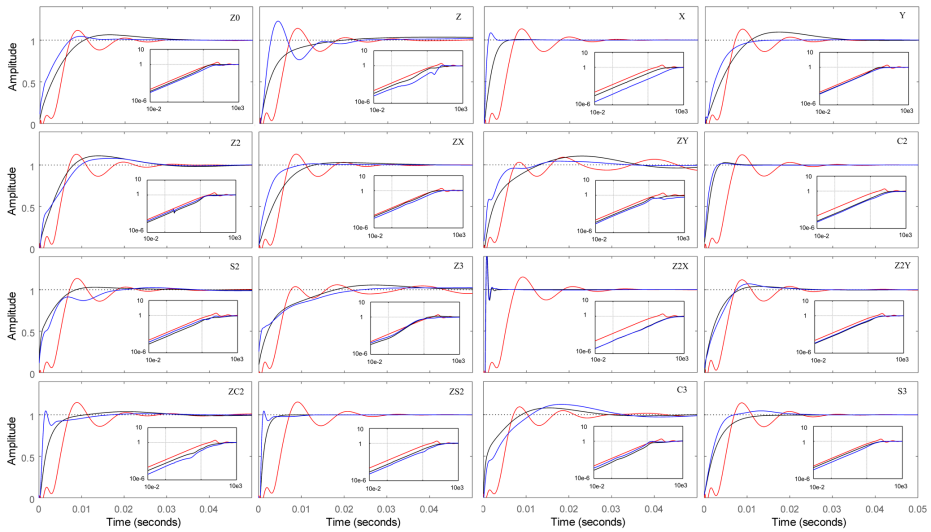

Figure 13: Closed-loop time-domain responses of the diagonal self-terms for a full 3$^{\text{rd}}$ degree/order shim system using dynamic decoupling (red), static decoupling (black) and static decoupling (blue) using the Vaes method [26]. Sensitivity functions for each of the closed-loop responses are also shown in the frequency domain. The sensitivity function is defined as $\frac{1}{1+K(s).G(s)}$, where $G(s)$ is the system, $K(s)$ is the controller.

effort were used as the objective functions. The domain space for the input parameters were constrained using the Routh-Hurwitz stability criteria and by defining a minimum closed-loop response time. The results showed that the dominant features could be described by the settling time and sensivity function; there was also a trade-off between these two features. Therefore, in `Publication 5`, only two features were used: 1) the phase margin as a place-holder for the sensitivity function and 2) the integral-absolute-error (IAE) as a placeholder for the settling-time. Since, in this case, the robustness was more important due to possible cross-coupling of a multi-input multi-output system, the phase margin was used as the objective function and the IAE was used as a constraint. This made the optimisation problem much simpler and the results show good robustness for all the channels while satisfying the settling time constraint. The closed-loop time-domain responses of the diagonal self-terms along with the frequency domain sensitivity functions are shown in Fig. 13 for all three decoupling methods.

Therefore, we showed that for a spherical harmonic-based shim system, decoupling

control could be used effectively to improve the closed-loop response of the system. Secondly, we presented an optimisation method for PI controller tuning instead of using the Ziegler-Nichols method.

1.7 Summary

In this thesis, we presented an amalgamation of software, hardware and design improvements for the application of B_0 shimming of magnetic fields. An optimal algorithm was developed that takes into account the hardware constraints of the amplifiers and was tested on for multiple ROIs and applications. Global static whole-brain shimming was demonstrated at 9.4T using very high order B_0 shimming. This could only be achieved by accounting for the imperfections in each shim field. It was also demonstrated that this methodology works for dynamic slice-wise B_0 shim updating using a very high order shim system and is also comparable to using a 16 channel multi-coil array. Next, a field camera was constructed and the position calibration of the field probes was optimised for better field monitoring. Finally, the field camera was used to measure the time dynamics of the shim system and this model was used to design a decoupling controller with optimised PI controllers.

Needless to say, further investigation is still required for even better B_0 homogeneity. However, with the current progress in this research field, sufficiently homogeneous magnetic fields should be possible for ultra high field applications.

References

[1] Mads Andersen, Lars G Hanson, Kristoffer H Madsen, Joep Wezel, Vincent Boer, Tijl van der Velden, Matthias JP van Osch, Dennis Klomp, Andrew G Webb, and Maarten J Versluis. Measuring motion-induced B_0-fluctuations in the brain using field probes. *Magnetic Resonance in Medicine*, 75(5):2020–2030, 2016.

[2] Karl Johan Åström and Tore Hägglund. Revisiting the Ziegler–Nichols step response method for PID control. *Journal of Process Control*, 14(6):635–650, 2004.

[3] Christoph Barmet, Nicola De Zanche, Bertram J Wilm, and Klaas P Pruessmann. A transmit/receive system for magnetic field monitoring of in vivo MRI. *Magnetic Resonance in Medicine*, 62(1):269–276, 2009.

[4] Christoph Barmet, Nicola De Zanche, and Klaas P Pruessmann. Spatiotemporal magnetic field monitoring for MR. *Magnetic Resonance in Medicine*, 60(1):187–197, 2008.

[5] Vincent O Boer, Gerard van Vliet, Peter R Luijten, Dennis WJ Klomp, et al. Direct B_0 field monitoring and real-time B_0 field updating in the human breast at 7 Tesla. *Magnetic Resonance in Medicine*, 67(2):586–591, 2012.

[6] Ch Boesch, R Gruetter, and E Martin. Temporal and spatial analysis of fields generated by eddy currents in superconducting magnets: optimization of corrections and quantitative characterization of magnet/gradient systems. *Magnetic Resonance in Medicine*, 20(2):268–284, 1991.

[7] Gustavo Maia de Almeida, Valceres Vieira Rocha e Silva, Erivelton Geraldo Nepomuceno, and Ryuichi Yokoyama. Application of genetic programming for fine tuning PID controller parameters designed through Ziegler-Nichols technique. In *International Conference on Natural Computation*, pages 313–322. Springer, 2005.

[8] Yolanda Duerst, Bertram J Wilm, Benjamin E Dietrich, S Johanna Vannesjo, Christoph Barmet, Thomas Schmid, David O Brunner, and Klaas P Pruessmann. Real-time feedback for spatiotemporal field stabilization in MR systems. *Magnetic Resonance in Medicine*, 73(2):884–893, 2015.

[9] Ariane Fillmer, Thomas Kirchner, Donnie Cameron, and Anke Henning. Constrained image-based B_0 shimming accounting for local minimum traps in the optimization and field inhomogeneities outside the region of interest. *Magnetic Resonance in Medicine*, 73(4):1370–1380, 2015.

[10] Ariane Fillmer, Signe Johanna Vannesjo, Matteo Pavan, Milan Scheidegger, Klaas Paul Pruessmann, and Anke Henning. Fast iterative pre-emphasis calibration method enabling third-order dynamic shim updated fMRI. *Magnetic Resonance in Medicine*, 75(3):1119–1131, 2016.

[11] R Gruetter. Localized in vivo adjustment of all first-and second-order shim coils. *Magnetic Resonance Imaging*, 20:801–811, 1993.

[12] Aaron T Hess, M Dylan Tisdall, Ovidiu C Andronesi, Ernesta M Meintjes, and André JW van der Kouwe. Real-time motion and B_0 corrected single voxel spectroscopy using volumetric navigators. *Magnetic Resonance in Medicine*, 66(2):314–323, 2011.

[13] Hoby P Hetherington, Wen-Jang Chu, Oded Gonen, and Jullie W Pan. Robust fully automated shimming of the human brain for high-field ^{1}H spectroscopic imaging. *Magnetic Resonance in Medicine*, 56(1):26–33, 2006.

[14] P Jehenson, M Westphal, and N Schuff. Analytical method for the compensation of eddy-current effects induced by pulsed magnetic field gradients in NMR systems. *Journal of Magnetic Resonance (1969)*, 90(2):264–278, 1990.

[15] Peter Jezzard and Robert S Balaban. Correction for geometric distortion in echo planar images from B_0 field variations. *Magnetic Resonance in Medicine*, 34(1):65–73, 1995.

[16] Christoph Juchem, Terence W Nixon, Piotr Diduch, Douglas L Rothman, Piotr Starewicz, and Robin A De Graaf. Dynamic shimming of the human brain at 7T. *Concepts in Magnetic Resonance Part B: Magnetic Resonance Engineering*, 37(3):116–128, 2010.

[17] Christoph Juchem, Terence W Nixon, Scott McIntyre, Vincent O Boer, Douglas L Rothman, and Robin A de Graaf. Dynamic multi-coil shimming of the human brain at 7T. *Journal of Magnetic Resonance*, 212(2):280–288, 2011.

[18] Christoph Juchem, S Umesh Rudrapatna, Terence W Nixon, and Robin A de Graaf. Dynamic multi-coil technique (DYNAMITE) shimming for echo-planar imaging of the human brain at 7 Tesla. *NeuroImage*, 105:462–472, 2015.

[19] Brian Keating and Thomas Ernst. Real-time dynamic frequency and shim correction for single-voxel magnetic resonance spectroscopy. *Magnetic Resonance in Medicine*, 68(5):1339–1345, 2012.

[20] Dong-Hyun Kim, Elfar Adalsteinsson, Gary H Glover, and Daniel M Spielman. Regularized higher-order in vivo shimming. *Magnetic Resonance in Medicine*, 48(4):715–722, 2002.

[21] Kevin M Koch, Scott McIntyre, Terence W Nixon, Douglas L Rothman, and Robin A de Graaf. Dynamic shim updating on the human brain. *Journal of Magnetic Resonance*, 180(2):286–296, 2006.

[22] Jullie W Pan, Kai-Ming Lo, and Hoby P Hetherington. Role of very high order and degree B_0 shimming for spectroscopic imaging of the human brain at 7 Tesla. *Magnetic Resonance in Medicine*, 68(4):1007–1017, 2012.

[23] Françoise Roméo and DI Hoult. Magnet field profiling: analysis and correcting coil design. *Magnetic Resonance in Medicine*, 1(1):44–65, 1984.

[24] Jun Shen, Robert E Rycyna, and Douglas L Rothman. Improvements on an in vivo automatic shimming method (FASTERMAP). *Magnetic Resonance in Medicine*, 38(5):834–839, 1997.

[25] Jason P Stockmann, Thomas Witzel, Boris Keil, Jonathan R Polimeni, Azma Mareyam, Cristen LaPierre, Kawin Setsompop, and Lawrence L Wald. A 32-channel combined RF and B_0 shim array for 3T brain imaging. *Magnetic Resonance in Medicine*, 75(1):441–451, 2016.

[26] D Vaes, Kurt Engelen, Jan Anthonis, Jan Swevers, and Paul Sas. Multivariable feedback design to improve tracking performance on tractor vibration test rig. *Mechanical Systems and Signal Processing*, 21(2):1051–1075, 2007.

[27] P Van Gelderen, JA De Zwart, P Starewicz, RS Hinks, and JH Duyn. Real-time shimming to compensate for respiration-induced B_0 fluctuations. *Magnetic Resonance in Medicine*, 57(2):362–368, 2007.

[28] S Johanna Vannesjo, Yolanda Duerst, Laetitia Vionnet, Benjamin E Dietrich, Matteo Pavan, Simon Gross, Christoph Barmet, and Klaas P Pruessmann. Gradient and shim pre-emphasis by inversion of a linear time-invariant system model. *Magnetic Resonance in Medicine*, 2016.

[29] Signe J Vannesjo, Maximilan Haeberlin, Lars Kasper, Matteo Pavan, Bertram J Wilm, Christoph Barmet, and Klaas P Pruessmann. Gradient system characterization by impulse response measurements with a dynamic field camera. *Magnetic Resonance in Medicine*, 69(2):583–593, 2013.

[30] Heidi A Ward, Stephen J Riederer, and Clifford R Jack. Real-time autoshimming for echo planar timecourse imaging. *Magnetic Resonance in Medicine*, 48(5):771–780, 2002.

[31] Bertram J Wilm, Yolanda Duerst, Benjamin E Dietrich, Michael Wyss, S Johanna Vannesjo, Thomas Schmid, David O Brunner, Christoph Barmet, and Klaas P Pruessmann. Feedback field control improves linewidths in in vivo magnetic resonance spectroscopy. *Magnetic Resonance in Medicine*, 71(5):1657–1662, 2014.

[32] James L Wilson, Mark Jenkinson, and Peter Jezzard. Optimization of static field homogeneity in human brain using diamagnetic passive shims. *Magnetic Resonance in Medicine*, 48(5):906–914, 2002.

2 List of Publications

2.1 Appended Publications

1. S Nassirpour*, **P Chang***, A Fillmer, A Henning, "A Comparison of Optimization Algorithms for Localized *In Vivo* B_0 Shimming" *Magnetic Resonance in Medicine*, 2017, doi:10.1002/mrm.26758.

2. **P Chang***, S Nassirpour*, A Henning, "Modeling Real Shim Fields for Very High Degree (and Order) B_0 Shimming of the Human Brain at 9.4T" *Magnetic Resonance in Medicine*, 2017, doi:10.1002/mrm.26658.

3. **P Chang***, S Nassirpour*, A Henning, "Dynamic B_0 Shimming at Ultra High Fields for Proton Spectroscopic Imaging of the Human Brain" *(in preparation)*

4. **P Chang**, S Nassirpour, M Eschelbach, K Scheffler, A Henning, "Constrained Optimisation for Position Calibration of a NMR Field Camera" *Magnetic Resonance in Medicine*, 2017, doi:10.1002/mrm.27010.

5. **P Chang**, S Nassirpour, A Henning, "Controller Design for Feedback of B_0 Shim Systems" *Magnetic Resonance in Medicine*, 2018 *(submitted)*.

6. **YC Chang**, N Avdievitch, A Henning, "System Identification and Signal Processing for PID Control of B_0 Shim Systems in Ultra-High Field Magnetic Resonance Applications" *Proc. of 19th World Congress of the International Federation of Automatic Control*, 47(3), pp. 7517-7522, 2014.

2.2 Other Recent Publications

Journal Articles

1. **P Chang***, S Nassirpour*, N Avdievich, A Henning, "Non-water Suppressed ^{1}H FID-MRSI at 3T and 9.4T" *Magnetic Resonance in Medicine*, 2017 doi:10.1002/mrm.27049.

*Equal contributions to the publication

2. S Nassirpour*, **P Chang***, A Henning, "Over-discretized SENSE reconstruction and B0 correction for accelerated non-lipid suppressed 1H FID MRSI of the human brain at 9.4T" *NMR in Biomedicine*, 2017 [submitted]

3. S Nassirpour*, **P Chang***, N Avdievich, A Henning, "Compressed Sensing for High-Resolution Non-lipid Suppressed ^{1}H FID MRSI of the Human Brain at 9.4T" *Magnetic Resonance in Medicine*, 2017 [accepted]

4. S Nassirpour, **P Chang**, A Henning, "High and ultra-high resolution metabolite mapping of the human brain using ^{1}H FID MRSI at 9.4T" *NeuroImage*, 2016, doi: 10.1016/j.neuroimage.2016.12.065.

Conference Papers

1. J Handwerker, M Ortmanns, J Anders, M Eschelback, **P Chang**, A Henning, K Scheffler, "An active TX/RX NMR probe for real-time monitoring of MRI field imperfections" IEEE Biomedical Circuits and Systems Conference, pp. 194-197, 2013.

Talks

1. **P Chang**, S Nassirpour, A Aghaeifar, K Scheffler, A Henning, "Dynamic B0 Shimming for Multi-Slice Metabolite Mapping at Ultra-High Field in the Human Brain: Very High Order Spherical Harmonics vs. Multi-Coil" *Proc. of the 26th Annual Meeting of the International Society for Magnetic Resonance in Medicine*, 2018 [abstract accepted].

2. S Nassirpour, **P Chang**, A Henning, "Whole Brain High Resolution Metabolite Mapping Using 1H FID MRSI with Slice-wise B0 Shim Updating at 9.4T" *Proc. of the 26th Annual Meeting of the International Society for Magnetic Resonance in Medicine*, 2018 [abstract accepted].

3. **P Chang**, S Nassirpour, A Henning, "ConsTru: an Optimal B0 Shimming Solution", *Proc. of the 34th Annual Meeting of the European Society of Magnetic Resonance in Medicine and Biology*, 2017.

4. S Nassirpour, **P Chang**, A Henning, "Over-discrete SENSE and B0 Correction for Accelerated 1H FID MRSI of the Human Brain at 9.4T" *Proc. of the 34th Annual Meeting of the European Society of Magnetic Resonance in Medicine and Biology*, 2017.

5. **P Chang**, S Nassirpour, A Henning, "Fast non-water suppressed metabolite cycled 1H FID MRSI at both 3T and 9.4T" *Proc. of the 25th Annual Meeting of the International Society for Magnetic Resonance in Medicine*, 2017.

6. S Nassirpour, **P Chang**, A Henning, "High resolution maps of individual macromolecule components in the human brain at 9.4T" *Proc. of the 25th Annual Meeting of the International Society for Magnetic Resonance in Medicine*, 2017.

7. S Nassirpour, **P Chang**, A Henning, "Pushing the limits of ultra-high field MRSI: benefits and limitations of 9.4T for metabolite mapping of the human brain" *Proc. of the 25th Annual Meeting of the International Society for Magnetic Resonance in Medicine*, 2017.

8. S Nassirpour, **P Chang**, A Henning, "Multi-slice metabolite mapping with Very-High Degree Dynamic B_0 Shim Updating at 9.4T using Accelerated ^{1}H FID MRSI" *Proc. of the 25th Annual Meeting of the International Society for Magnetic Resonance in Medicine*, 2017.

9. **P Chang**, S Nassirpour, A Henning, "Very High-Order B_0 Shimming for Ultra-High Field Magnetic Resonance" *ISMRM Workshop on MR Spectroscopy: From Current Best Practice to Latest Frontiers*, 2016.

10. S Nassirpour, **P Chang**, A Henning, "Metabolite Mapping of the Human Brain Using 1H FID MRSI at 9.4T" *ISMRM Workshop on MR Spectroscopy: From Current Best Practice to Latest Frontiers*, 2016.

11. S Nassirpour, **P Chang**, A Henning, "A Comparison of Optimization Algorithms for Localized In-Vivo Shimming" *ISMRM Workshop on MR Spectroscopy: From Current Best Practice to Latest Frontiers*, 2016.

12. S Nassirpour, **P Chang**, A Henning, "A Comparison of Optimization Algorithms for Localized *in-vivo* B_0 Shimming" *Proc. of the 24th Annual Meeting of the International Society for Magnetic Resonance in Medicine*, 2016.

13. M Eschelbach, A Loktyushin, **P Chang**, J Handwerker, J Anders, A Henning, A Thielscher, K Scheffler, "A Comparison of ^{19}F NMR Field Probes and an Optical Camera System for Motion Tracking" *Proc. of the 24th Annual Meeting of the International Society for Magnetic Resonance in Medicine*, 2016.

Posters

1. **P Chang**, S Nassirpour, A Henning, "Highly Accelerated (R=14) Water Reference Acquisition for High Resolution 1H MRSI using Compressed Sensing" *Proc. of the 26th Annual Meeting of the International Society for Magnetic Resonance in Medicine*, 2018 [abstract accepted].

2. **P Chang**, S Nassirpour, A Henning, "Measuring Eddy Currents Induced by Switching Gradient/Shim Currents" *Proc. of the 26th Annual Meeting of the International Society for Magnetic Resonance in Medicine*, 2018 [abstract accepted].

3. S Nassirpour, **P Chang**, A Henning, "MultiNet PyGRAPPA: A Novel Method for Highly Accelerated Metabolite Mapping" *Proc. of the 26th Annual Meeting of the International Society for Magnetic Resonance in Medicine*, 2018 [abstract accepted].

4. S Nassirpour, **P Chang**, A Henning, "SNR Requirements for Successful Application of Compressed Sensing Acceleration to Non-lipid suppressed 1H MRSI at Ultra-High Fields" *Proc. of the 26th Annual Meeting of the International Society for Magnetic Resonance in Medicine*, 2018 [abstract accepted].

5. S Nassirpour, **P Chang**, A Henning, "Over-discretized SENSE reconstruction and B0 correction for accelerated non-lipid suppressed 1H FID MRSI of the human brain at 9.4T" *Proc. of the 26th Annual Meeting of the International Society for Magnetic Resonance in Medicine*, 2018 [abstract accepted].

6. A Wright, S Nassirpour, **P Chang**, A Henning, "Toward Absolute Quantification Using External Reference Standards at 3T and 9.4T" *Proc. of the 26th Annual Meeting of the International Society for Magnetic Resonance in Medicine*, 2018 [abstract accepted].

7. **P Chang**, S Nassirpour, A Henning, "Magnetic Field Homogeneity for Small Volume MR Spectroscopy" *European Society of Molecular Imaging*, Les Houches, France, 2018.

8. S Nassirpour, **P Chang**, A Henning, "Pushing the Limits of MR Spectroscopic Imaging: Benefits and Limitations of Ultra-high Field Strengths for Metabolite Mapping of the Human Brain" *European Society of Molecular Imaging*, Les Houches, France, 2018.

9. **P Chang**, S Nassirpour, A Henning, "Low SAR Lipid Suppression for MRSI at Ultra-high Fields" *Proc. of the 34th Annual Meeting of the European Society of Magnetic Resonance in Medicine and Biology*, 2017.

10. **P Chang**, S Nassirpour, A Henning, "Compressed Sensing for ^{1}H MRSI in the Human Brain" *Proc. of the 34th Annual Meeting of the European Society of Magnetic Resonance in Medicine and Biology*, 2017.

11. S Nassirpour, **P Chang**, A Henning, "The Necessity of Parametrizing Macromolecules for Accurate Quantification of Ultra-short TE and TR 1H FID MRSI Data at 9.4T"*Proc. of the 34th Annual Meeting of the European Society of Magnetic Resonance in Medicine and Biology*, 2017.

12. S Nassirpour, **P Chang**, A Henning, "Comparison of different acceleration methods for high-resolution metabolite mapping using ^{1}H FID MRSI at 9.4T" *Proc. of the 25th Annual Meeting of the International Society for Magnetic Resonance in Medicine*, 2017.

13. **P Chang**, S Nassirpour, A Henning, "Decoupling Controller Design for Real-time Feedback of B_0 Shim Systems" *Proc. of the 25th Annual Meeting of the International Society for Magnetic Resonance in Medicine*, 2017.

14. **P Chang**, S Nassirpour, A Henning, "Dynamic B_0 Shim Controller for Digital Pre-emphasis with Sub-millisecond Update Rate" *Proc. of the 25th Annual Meeting of the International Society for Magnetic Resonance in Medicine*, 2017.

15. **P Chang**, S Nassirpour, A Henning, "Flexible General-Purpose Embedded System for Real-time Feedback and Dynamic B_0 Shimming" *Proc. of the 25th Annual Meeting of the International Society for Magnetic Resonance in Medicine*, 2017.

16. **P Chang**, S Nassirpour, A Henning, "Limitations of NMR Field Cameras for B_0 Field Monitoring" *Proc. of the 25th Annual Meeting of the International Society for Magnetic Resonance in Medicine*, 2017.

17. **P Chang**, S Nassirpour, A Fillmer, A Henning, "Correcting Geometric Distortion in B_0 Mapping" *Proc. of the 24th Annual Meeting of the International Society for Magnetic Resonance in Medicine*, 2016.

18. **P Chang**, S Nassirpour, A Henning, "Very High Order B_0 Shimming of the Human Brain at 9.4T Considering Real B_0 Shim Fields" *Proc. of the 24th Annual Meeting of the International Society for Magnetic Resonance in Medicine*, 2016.

19. **P Chang**, S Nassirpour, A Henning, "Very High-order B_0 Shimming for Single-Shot EPI at 9.4T in the Human Brain" *ISMRM Workshop on Ultra High Field MRI: Technological Advances and Clinical Applications*, 2016.

20. **P Chang**, M Eschelbach, R Syha, K Scheffler, A Henning, "Impact of Gradient Nonlinearity on the Accuracy of NMR Field Camera Readouts" *Proc. of the 23rd Annual Meeting of the International Society for Magnetic Resonance in Medicine*, 2015.

21. M Eschelbach, **P Chang**, J Handwerker, J Anders, A Henning, K Scheffler, "Tracking Motion and Resulting Field Fluctuations Using ^{19}F NMR Field Probes" *Proc. of the 23rd Annual Meeting of the International Society for Magnetic Resonance in Medicine*, 2015.

22. T Shao, NI Avdievich, **P Chang**, J Hoffmann, K Scheffler, A Henning, "Systematic Investigation of Influence Factor on Parallel Transmit Pulse Performance at 9.4 Tesla" *Proc. of the 23rd Annual Meeting of the International Society for Magnetic Resonance in Medicine*, 2015.

23. **P Chang**, M Eschelbach, N Avdievich, K Scheffler, A Henning, "Fast Method for Parametric System Identification of Gradient Systems" *Proc. of the Joint Annual Meeting of the ISMRM and ESMRMB*, 2014.

24. **P Chang**, M Eschelbach, K Scheffler, A Henning, "Hybrid Digital Phase-Locked Loop and Moving Average Filtering Improves SNR in Spatio-Temporal Field Monitoring" *Proc. of the Joint Annual Meeting of the ISMRM and ESMRMB*, 2014.

3 Statement of Contributions

3.1 A Comparison of Optimization Algorithms for Localized *In Vivo* B_0 Shimming

In vivo B_0 maps were acquired from ultra high field MRI scanners and multiple different algorithms were used to shim the B_0 maps. The algorithms that were compared were the ones that are typically used in the literature and hardware constraints were applied to the optimisation problem. The algorithms were compared for different regions-of-interest and multiple criteria were used to evaluate the performance and robustness of each algorithm.

- **P. Chang** - Designed the test criteria for the algorithm comparisons and the *in vivo* experiments. Collected data from the Siemens 9.4T MRI scanner. Implemented all the hardware/software interface with the very high order B_0 shim system. Devised and developed the main idea for the *ConsTru* algorithm. Wrote parts of the manuscript.
- **S. Nassirpour** - Designed the test criteria for the algorithm comparisons and the *in vivo* experiments. Collected data from the Siemens 9.4T MRI scanner. Implemented the other optimization algorithms in a custom script for performing the comparisons. Wrote the majority of the manuscript.
- **A. Fillmer** - Provided the Philips 7T *in vivo* data.
- **A. Henning** - Supervised and advised on the manuscript.

3.2 Modeling Real Shim Fields for Very High Degree (and Order) B_0 Shimming of the Human Brain at 9.4T

An implementation of very high degree spherical harmonic shimming of the human brain at 9.4T. B_0 maps were acquired for each shim channel at different current amplitudes. All shim fields were modelled and used for B_0 shimming. The study demonstrated the advantage of using higher degree spherical harmonic shimming in the human brain.

- **P. Chang** - Implemented the scripts for field modelling in addition to all the hardware/software interface with the very high order B_0 shim system. Optimised the experimental protocol and collected all the phantom and *in vivo* data at 9.4T. Conducted the *in vivo* applications (MRSI, single-voxel spectroscopy and EPI experiments). Wrote the majority of the manuscript.

- **S. Nassirpour** - Optimised the experimental protocol and collected all the phantom and *in vivo* data at 9.4T. Primarily performed the geometric distortion and amplitude non-linearity section of the study. Conducted the *in vivo* applications (MRSI, single-voxel spectroscopy and EPI experiments). Wrote parts of the manuscript.

- **A. Henning** - Supervised and advised on the manuscript.

3.3 Dynamic B_0 Shimming at Ultra High Fields for Proton Spectroscopic Imaging of the Human Brain*(in preparation)*

Comparison of dynamic B_0 shimming using a very high degree spherical harmonic shim system and a multi-coil shim system. Advantage of dynamic shimming over static global shimming was shown in the human brain. Applications in proton spectroscopic imaging were shown for both shim systems.

- **P. Chang** - Implemented all the hardware/software interface with the very high order B_0 shim system. Implemented the dynamic shim updating pipeline. Collected the MRSI data with the very high order shim system. Performed the processing and analysis for B_0 shim comparisons. Wrote the parts of the manuscript.

- **S. Nassirpour** - Developed the acceleration and reconstruction schemes for MRSI acquisition. Collected the MRSI data with the very high order shim system. Processed and analysed the MRSI data. Wrote the parts of the manuscript.

- **A. Aghaeifar** - Provided the multi-coil shim setup and helped collect the *in vivo* data with the multi-coil.
- **N. Avdievich** - Built the RF coil that was used in the study.
- **K. Scheffler** - Supervised and advised on the construction of the multi-coil.
- **A. Henning** - Supervised and advised on the manuscript.

3.4 Constrained Optimisation for Position Calibration of a NMR Field Camera

This study investigated different methods for position calibration of a NMR field camera. Gradient nonlinearities were taken into account (whereas previously gradient fields were assumed to be perfectly linear for the calibration). Furthermore, constrained relative positions of the field probes were used accounted for. The suggested optimisation algorithm for position calibration proved to be more robust when measuring higher order spherical harmonic shim fields.

- **P. Chang** - Devised the main concept of optimising the position calibration based on the measured gradient fields. Built the NMR field cameras including the mount, field probes, tuning/matching boards and cable traps. Measured the shim fields for each shim coil of the very high order insert shim system at 9.4T. Wrote the majority of the manuscript.
- **S. Nassirpour** - Measured the shim fields for each shim coil of the very high order insert shim system at 9.4T. Analysed the B_0 imaging data.
- **M. Eschelbach** - Helped with the manufacturing of the field probes and with performing the gradient measurements at 9.4T.
- **N. Avdievich** - Built the TR switches.
- **K. Scheffler** - Supervised and advised on the construction of the field probes.
- **A. Henning** - Supervised and advised on the manuscript.

3.5 Controller Design for Feedback of B_0 Shim Systems *(submitted)*

Investigated controller design for large multivariable shim systems. System identification was performed on a full 4^{th} degree spherical harmonic shim system. The modelled system was used to investigate different decoupling strategies for closed-loop control. Performance, robustness and control effort were used to analysis the different controllers.

- **P. Chang** - Performed all measurements that were conducted using the field camera at 9.4T. Analysed the data and modelled the system and also performed the investigation of controller design and evaluation of the design. Wrote the manuscript.
- **S. Nassirpour** - Performed all measurements that were conducted using the field camera at 9.4T.
- **A. Henning** - Supervised and advised on the manuscript.

3.6 System Identification and Signal Processing for PID Control of B_0 Shim Systems in Ultra-High Field Magnetic Resonance Applications

Investigated signal processing of data from a NMR field camera. The gradient coil system was measured using a NMR field camera and the data were used to perform system identification in the time-domain. The modelled gradient system was used to investigate multi-objective optimisation of PI controllers, accounting for performance and robustness of the closed-loop system.

- **P. Chang** - Constructed the field camera and developed the signal processing scripts and pipeline for analysis of the data. Acquired the data and performed the experiments. Performed system identification of the system and designed of PID controllers. Wrote the manuscript.
- **N. Avdievich** - Constructed the TR switches for the field camera.

- **A. Henning** - Supervised and advised on the manuscript.

4 Appended Publications

Publication I

"A Comparison of Optimization Algorithms for Localized *In Vivo* B_0 Shimming"

S Nassirpour*, **P Chang***, A Fillmer, A Henning

Magnetic Resonance in Medicine, 2017, DOI: 10.1002/mrm.26758.

FULL PAPER

Magnetic Resonance in Medicine 00:00–00 (2017)

A Comparison of Optimization Algorithms for Localized In Vivo B_0 Shimming

Sahar Nassirpour,[1,2†]* Paul Chang,[1,2†] Ariane Fillmer,[4] and Anke Henning[1,3]

Purpose: To compare several different optimization algorithms currently used for localized in vivo B_0 shimming, and to introduce a novel, fast, and robust constrained regularized algorithm (*ConsTru*) for this purpose.

Methods: Ten different optimization algorithms (including samples from both generic and dedicated least-squares solvers, and a novel constrained regularized inversion method) were implemented and compared for shimming in five different shimming volumes on 66 in vivo data sets from both 7 T and 9.4 T. The best algorithm was chosen to perform single-voxel spectroscopy at 9.4 T in the frontal cortex of the brain on 10 volunteers.

Results: The results of the performance tests proved that the shimming algorithm is prone to unstable solutions if it depends on the value of a starting point, and is not regularized to handle ill-conditioned problems. The *ConsTru* algorithm proved to be the most robust, fast, and efficient algorithm among all of the chosen algorithms. It enabled acquisition of spectra of reproducible high quality in the frontal cortex at 9.4 T.

Conclusions: For localized in vivo B_0 shimming, the use of a dedicated linear least-squares solver instead of a generic nonlinear one is highly recommended. Among all of the linear solvers, the constrained regularized method (*ConsTru*) was found to be both fast and most robust. **Magn Reson Med 000:000–000, 2017.** **© 2017 International Society for Magnetic Resonance in Medicine.**

Key words: B_0 shimming; ultrahigh field strengths; constrained regularization; single-voxel; constrained optimization

INTRODUCTION

B_0 shimming is crucial for magnetic resonance spectroscopy and imaging, as an inhomogeneous B_0 field introduces several artifacts such as geometric distortion, loss of signal-to-noise ratio, signal dropout, and loss of resolution as a result of blurring in imaging applications (1–5) and line broadening, localization problems, and loss of spectral resolution in spectroscopy applications (6). The problem becomes even worse at higher field strengths.

The task of B_0 shimming is usually accomplished by measuring the magnetic field and calculating the required currents that have to be applied to a set of shim coils to cancel the nonuniformities of the original field. Many different methods have been proposed to find the optimal shim currents. Ideally, one should find an automated B_0 shimming algorithm that is robust, numerically stable, and applicable to any arbitrary volume of interest. This algorithm should also handle the hardware limits of the shim system. Finally, it should be able to take the real shim field models into account in case the imperfections in the design cause the generated shim fields to deviate from the ideal spherical harmonics model (7–9).

The need for a reliable B_0 shimming algorithm becomes even more important in the case of small regions of interests (ROIs) or when the ROI lies somewhere off-center relative to the iso-center of the magnet, where the shim fields are no longer orthogonal. In both of these cases, solving the shimming problem is tricky, as the problem becomes increasingly ill-conditioned, and unless a robust shimming algorithm is used, one may end up with unreasonably high shim values that are prone to noise in the input (19).

Over the years, different approaches for B_0 shimming have been proposed. These methods can be classified into two general categories: projection and volumetric mapping methods. Projection mapping methods like FASTMAP, FASTERMAP, FASTESTMAP, or Pencil Beam (10–14) only measure a few linear projections, and hence have the advantage of being less time-consuming. The drawback, however, is that the localization techniques used to acquire these projections make it impossible to apply them to disjoint regions of interest such as in multivoxel spectroscopy. Moreover, because only a limited number of projections are acquired, they cannot always capture all of the local inhomogeneities.

Alternatively, the volumetric image-based mapping methods require longer acquisition times, but provide a full 3D map of the field. These B_0 shimming routines then use a range of optimization algorithms to calculate the optimal shim values. Some approaches just calculate the required shim currents by simple matrix inversion, which provides the minimum-norm solution that minimizes residual B_0 inhomogeneity in a least-squares sense (15–19). However, simple inversion is inherently unconstrained and cannot take the limits of the shim system into account. Although Juchem et al (16), Wen and Jaffer (17), and Webb and Macovski (18) report that exceeding shim values never happened in their in vivo applications, there is no guarantee that this will hold for all other shim applications or different systems. Wen and Jaffer (17) proposed a method based on Powell (20), in

[1]Max Planck Institute for Biological Cybernetics, Tuebingen, Germany.

[2]IMPRS for Cognitive and Systems Neuroscience, Eberhard-Karls University of Tuebingen, Germany.

[3]Institute for Biomedical Engineering, UZH and ETH Zürich, Zürich, Switzerland.

[4]Physikalisch-Technische Bundesanstalt, Berlin, Germany.

*Correspondence to: Sahar Nassirpour, MSc, Max Planck Institute for Biological Cybernetics, Spemannstrasse 41, 72076 Tübingen, Germany. Tel: + 49 7071 939; E-mail: sahar.nassirpour@tuebingen.mpg.de.

†These authors contributed equally to this work.

Received 15 November 2016; revised 5 April 2017; accepted 29 April 2017

DOI 10.1002/mrm.26758

Published online 00 Month 2017 in Wiley Online Library (wileyonlinelibrary.com).

© 2017 International Society for Magnetic Resonance in Medicine

which the simple matrix inversion is combined with an additional step in which they clip the shim currents that exceed their limit and recalculate new first-order values that compensate for the clipped higher-order shim values. However, this method is also not guaranteed to yield the best possible shim, as some inhomogeneities by nature cannot be compensated by only first-order terms. Adalsteinsson et al (19) proposed a truncated singular value decomposition (TSVD) to regularize the problem. However, the constraints of the system are not directly taken into account, and it is not clear how the threshold for truncating the singular values should be chosen.

Another common trend is to use a constrained minimization algorithm to solve the problem. Klassen and Menon (21) used a linear least-squares optimization method based on the MATLAB (The MathWorks, Natick, MA) *lsqlin* function, and removed shim coils from the computation when the ROI is small, to prevent ill-conditioning. Both van Gelderen et al (22) and Weiger et al (23) used a least-squares optimization method but did not mention the specific algorithm or implementation. Hetherington et al (24) proposed a three-step shimming method that would "minimize the possibility of becoming trapped in a high-order local solution." In this method they start by fitting only the first-order shim terms and then use this as a starting value for the fit of higher-order shims in each step. Recently, more and more groups (8,25–27) have used a Levenberg-Marquardt nonlinear least-squares minimization routine (28). Fillmer et al (27) built upon this method by performing a multiple starting value search and including a region of less interest to avoid "local minimum traps."

As shown by this brief literature review, several different methods are used by different groups on a range of B_0 shimming applications. However, there is still a need for a systematic comparison of these algorithms. The aim of this work is to evaluate and compare the performance of 10 optimization algorithms in a range of B_0 shimming applications in human brain on both a 7T and a 9.4T scanner.

THEORY

The B_0 shimming problem can be characterized as an overdetermined system of linear equations, which can be cast as

$$\min_x ||(Ax - b)||^2 \quad [1]$$

where b is a n x 1 vector (n is the number of voxels in the ROI) that holds all of the unshimmed B_0 field map voxels stacked column-wise to convert from a 2D or 3D ROI to a single vector; and A is a nxc matrix (c is the number of shim terms). The columns of A hold the fields produced by different shim coils, whereas the rows correspond to different voxels. Finally, x is a c x 1 vector of the unknown shim currents that need to be calculated.

The hardware limitations of the shim system can be included as box-constraints $lb \leq x \leq ub$.

As with any linear least-squares problem, this optimization problem can be rewritten in the following quadratic form:

$$\min_x \left(\frac{1}{2}x^T Qx - c^T x\right) \quad [2]$$

where $Q = A^T.A$ and $c^T = A^T b$. This is a quadratic programming problem, and hence convex. Therefore, any solution to this problem is a global minimum. This means that the algorithm should not depend on a starting value and should always converge to the same global minimum.

$Q = A^T A.$ is always positive semidefinite. In case it becomes positive definite, there is a unique solution to this problem. However, even when the matrix is only positive semidefinite, even though there are multiple solutions, they all yield the same global minimum. Note that this is true for all shimming applications, and having the box constraints does not change this fact.

However, depending on the shimming application, the problem can become very ill-posed. In this case, the shim fields produced by the shim coils no longer form an orthogonal basis, and the columns of the matrix A will be nearly linearly dependent. By definition, an ill-posed problem is a problem in which the solution does not depend continuously on the input (29), meaning that arbitrary small perturbations can cause arbitrary large changes in the solution (19). According to the perturbation theory (19), even a small amount of noise in measuring the B_0 field or estimating the sensitivity of the shim coils, or even precision round-off errors, can drastically change the results.

It is important to note that the ill-conditioning does not mean that a meaningful approximate solution cannot be computed. Rather, it implies that standard optimization methods cannot be used in a straightforward manner. Instead, more sophisticated methods must be applied to ensure the computation of a meaningful solution. This is the essential goal of regularization methods.

What is usually mistaken for local minima traps (27) or high-order local solutions (24) are actually the unstable behavior of the global solution that is typically physically meaningless and can change drastically by perturbing the input data.

Considering the theory behind this problem, even though it is a conventional linear least-squares minimization problem, extra care should be taken in choosing an algorithm that calculates stable solutions independent of the shimming application at hand.

METHODS

Algorithms

Ten different optimization algorithms were embedded in a software framework written in MATLAB R2013b. The chosen set of algorithms includes sample algorithms from both generic and dedicated quadratic solvers. A new regularized constrained inversion algorithm (algorithm 10, as described subsequently) was also included. Here is a brief explanation of each of these methods:

1. Unconstrained pseudo-inversion (*pinv*): If the shimming problem in Equation [1] was unconstrained, the obvious solution to it would be

$$x = A^{\dagger} b \quad [3]$$

where $A^{\dagger}$ is the pseudo-inverse of the matrix A. This solution always yields the best shim quality achievable when the system is not bound by constraints. Therefore, the unconstrained pseudo-inversion algorithm (*pinv*) using the MATLAB *pinv* function was considered as the benchmark for comparison purposes.

2–5. Generic constrained nonlinear optimization methods using the MATLAB *fmincon* function with three methods: active-set (*nonlin-as*) (30), interior-point (*nonlin-ip*) (31) and sequential quadratic programming (*sqp*) (30), and another one using Levenberg-Marquardt's algorithm implemented in IDL (*levMar*) (28).

6. A dedicated quadratic programming solver using the interior-point-convex method (QP) (32) using the MATLAB *quadprog* function.

7. A dedicated linear least-squares solver using the MATLAB *lsqlin* function.

8. A constrained inversion algorithm in which the system is iteratively inverted and the values that exceed the limits are clipped to their maximum (*Clipped-it*). This method handles the constraints in an iterative manner while still keeping the problem at each step essentially unconstrained. Let us assume that in the first iteration we calculate the solution to the shim problem as

$$x = A^{\dagger} b. \quad [4]$$

And suppose that the calculated values for two of the shim terms (x_i, x_j) exceeded their limits ($x_i > u_i$, $x_j > u_j$). These two terms are clipped to their maximum value (set $x_i = u_i$, $x_j = u_j$) and the b vector is updated by subtracting their contribution from the measured field vector as follows:

$$b' = b - A * [\,0 \quad \ldots \quad u_i \quad \ldots \quad u_j \quad \ldots \quad 0\,]^T. \quad [5]$$

In the next iteration, the updated b vector (b'), and an updated matrix A that is obtained by eliminating the rows corresponding to shim terms i and j, form the updated problem

$$x' = A'^{\dagger} b'. \quad [6]$$

This is repeated until all constraints are satisfied.

9. Similar to method 8, except that before starting the iterative inversion, the singular values of matrix A are truncated to a fixed and empirically chosen threshold (0.003) (*Fixed-tsvd*).

10. A new method (constrained TSVD inversion method, or *ConsTru*) in which we simply solve the shim problem by pseudo-inverting the matrix A, but if any of our hardware limit constraints are violated, we truncate the smallest singular value of the matrix A and re-invert the new matrix. We continue doing this by truncating the next smallest singular value in each step until the calculated solution does not violate any hardware constraints. The rationale behind this algorithm is that if we consider the singular value decomposition of the matrix A

$$A = U \sum V \quad [7]$$

where $\sum$ is a diagonal matrix with the singular values of the matrix A as its nonzero elements, then we can write the pseudo-inverse of the matrix A as

$$A^{\dagger} = V \sum{}^{\dagger} U^{*} \quad [8]$$

where $\sum^{\dagger}$ is calculated by taking the reciprocal of each nonzero element on the diagonal and transposing the matrix. This equation shows that if matrix A has small singular values (which is the case when the shim problem is ill-conditioned), the reciprocal of these values on the diagonal of $\sum^{\dagger}$ would contribute significantly to the norm of the solution $x = A^{\dagger} b$. This is problematic not only because this high norm solution would most probably violate the hardware limits, but also because according to the perturbation theory (19), these high values will amplify any input noise and result in numerically unstable solutions. It is therefore clear why truncating the small singular values of the matrix A before inverting it would help condition the problem and result in a minimum norm solution. A more comprehensive mathematical description of this can be found in Appendix A.

Data Acquisition

For this study, a total of 66 in vivo data sets from the brains of healthy volunteers were considered. Half of these data sets were acquired on a 7T magnet, and the other half on a 9.4T system. All participating volunteers gave written informed consent in accordance with local ethics regulations. Whole-brain B_0 maps covering the entire cerebrum, cerebellum, and brain stem were acquired.

The 7T data sets were acquired on a 7T Achieva system (Philips Healthcare, Cleveland, OH) with a Nova Medical 32-channel Tx/Rx coil using a 2D gradient echo (GRE) sequence with repetition time (TR) = 6.86 ms; echo time (TE) = 3.1/4.1 ms; field of view (FOV) = $240 \times 240\,mm^2$; in-plane resolution = $2 \times 2\,mm^2$; 110 slices and slice thickness = 2 mm.

The 9.4T data sets were acquired on a 9.4T human whole-body Siemens scanner (Siemens, Erlangen, Germany) with an in-house-developed 8-channel transmit/receive coil (33). The B_0 maps were acquired with a 2D GRE sequence with TR of 100 ms; TE = 4.01/4.77 ms; FOV = $200 \times 200\,mm^2$; in-plane resolution = $1.56 \times 1.56\,mm^2$; 50 slices and slice thickness = 4 mm.

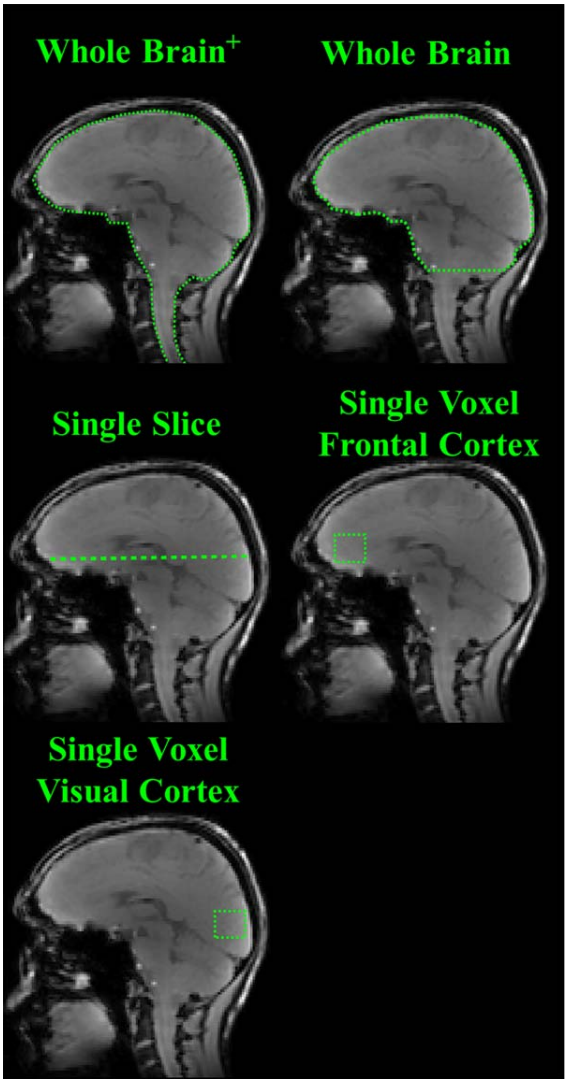

FIG. 1. Anatomical image overlaid with five different shim volumes chosen for this study: (i) a whole-brain global shimming application for a region covering the entire cerebellum, cerebrum, and brain stem indicated as whole brain^{+}; (ii) another whole-brain global shimming application covering the whole cerebellum minus the medulla and the cervical spine; (iii) a single-slice shimming application for a slice positioned off-center relative to the iso-center of the magnet; (iv) a single-voxel shimming application for a voxel located in the frontal cortex; and (v) another one in the visual cortex.

Tests

For each volunteer, the performance of the algorithms for up to third-order shimming in five different shim volumes were studied (Fig. 1): (i) a whole-brain region covering the entire cerebrum, cerebellum, and brain stem; (ii) another global application covering the whole brain minus the medulla and the cervical spine; (iii) a single slice positioned off-center and going through the frontal sinus air cavity; (iv) a single voxel ($2 \times 2 \times 2\,cm^3$) located in the frontal cortex; and (v) in the visual cortex. The hardware limits of the shim system given in Table 1 were taken into account. The algorithms were tested against the following criteria.

Sensitivity to Starting Values

Out of the 10 algorithms, four of them (namely, the generic nonlinear solvers (Algorithms [2] to [5])), require a starting value. Because these are numerical algorithms, they might not always converge within the given number of iterations; hence, the announced solution might well depend on where the search starts. Therefore, in this test the robustness of each of these algorithms is evaluated against the starting values. For each volunteer and shimming application, 1000 random starting point values were generated.

Numerical Stability

As the shimming problem becomes increasingly ill-conditioned, it becomes more and more challenging to calculate a meaningful and numerically stable solution; hence, the shim algorithm should be robust against any kind of perturbations by means of better-conditioning the problem. In this test, the robustness of each of the 10 algorithms was tested against noisy inputs. For each volunteer, 1000 different noisy B_0 maps were generated by adding random white noise to the measured maps. The maximum amplitude of the noise was kept within $\pm 1\%$ of the original measured value.

Speed

Any time spent on calculating a stable solution for B_0 shimming is an overhead to the scan time. Hence, in this test the speed of each of these algorithms was tested. The run times were calculated based on a 2.3-GHz 6-core Intel CPU with 16 GB of RAM.

Overall Performance in Different Shimming Applications

As mentioned previously, the theoretical limit on how well the shimming can do for the least-squares objective function, given a certain number of shim terms, is always given by the *pinv* algorithm. In practice, the

Table 1
Shim Terms, Their Sensitivities, and Their Maximum Strength for the Philips 7T Shim System

Shim term	Spherical harmonic function	Sensitivity (Hz/cm^n/A)	Maximum (mT/m^n)
X	x	42.15	0.99
Y	y	42.15	0.99
Z	z	42.15	0.99
Z2	$z^2 - 1/2*(x^2+y^2)$	1.97	4.63
ZX	Zx	3.35	7.88
ZY	Zy	3.30	7.75
C2	$x^2 - y^2$	3.20	7.52
S2	2xy	3.13	7.35
Z3	$z(z^2 - 3/2*(x^2+y^2))$	0.012	2.82
Z2X	$x(z^2 - 1/4*(x^2+y^2))$	0.016	3.76
Z2Y	$y(z^2 - 1/4*(x^2+y^2))$	0.016	3.76
ZC2	$z(x^2 - y^2)$	0.1	23.72
ZS2	2zxy	0.099	23.25
C3	$x(x^2 - 3y^2)$	0.045	10.57
S3	$y(3x^2 - y^2)$	0.044	10.33

Note: The maximum available current for each shim channel was 10 A.

shimming problem is always bound by hardware limits. Therefore, it may be impossible to achieve this theoretical limit. In this test, we evaluate how close the result of each of these algorithms gets to the theoretical limit. The test was performed on all volunteers and in all shimming applications for both second and third order.

Only the in vivo data sets acquired at 7 T were used for these four tests.

Overall Performance on 7T versus 9.4T Data Sets

It is well-known that B_0 field homogeneity becomes more problematic at higher field strengths. Therefore, it would be interesting to evaluate how well each of the algorithms would handle the higher inhomogeneity in the B_0 fields measured at 9.4 T compared with those measured at 7 T, and to compare the best shim quality one can achieve on each of them. So, in this test we compared the best shim quality achievable given the hardware limits of the shim system in all shimming application on both 7T and 9.4T data sets. For this test the best shimming algorithm (judged by the results of all of these performance tests) was used. For the comparison to be purely about the field strength and not the shim system specifications, the same hardware constraints (as stated in Table 1) were used in simulation on both 7T and 9.4T data sets.

Application in In Vivo Single-Voxel Spectroscopy

One of the most challenging shimming applications (in the sense of robustly finding the optimal shim solution) is single-voxel spectroscopy (such as in the frontal cortex of the brain). The shim quality directly affects the linewidth of the peaks in the spectrum. The purpose of this test was to apply the best shimming algorithm (judged by the results of all these performance tests) to shim a single voxel located in the frontal cortex of the brain, acquire non-water suppressed spectra, and evaluate the shim quality by calculating the linewidth of the unsuppressed water peak. The results were compared with those of shimming the same region with the vendor-implemented shimming routine. The effect of higher-order shimming was also studied by shimming the same volume with incremental second, third, fourth, and partial fifth/sixth-order spherical harmonic shim terms.

This test was performed on a 9.4T whole-body Siemens scanner with an in-house-developed eight-channel transmit/receive coil (33). To perform higher-order B_0 shimming, an insert shim (MX10W-28) from Resonance Research Inc (Billerica, MA) was used. Twenty-eight channels including complete second, third, and fourth-degree spherical harmonics (and partial fifth and sixth-degree harmonics) were available. The sensitivities of each shim channel can be found in Table 2. A total of 10 healthy volunteers were scanned for this test. A STEAM sequence was used to acquire non-water-suppressed spectra with the following parameters: voxel size $2 \times 2 \times 2\,cm^3$, 16 averages, TR of 5 s, TE of 11 ms, flip angle of 90°, 1024 complex points, and spectral bandwidth of 8 kHz. The maximum shim current for each shim channel was limited to 2 A, and a total of 20 A was dedicated to the positive and negative rails (10 A each).

Table 2
Shim Terms, Insert Shim Coil Sensitivities, and Maximum Strength Used on the 9.4T System

Shim term	Spherical harmonic function	Sensitivity ($Hz/cm^n/A$)	Maximum (mT/m^n)
Z0	1	6058	0.28
Z2	$z^2-1/2*(x^2+y^2)$	6.942	3.26
ZX	zx	24.15	11.34
ZY	zy	24.15	11.34
C2	x^2-y^2	3.64	1.71
S2	2xy	3.64	1.71
Z3	$z(z^2-3/2*(x^2+y^2))$	0.4923	23.12
Z2X	$x(z^2-1/4*(x^2+y^2))$	1.0	46.97
Z2Y	$y(z^2-1/4*(x^2+y^2))$	1.0	46.97
ZC2	$z(x^2-y^2)$	1.77	83.14
ZS2	2zxy	1.77	83.14
C3	$x(x^2-3y^2)$	0.188	8.83
S3	$y(3x^2-y^2)$	0.188	8.83
Z4	$z^4-3z^2(x^2+y^2)+3/8*(x^2+y^2)$	0.04206	197.57
Z3X	$zx(z^2-3/4*(x^2+y^2))$	0.123	577.78
Z3Y	$zy(z^2-3/4*(x^2+y^2))$	0.123	577.78
Z2C2	$z(x^2-y^2)(z^2-1/6*(x^2+y^2))$	0.093	436.86
Z2S2	$2z(xy)(z^2-1/6*(x^2+y^2))$	0.093	436.86
ZC3	$x(x^2-3y^2)(z^2-1/8*(x^2+y^2))$	0.121	568.38
ZS3	$x(x^2-3y^2)\ (z^2-1/8*(x^2+y^2))$	0.121	568.38
C4	$x^4-6x^2y^2+y^4$	0.0187	87.84
S4	$4xy(x^2-y^2)$	0.0187	87.84
ZC4	$z(x^4-6x^2y^2+y^4)$	5.71E-3	2682.20
ZS4	$4zxy(x^2-y_2)$	5.71E-3	2682.20
C5	$x(x^4-10x^2y^2+5y^4)$	9.9E-4	465.04
S5	$y(y^4-10x^2y^2+5x^4)$	9.9E-4	465.04
ZC5	$zx(x^4-10x^2y^2+5y^4)$	3.21E-4	15078.56
ZS5	$zy(y^4-10x^2y^2+5x^4)$	3.21E-4	15078.56

Note: The maximum shim current for each shim channel was limited to 2 A, and a total of 20 A was dedicated to the positive and negative rails (10 A each).

RESULTS

Sensitivity to Starting Values

To evaluate the quality of the shim and how dependent it is on the starting values, the standard deviation of the frequency shifts (σB_0) in the shimmed map was chosen as a metric. Figure 2 shows the results for a single voxel shimming application located in the frontal cortex. The results are shown only for the four algorithms that require a starting point value to operate. Each box in the box plot contains 33000 σB_0 values, which are the results of applying the corresponding algorithm to all 33 volunteers (the ones acquired on the 7T magnet) with all 1000 different randomly generated starting point values. For comparison purposes, the best shim quality achievable through an unconstrained inversion (*pinv*) is also shown. On each box, the central mark (–) indicates the median, and the bottom and top edges of the box indicate the 25th and 75th percentiles, respectively. The mean value is shown with a cross symbol (†), and the whiskers span from 9 to 91% of the data. To better visualize how the outcome of the algorithms changes depending on the starting value, the results of the first

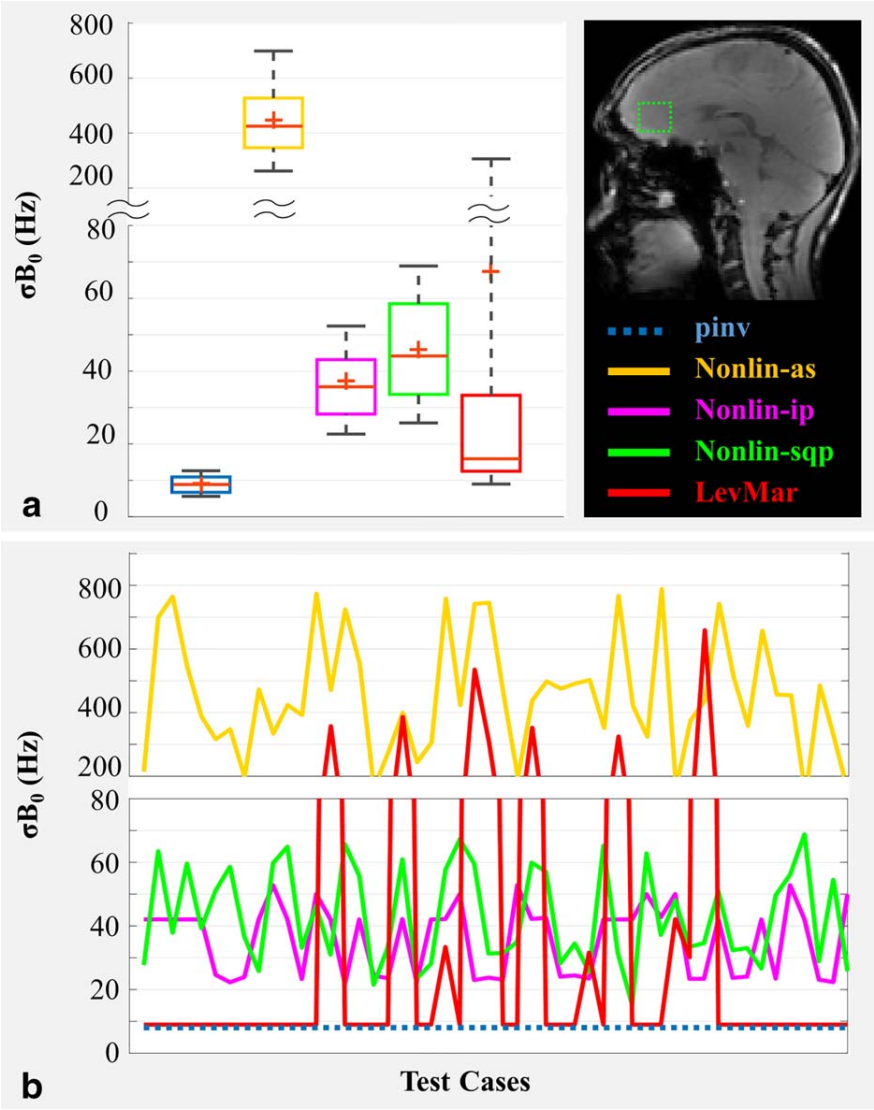

FIG. 2. Starting-value sensitivity test results for a single voxel located in the frontal cortex. **a**: Box plot of the σB_0 (standard deviation of the frequencies in the shimmed B_0 map) resulting from applying each shimming algorithm to all 33 of the 7T in vivo data sets for all 1000 starting-point test cases. The best shim quality achievable through an unconstrained *pinv* algorithm is also shown for comparison purposes. **b**: Results of the same test in one representative in vivo data set (only 50 out of 1000 test cases are shown for better visualization).

50 test cases are plotted in Figure 2b for a representative volunteer.

These results, and those for single-slice and whole-brain applications, are summarized in Supporting Table S1.

The results show that the *LevMar* method gets closest to the best theoretical shim in most cases. All four algorithms depend heavily on the value of the starting point. However, as shown in Figure 2b, the *LevMar* method is the most robust against changes in the starting-point value except for cases in which it completely fails to converge. Note that the ill-conditioned problem has caused the *nonlin-as* method to result in unreasonably high values of the solution.

Numerical Stability

Figure 3a shows the box plot of the results of applying the 10 algorithms to all 33 volunteer data sets on 1000 noisy B_0 maps each. For comparison purposes, the results of the unconstrained *pinv* algorithm is shown in the first column. Figure 3b shows the same results but only for the first 50 test cases on a representative volunteer for better visualization. The results shown in this figure, as well as those for single-slice and whole-brain applications are summarized in Supporting Table S1.

It is evident that the *ConsTru* algorithm follows the best theoretical shim quality most closely and is most robust against the noisy inputs. All other algorithms are more sensitive to the perturbations in the input; hence, their optimal convergence in the case of ill-conditioned problems is not guaranteed.

Speed

The average runtimes of the 10 algorithms across all volunteers are shown in Figure 4. The four nonlinear optimization methods (*LevMar, Nonlin-as, Nonlin-ip, Nonlin-SQP)* are orders of magnitude slower than the rest, and the *Clipped-it, Fixed-tsvd, ConsTru* and the *QP* methods prove to be the fastest. The results are summarized in Supporting Table S2.

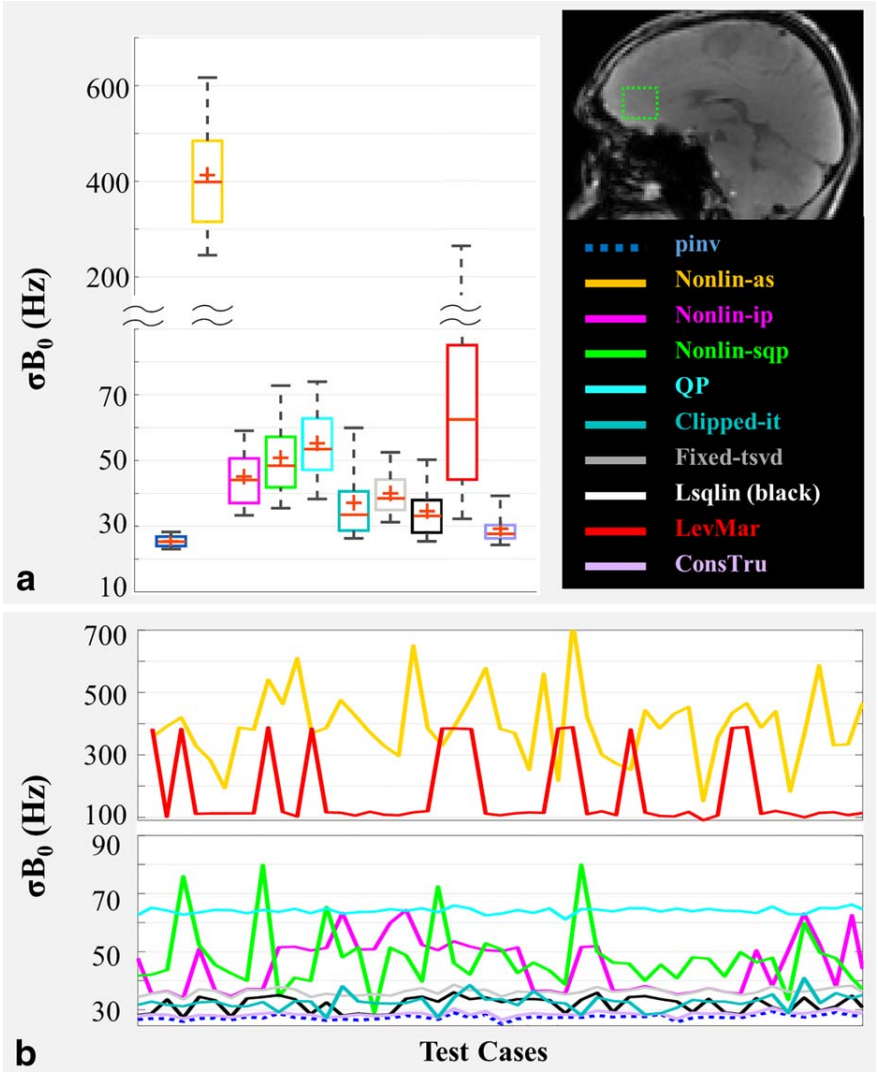

FIG. 3. Numerical stability test results for a single voxel located in the frontal cortex. **a**: Box plot of the of the σB_0 (standard deviation of the frequencies in the shimmed B_0 map) resulting from applying each shimming algorithm to all 33 of the 7T in vivo data sets for all 1000 noisy test cases. The best shim quality achievable through an unconstrained *pinv* algorithm is also shown for comparison purposes. **b**: Results of the same test in one representative in vivo data set (only 50 out of 1000 test cases are shown for better visualization).

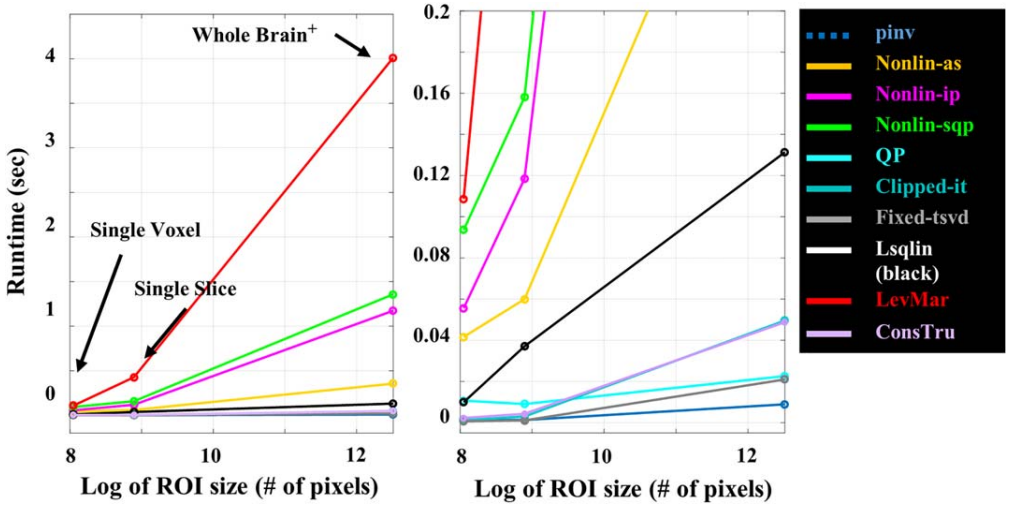

FIG. 4. Comparison of the average runtime of the algorithms across all 33 of the 7T in vivo data sets as a function of the ROI size (shown on a log scale) on the left. A more zoomed in view is found on the right.

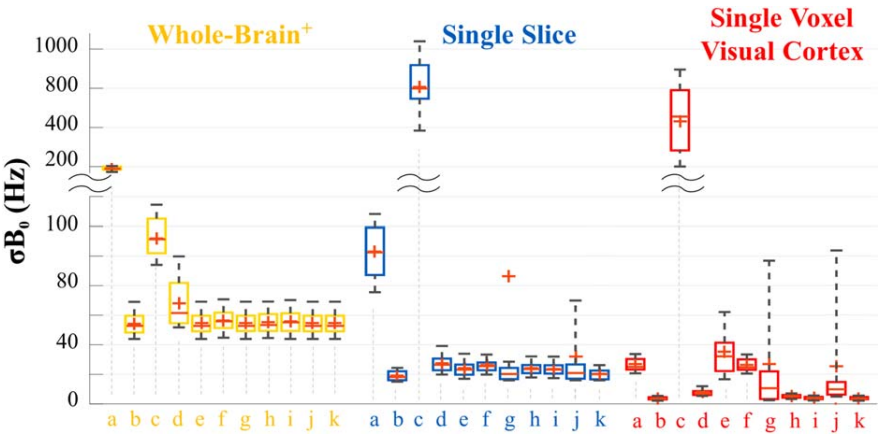

FIG. 5. The overall performance of the different shimming algorithms in three different shimming applications. Each box contains the σB_0 (standard deviation of the frequencies in the shimmed B_0 map) resulting from applying each of the corresponding shimming algorithm to all 33 of the 7T in vivo data sets. The best shim quality achievable through an unconstrained *pinv* algorithm is also shown for comparison purposes. The different algorithms are indicated as follows: (a) unshimmed, (b) *pinv*, (c) *nonlin-as*, (d) *nonlin-ip*, (e) *nonlin-sqp*, (f) *QP*, (g) *Clipped-it*, (h) *Fixed-tsvd*, (i) *Lsqlin*, (j) *LevMar*, and (k) *ConsTru*.

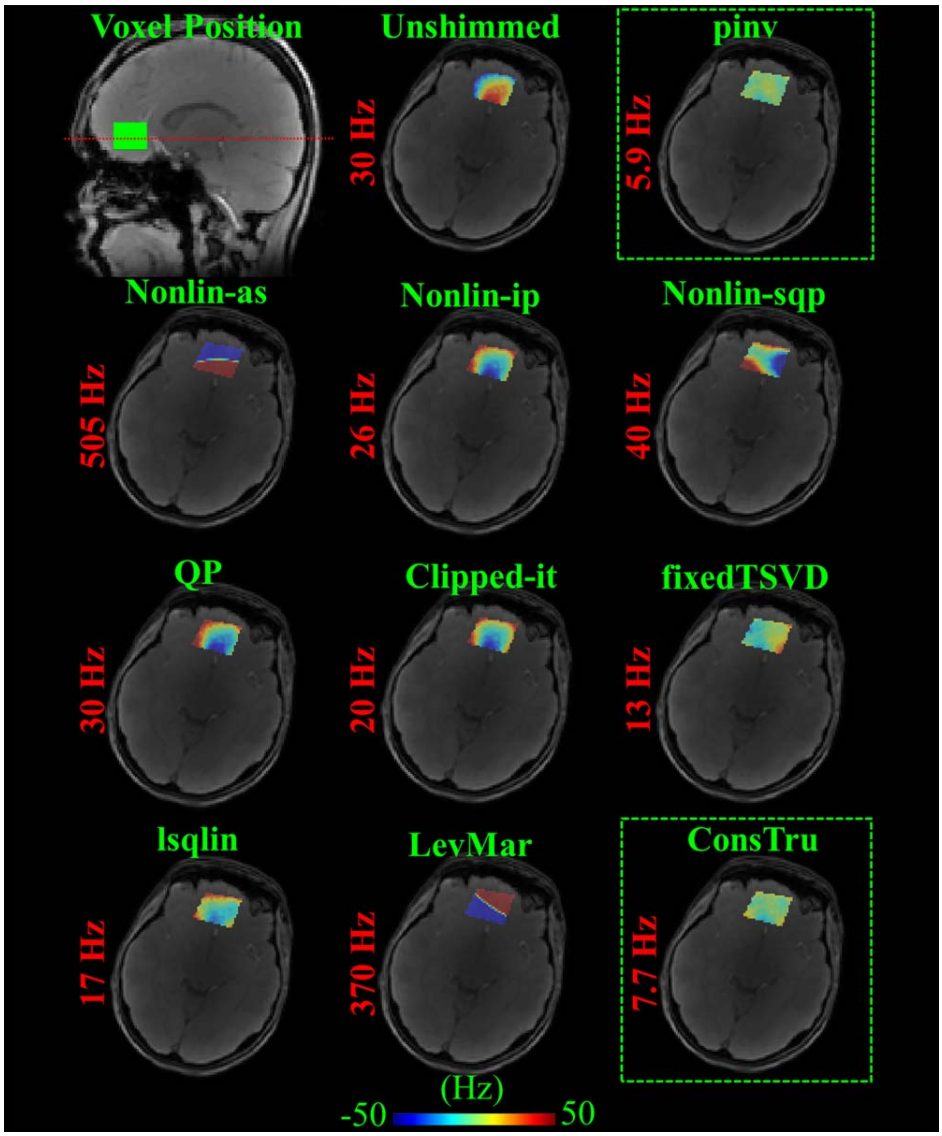

FIG. 6. The resulting shim quality of 10 different shimming algorithms for a single-voxel shimming region located in the frontal cortex. B_0 maps from a representative volunteer are shown along with the resulting standard deviation of the frequencies in the ROI. All B_0 maps are displayed between −50 and 50 Hz.

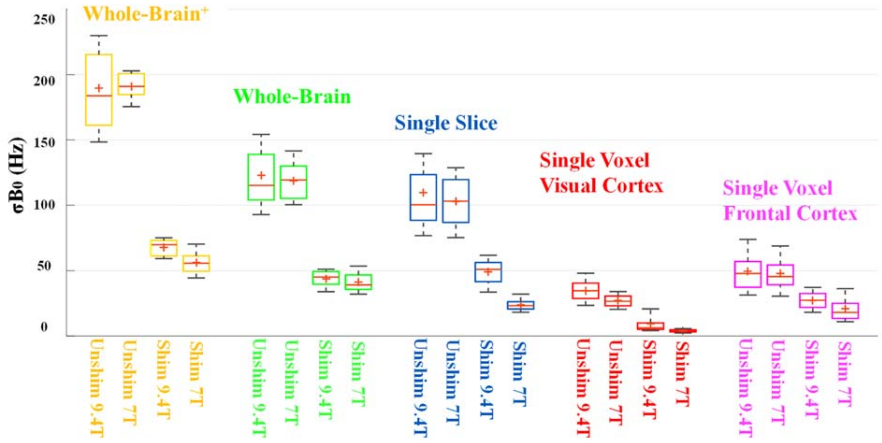

	Unshimmed 9.4 T	Unshimmed 7T	Shimmed (w/ *ConsTru*) 9.4 T	Shimmed (w/ *ConsTru*) 7 T
Whole brain +	189.56 ± 29.93	189.90 ± 10.92	67.86 ± 7.72	54.71 ± 8.81
Whole-Brain	122.86 ± 28.71	118.53 ± 14.87	43.85±6.98	38.33 ± 7.33
Single slice	110.74 ± 35.69	102.99 ± 19.87	49.25 ± 10.62	20.03 ± 4.28
Single voxel (visual cortex)	34.67 ± 9.60	26.90 ± 5.09	9.33 ± 6.98	3.79 ± 1.15
Single voxel (frontal cortex)	50.70 ± 30.69	48.0 ± 13.59	25.20 ± 10.62	15.01 ± 6.90

FIG. 7. Comparison of the performance of the *ConsTru* shimming algorithms on a 7 T versus 9.4 T magnet in five different shimming applications. Each box contains the results of applying the *ConsTru* shimming algorithm to all 33 in vivo data sets. The average (± standard deviation) shim quality across all 33 volunteers for each algorithm is summarized in the table below the box plot.

Overall Performance in Different Shimming Applications

Figure 5 shows the overall performance of these algorithms in three of the five shimming applications (the other two are shown in Supporting Fig. S1). Each algorithm was applied to all 33 volunteer data sets acquired at a 7T field strength. The average shim quality across all volunteers is shown in Supporting Table S3 for both second-order and third-order shimming. It can be seen that in the case of bigger ROIs, all of the algorithms (except for *Nonlin-as* and *Nonlin-ip*) perform similarly. This is expected, as the problem is well-conditioned in these cases. The differences start to show more as we move on to smaller ROIs. It can be seen that the *ConsTru* algorithm consistently gets closest to the best shim quality possible and is less prone to differences in the input data.

Furthermore, to visualize how the σB_0 values translate into shim quality, Figure 6 shows the resulting shimmed B_0 map for a representative volunteer in a single-voxel shimming application. It can be seen that the ill-conditioned problem has caused some of these algorithms to result in unreasonable solutions. Once again, the *ConsTru* algorithm proves to have the best performance by getting closest to the best theoretical shim quality achievable.

From the results of the performance tests so far, it is evident that the *ConsTru* algorithm consistently performs most robust and among the fastest.

Overall Performance on 7T versus 9.4T Data

Figure 7 shows a comparison of the overall performance of the *ConsTru* algorithm on 7 T versus 9.4 T in five shimming applications. For each field strength, 33 in vivo data sets were available.

Application in In Vivo Single-Voxel Spectroscopy

Figure 8a shows the box plot of the linewidth of the unsuppressed water peak in a single voxel in the frontal cortex after applying the vendor-implemented second-order shimming routine as well as those for the *ConsTru* algorithm for up to second, third, fourth, and partial fifth/sixth-order shimming. Each box contains the values obtained on 10 volunteers at 9.4 T. The total amount of current needed to achieve the shim (excluding the first-order terms) are shown in the accompanying table.

Figure 8b shows the unsuppressed water peaks from a representative volunteer acquired with different shimming methods. Although the difference between the vendor-implemented second-order shim and *ConsTru*'s second-order shim is clear, the difference between the *ConsTru*'s second, third, fourth, and partial fifth/sixth order is not as big and is only visible when we magnify the top portion of the peak.

DISCUSSION

The task of B_0 shimming can be very tricky when the shimming problem becomes ill-conditioned. Noise or error in the input data can be present for a number of reasons, such as limited spatial resolution, errors in the measurement of the reference field map, motion artifacts, limited signal-to-noise ratio and residual phase wrapping errors (in case multi-echo B_0 mapping sequences (16,34) are not used), and deviation of the shim fields generated by the coils from the ideal spherical harmonic functions.

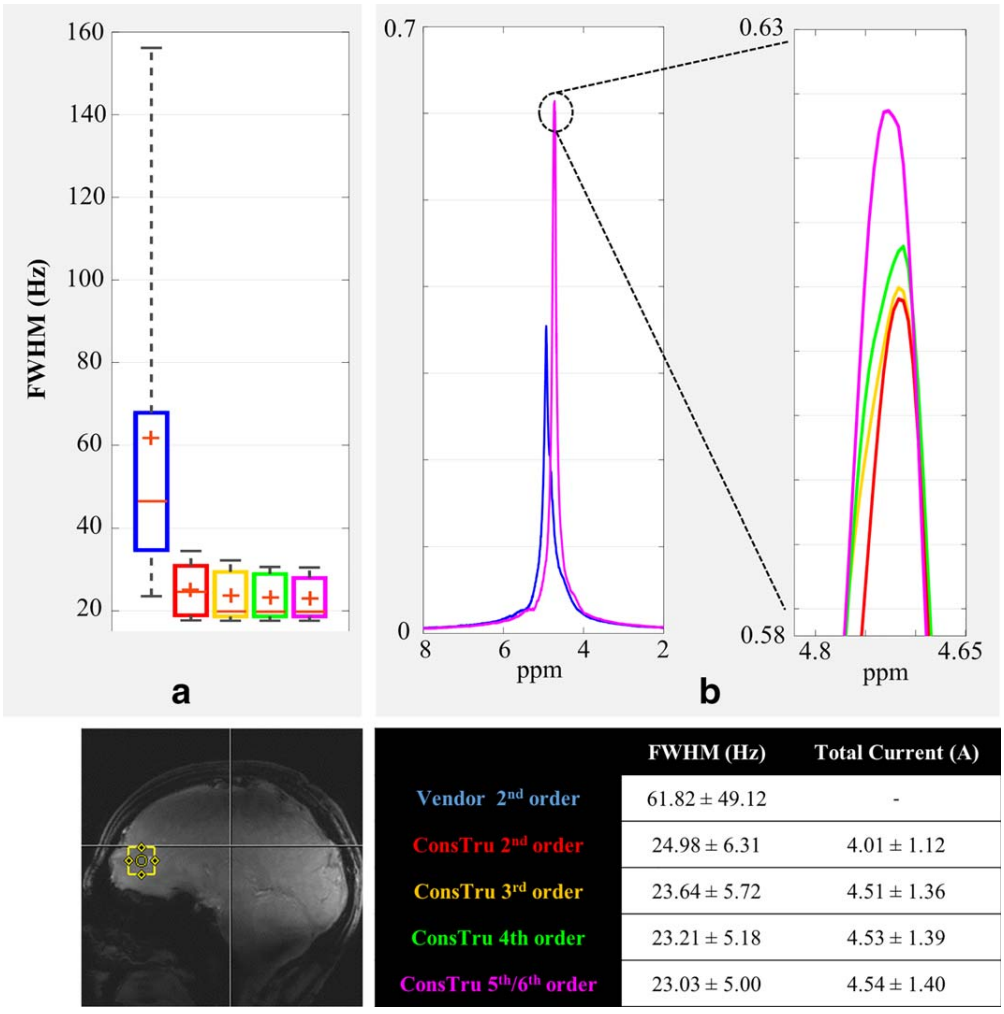

	FWHM (Hz)	Total Current (A)
Vendor 2nd order	61.82 ± 49.12	-
ConsTru 2nd order	24.98 ± 6.31	4.01 ± 1.12
ConsTru 3rd order	23.64 ± 5.72	4.51 ± 1.36
ConsTru 4th order	23.21 ± 5.18	4.53 ± 1.39
ConsTru 5th/6th order	23.03 ± 5.00	4.54 ± 1.40

FIG. 8. Comparison of the vendor-implemented second-order shim and the *ConsTru* algorithm for shimming up to second, third, fourth, and partial fifth/sixth order for single-voxel spectroscopy in the frontal cortex at 9.4 T. **a**: Box plot of the full width at half maximum of the unsuppressed water. Each box contains the results of applying the corresponding algorithm to 10 volunteers. The average (± standard deviation) of the results averaged across 10 volunteers, along with the amount of current needed to achieve the shim results, are summarized in the table below the plots. Same color codes as the table are used in the box plot. **b**: Representative unsuppressed water spectrum from one volunteer along with the voxel position. The magnified version of the tip of the peak is shown on the right, for better visualization of the differences between incremental higher orders of shimming.

Additionally, there is always a limit on the maximum amount of shim currents. Considering all of this, the shimming algorithm should be robust and able to tolerate certain levels of noise and uncertainty in the input data, and yet result in reasonably low values of the solution.

The sensitivity to the starting-point-value test demonstrates that any nonlinear least-squares optimization method that requires a starting point to operate is prone to numerical instability. The next choice would be dedicated quadratic solvers that do not require a starting-point value. However, the results of the numerical stability test also show that unless some measure is taken to better condition the problem, unstable and suboptimal solutions are inevitable.

Typically, the way shim routines are designed to handle the ill-conditioned problem or errors in the input is either by preventing the problem from becoming ill-conditioned (by excluding certain shim fields) (18,21), or by performing multiple iterations of the shim algorithm to ensure convergence (19,27). The first method cannot be easily applied to any arbitrary ROI, because depending on the shape, size, or angulation of the ROI, different shim terms contribute differently to the shim; hence, direct operator supervision is required to exclude the correct shim terms. The second method, which either performs multiple iterations by measuring the reference field and solving the problem multiple times (19) or by feeding multiple starting values to the algorithm to get rid of the instability in the results (27), is also not ideal, because in the interest of reducing the overhead time, the algorithm should be fast and ideally require only one iteration.

The third option to better condition the problem is to regularize the shim matrix using methods such as SVD truncation or Tikhonov regularization methods (19,35). Both of these are essentially minimum-norm solution

methods and have the advantage of being noniterative, ROI-independent, fast, and robust. For the purposes of this study, the TSVD method was chosen (a more formal discussion is presented in Appendix B).

There will always be a trade-off between regularization and data fidelity; therefore, extra care should be taken in choosing the regularization parameter. The reason is that after regularization, we are no longer solving the original problem, but rather an approximated version of it. The regularization parameter can either be chosen empirically (*Fixed-tsvd*) or adaptively (*ConsTru*). It is always possible that by choosing an unnecessarily high value of the regularization parameter, we do not get as close to the best shim quality achievable (Fig. 6), or the measured shim quality in practice would be worse than the predicted one. Therefore, the adaptive regularization method (*ConsTru*) is preferable.

After sufficiently regularizing the matrix, finding the solution reduces to a simple matrix inversion. The only remaining issue is finding a way to constrain the solution. Two different methods were considered in this study: clipping the exceeding values and projecting the remaining inhomogeneities on other shim terms iteratively (*Clipped-it, Fixed-tsvd*), or adaptively choosing the regularization parameter that will satisfy the constraints while maintaining as much data fidelity as possible (*ConsTru*). The results of the overall performance test proved that the latter method on average got closest to the best theoretical shim quality.

Another advantage of the *ConsTru* algorithm is its flexibility in handling arbitrary constraints. This is because cost functions are directly calculated in each iteration, and more regularization is applied in the next step if constraints are being violated. This is of particular interest in cases in which the shim system has both limits on the maximum shim current of each channel and the total amount of positive and negative shim currents that the amplifiers can provide as a whole.

Although there are inherent differences between the levels of B_0 inhomogeneities on a 7T versus 9.4T magnet, the *ConsTru* algorithm was able to successfully shim both data sets (Fig. 7). The residual differences between the shimmed maps on 7 T versus 9.4 T can be explained by noting that the same hardware constraints were used to shim both sets of data.

Applying the *ConsTru* algorithm to a single-voxel ROI in the frontal cortex at 9.4 T resulted in reproducible spectral linewidths that were much better than the vendor-implemented shim routine (Fig. 8). Increasing the number of orders decreased the mean linewidth; however, the improvement was not statistically significant (paired t-test). Additionally, despite the ill-conditioning, the *ConsTru* algorithm was always able to shim without requiring high amounts of currents (< 4.5 A in total) because of its regularized nature.

In summary, this study showed in simulation that the proposed method *(ConsTru)* enabled successful and robust B_0 shimming for a range of shimming applications, shimming orders, and field strengths. The method proved to be most robust and among the fastest compared with a wide range of algorithms derived from diverse concepts. The effectiveness of the algorithm was demonstrated in vivo for single-voxel spectroscopy. Because this algorithm calculates the analytical closed-form solution, it is very easy to implement. Furthermore, it is easily applicable to any arbitrary ROI, including multivoxel or multi-object shimming applications, and can be used to enable dynamic shimming.

CONCLUSIONS

For localized in vivo B_0 shimming, the use of a dedicated linear least-squares solver instead of a generic nonlinear solver is highly recommended. The reason is that these solvers do not depend on a starting value and converge much faster. Among the linear least-squares solvers, the constrained TSVD inversion method (*ConsTru*) was found to be the most robust and among the fastest ones. The algorithm is easy to implement and applicable to any arbitrary ROI or shim system. The proposed method was used in a single-voxel spectroscopy application at 9.4 T, where it enabled the acquisition of high-quality spectra in the frontal cortex of the brain.

REFERENCES

1. Baldwin LN, Wachowicz K, Thomas SD, Rivest R, Fallone BG. Characterization, prediction, and correction of geometric distortion in 3 T MR images. Med Phys 2007;34:388–399.
2. Lipton ML. Totally accessible MRI: a user's guide to principles, technology, and applications. Berlin, Germany: Springer; 2008.
3. McRobbie DW, Moore EA, Graves MJ, Prince MR. MRI from picture to proton. Cambridge, UK: Cambridge University Press; 2007.
4. Jezzard P. The physical basis of spatial distortions in magnetic resonance imaging. In: Handbook of medical image processing and analysis. Cambridge, MA: Academic Press; 2008.
5. Yang QX, Smith MB, Wang J. Magnetic susceptibility effects in high field MRI. Ultra high field magnetic resonance imaging. New York: Springer Science & Business Media; 2007.
6. Pan JW, Lo KM, Hetherington HP. Role of very high order and degree B0 shimming for spectroscopic imaging of the human brain at 7 tesla. Magn Reson Med 2012;1:1007–1017.
7. Boer VO, Klomp DWJ, Juchem C, Luijten PR, de Graaf RA. Multi-slice 1H MRSI of the human brain at 7T using dynamic B0 and B1 shimming. Magn Reson Med 2012;68:662–670.
8. Juchem C, Nixon TW, McIntyre S, Boer VO, Rothman DL, de Graaf RA. Dynamic multi-coil shimming of the human brain at 7 Tesla. J Magn Reson 2011;212:280–288.
9. Chang P, Nassirpour S, Henning A. Modelling real shim fields for very high degree B_0 shimming of the human brain at 9.4T. Magn Reson Med 2017. doi: 10.1002/mrm.26658.
10. Gruetter R, Boesch C. Fast non-iterative shimming of spatially localized signals. In vivo analysis of the magnetic field along axes. J Magn Reson 1992;96:323–334.
11. Gruetter R. Automatic, localizeed in vivo adjustment of all first and second-order shim coils. Magn Reson Med 1993;29:804–811.
12. Shen J, Rycyna RE, Rothman DL. Improvements on an in-vivo automatic shimming method (FASTERMAP). Magn Reson Med 1997; 38834–38839.
13. Gruetter R, Tkac I. Field mapping without reference scan using asymmetric echo-planar techniques. Magn Reson Med 2000;43:319–323.
14. Shen J, Rothman DL, Hetherington HP, Pan JW. Linear projection method for automatic slice shimming. Magn Reson Med 1999;42: 1082–1088.
15. Hoult DI. Shimming on spatially localized signals. J Magn Reson 1987;73:147–177.
16. Juchem C, Nixon TW, Diduch P, Rothman DL, Starewicz P, de Graaf RA. Dynamic shimming of the human brain at 7 Tesla. Concept Magn Reson B Magn Reson Imaging 2010;37B:116–12813.
17. Wen H, Jaffer FA. An in vivo automated shimming method taking into account shim current constraints. Magn Reson Med 1995;34: 898–904.

18. Webb P, Macovski A. Rapid, fully automatic, arbitrary-volume in vivo shimming. Magn Reson Med 1991;20:113–122.
19. Kim DH, Adalsteinsson E, Glover GH, Spielman DM. Regularized higher-order in vivo shimming. Magn Reson Med 2002;48:715–722.
20. Powell MJD. Numerical methods for constrained optimization. London: Academic Press; 1974:16–18.
21. Klassen LM, Menon RS. Robust automated shimming technique using mapping acquisition parameters (RASTAMAP). Magn Reson Med 2004;51:881–887.
22. Van Gelderen P, de Zwart JA, Starewicz P, Hinks RS, Duyn JH. Real-time shimming to compensate for respiration-induced B0 fluctuations. Magn Reson Med 2007;57:362–368.
23. Weiger M, Speck T, Fey M. Gradient shimming with spectrum optimization. J Magn Reson 2006;182:38–48.
24. Hetherington HP, Chu WJ, Gonen O, Pan JW. Robust fully automated shimming of the human brain for high-field 1H spectroscopic imaging. Magn Reson Med 2006;56:26–33.
25. Koch KM, McIntyre S, Nixon TW, Rothman DL, de Graaf RA. Dynamic shim updating on the human brain. J Magn Reson 2006;180:286–296.
26. Schaer M, Kozerke S, Fischer SE, Boesiger P. Cardiac SSFP imaging at 3 Tesla. Magn Reson Med 2004;51:799–806.
27. Fillmer A, Kirchner T, Cameron D, Henning A. Constrained image-based B_0 shimming accounting for "local minimum traps" in the optimization and field inhomogeneities outside the region of interest. Magn Reson Med 2015;73:1370–1380.
28. Marquardt DW. An algorithm for least-squares estimation of nonlinear parameters. J Soc Indust Appl Math 1963;11:431–441.
29. Hadamard J. Sur les problemes aux derivees partielles et leur signification physique. Princeton Univ Bull 1902:49–52.
30. Fletcher R. Practical methods of optimization. Hoboken, NJ: John Wiley and Sons; 1987.
31. Byrd RH, Gilbert JC, and Nocedal J. A trust region method based on interior point techniques for nonlinear programming. Math Prog 2000;89:149–185.
32. Gill PE, Murray W, Wright MH. Numerical linear algebra and optimization. Boston, MA: Addison-Wesley; 1991:1.
33. Avdievich NI, Hoffman J, Shajan G, Pfrommer A, Giapitzakis IA, Scheffler K, Henning A. Evaluation of transmit efficiency and SAR for a tight fit transceiver human head phased array at 9.4T. NMR Biomed 2017;30:e3680.
34. Juchem C, Brown PB, Nixon TW, McIntyre S, Rothman DL, de Graaf RA. Multicoil shimming of the mouse brain. Magn Reson Med 2011; 66:893–900.
35. Tikhonov AN. Solution of incorrectly formulated problems and the regularization method. Soviet Math Dokl 1963;4:1035–1038.

SUPPORTING INFORMATION

Additional Supporting Information may be found in the online version of this article.

Fig. S1. The overall performance of the different shimming algorithms in two additional shimming applications (in addition to Fig. 5). Each box contains the σB_0 (standard deviation of the frequencies in the shimmed B_0 map) resulting from applying each of the corresponding shimming algorithm to all 33 of the 7T in vivo data sets. The best shim quality achievable through an unconstrained ***pinv*** algorithm is also shown for comparison purposes. The different algorithms are indicated with different letters as unshimmed (**a**), *pinv* (**b**), *nonlin-as* (**c**), *nonlin-ip* (**d**), *nonlin-sqp* (**e**), *QP* (**f**), *Clipped-it* (**g**), *Fixed-tsvd* (**h**), *Lsqlin* (**i**), *LevMar* (**j**), and *ConsTru* (**k**).

Table S1. Results of the Robustness Performance Tests

Note: Perturbation robustness is shown on the left and starting-value sensitivity is shown on the right. The average ($\pm$ standard deviation) shim quality (standard deviation of the shimmed B_0 maps) across all 33000 test cases for each algorithm is shown for three different shimming applications. The best performances are highlighted in light green.

Table S2. Comparison of the Runtimes of the Algorithms in Three Different Shimming Applications

Note: The average ($\pm$ standard deviation) runtime of the algorithms averaged across all 33 of the 7T in vivo data sets are shown. The best performances are highlighted in green.

Table S3. Overall Performance of the Different Shimming Algorithms in Five Different Shimming Applications for Both Second-Order and Third-Order Shimming

Note: The average ($\pm$ standard deviation) shim quality (standard deviation of the shimmed B_0 maps) across all 33 of the 7T in vivo data sets for each algorithm is shown. The best performances are highlighted in light green.

APPENDIX A. Mathematical Description of the *ConsTru* Method

APPENDIX B. Mathematical Discussion of Tikhonov versus TSVD Regularization Methods

Supporting Figure S1- The overall performance of the different shimming algorithms in 2 additional shimming applications (in addition to Figure 5). Each box contains the σB_0 (standard deviation of the frequencies in the shimmed B_0 map) resulting from applying each of the corresponding shimming algorithm to all 33 of the 7T in-vivo datasets. The best shim quality achievable through an unconstrained ***pinv*** algorithm is also shown for comparison purposes. The different algorithms are indicated with different letters as: (a) unshimmed, (b) ***pinv***, (c) ***nonlin-as***, (d) ***nonlin-ip***, (e) ***nonlin-sqp***, (f) ***QP***, (g) ***Clipped-it***, (h) ***Fixed-tsvd***, (i) ***Lsqlin***, (j) ***LevMar***, and (k) ***ConsTru***.

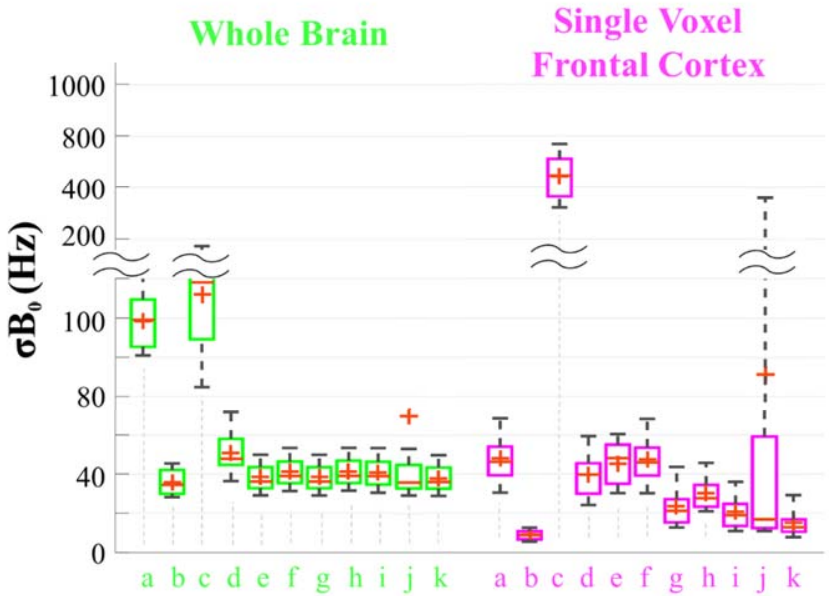

Supporting Table S1- Results of the robustness performance tests. Perturbation robustness is shown on the left and starting-value sensitivity is shown on the right. The average (± standard deviation) shim quality (standard deviation of the shimmed B_0 maps) across all 33000 test cases for each algorithm are shown for three different shimming application. The best performances are highlighted in light green.

$\sigma B_0(Hz)$	Whole Brain$^+$	Single Slice	Single Voxel	Whole Brain$^+$	Single Slice	Single Voxel
	Perturbation Robustness			Starting-value Robustness		
Unshimmed	191.35 ± 11.00	105.72 ± 19.64	55.52 ± 12.69	189.90 ± 10.92	102.99 ± 19.87	48.0 ± 13.59
Pinv	61.74 ± 8.70	33.93 ± 5.29	25.45 ± 1.99	54.42 ± 8.87	19.14 ± 3.94	9.08 ± 2.77
Nonlin-as	70.53 ± 13.58	572.30 ± 151.19	411.12 ± 138.79	119.60 ± 16.76	464 ± 238.48	448.88 ± 154.94
Nonlin-ip	72.64 ± 16.52	36.93 ± 7.24	45.19 ± 10.49	69.90 ± 17.78	62.70 ± 41.82	37.15 ± 12.16
Nonlin-sqp	61.74 ± 8.70	35.45 ± 5.83	50.83 ± 13.133	54.89 ± 9.02	70.53 ± 62.07	46.05 ± 16.10
QP	61.74 ± 8.70	33.95 ± 7.22	55.21 ± 12.61	-	-	-
Clipped-it	61.74 ± 8.70	33.93 ± 5.29	37.05 ± 12.06	-	-	-
Fixed-tsvd	61.74 ± 8.70	33.93 ± 5.29	39.06 ± 7.21	-	-	-
Lsqlin	61.74 ± 8.70	33.93 ± 5.29	34.55 ± 8.15	-	-	-
LevMar	61.95 ± 9.10	38.53 ± 7.98	91.04 ± 91.08	55.05 ± 10.19	85.95 ± 73.76	67.48 ± 129.31
ConsTru	61.74 ± 8.70	33.93 ± 5.29	29.07 ± 4.95	-	-	-

Supporting Table S2- Comparison of the runtime of the algorithms in 3 different shimming application. The average (± standard deviation) runtime of the algorithms averaged across all 33 of the 7T in-vivo datasets are shown in the table. The best performances are highlighted in green.

Run-time (sec)	Whole Brain^{+}	Single Slice	Single Voxel
Pinv	0.009 ± 0.002	0.0013 ± 0.003	0.0012 ± 0.002
Nonlin-as	0.35 ± 0.25	0.06 ± 0.09	0.04 ± 0.09
Nonlin-ip	1.17 ± 0.40	0.12 ± 0.42	0.06 ± 0.04
Nonlin-sqp	1.36 ± 0.48	0.16 ± 0.07	0.09 ± 0.08
QP	0.023 ± 0.012	0.011 ± 0.02	0.010 ± 0.03
Clipped-it	0.050 ± 0.012	0.003 ± 0.012	0.0013 ± 0.002
Fixed-tsvd	0.021 ± 0.004	0.0011 ± 0.001	0.0007 ± 0.001
Lsqlin	0.13 ± 0.04	0.037 ± 0.05	0.01 ± 0.012
LevMar	4.01 ± 2.91	0.43 ± 0.15	0.11 ± 0.06
ConsTru	0.048 ± 0.001	0.004 ± 0.0006	0.0023 ± 0.005

Supporting Table S3- The overall performance of the different shimming algorithms in 5 different shimming applications for both 2nd order and 3rd order shimming. The average (± standard deviation) shim quality (standard deviation of the shimmed B_0 maps) across all 33 of the 7T in-vivo datasets for each algorithm are shown. The best performances are highlighted in light green.

σB_0(Hz)	Whole Brain+	Whole Brain	Single Slice	Single voxel (visual cortex)	Single voxel (frontal cortex)
	2nd Order				
Unshimmed	189.90 ± 10.92	118.53 ± 14.87	102.99 ± 19.87	26.90 ± 5.09	48.0 ± 13.59
Pinv	57.40 ± 9.02	41.87 ± 8.02	24.21 ± 6.09	3.95 ± 1.19	15.06 ± 5.11
Nonlin-as	67.76 ± 11.85	104.96 ± 34.99	569.68 ± 150.50	492.07 ± 280.47	406.86 ± 158.53
Nonlin-ip	65.04 ± 12.85	49.33 ± 12.83	28.15 ± 7.35	17.96 ± 5.06	39.20 ± 11.89
Nonlin-sqp	57.40 ± 9.02	41.88 ± 8.03	24.29 ± 6.09	34.27 ± 6.96	49.86 ± 16.28
QP	57.40 ± 9.02	41.88 ± 8.03	26.33 ± 6.38	26.66 ± 5.16	47.69 ± 13.85
Clipped-it	57.40 ± 9.02	41.87 ± 8.02	24.22 ± 6.09	3.95 ± 1.19	17.45 ± 8.05
Fixed-tsvd	57.40 ± 9.02	41.87 ± 8.02	24.22 ± 6.09	5.17 ± 1.33	30.39 ± 8.94
Lsqlin	57.40 ± 9.02	41.87 ± 8.02	24.22 ± 6.09	3.95 ± 1.19	20.95 ± 8.73
LevMar	57.40 ± 9.02	41.93 ± 8.07	60.30 ± 6.09	21.65 ± 41.56	38.89 ± 72.12
ConsTru	57.40 ± 9.02	41.87 ± 8.02	24.22 ± 6.09	3.95 ± 1.19	16.12 ± 7.05
	3rd Order				
Unshimmed	189.90 ± 10.92	118.53 ± 14.87	102.99 ± 19.87	26.90 ± 5.09	48.0 ± 13.59
Pinv	54.42 ± 8.87	36.11 ± 6.55	19.14 ± 3.94	3.67 ± 1.11	9.08 ± 2.77
Nonlin-as	111.87 ± 15.05	131.96 ± 30.58	608.51 ± 155.59	433.05 ± 188.47	443.94 ± 108.81
Nonlin-ip	68.15 ± 16.92	51.026 ± 11.45	27.58 ± 6.86	8.05 ± 3.79	39.62 ± 12.25
Nonlin-sqp	54.76 ± 8.81	38.37 ± 7.32	24.27 ± 5.83	35.29 ± 17.37	45.54 ± 12.13
QP	56.65 ± 8.81	41.15 ± 7.652	26.28 ± 6.24	26.65 ± 5.05	47.69 ± 13.54
Clipped-it	54.71 ± 8.81	38.33 ± 7.33	86.35 ± 310.17	26.77 ± 39.88	23.73 ± 11.92
Fixed-tsvd	55.31 ± 8.82	41.42 ± 7.72	24.08 ± 5.95	5.16 ± 1.30	30.38 ± 8.74
Lsqlin	55.58 ± 9.02	40.77 ± 7.71	23.43 ± 5.56	3.89 ± 1.15	20.94 ± 8.64
LevMar	54.74 ± 8.81	69.94 ± 148.58	32.13 ± 33.65	25.06 ± 43.64	91.47 ± 137.88
ConsTru	54.74 ± 8.81	38.33 ± 7.33	20.03 ± 4.28	3.79 ± 1.15	15.01 ± 6.90

Appendix A.

The minimum-norm solution to any shimming problem defined as:

$$\min_x \|(Ax - b)\|^2 \tag{1}$$

can be calculated using the ***pinv*** method as:

$$x = A^{\dagger} b \tag{2}$$

Where $A^{\dagger}$ is the pseudo-inverse of the matrix A. If we perform the singular value decomposition of the system matrix A, we have:

$$A = U\sum V = \sum_{i=1}^{n} \sigma_i u_i v_i^T \tag{3}$$

Where n is the number of shim terms or columns of matrix A, u_i and v_i are the columns of the matrices U and V resulting from the singular value decomposition of matrix A (commonly called the left and right singular vectors, respectively) pertaining to each singular value σ_i.

To put this all together, we can rewrite the shim solution as:

$$x = \sum_{i=1}^{n} \frac{u_i^T b}{\sigma_i} \, v_i \tag{4}$$

Where b is the vector of the unshimmed B_0 values. Since the singular vectors are orthogonal, we can write the norm of the solution as:

$$\|x\| = \left\| \sum_{i=1}^{n} \frac{u_i^T b}{\sigma_i} \, v_i \right\| = \sum_{i=1}^{n} \left\| \frac{u_i^T b}{\sigma_i} \, v_i \right\|. \tag{5}$$

From this formula, we can see that each singular value and the respective u_i and v_i contribute a certain term in this summation to the norm of the actual solution. So by removing a singular value (eliminating terms one by one from this summation), we decrease the norm of the solution which will enable it to eventually satisfy the constraints. It can also be seen that the smallest singular values contribute the most to this norm. So by truncating the smallest singular values, we are serving the purpose of reducing the norm of the solution as well as avoiding noise amplification in the calculated solution. No matter what the constraints of the system are, we can continue doing this and truncate more singular values to satisfy the constraints (the solution norm goes to 0 in the extreme case). So it is guaranteed that we will satisfy the constraints eventually. It is only a matter of introducing too much bias (or regularization error) into the solution by truncating more and more singular values.

To the trade-off between regularization error (bias) and the norm of the solution clearer, the bias introduced by truncating the singular values can be written as:

$$\left\| \sum_{i=1}^{n} \frac{u_i^T b}{\sigma_i} \, v_i - \sum_{i=1}^{n} f_i \frac{u_i^T b}{\sigma_i} \, v_i \right\| \tag{6}$$

$$f_i = \begin{cases} 0 \; for \; the \; truncated \; SVs \\ 1 \; for \; the \; rest \end{cases}$$

Where first term is the true solution to the problem and the second term is the approximated TSVD solution and f_is in the approximate solution are binary values which indicate whether or not the i[th] singular value is truncated. So, it can readily be seen that the more singular values we truncate (the more $f_i s$ equal to 0) the bigger the bias will be.

Appendix B.

Both Tikhonov and TSVD are regularization methods that result in a minimum-norm solution. The advantages of using TSVD over using Tikhonov is merely the simplicity of the TSVD, where at each iteration it is clear what the next step should be: truncating the next smallest singular value as is done in ***ConsTru***. If a similar adaptive regularization method was to be used for Tikhonov, it is not very clear where the search for the regularization parameter should begin or how small the step for varying it should be. In the search for the easiest and most user-independent shimming algorithm, we decided to consider ***ConsTru*** in our study.

The bias introduced by Tikhonov regularization might be smaller than that introduced by ***ConsTru***. In fact the biases for the two can be written as:

$$\left\| \sum_{i=1}^{n} x_{true} - \sum_{i=1}^{n} f_i \frac{u_i^T b}{\sigma_i} \, v_i \right\| \tag{7}$$

Where:

$$f_i = \begin{cases} 0 \; for \; the \; truncated \; SVs \\ 1 \; for \; the \; rest \end{cases} \quad in \; the \; \boldsymbol{ConsTru} \; method$$

And,

$$f_i = \frac{\sigma_i^2}{\sigma_i^2 + \lambda} \; in \; the \; \boldsymbol{Tikhonov} \; method \; (\lambda \; is \; the \; Tikhonov \; parmeter)$$

However, the perturbation error for these two methods can be written as:

$$\left\| \sum_{i=1}^{n} f_i \frac{u_i^T b}{\sigma_i} \, v_i \right\| . \epsilon \tag{8}$$

where ϵ is the error in the input.

In summary, TSVD is a more simple method for finding the regularization parameter, while Tikhonov allows more flexibility (since the Tikhonov regularization parameter can be any real number). Secondly, there is a trade-off between regularization error (bias) and perturbation error (sensitivity). Less bias results in a higher solution norm which results in more perturbation error.

While a thorough comparison between TSVD and Tikhonov is beyond the scope of this paper, we expect the methods to perform similarly (as is often found in the literature).

Publication II

"Modeling Real Shim Fields for Very High Degree (and Order) B_0 Shimming of the Human Brain at 9.4T"

P Chang*, S Nassirpour*, A Henning

Magnetic Resonance in Medicine, 2017, doi:10.1002/mrm.26658.

FULL PAPER

Magnetic Resonance in Medicine 00:00–00 (2017)

Modeling Real Shim Fields for Very High Degree (and Order) B_0 Shimming of the Human Brain at 9.4 T

Paul Chang,[1,2†]* Sahar Nassirpour,[1,2†] and Anke Henning[1]

Purpose: To describe the process of calibrating a B_0 shim system using high-degree (or high order) spherical harmonic models of the measured shim fields, to provide a method that considers amplitude dependency of these models, and to show the advantage of very high-degree B_0 shimming for whole-brain and single-slice applications at 9.4 Tesla (T).

Methods: An insert shim with up to fourth and partial fifth/sixth degree (order) spherical harmonics was used with a Siemens 9.4T scanner. Each shim field was measured and modeled as input for the shimming algorithm. Optimal shim currents can therefore be calculated in a single iteration. A range of shim currents was used in the modeling to account for possible amplitude nonlinearities. The modeled shim fields were used to compare different degrees of whole-brain B_0 shimming on healthy subjects.

Results: The ideal shim fields did not correctly shim the subject brains. However, using the modeled shim fields improved the B_0 homogeneity from 55.1 (second degree) to 44.68 Hz (partial fifth/sixth degree) on the whole brains of 9 healthy volunteers, with a total applied current of 0.77 and 6.8 A, respectively.

Conclusions: The necessity of calibrating the shim system was shown. Better B_0 homogeneity drastically reduces signal dropout and distortions for echo-planar imaging, and significantly improves the linewidths of MR spectroscopy imaging.
Magn Reson Med 000:000–000, 2017. © 2017 International Society for Magnetic Resonance in Medicine.

Key words: B_0 shimming; field modeling; ultrahigh field strengths; high-order shimming

INTRODUCTION

One of the many challenges of high field strengths in MRI is the inhomogeneity of the B_0 field. Clinical human MRI systems are usually equipped with spherical harmonic shim coils up to either first- or second-degree shim terms. However, as the field strength of MRI systems increases to ultrahigh field strengths such as 7 and 9.4 Tesla (T), B_0 inhomogeneity becomes even more severe and therefore requires more attention.

B_0 inhomogeneity directly affects the image quality. Various artifacts can result from poor B_0 homogeneity, such as signal dropout, geometric distortion, blurring, curved slice profiles, and Moiré artifacts (1–4). Echo-planar imaging (EPI) sequences are especially susceptible to many of these artifacts (5). B_0 homogeneity is even more important for MR spectroscopy (MRS), as some of the peaks that need to be separated differ by only a few hertz (eg, the characteristic splitting of lactate is only 7 Hz) (6,7). Poor B_0 homogeneity results in the broadening of linewidths. Furthermore, any water and fat-suppression technique will be compromised by inhomogeneity (8).

Current state-of-the-art B_0 shimming hardware either extends the degrees (and orders) of the spherical harmonic terms to third-degree (9) and even fourth-degree systems (10), or alternatively, discard the spherical harmonic paradigm for more localized multicoil shim arrays (11). The multicoil shimming approach uses a large array of small coils to shim the B_0 field. In the case of Juchem et al (11), 48 coils were used. The advantages of the multicoil shim system is that there are more degrees of freedom. The advantages of spherical harmonic shimming are that the hardware is normally available with the MRI scanner or otherwise can be purchased commercially, and that the shim coils generate orthogonal shim fields and are based on analytical models.

Both of these systems require knowledge of the real shim field produced by each coil for calibration so that they can be used in the B_0 shimming algorithm (12–15). Spherical harmonic shim systems are based on analytical models (from the Legendre polynomials), and vendor-implemented B_0 shimming algorithms assume that the shim fields generated by each of the shim coils are identical to the desired spherical harmonic function (15,16) (ie, shim fields are usually assumed to be ideal). If the shim coils generate fields that are similar to the ideal fields, this assumption is feasible. However, if this is not the case, then to improve the shim, the shimming needs to be done iteratively until sufficient convergence is achieved (12,16). Alternatively, field reference maps can be acquired for each shim coil to correct for field imperfections. This has been done previously for very high-degree (or very high-order) shim systems used on a 7T magnet, in which the higher-degree shim coils do not generate ideal fields (9,10,17). Field reference maps were successfully used to shim using up to second (12,13) and third-degree shim terms (9,10,17), and even fourth with partial fourth-plus-degree shim terms (18).

The advantage of using modeled shim fields (as opposed to directly using the field reference maps, which was done previously) is that there are no problems with either noise or different field of views (FOVs) or different resolutions or different position offsets.

[1]Max Planck Institute for Biological Cybernetics, Tuebingen, Germany.

[2]IMPRS for Cognitive and Systems Neuroscience, Eberhard-Karls University of Tuebingen, Germany

*Correspondence to: Paul Chang, MSc, Max Planck Institute for Biological Cybernetics, Spemannstrasse 41, 72076 Tübingen, Germany. Tel: +49 7071 601 938; E-mail: paul.chang@tuebingen.mpg.de.

†These authors contributed equally to this study.

Received 20 October 2016; revised 6 February 2017; accepted 6 February 2017

DOI 10.1002/mrm.26658

Published online 00 Month 2017 in Wiley Online Library (wileyonlinelibrary.com).

© 2017 International Society for Magnetic Resonance in Medicine

Furthermore, because the reference maps are compressed into the analytical model, the reference maps do not need to be stored on the system. This makes the B_0 shimming algorithm less cumbersome without sacrificing the quality of the shim. Furthermore, by using the analytical models instead of reference maps to characterize the shim fields, we can account for any nonlinearity of the shim amplifiers. Modeling of the shim fields has been reported previously in (10,17,19), where they used up to third-degree shim coils. More recently, Song et al (20) also modeled shim fields using "virtual" shim functions and a maximum likelihood method to denoise the acquired B_0 maps. However, neither of these methods used all cross-terms, but rather used a subset of the spherical harmonic functions in which the degree of the functions was equal to or less than the intended degree. Although Juchem et al (17) also used a range of current amplitudes, only linear amplitude models were used.

The acquisition procedure for B_0 shimming has been investigated in many previous studies (12–15,21). As mentioned previously, acquiring reference field maps for B_0 shimming has already been done. However, to our knowledge, modeling of the real shim fields has not been described previously in sufficient detail and did not consider the influence of geometric distortions or fully account for amplitude nonlinearity.

In this work, we provide a quantitative evaluation of shim field imperfections and their effect on shim quality. We provide a comprehensive description of how to calibrate a B_0 shim system by acquiring and modeling reference field maps of the shim fields while accounting for geometric distortion and amplitude nonlinearity. Using the modeled field maps, the optimal shim currents can be calculated in a single iteration. Finally, we show very high-degree B_0 shimming (or very high-order B_0 shimming) of the human brain at 9.4 T. Although this study uses very high-degree shims at ultrahigh field, the described method can be used for any field strength and for spherical harmonic shim systems of any degree.

METHODS

Study Design

This investigation was performed using an ultrahigh field 9.4T human whole-body Siemens MRI scanner (Erlangen, Germany), in which B_0 inhomogeneity is of particular concern. To investigate high-order and high-degree B_0 shimming, an insert shim MX10W-28 from Resonance Research Inc (RRI) (Billerica, MA, USA) was used. Twenty-eight channels, including complete second, third and fourth-degree spherical harmonics (and partial fifth and sixth-degree harmonics), were available (Table 1). The maximum current that could be applied was 10 A for each coil, and the maximum total current was 40 A. The sensitivities of each shim channel can be found in Table 1.

In the first section of the study, we investigated how to minimize geometric distortion in acquiring the reference field maps. We used a large cylindrical phantom with a diameter of 250 mm and a plastic grid with equidistant spacings of 15 mm. The phantom was filled with silicon oil because of its low dielectric constant, which yielded good B_1 homogeneity. A radiofrequency (RF) coil with 16-channel Tx/15 Rx element receive array (22) was used to acquire the images for the geometric distortion. A 3D gradient-echo (GRE) B_0-mapping sequence (1) with the following parameters was used to measure the fields: resolution = $1.4 \times 1.4 \times 1.4\,mm^3$; field of view (FOV) = $270 \times 270 \times 270\,mm^3$; echo time (TE) = 4.00/4.76 ms; repetition time (TR) = 10 ms.

Table 1
Shim Terms and Insert Shim Coil Sensitivities

Shim term	Spherical harmonic function	Sensitivity ($Hz/cm^n/A$)
Z0	1	6058
Z2	$z^2-1/2*(x^2+y^2)$	6.942
ZX	zx	24.15
ZY	zy	24.15
C2	x^2-y^2	3.64
S2	2xy	3.64
Z3	$z(z^2-3/2*(x^2+y^2))$	0.4923
Z2X	$x(z^2-1/4*(x^2+y^2))$	1.0
Z2Y	$y(z^2-1/4*(x^2+y^2))$	1.0
ZC2	$z(x^2-y^2)$	1.77
ZS2	2zxy	1.77
C3	$x(x^2-3y^2)$	0.188
S3	$y(3x^2-y^2)$	0.188
Z4	$z^4-3z^2(x^2+y^2)+3/8*(x^2+y^2)$	0.04206
Z3X	$zx(z^2-3/4*(x^2+y^2))$	0.123
Z3Y	$zy(z^2-3/4*(x^2+y^2))$	0.123
Z2C2	$z(x^2-y^2)(z^2-1/6*(x^2+y^2))$	0.093
Z2S2	$2z(xy)(z^2-1/6*(x^2+y^2))$	0.093
ZC3	$x(x^2-3y^2)(z^2-1/8*(x^2+y^2))$	0.121
ZS3	$x(x^2-3y^2)\,(z^2-1/8*(x^2+y^2))$	0.121
C4	$x^4-6x^2y^2+y^4$	0.0187
S4	$4xy(x^2-y^2)$	0.0187
ZC4	$z(x^4-6x^2y^2+y^4)$	5.71e-3
ZS4	$4zxy(x^2-y_2)$	5.71e-3
C5	$x(x^4-10x^2y^2+5y^4)$	9.9e-4
S5	$y(y^4-10x^2y^2+5x^4)$	9.9e-4
ZC5	$zx(x^4-10x^2y^2+5y^4)$	3.21e-4
ZS5	$zy(y^4-10x^2y^2+5x^4)$	3.21e-4

After the investigation of geometric distortion, the rest of the phantom and in vivo experiments were performed using an in-house eight-channel transceiver-phased array RF coil (23) and a 2D GRE B_0-mapping sequence (24) with the following parameters: in-plane resolution = $1.56 \times 1.56\,mm^2$; slices = 40; slice thickness = 4 mm (0% distance factor); FOV = $200 \times 200\,mm^2$; TE = 4.00/4.76 ms; TR = 1200 ms; read-out bandwidth = 1500 Hz/Px.

The reference field map of each shim coil was measured on a spherical silicon oil phantom of diameter 170 mm. This phantom was used to cover the volume of an average human brain. After acquiring and modeling the reference field maps, the models were verified on a head-and-shoulder phantom filled with a mixture of agar gel and sugar (to mimic the dielectric properties of the human brain at 9.4 T). In vivo experiments were done by performing B_0 shimming on the brains of nine healthy volunteers with the approval of the institutional review board. All volunteers gave their written informed consent.

The B_0-mapping sequences had a delta TE of 0.76 ms, as this ensures that the fat and water (for in vivo

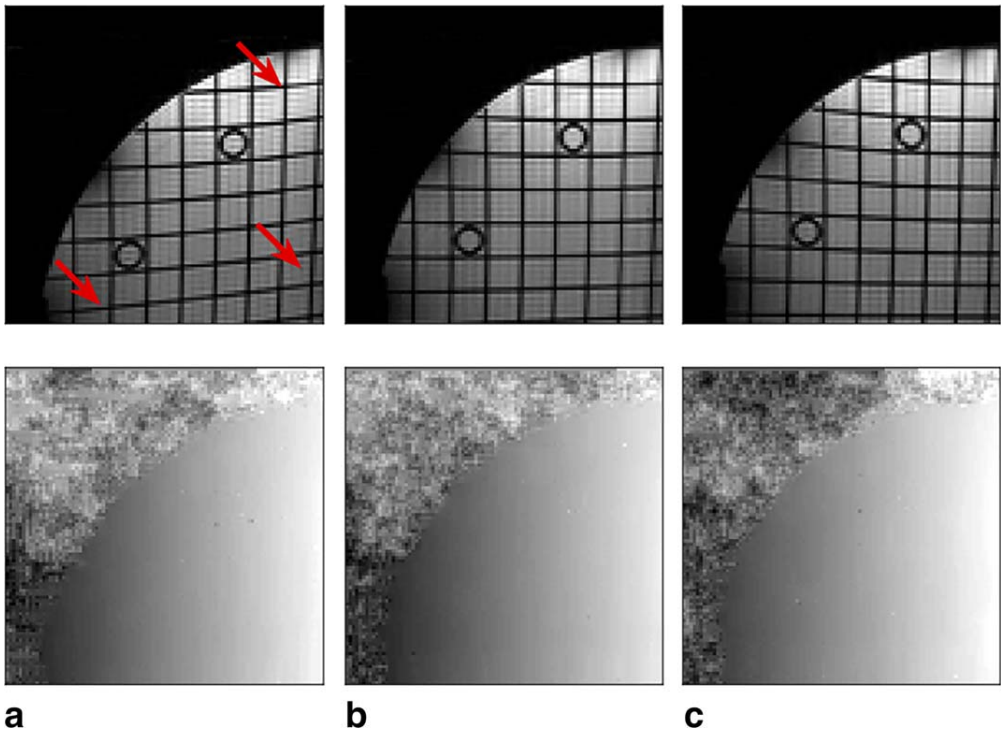

FIG. 1. Section of a slice measured with a read-out gradient of 250 Hz/Px (**a**), 500 Hz/Px (**b**), and 1300 Hz/Px (**c**). Magnitude images in the top row show clear distortions, whereas the B_0 maps on the bottom row do not.

experiments) are in phase, and it minimizes the amount of phase wrapping in the B_0 map. Any phase unwrapping that was required was performed slice-wise using the max-flow graphs (PUMA) algorithm implemented by (25).

Geometric Distortion

Strong shim fields introduce strong inhomogeneities in the B_0 field, and this results in geometric distortion in the images. Figure 1 shows that although the geometric distortion is not very obvious in the B_0 maps, it can be clearly seen in the magnitude images of the grid-phantom acquired from the same data set. For this investigation, two methods of reducing geometric distortions were compared: (i) using retrospective geometric correction with a grid phantom, and (ii) using a higher read-out bandwidth while acquiring the B_0 maps. Even though a higher read-out bandwidth can reduce distortions, this comes at the cost of a lower signal-to-noise ratio (SNR).

The study was performed on two second-degree shim terms (ZY and XY) with an amplitude of 4 mT/m^2 each. The B_0 maps of the phantom were acquired using read-out bandwidths of 250 Hz/Px, 500 Hz/Px, and 1300 Hz/Px for comparison. The benchmark B_0 map that was used for comparison was obtained using the highest available read-out bandwidth (1500 Hz/Px) with a grid-free phantom to reduce magnetic susceptibility effects between the silicon oil and the plastic grid.

The retrospective geometric correction was performed using the cross-points of the grid and a custom semi-automatic MATLAB (MathWorks, Natick, MA, USA) feature detection script based on the Harris-Stephens algorithm (26). Note that using the retrospective correction down-samples the B_0 map, because only the cross-points of the grid are used. The retrospective correction was used in combination with the different read-out bandwidths. The shim fields were modeled using spherical harmonic decomposition (described in the next subsection) using either:

1. The entire B_0 map of the phantom, or
2. The B_0 values (using the phantom grid as a reference) without position correction; and
3. With position correction.

The field models were then reconstructed on a $100 \times 100 \times 100\,mm^3$ FOV and compared with the benchmark B_0 map (acquired at 1500 Hz/Px without the grid). The method that best minimized the geometric distortions of the reconstructed maps was used for the remainder of the investigation.

Mapping and Modeling Reference Shim Fields

As mentioned in the study design, the reference maps for modeling the shim fields were acquired on a smaller spherical phantom approximately the size of the human brain, as we did not want to model the fields outside the volume of interest (VOI) and let the strong inhomogeneities outside the VOI bias the model in the region where we were interested in imaging.

The reference fields of each of the 28 shim coils were acquired at a range of different input current amplitudes (± 1000 mA, ± 500 mA, ± 200 mA, and ± 100 mA), so that any potential amplitude nonlinearities could be

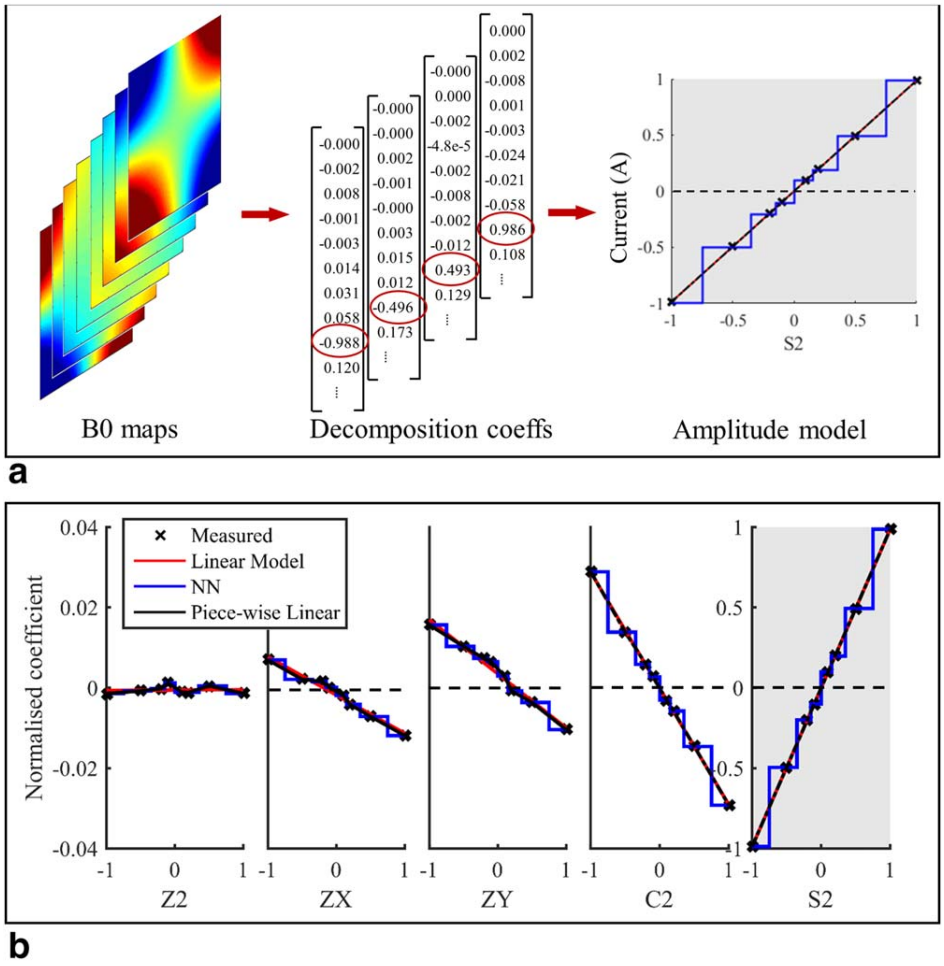

FIG. 2. (**a**) Processing pipeline of the B_0 maps. Eight B_0 maps were acquired for each shim field at different current amplitude. Each B_0 map was decomposed into sixth-degree spherical harmonics (only four of the eight decomposition coefficients are shown for illustration purposes), and the self-terms are shown in the red ellipses. Each column of coefficients has 49 elements, as sixth-degree spherical harmonics were used. Each coefficient was modeled with an amplitude model. (**b**) Second-degree coefficients for the S2 shim term at a range of current amplitudes (on the x-axis). The figure shows the self-term and the cross-terms. Note that this was done for all coefficients up to the sixth degree. The different models used to correct for amplitude nonlinearities are shown: linear model, nearest neighbor (NN), and piece-wise linear.

modeled and accounted for. Most shim coils did not introduce a large frequency shift; therefore, the B_0 maps could be acquired using the same reference frequency. However, for the Z4 coil that induced a large frequency shift, the reference frequency was re-adjusted and the frequency offset was retrospectively added back to the B_0 maps. The frequency drift of the Z4 that was observed was − 11.38 kHz per ampere.

The eight reference fields (for different current amplitudes) of each shim coil were modeled using a spherical harmonic decomposition (27,28). A 3D scalar spatial field distribution $B_0(\boldsymbol{r})$ could be approximated using a set of 3D-spatial basis functions $F_n(\boldsymbol{r})$, in which $\boldsymbol{r} = (x, y, z)$ is the position vector:

$$B_0(\boldsymbol{r}) \approx \sum_{n=1}^{N} b_n \cdot F_n(\boldsymbol{r}) \qquad [1]$$

and b_n are constants and N is the number of basis functions.

Because the shim coils are based on spherical harmonics, a natural choice of basis functions would be the spherical harmonic functions $A_{l,m}(\boldsymbol{r})$ and the shim fields can thus be modeled as follows:

$$B_0(\boldsymbol{r}) \approx \sum_{l=0}^{L} \sum_{m=-l}^{l} b_{l,m} \cdot A_{l,m}(\boldsymbol{r}) \qquad [2]$$

where $b_{l,m}$ are constants, l is the degree of the spherical harmonic function, and m is the order. The degree of the approximation is given by L. When modeling the shim fields, the degree of approximation L was also carefully considered. The model can be improved by fitting higher and higher degrees of the spherical harmonic functions. However, the marginal improvement decreases and the model may even start to overfit the data from a certain degree onward. Hence, we determined the optimal degree of spherical harmonic functions with which to model the real shim fields. Each measured shim field was modeled with an increasing number of spherical

harmonic functions from the second degree to the ninth degree. The residual mean square errors (RMSEs) between the measured fields and the modeled fields were calculated. The degree of the spherical harmonic functions to use for modeling was chosen such that the accuracy of the fit no longer improved.

The spherical harmonic decomposition was performed by solving the standard overdefined linear system of equations for n positions (in this case, up to sixth-degree spherical harmonic functions):

$$\begin{bmatrix} A_{0,0}(\boldsymbol{r}_1) & A_{1,-1}(\boldsymbol{r}_1) & A_{1,0}(\boldsymbol{r}_1) & A_{1,1}(\boldsymbol{r}_1) & \cdots & A_{6,6}(\boldsymbol{r}_1) \\ A_{0,0}(\boldsymbol{r}_2) & A_{1,-1}(\boldsymbol{r}_2) & A_{1,0}(\boldsymbol{r}_2) & A_{1,1}(\boldsymbol{r}_2) & & A_{6,6}(\boldsymbol{r}_2) \\ \vdots & & & & \ddots & \vdots \\ A_{0,0}(\boldsymbol{r}_n) & A_{1,-1}(\boldsymbol{r}_n) & A_{1,0}(\boldsymbol{r}_n) & A_{1,1}(\boldsymbol{r}_n) & \cdots & A_{6,6}(\boldsymbol{r}_n) \end{bmatrix} \cdot \begin{bmatrix} b_{0,0} \\ b_{1,-1} \\ \vdots \\ b_{6,6} \end{bmatrix} = \begin{bmatrix} b0_1 \\ b0_2 \\ \vdots \\ b0_n \end{bmatrix} \quad [3]$$

where $A_{l,m}$ is given by the Legendre polynomials. The values $b0_k$ are the B_0 values at position $\boldsymbol{r}_k$, calculated from the phase map:

$$b0_k = \frac{\Delta\varphi}{\Delta TE}/\gamma \quad [4]$$

where γ is the Larmor frequency, $\Delta\varphi$ is the measured phase difference obtained from the sequence, and ΔTE is the difference between the echo times of the two phases. Thus, the fields are modeled using a vector of coefficients $\boldsymbol{b}$ calculated from the linear system:

$$A \cdot \boldsymbol{b} = \boldsymbol{b}_0 \quad [5]$$

The B_0 value at an arbitrary position $\boldsymbol{r}_k$ can be estimated by forming the A matrix and multiplying by the coefficient vector $\boldsymbol{b}$.

To account for amplifier nonlinearity, for each of the shim coils, decomposition coefficients were calculated from the field maps driven at the eight different current amplitudes mentioned previously. To avoid confusion later, the decomposition coefficients used to characterize the shim fields will be denoted as the vector $\boldsymbol{c}$ (instead of $\boldsymbol{b}$). Each of the coefficients was fit with different amplitude-dependent models (as depicted in Fig. 2a). Three different models were tested: a linear model, a nearest-neighbor model, and a linearly interpolated model (Fig. 2b).

The linear model assumes that the coefficients are linear with respect to the current amplitude. The nearest-neighbor model uses the coefficient vector of the current amplitude that is nearest to the input current. The linear-interpolated model is basically a piece-wise linear model that interpolates between each of the measured current amplitudes.

The head-and-shoulder phantom (mentioned in the "Study Design" subsection) was used to test each of the three proposed amplitude models. The B_0 shimming procedure was as follows:

1. Initialize the coefficients using the fields measured at 100 mA;
2. Calculate the shim currents;
3. Recalculate the coefficients (for the fields generated by the new shim currents) using one of the three proposed methods; and
4. If the shim current values do not change then STOP; otherwise go to step 2.

Conventional B_0 shimming involves acquiring the b_0 target vector and generating the A matrix (based on ideal spherical harmonic function) and then solving Equation [5] to acquire b as the shim terms to be applied. However, we do not assume ideal spherical harmonic functions but rather use them as basis functions for approximating the shim fields. Therefore, the fields generated by the shim coils can be estimated using the decomposition coefficients C, and Equation [5] becomes

$$(A \cdot C) \cdot \boldsymbol{b} = \boldsymbol{b}_0 \quad [5]$$

for $A \in \mathbb{R}^{P\times Q}$, $C \in \mathbb{R}^{Q\times R}$, $\boldsymbol{b} \in \mathbb{R}^R$ and $\boldsymbol{b}_0 \in \mathbb{R}^P$, where P is the number of positions, Q is the number of spherical harmonic functions used to approximate the reference shim fields, and R is the number of shim coils. The shim terms were calculated using a regularized pseudo-inversion approach (as described in (29)) to solve Equation [6]. The head-and-shoulder phantom was B_0 shimmed using second, third, and fourth-degree shim terms with each of the three amplitude models described to validate the reference shim field models.

In Vivo B_0 Shimming

B_0 shimming was performed in vivo on nine healthy volunteers using a whole-brain VOI (including the cerebellum). This was done assuming ideal-shim fields and compared with shimming while considering the real-shim field models. Thereafter, the real-shim field models were used to compare lower-degree shimming with higher-degree shimming using second, third, fourth, and fourth-plus (including partial fifth and sixth) degree shim terms. B_0 homogeneity was evaluated by considering the standard deviation of the B_0 maps over the VOI.

We show the advantage of the fourth-plus-degree B_0 shimming over the vendor-implemented second-degree shimming in two applications: a whole brain global B_0 shimming application (EPI) and a single-slice B_0 shimming application (MRSI).

The single-shot EPI sequence parameters were: TR = 1740 ms; TE = 20 ms; FOV = 210 × 210 mm; slices = 35; slice thickness = 3 mm; resolution = 3.28 × 3.28 mm^2; flip angle = 65°; read-out bandwidth = 1954 Hz/Px; echo spacing = 0.58 ms; GRAPPA acceleration factor = 2.

The ^{1}H MRSI data were acquired using a custom free-induction decay (FID) MRSI sequence (30,31) with a

numerically optimized three-pulse water-suppression scheme. The sequence parameters were: FOV = 210 × 210 mm^2; matrix size = 64 × 64; acquisition delay = 1.5 ms, bandwidth = 8000 Hz; sample points = 1024; TR = 340 ms; flip angle = 30°. The spectra were processed using spatial Hanning filtering, eddy current, and zeroth-order phase correction using the reference water signal, recovering the missing FID points by linear backward prediction (32) and HSVD water removal (33). No additional apodization filtering or phase correction was performed. The spectra acquired using the two B_0 shim settings were compared. To keep the TR short and the specific absorption rate low, no lipid or outer volume suppression was used.

Finally, unsuppressed water spectra were acquired in the frontal cortex using a STEAM sequence: voxel size = 2 × 2 × 2 cm^3; averages = 16; TR = 5 s; TE = 11 ms; flip angle = 90°; bandwidth = 8 kHz.

RESULTS

Geometric Distortion

Three different read-out bandwidths and three different B_0 modeling methods were used. Hence, a total of nine comparisons were available for each shim term (XY and ZY).

The distance between uncorrected and corrected positions showed that higher read-out bandwidths reduced the geometric distortion. The mean (and standard deviation) distance between the corrected and uncorrected positions was 5.007 ± 3.172, 3.876 ± 2.453, and 3.266 ± 2.623 pixels for 250 Hz/Px, 500 Hz/Px and 1300 Hz/Px, respectively.

Comparison with the benchmark B_0 map (acquired at 1500 Hz/Px without the grid) showed that using the phantom grid to model the field introduced an RMSE of 13.82% in the model because of the spatial downsampling. This error was calculated by comparing the error between the field maps and averaged for both shim terms. The accuracy of the model using the phantom grid could be improved by correcting for geometric distortion using the grid; however, this only improved the accuracy by 1.48%. Therefore, even though correcting for the positions (ie, correcting geometric distortions) improves the accuracy of the model, the information lost in downsampling the spatial data as a result of the cross points resulted in poorer modeling accuracy.

In contrast, for both of the shim terms that were tested, increasing the read-out bandwidth consistently gave better field models. A read-out bandwidth of 1500 Hz/Px was used for all subsequent B_0 mapping sequences, and no further geometric distortion correction was used.

Mapping and Modeling Reference Shim Fields

The model approximations of the fields were compared with the measured reference field and the RMSE between them (in hertz) (Fig. 3). Figure 3 shows the aggregated error of all 28 of the shim coils of the RRI insert shim. It can clearly be seen that as the degree increases, the error of the fit decreases. For low-degree approximations of the shim fields, the error for modeling the lower-degree shim terms is small, but naturally the low-degree model cannot fully model the higher-degree shim terms. This results in a larger standard deviation of errors for low-degree approximations (Fig. 3). After approximately the sixth degree, there is no longer an improvement as the degree of the models increase. The means of the RMSE for the fifth, sixth, and seventh-degree models were 2.71, 2.67 and 2.78 Hz, respectively.

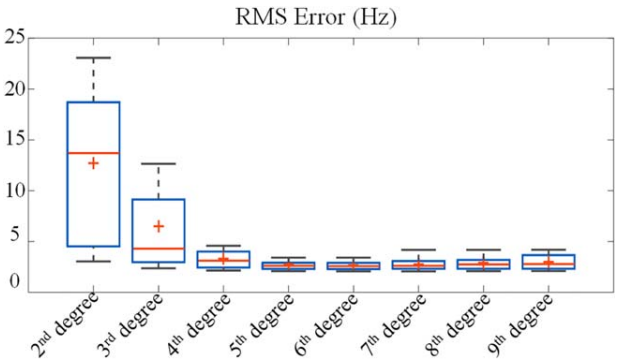

FIG. 3. Root mean square of the residual error between the measured and the modeled fields for all 28 shim terms. All shim terms are modeled using different number of spherical harmonic functions from second to ninth degree.

The shim fields reconstructed from these models, along with ideal shim fields and their differences, are shown in Supporting Figure S1. The figure confirms that there are deviations between the perfect shim field assumption and the actual field generated by the coils. This would result in suboptimal or incorrect B_0 shimming if the real field models are not considered in the shim algorithm. The figure shows that some terms, such as the S2, Z2X and Z2Y, are inverted (relative to the scanner co-ordinates). In addition to these terms, many terms such as the ZC2 and Z2C2 terms had significant deviations from the ideal spherical harmonic fields.

The three amplitude nonlinearity models were tested on the head-and-shoulder phantom. For second-degree B_0 shimming, the mean standard deviations of the B_0 maps were 26.7, 27.0, and 26.6 Hz for the linear, nearest-neighbor and linearly interpolated models, respectively. For third-degree B_0 shimming, the standard deviations were 18.6, 18.7, and 19.0 Hz; and for fourth-degree shimming, 15.35, 15.37, and 15.43 Hz.

It can be seen that each of the three amplitude models provided similar results. Therefore, it can be concluded that the shim fields are relatively linear with respect to the current amplitude. Because the linear model requires the least computational resources, this method was used to model the shim fields. Even though our shim system was linear, this approach can be used to model any arbitrary system to account for amplitude nonlinearities. For example, the effect of saturation of the shim amplifiers on the generated shim fields can be modeled and accounted for using this method.

In summary, each shim channel was modeled with a sixth-degree decomposition, in which each coefficient was modeled with a linear model (with respect to the current amplitude). The coefficients for each channel

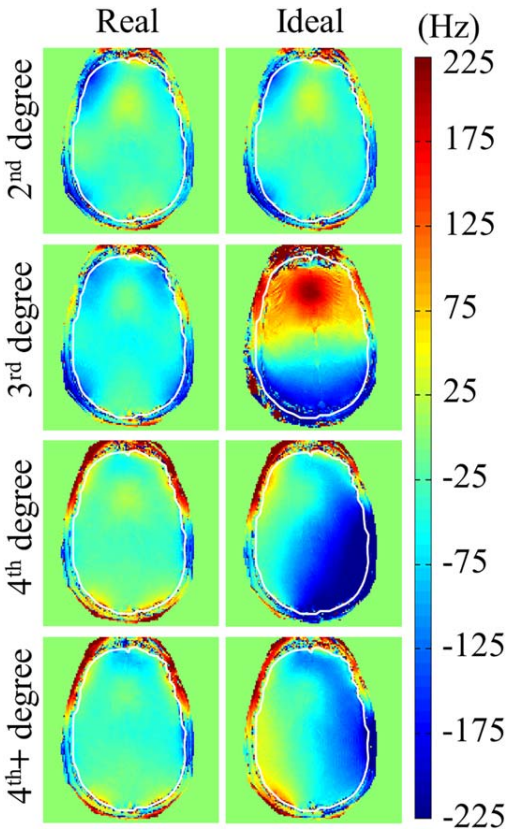

FIG. 4. Comparison of in vivo shimmed B_0 maps when assuming ideal fields and when using modeled real fields. The VOI masks are shown in white and were defined using a custom MATLAB GUI.

can be found in Supporting Table S1 (coefficients normalized by their coil design sensitivities).

In Vivo B_0 Shimming

We performed global B_0 shimming with ideal-field models and compared it with B_0 shimming with real-field models. The B_0 map is shown for one of the nine volunteers in Figure 4. The second-degree shimming is shown for the real-field and ideal-field models. However, for higher degrees, if ideal shim fields are used then the B_0 shimming fails. In contrast, if we consider the real-field models in the shimming algorithm, we can consistently achieve better B_0 homogeneity. Figure 4 depicts only one slice; however, this holds for all slices.

Figure 5 shows the results of B_0 shimming with different degrees of shim terms (when real-field models are used) for one of the volunteers. This shows the improvement of B_0 homogeneity when higher-degree shim terms are used.

Figure 6 shows the B_0 shim results across all nine volunteers using different degrees of shim terms and using ideal-shim fields and real-shim field models. The second-degree shimming for both the ideal and real fields improves the shim from a mean standard deviation of 159.2 Hz (reference map) to a mean standard deviation of approximately 55 Hz across the whole brain at 9.4 T.

If ideal-shim fields are assumed, then the B_0 shim no longer succeeds for higher-degree shimming and the standard deviations are worse than the reference map (acquired without B_0 shimming). However, if the modeled fields are considered, the homogeneity improves from 55.1 ($\pm$6.4) Hz to 48.68 ($\pm$6.39) Hz and 44.68 ($\pm$7.09) Hz, for the respective second, third, and fourth-degree shimming. The total applied currents that were required were 0.77 ($\pm$0.18) A, 6.03 ($\pm$0.59) A and 6.8 ($\pm$2.23) A, respectively. The applied shim strengths and shim currents are shown in Supporting Table S2 and Supporting Figure S2.

The shim strengths that were used for the whole-brain shimming application (EPI) and single-slice shimming application (MRSI) are given in Table 2.

Figure 7 shows the EPI data for second-degree and fourth-plus-degree shimming. Distortions in the images are more severe for second-degree shimming than the fourth-plus-degree shimming. Furthermore, signal dropout in lower slices can be recovered using higher-degree B_0 shimming.

Figure 8 shows a comparison of the effect of very high-order B_0 shimming on ^{1}H FID MRSI. The standard deviation of the frequency shifts in the shimmed B_0 map was 24.6 Hz for the second-degree shim versus 16.50 Hz for the fourth-plus-degree shim. The full linewidth at half maximum (FWHM) of the water peak averaged over the entire FOV was 22 $\pm$ 5 Hz using second-degree shimming compared with 15.3 $\pm$ 2.8 Hz using partial fourth-plus-degree shimming. Narrower linewidths allow better fitting and quantification of metabolite concentrations (18). The FWHM of the unsuppressed water peaks were also calculated, and Figure 8 shows the maps of these FWHMs. It can be seen that the fourth-plus-degree B_0 shimming has much narrower lines than the second degree. Sample spectra are shown in Supporting Figure S3.

For single-voxel spectroscopy in the frontal cortex, the water linewidths were as follows: 24.98, 23.64, 23.21, and 23.03 using second, third, fourth and fourth-plus-degree B_0 shimming, respectively. The total shim currents did not exceed 5 A in all cases.

DISCUSSION

Geometric Distortion

The reference fields of each shim coil were measured at a range of current amplitudes, whereas most previous studies only used a single-current amplitude. However, large-current amplitudes introduce geometric distortions.

In our investigation, we considered the effect of geometric distortion on the measured B_0 maps. This has not been mentioned in previous studies, because the field deviations of the shim fields are usually chosen to be low (less than 100 Hz for (13)) to minimize phase wrapping and geometric distortion. However, by accounting for the effect of geometric distortion, we can measure and model the shim fields for a large range of current amplitudes.

The results showed that although the retrospective geometric distortion correction can improve the accuracy of the modeling, the improvement was not always significant. Downsampling the number of points in the

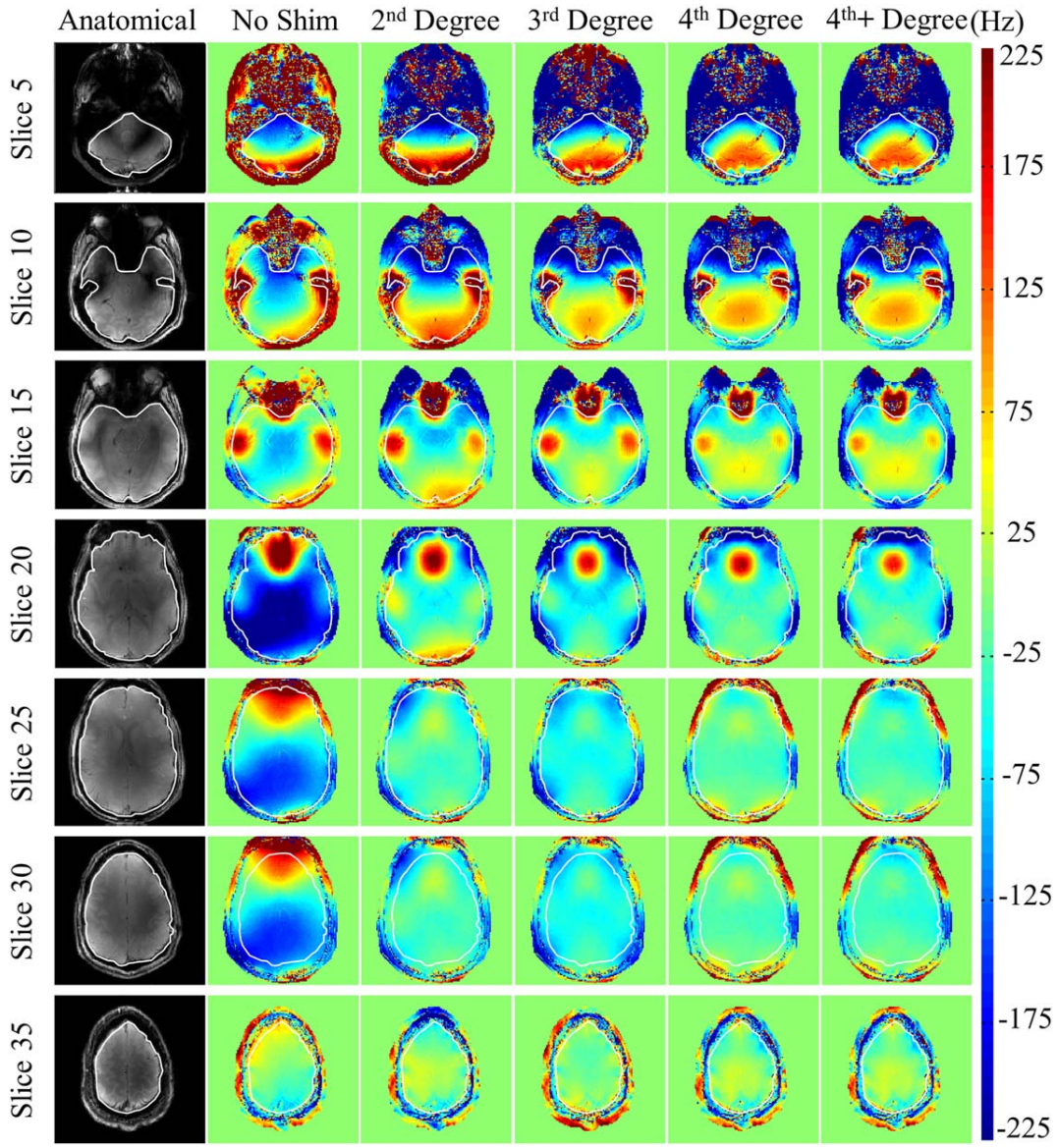

FIG. 5. In vivo B_0 maps shimmed on a whole-brain using the modeled real fields using second, third, fourth, and fourth-plus-degree shim terms. The VOI masks are shown in white and were defined using a custom MATLAB GUI.

modeling of the fields showed that this reduces the accuracy of the model quite significantly. Retrospective correction was not able to compensate for the inaccuracy introduced by the downsampling.

The most significant reduction in geometric distortion was seen when a high read-out bandwidth was used to acquire the maps. Thus, the highest possible bandwidth was used for the read-out gradient.

Mapping and Modeling Reference Shim Fields

In this study, we provide a comprehensive description of modeling and calibrating a very high-degree B_0 shim system while accounting for amplitude nonlinearity. Previous studies (12,13) acquired reference field maps of the shim coils and used them directly without modeling to perform B_0 shimming. In both (12) and (13), B_0 shimming was performed using only second-degree and a single third-degree (Z3) shim terms. This has also been done for higher-degree shim terms such as third-degree (9,10,17) and even fourth-degree systems on a 7T system (18). Although these studies used the reference field maps directly for B_0 shimming, we modeled the reference fields using spherical harmonic functions. Some previous studies also modeled the reference fields using spherical harmonic functions (15,19). However, the details were not fully described and the fields were modeled with only lower-degree spherical harmonic terms, whereas we used full sixth-degree terms for all shim fields. Furthermore, amplitude nonlinearities were not considered. Only Juchem et al (17) considered linear current amplitudes. Modeling the fields reduces the

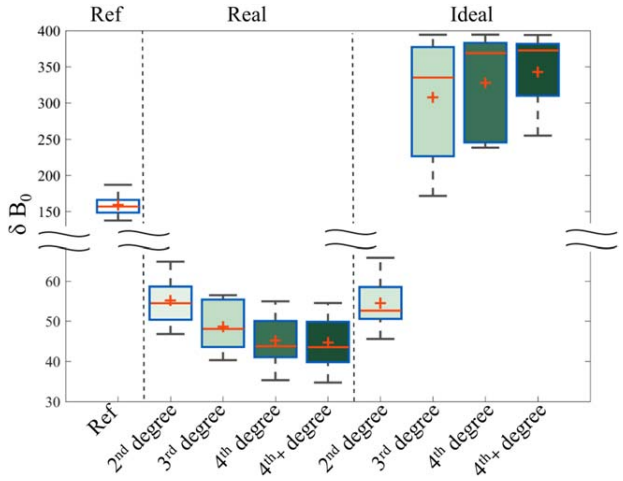

FIG. 6. Standard deviations (hertz) of in vivo B_0 maps of a whole-brain VOI for nine volunteers. Comparison of shimming with ideal fields and real fields, as well as comparing second, third, fourth, and fourth-plus-degree shimming.

complexity of the B_0-shimming algorithm and makes it more flexible (independent of FOVs and position of different scan sessions).

Another benefit of modeling the reference shim fields is that this intrinsically denoises the data. This is also advantageous because the method is somewhat forgiving when it comes to the SNR of the measured field maps. Therefore, higher-SNR B_0-mapping methods, such as multiple-echoes field mapping (18), is not required. In addition, because the method can tolerate some SNR penalty, a high read-out bandwidth (that reduces distortion but also reduces SNR) can be used to measure the fields, which also reduces geometric distortions.

We investigated the optimum degree of spherical harmonics to use for modeling the shim fields. Although we did not see any improvement beyond sixth-degree harmonics, this may differ for different shim coils. A drawback of modeling with spherical harmonics is that the components are always radially symmetrical, which makes it difficult to model local deviations in the field. In principle, modeling the reference fields of the shim coils does not have to be restricted to spherical harmonics, and can be used for the multicoil shim systems (11); however, finding an appropriate basis set may be more difficult, and different parametric models may need to be used.

In previous works, a single current is applied to the shim coils. In (12) the current was chosen to be as large as possible without phase wrapping or significant signal dropout. In (13) the shim coils are driven such that the maximum field deviation is 100 Hz. We know that in practical B_0 shimming applications (14), a range of current offsets ere used; however, the details of how the

Table 2
Applied Shim Strengths (and Percentage of the Maximum Available Shim Strengths) for the EPI Application and the Single-Slice MRSI Application

	Whole Brain (EPI)				Single Slice (MRSI)			
	Second Degree		Fourth-Plus Degree		Second-Degree		Fourth-Plus Degree	
	Hz/cm^n	%	Hz/cm^n	%	Hz/cm^n	%	Hz/cm^n	%
Z0	—	—	—	—	—	—	—	—
Z2	3.912	5.64	9.309	13.41	3.325	4.79	3.913	5.64
ZX	0.123	0.05	−0.628	0.26	−0.544	0.23	0.558	0.23
ZY	0.512	0.21	−5.311	2.20	−1.552	0.64	−3.111	1.29
C2	0.617	1.69	−1.053	2.89	−1.041	2.86	−0.639	1.76
S2	−0.372	1.02	0.333	0.92	0.014	0.38	−0.076	0.21
Z3			−1.137	23.10			0.166	3.38
Z2X			−0.239	2.39			−0.140	1.40
Z2Y			−2.041	20.41			0.337	3.37
ZC2			0.080	0.45			0.874	4.94
ZS2			−0.158	0.89			−0.019	0.11
C3			−0.027	1.43			−0.007	0.36
S3			−0.247	13.15			−0.089	4.74
Z4			0.108	25.66			−0.004	0.85
Z3X			−0.027	2.18			−0.014	1.16
Z3Y			−0.227	18.45			−0.125	10.14
Z2C2			−0.065	7.35			0.006	0.67
Z2S2			0.008	0.85			−0.015	1.62
ZC3			−0.008	0.67			−0.002	0.13
ZS3			0.088	7.25			0.010	0.79
C4			0.023	12.31			−0.009	4.62
S4			0.006	2.98			−0.002	1.08
ZC4			−1.12e-2	19.62			1.20e-5	0.02
ZS4			−1.08e-3	1.90			−2.28e-6	0.00
C5			−2.46e-4	2.48			6.63e-5	0.67
S5			−3.39e-4	3.43			−4.79e-5	0.48
ZC5			−2.85e-5	0.89			3.85e-6	0.12
ZS5			−1.24e-5	0.39			1.62e-6	0.05

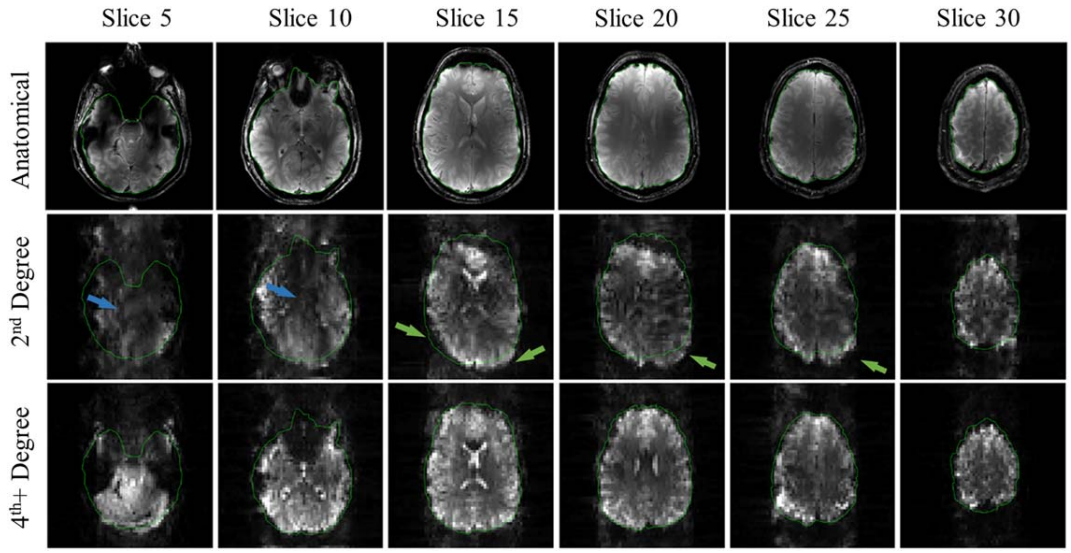

FIG. 7. Single-shot 2D EPI with whole-brain B_0 shimming using second-degree and fourth-plus-degree shim terms. The anatomical images were acquired with a 2D flash sequence. The VOI mask is shown in light green. The signal dropout on slices 5 and 10 with the second-degree shimming are recovered with fourth-plus-degree shimming (blue arrows). Distortions are more severe with second-degree shimming than fourth-plus-degree shimming (green arrows).

nonlinearity was modeled or the degree of nonlinearity were not reported. Furthermore, in our investigation, in addition to using a range of currents to account for possible amplitude nonlinearities in the shim fields, we modeled these nonlinearities using three different models, which was not done in previous studies. Note that each of these current amplitudes corresponds to a different shim strength (Table 1).

We showed that the shim fields were linear with respect to the current amplitude. This is because of the linearity of the shim amplifiers. However, if the shim amplifiers are not linear, this should also be considered in the models or the amplifiers need to be tuned to be linear.

In Vivo B_0 Shimming

The B_0 shim failed when ideal shim fields were assumed; thus, measuring the real shim fields was necessary. The reconstructed models showed differences

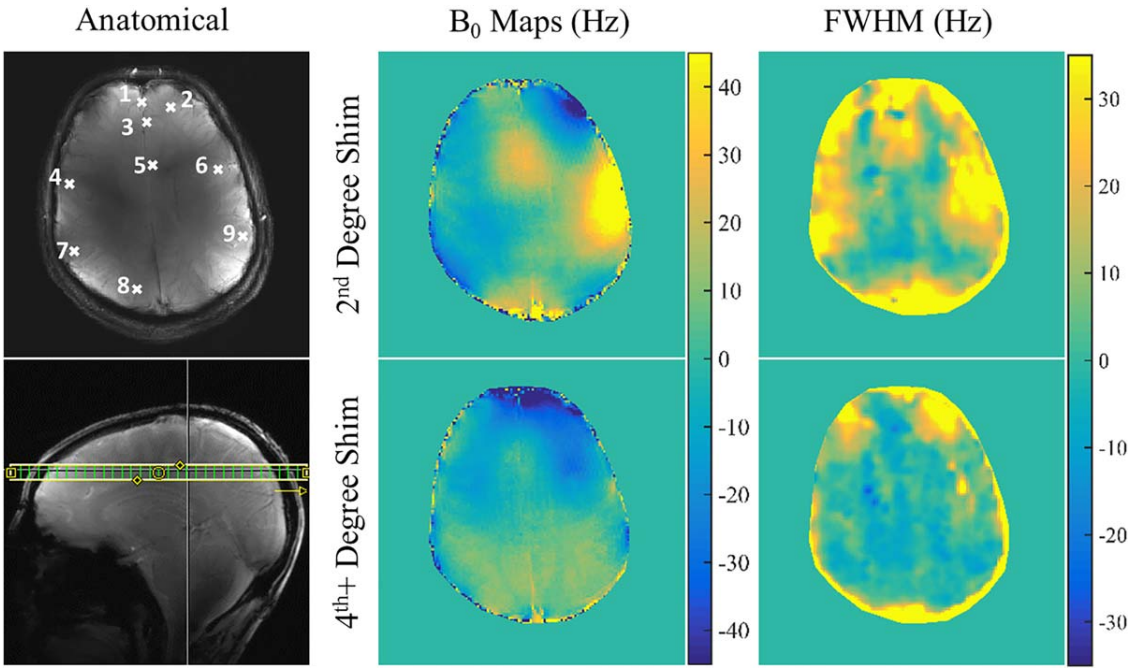

FIG. 8. Effect of very high-degree B_0 shimming on single-slice ^{1}H FID MRSI. The B_0 maps along with the FWHM of water are shown for the second and fourth-plus-degree B_0 shimming. The spectra of the marked voxels are shown in Supporting Figure S3.

between the ideal fields and the real field models (for shim terms higher than the second degree). This can explain why the in vivo experiments failed when assuming ideal shim fields and shimming with more than second-degree shim terms (Fig. 4).

For in vivo B_0 shimming of the human brain at 9.4 T, the B_0 homogeneity improved as more shim degrees were used (with real-field models). Although it was shown that increasing the number of degrees improves the homogeneity, the improvement is less significant as we move to higher degrees. This has also previously been shown in (9,18).

In (18), a similar study was performed on a 7T MRI scanner on the whole brain. The second, third, and fourth-plus-degree B_0 shimming that was achieved was 23.5, 18.1 and 12.3 Hz, respectively. We see a similar trend to our results: As the degree of B_0 shim terms increase, the better the B_0 homogeneity. However, there is a significant difference between our mean standard deviations and those reported in (18). This difference can be partially accounted for by the difference in field strength (higher B_0 inhomogeneity at higher field strengths). However, the significant difference is that we perform a whole-brain B_0 shim (including the cerebellum), as shown in Figure 5, whereas (18) covers only the top half of the cerebrum.

From the whole-brain (EPI) and single-slice (MRSI) applications shown in this study, we can see the advantage of fourth-plus-degree over second-degree B_0 shimming. The distortion in the EPI images is significantly less and the B_0 field is much more homogeneous (Supporting Fig. S4). Although there are small local areas where the FWHM of the second-degree shimming is slightly better, the FWHM of higher-degree shimming is on average significantly lower.

One limitation of this study is that coupling between the shim coils and the gradient coils was not compensated. Fast switching of strong gradient currents induces eddy currents in the shim coils; this can be clearly seen in the EPI images where there are significant ghosting artifacts (Fig. 7; Supporting Fig. S5). Fast switching of strong shim currents, for applications such as dynamic B_0 shimming (9,17,34), will also induce eddy currents. Dynamic B_0 shimming updates the shim currents for each slice acquisition, rather than shimming the entire volume. One method for reducing the coupling between the shim coils is to perform pre-emphasis (17).

Other limitations of this study include the higher B_1^+ inhomogeneity at ultrahigh fields. This resulted in signal dropouts, particularly in the anatomical images and lower slices. B_1^+ inhomogeneity can be reduced with coils that provide more transmit homogeneity or with better RF shimming using techniques such as parallel transmission (35,36). Moreover, B_0 maps could be improved with the use of multi-echoes with alternating gradient polarities to eliminate the effect of gradient asymmetries (14). In our case, we found that single-echo B_0 maps were sufficient, which is in accordance with Juchem et al (37).

Finally, in the case of single-voxel spectroscopy in the frontal cortex, higher degrees of shimming did not significantly improve the linewidth of water, and second-degree B_0 shimming is sufficient for voxel sizes of $2 \times 2 \times 2\,cm^3$ or less.

CONCLUSIONS

In this study, we quantitatively evaluated the imperfections of the shim fields, which has not been shown previously. We provided a comprehensive description of modeling and calibrating a very high-degree B_0 shim system while accounting for geometric distortion and amplitude nonlinearity. Optimal shim currents were calculated in one iteration. We showed the benefit of very high-order B_0 shimming at 9.4 T in the human brain. A range of shim degrees were compared, up to and including, fourth-plus-degree shim terms.

ACKNOWLEDGMENTS

We would like to thank Dr. Ariane Fillmer for providing the grid phantom that was used for the geometric distortion part of the study.

REFERENCES

1. Baldwin LN, Wachowicz K, Thomas SD, Rivest R, Fallone BG. Characterization, prediction, and correction of geometric distortion in 3 T MR images. Med Phys 2007;34:388–399.
2. Lipton ML. Totally accessible MRI: A User's Guide to Principles, Technology, and Applications. New York: Springer-Verlag; 2008.
3. McRobbie DW, Moore EA, Graves MJ, Prince MR. MRI from Picture to Proton. 2nd Ed. Cambridge, United Kingdom: Cambridge University Press; 2007.
4. Bankman I, ed. The physical basis of spatial distortions in magnetic resonance imaging. In: Handbook of Medical Image Processing and Analysis. San Diego, CA, USA: Academic Press; 2008.
5. Robitaille P-M, Berliner L. Magnetic susceptibility effects in high field MRI. In: Ultra High Field Magnetic Resonance Imaging. New York: Springer Science & Business Media; 2007.
6. Klose U. In vivo proton spectroscopy in presence of eddy currents. Magn Reson Med 1990;14:26–30.
7. Kreis R, Ernst T, Ross BD. Development of the human brain: in vivo quantification of metabolite and water content with proton magnetic resonance spectroscopy. Magn Reson Med 1993;30:424–437.
8. Bley TA, Wieben O, François CJ, Brittain JH, Reeder SB. Fat and water magnetic resonance imaging. J Magn Reson Imaging 2010; 31:4–18.
9. Boer VO, Klomp DWJ, Juchem C, Luijten PR, de Graaf RA. Multislice 1H MRSI of the human brain at 7T using dynamic B0 and B1 shimming. Magn Reson Med 2012;68:662–670.
10. Hetherington HP, Chu W-J, Gonen O, Pan JW. Robust fully automated shimming of the human brain for high-field 1H spectroscopic imaging. Magn Reson Med 2006;56:26–33.
11. Juchem C, Nixon TW, McIntyre S, Boer VO, Rothman DL, de Graaf RA. Dynamic multi-coil shimming of the human brain at 7 Tesla. J Magn Reson 2011;212:280–288.
12. Kim D-H, Adalsteinsson E, Glover GH, Spielman DM. Regularized higher-order in vivo shimming. Magn Reson Med 2002;48:715–722.
13. Webb P, Macovski A. Rapid, fully automatic, arbitrary-volume in vivo shimming. Magn Reson Med 1991;20:113–122.
14. Klassen LM, Menon RS. Robust automated shimming technique using mapping acquisition parameters (RASTAMAP). Magn Reson Med 2004;51:881–887.
15. Gruetter R. Automatic, Localized in vivo adjustment of all first- and second-order shim coils. Magn Reson Med 1993;29:804–811.
16. Weiger M, Speck T. Shimming for high-resolution NMR spectroscopy. eMagRes 2011. doi: 10.1002/9780470034590.emrstm1228.
17. Juchem C, Nixon TW, Diduch P, Rothman DL, Starewicz P, de Graaf RA. Dynamic shimming of the human brain at 7 Tesla. Concept Magn Reson B 2010;37B:116–128.
18. Pan JW, Lo KM, Hetherington HP. Role of very high order and degree B0 shimming for spectroscopic imaging of the human brain of 7 Tesla. Magn Reson Med 2012;68:1007–1017.

19. Wen H, Jaffer FA. An in vivo automated shimming method taking into account shim current constraints. Magn Reson Med 1995;34:898–904.
20. Song K, Bao Q, Chen F, Huang C, Feng J, Liu C. Gradient shimming based on regularized estimation for B0-field and shim functions. J Magn Reson 2016;268:1–9.
21. Wilson JL, Jenkinson M, de Araujo I, Kringelbach ML, Rolls ET, Jezzard P. Fast, fully automated global and local magnetic field optimization for fMRI of the human brain. NeuroImage 2002;17:967–976.
22. Shajan G, Hoffmann J, Pohmann R. A 15-channel receive array and 16 channel detunable transmit coil for human brain imaging at 9.4T. In Proceedings of the 19th Annual Meeting of the ISMRM, Montréal, Canada, 2011. p. 3825.
23. Avdievich NI, Pfrommer A, Hoffmann J, Chadzynski GL, Scheffler K, Henning A. Transceive phased array with high transmit performance for human brain application at 9.4T. Joint Annual Meeting of the ISMRM-ESMRMB, Milano, Italy, 2014. p. 0622.
24. Jezzard P, Balaban RS. Correction for geometric distortion in echo planar images from B0 field variations. Magn Reson Med 1995;34:65–73.
25. Bioucas-Dias J, Valadao G. Phase unwrapping via graph cuts. IEEE Trans Image Process 2007;16:698–709.
26. Harris C, Stephens M. A combined corner and edge detector. In Proceedings of the 4th Alvey Vision Conference, Manchester, United Kingdom, 1988. p. 147–151.
27. Anderson WA. Electrical current shims for correcting magnetic fields. Rev Sci Instrum 1961;32:241–250.
28. Eccles CD, Crozier S, Westphal M, Doddrell DM. Temporal spherical-harmonic expansion and compensation of eddy-current fields produced by gradient pulses. J Magn Reson A 1993;103:135–141.
29. Nassirpour S, Chang P, Fillmer A, Henning A. A comparison of optimization algorithms for localized in-vivo B0 shimming. In Proceedings of the 24th Annual Meeting of the ISMRM, Singapore, 2016. p. 1142.
30. Henning A, Fuchs A, Murdoch JB, Boesiger P. Slice-selective FID acquisition, localized by outer volume suppression (FIDLOVS) for 1H-MRSI of the human brain at 7 T with minimal signal loss. NMR Biomed 2009;22:683–696.
31. Bogner W, Gruber S, Trattnig S, Chmelik M. High-resolution mapping of human brain metabolites by free induction decay 1H MRSI at 7 T. NMR Biomed 2012;25:873–882.
32. Kay SM. Modern Spectral Estimation: Theory and Application. Englewood Cliffs, NJ, USA: Prentice Hall; 1998.
33. Pijnappel WWF, van den Boogaart A, de Beer R, van Ormondt D. SVD-based quantification of magnetic resonance signals. J Magn Reson 1992;97:122–134.
34. Koch KM, McIntyre S, Nixon TW, Rothman DL, de Graaf RA. Dynamic shim updating on the human brain. J Magn Reson 2006;180:286–296.
35. Padormo F, Beqiri A, Hajnal JV, Malik SJ. Parallel transmission for ultrahigh-field imaging. NMR Biomed 2016;29:1145–1161.
36. Wu X, Adriany G, Ugurbil K, van de Moortele P. Correcting for strong eddy current induced B0 modulation enables two-spoke RF pulse design with parallel transmission: demonstration at 9.4T in the human brain. PLoS One 2013;8:1–7.
37. Juchem C, Rudrapatna SU, Nixon TW, de Graaf RA. Dynamic multi-coil technique (DYNAMITE) shimming for echo planar imaging of the human brain at 7 Tesla. NeuroImage 2015;105:462–472.

SUPPORTING INFORMATION

Additional Supporting Information may be found in the online version of this article.

Table S1. Coefficients for Shim Channels (Normalized by Coil Design Sensitivities)
Note: Each column corresponds to a shim channel, and the coefficients are shown in each row.
Table S2. Applied Shim Strengths for Whole-Brain B_0 Shimming for Nine Healthy Volunteers
Fig. S1. B_0 maps of shim terms at 1.0-A applied current on a 200 $\times$ 200 mm FOV. Both the ideal fields and real fields and their difference are shown.
Fig. S2. Applied shim currents (corresponding to the shim strengths in Supporting Table S2). The maximum available current strength for each channel is 10 A. None of the applied shim currents exceeded 2.5 A.
Fig. S3. Effect of very high-degree B_0 shimming on single-slice ^{1}H FID MRSI. Sample spectra from nine different voxels across the slice are shown from 0.5 to 4.2 ppm for second-degree (red) and fourth-plus-degree (black) B_0 shimming. The voxels are shown from the positions marked in Figure 8.
Fig. S4. Echo-planar imaging of a spherical phantom with (**a**) and without (**b**) the insert shim in the scanner bore. The same sequence, parameters, and shim values were used for both cases. Ghosting artifacts cause significant problems as a result of eddy currents generated in the shim coils.
Fig. S5. B_0 maps of the EPI data for second-degree and fourth-plus-degree whole-brain B_0 shimming.

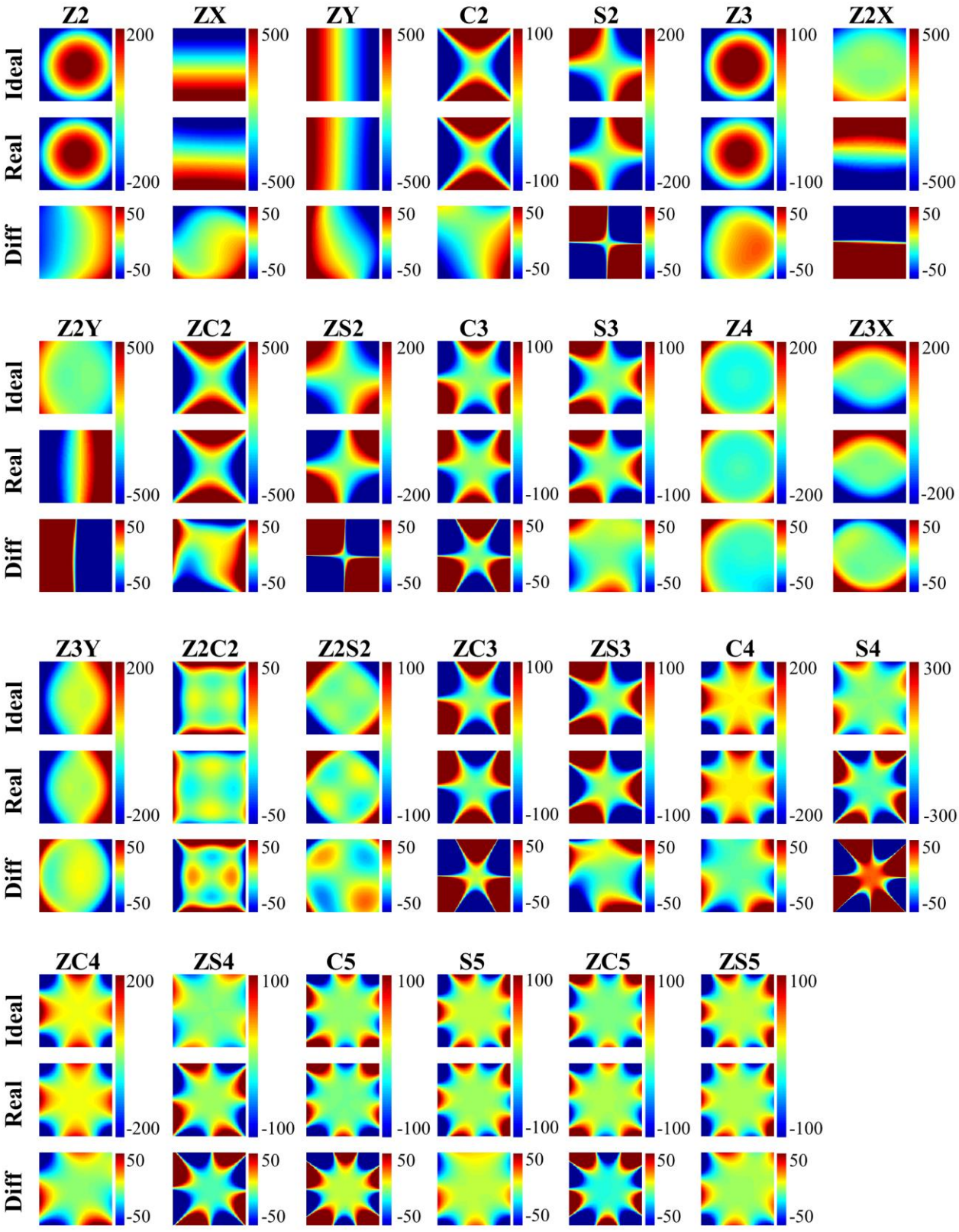

Supporting Figure S1 The B_0 maps of shim terms at 1.0 A applied current on a 200x200 mm FOV. Both the ideal-fields and real-fields and their difference are shown.

Supporting Table S1: Coefficients for shim channels (normalised by coil design sensitivities).
Each column corresponds to a shim channel and the coefficients are shown in each row.

	Z2	ZX	ZY	C2	S2	Z3	Z2X	Z2Y	ZC2	ZS2
Z0	-0.00764	8.54E-07	-4.54E-05	-0.00017	-7.92E-05	6.43E-05	3.65E-06	-4.64E-05	-3.63E-06	-3.08E-06
Z	-0.00813	0.000609	-0.0041	-0.00169	-0.00197	-0.03128	-7.48E-05	2.87E-05	-1.88E-05	3.05E-06
X	-0.00086	-0.0015	5.85E-05	0.00071	0.008199	-3.16E-05	0.009324	-0.00025	2.81E-05	-4.04E-05
Y	0.004325	-0.00012	-0.00201	0.007565	-0.00103	-2.79E-05	0.000288	0.009113	-4.50E-05	-2.98E-05
Z2	**0.9978**	-0.00517	0.000743	-0.01175	0.006252	-0.00157	-0.00103	0.004162	-0.00032	-0.00017
ZX	0.01644	**1.045**	-0.03106	-0.03343	0.02138	-0.00472	-0.00078	0.000739	0.000777	0.009966
ZY	0.002077	0.03239	**1.021**	0.01777	0.03258	0.01225	-0.00033	-0.00061	0.008731	-0.00083
C2	-0.00533	3.93E-05	0.00097	**0.9992**	0.0577	0.000434	0.000307	0.000985	-0.00216	-0.00011
S2	-0.00682	0.002967	0.001911	0.1139	**-1.982**	-0.00031	-0.00205	0.000285	1.61E-05	0.005827
Z3	-0.3489	-0.05466	-0.01514	0.04752	-0.03673	**0.9378**	0.004098	0.004489	-0.00073	-0.0026
Z2X	-0.07997	-0.1907	0.005579	0.1367	-0.3357	0.01421	**-0.941**	0.02752	-0.01348	-0.0589
Z2Y	0.2703	0.000149	-0.1214	0.4134	0.02611	0.05206	-0.01492	**-0.908**	-0.01197	0.02606
ZC2	-0.00505	0.05557	-0.00345	-0.37	0.09648	-0.03038	0.002794	0.005054	**1.053**	0.06336
ZS2	0.1924	-0.01353	0.05253	0.2128	-1.443	-0.00301	-0.01434	-0.01511	0.1298	**-2.234**
C3	-0.01992	-0.00865	-0.00361	-0.04565	-0.05744	0.001929	0.009776	-0.00112	0.0022	-0.00549
S3	-0.00687	0.006606	-0.00534	-0.00349	0.008635	-0.00889	0.001685	-0.00153	0.000755	-0.00144
Z4	10.78	-0.1771	0.7086	0.1825	-0.6997	0.7611	0.1172	-0.1211	0.02363	0.04779
Z3X	2.387	7.15	0.3759	-0.7612	-0.4248	0.4679	-0.3131	0.005441	-0.1185	0.3856
Z3Y	-7.645	0.1441	6.144	-10.28	0.01543	-0.1951	-0.2023	-0.5218	-0.1524	-0.04439
Z2C2	1.426	-0.5032	1.576	44.42	2.831	0.05463	-0.1069	-0.1044	-0.2945	-0.07147
Z2S2	-2.506	-2.345	0.4034	-0.4304	12.8	0.1884	0.2891	0.04522	-0.38	7.376
ZC3	0.6264	0.8397	-0.1041	0.5864	-0.6526	-0.06165	-0.08309	-0.02854	-0.0182	0.08415
ZS3	0.4978	-0.3124	0.1317	-3.494	-1.093	-0.04493	-0.00928	-0.02775	-0.1028	-0.02948
C4	-0.2208	-0.00175	-0.1781	0.3391	0.3129	-0.02622	0.01031	-0.00017	-0.00223	0.005221
S4	-0.4363	0.2062	-0.2694	2.674	-0.4451	0.05698	-0.06977	0.01253	0.04577	0.002082
Z5	-92.1	-0.4375	-2.477	-2.308	6.599	4.992	-0.6314	0.3572	0.2084	-0.026
Z4X	-31.79	-77.07	-7.519	-6.525	49.7	-7.341	4.338	-0.7229	0.6291	-1.441
Z4Y	33.06	-3.729	-67.97	42.98	-5.137	2.355	0.6228	6.246	-1.488	-0.03996
Z3C2	-5.972	2.062	-5.364	-637.8	-59.8	-1.318	1.014	0.2873	-43.36	-2.385
Z3S2	-0.09495	-0.3094	-0.07299	-0.4893	1.313	0.007656	0.03832	0.0155	-0.101	0.6006
Z2C3	-1.607	-1.06	5.047	1.373	29.23	1.151	0.7711	0.2267	0.2668	-1.018
Z2S3	-2.428	2.443	-0.4474	32.98	14.58	1.053	0.01994	0.3665	-1.385	0.8864
ZC4	-0.8375	-1.762	1.278	5.731	8.079	-0.2184	-0.07065	0.2223	0.734	0.3618
ZS4	0.139	0.1064	-0.2468	1.315	0.03411	0.02606	-0.00747	0.02511	0.05129	0.008619
C5	0.2355	-0.6463	-0.04811	3.143	-0.1262	-0.07018	0.1587	-0.01	-0.00032	0.0828
S5	1.404	-0.1365	-0.01258	-2.331	-1.701	0.004723	0.04077	0.01735	0.0941	0.02541
Z6	-0.7806	-0.3415	-0.03384	-0.00925	-0.3036	0.02286	0.02103	-0.0167	0.03726	0.01056
Z5X	-4.115	-10.09	-0.9848	-0.9993	6.471	-0.9615	0.5682	-0.09375	0.075	-0.1923
Z5Y	3.422	-0.4572	-9.093	-9.277	-2.001	0.3203	0.1021	0.8312	-1.204	-0.06102
Z4C2	-1.175	0.2862	0.598	-69.23	-6.436	-0.1885	0.09656	-0.07903	-4.582	-0.2619
Z4S2	-0.2944	-0.659	0.005886	-0.1178	0.6489	-0.05592	0.04182	-0.00791	-0.00322	0.01811
Z3C3	-0.1087	-0.1019	0.4308	0.8202	2.421	0.09048	0.06154	0.016	0.07285	-0.07951
Z3S3	-0.3627	0.2379	-0.1781	-13.1	-0.2699	0.05228	0.02677	0.03858	-1.175	0.0148
Z2C4	0.0429	-0.08034	0.1476	-0.8024	-0.1534	-0.04192	-0.01165	-0.00536	0.09283	-0.00971
Z2S4	-0.01382	-0.01576	0.04181	0.03081	0.2554	0.009238	0.006983	0.001937	0.004183	-0.00808
ZC5	-0.04402	-0.1325	0.02321	1.356	0.1438	-0.01207	0.007911	-0.00584	0.09167	0.004249
ZS5	-0.02747	-0.1165	0.09144	0.3989	0.3453	-0.01403	-0.00076	0.006146	0.05639	0.01567
C6	-0.3898	-0.274	0.2381	-0.6713	0.1767	-0.04126	0.009513	-0.03008	-0.04249	-0.0049
S6	0.009246	-0.033	-0.01153	-1.137	-0.1164	-0.00917	0.006506	-0.00024	-0.08232	0.003496

C3	S3	Z4	Z3X	Z3Y	Z2C2	Z2S2	ZC3	ZS3	C4	S4
-3.68E-05	-1.04E-05	-1.14E+04	-1.69E-07	-9.76E-08	-1.12E-06	-1.23E-06	-1.85E-06	-1.47E-06	-1.41E-06	-1.92E-06
-0.00037	-0.00051	-7.95E-05	5.82E-07	1.03E-07	-1.49E-06	1.46E-07	7.81E-08	-8.89E-07	-7.18E-05	-8.71E-05
5.89E-05	-0.0001	1.67E-05	-3.67E-06	8.15E-07	-6.58E-07	6.88E-07	1.24E-06	-2.12E-07	-1.54E-06	-5.62E-07
2.01E-05	-0.00011	3.98E-07	-1.43E-06	-3.98E-06	8.64E-07	-1.97E-08	-1.88E-06	4.67E-07	4.60E-06	4.69E-06
-0.00026	0.000283	0.000422	-1.19E-05	5.41E-05	-1.49E-05	-3.93E-05	7.70E-05	9.54E-05	2.68E-05	-3.55E-06
-0.00042	0.000803	-4.26E-05	0.000291	-9.99E-06	2.30E-05	-0.00019	-1.22E-05	-4.94E-06	-8.66E-05	-8.30E-05
0.001217	0.00078	-0.00035	2.84E-05	0.000384	7.32E-05	5.52E-05	1.94E-05	-3.23E-05	3.18E-08	2.78E-05
-0.00305	-0.01245	0.000128	3.71E-06	2.92E-05	-7.29E-05	-8.54E-06	-1.04E-05	6.29E-05	-0.00014	5.01E-05
-0.02223	0.003279	4.59E-05	-4.45E-05	1.16E-06	1.01E-05	-4.63E-05	0.000106	7.02E-05	0.000373	0.000973
-0.00873	0.01887	-0.01781	0.000707	-0.00591	0.000455	0.000635	0.00059	0.000152	0.001218	0.004188
0.01345	0.04112	-0.00165	-0.01219	-0.00075	-0.00164	-0.00197	0.000665	0.001677	-0.00161	0.004109
0.01616	0.01115	0.03238	-0.00086	-0.01017	-0.01252	-0.00048	0.000601	-0.00012	0.000202	0.00101
0.07992	-0.06758	-0.00188	-0.00076	-0.00523	0.007827	0.000169	-0.00249	-0.01566	0.001129	-0.00253
-0.08504	-0.0507	-0.00116	0.008596	-0.00188	-0.00123	0.0185	-0.03007	0.00359	-0.00111	0.000807
-1.008	-0.09617	-0.00057	-0.0002	3.17E-05	0.000257	-0.00014	0.002752	6.97E-05	0.002627	0.0176
-0.08397	**0.9974**	-0.00043	0.000166	-4.42E-05	-0.00118	-0.00011	0.000265	-0.00237	0.01618	-0.00321
0.6904	-0.2021	**1.241**	-0.00915	0.03271	-0.00153	-0.01237	-0.00438	-0.00881	-0.01717	-0.02356
-0.0787	-0.3662	-0.03834	**1.305**	-0.01112	0.02155	-0.01099	-0.01786	-0.03337	0.03522	-0.05418
-0.1084	-0.377	-0.1784	0.05666	**1.253**	0.12	0.00299	-0.00411	0.005018	0.004277	0.02322
-0.9821	1.17	-0.01964	0.009782	0.07684	**-1.377**	-0.07439	0.02547	0.1002	-0.00647	0.05276
-1.01	-0.2941	0.02024	-0.07314	0.03189	-0.07367	**1.32**	0.1305	-0.05139	-0.01719	-0.05541
-1.068	-0.03608	0.01522	0.004841	-0.00358	-0.00834	-0.00172	**-1.195**	-0.1003	-0.04418	-0.02065
-0.2643	0.8281	0.002183	-0.01546	0.004187	0.03849	0.009652	-0.1088	**1.152**	0.03669	0.08358
0.06316	-0.04651	-0.00336	0.000148	0.00014	0.001428	0.00201	-0.00204	0.001954	**1.005**	0.1031
0.3628	0.1146	0.004441	0.000135	-0.00125	0.001264	0.00214	0.01411	0.009131	0.4741	**-4.146**
-2.684	1.485	-2.556	0.007839	-0.09684	0.00359	0.07202	-0.02076	0.04808	0.1598	0.2192
-2.003	-1.292	1.732	-4.528	-0.09788	0.03275	-0.495	0.1802	0.2774	0.03678	0.2481
3.255	0.6703	0.3832	-0.3165	-4.541	-0.5394	-0.00119	-0.03987	-0.07184	0.09764	-0.1631
11.68	-23.04	0.6033	-0.00317	-0.4736	8.458	0.4534	0.1163	-0.5112	-0.04519	0.1373
-0.371	0.6077	0.01381	-0.00511	-0.00625	0.001954	0.1023	0.02773	-0.04703	-0.0013	-0.00665
-72.17	-5.953	-0.3257	-0.1038	0.08029	0.0391	-0.3035	4.584	0.3251	-0.1863	-0.06333
-6.959	69.1	0.3246	0.2884	-0.06734	-0.3046	-0.1954	0.4088	-4.327	-0.2898	-0.2986
0.3505	-0.4592	-0.00801	-0.00609	-0.03264	-0.04664	-0.04492	0.02345	0.009141	1.972	0.5289
0.001386	0.3586	-0.00031	0.00614	-0.01691	-0.01561	-0.001	-0.01082	-0.02138	0.01093	-0.1162
-0.2443	-0.2876	-0.0137	-0.00139	0.000248	0.003573	0.004319	-0.01862	-0.01175	0.05642	-0.1848
-0.2931	0.7633	0.009389	-0.00183	-0.00112	-0.00325	0.007371	-0.02131	0.008476	-0.1378	-0.0883
0.2165	-0.02749	-0.01614	-0.00049	-0.00213	-0.00025	-0.00108	0.001068	-0.00078	-0.00696	0.007154
-0.3059	-0.2345	0.2267	-0.5995	-0.0131	0.006146	-0.06438	0.02699	0.04023	0.004683	0.03281
0.668	-0.4112	0.04239	-0.04264	-0.6151	0.1285	0.01097	-0.00214	-0.02269	0.0124	-0.01682
1.206	-3.166	0.05372	0.003752	0.02928	0.9194	0.05059	0.01246	-0.00974	-0.00326	0.02027
-0.406	0.0736	0.01399	-0.03835	0.002351	0.001292	1.74E-05	0.02662	-0.0039	-0.00079	0.001246
-5.808	-0.4941	-0.02622	-0.00943	0.008267	-0.00646	-0.02483	0.3708	0.02965	-0.01389	-0.00477
-0.267	4.992	0.04067	0.02285	-0.01795	0.186	-0.00448	0.03588	-0.3636	-0.01771	-0.01912
0.3307	-2.443	-0.01442	-0.00424	0.004548	0.007341	0.005056	-0.01797	0.1543	0.1173	0.03934
-0.6215	-0.06638	-0.00273	-0.00131	0.000622	7.81E-05	-0.00246	0.03949	0.003809	-0.00118	-0.00384
0.02746	-0.01752	0.000575	-0.00677	0.00308	-0.01724	-0.00103	-0.0032	0.004931	-0.00279	-0.00596
-0.01128	-0.08342	-0.00045	-0.00252	0.001266	-0.00522	-0.00195	0.001147	0.007354	0.08152	0.02077
0.2622	0.05968	0.005975	-0.01613	0.01864	0.009834	-0.00125	-0.01447	-0.00749	0.00968	0.01106
0.08591	-0.06602	0.002042	-0.00105	-0.00071	0.01635	0.001971	-0.00449	-0.00043	0.005705	-0.00869

ZC4	ZS4	C5	S5	ZC5	ZS5
-2.93E-07	-2.88E-07	-1.99E-07	-3.65E-07	-8.42E-08	-8.51E-08
3.71E-07	4.64E-07	-1.92E-05	-1.57E-05	-3.80E-08	-6.82E-08
-1.32E-07	4.61E-07	-7.90E-08	1.55E-06	5.06E-09	4.39E-09
-4.51E-07	1.07E-07	-1.15E-07	5.18E-07	5.48E-08	3.81E-08
-4.70E-06	8.51E-06	4.20E-05	-2.04E-05	3.07E-06	3.11E-06
5.49E-07	-2.83E-05	5.82E-06	-8.50E-06	-1.29E-06	9.06E-07
1.77E-05	2.24E-06	7.85E-06	-2.69E-05	1.81E-06	1.64E-07
-1.13E-06	1.50E-06	1.47E-05	-1.64E-05	3.44E-07	-4.43E-08
1.70E-06	-9.08E-06	5.04E-05	-5.73E-05	-3.94E-07	-6.49E-07
0.000263	-0.00011	0.000196	4.93E-08	1.45E-05	2.78E-06
-2.97E-05	0.000386	1.17E-05	-1.66E-05	1.75E-05	-2.14E-05
-0.00039	-6.18E-05	-0.0002	0.000199	-3.51E-05	-9.38E-09
-0.0003	-0.00021	0.000168	0.000353	1.98E-05	-9.22E-06
3.87E-05	0.001253	-0.00038	0.000146	4.52E-05	-1.44E-05
-1.91E-06	0.000875	-1.75E-05	0.000309	-1.19E-05	-2.89E-06
7.05E-05	-0.00014	-0.00019	-0.00035	-3.18E-06	-7.38E-06
-0.00316	0.001191	0.004145	0.01132	-0.00028	-3.85E-05
-0.00058	-0.00165	-0.00107	0.001093	-0.00032	0.000148
0.002577	0.001263	0.001828	0.00102	0.000224	-0.00016
0.001735	0.002493	-0.00694	-0.01617	-0.00041	0.000112
0.001974	-0.01279	-0.00015	0.004923	-0.0004	6.94E-05
0.002244	-0.01438	0.000159	-5.47E-05	0.000432	0.000544
0.0128	0.002498	0.002599	-0.00079	-4.97E-05	-0.00014
0.003433	0.000774	-0.00089	-0.02149	3.72E-05	-0.00104
0.01303	-0.1066	-0.08581	-0.00131	-0.00211	-6.24E-05
0.01454	-0.00902	-0.02625	-0.05499	-0.00032	-0.00046
0.000458	0.00032	0.01704	-0.01464	0.000508	-0.00077
-0.00257	-0.00016	-0.00467	-0.02589	-0.00029	0.001127
0.01571	0.00182	0.1057	0.1203	0.004617	-0.00206
0.001657	-0.00138	7.19E-05	0.00074	-2.53E-05	5.07E-05
0.002066	0.000587	0.0361	-0.01848	-0.0011	-0.00453
0.000873	0.000285	-0.04028	0.03502	0.000537	0.003127
0.8078	0.08277	0.0376	0.041	-0.00159	0.01883
0.00039	**-0.00336**	-0.00378	0.000934	-8.28E-05	4.71E-05
0.004039	-0.00127	**-1.053**	-0.1539	-0.02481	-0.0038
0.001258	-0.00137	-0.1614	**1**	-0.00368	0.02359
-1.68E-06	-0.00015	0.001379	0.000271	-8.91E-05	1.25E-05
1.92E-06	9.10E-05	0.002312	-0.00197	6.77E-05	-0.00011
-4.75E-05	-0.0001	0.001572	-0.00111	6.61E-05	8.95E-05
0.002048	0.000233	0.01181	0.01297	0.000492	-0.00027
0.000288	-6.61E-05	0.000322	-0.00012	-1.10E-06	-2.07E-05
0.000373	0.000153	0.002894	-0.00167	-9.39E-05	-0.00036
0.00312	0.00034	-0.0006	0.00589	0.00015	0.000265
0.05225	0.005466	0.003506	-3.30E-05	-0.0001	0.000896
2.02E-05	-8.89E-05	-9.29E-05	-0.00013	-1.95E-05	-3.90E-05
-0.00224	-0.00025	-0.02871	-0.00478	**-0.00068**	-0.00015
0.03541	0.003576	-0.0027	0.02882	-0.00017	**0.001457**
0.002606	0.000471	0.01278	-0.05291	0.000305	-0.00122
0.001665	-4.23E-05	-0.02808	-0.00593	-0.00066	-0.00012

Supporting Table S2: Applied shim strengths for whole brain B_0 shimming for 9 healthy volunteers.

Shim Term	Shim Strengths: Whole Brain (Hz/cm^n)											
	2nd Degree			3rd Degree			4th Degree			4th+ Degree		
	Mean	Std. Dev	Max Abs	Mean	Std. Dev	Max Abs	Mean	Std. Dev	Max Abs	Mean	Std. Dev	Max Abs
Z0	-	-	-	-	-	-	-	-	-	-		-
Z2	3.974	0.483	4.489	0.414	1.864	2.833	4.360	3.893	9.561	4.294	3.820	9.309
ZX	-0.226	0.684	1.360	-0.551	0.878	1.517	-0.563	1.095	1.988	-0.494	1.092	1.983
ZY	-0.409	1.333	1.968	2.258	3.156	5.745	-1.402	3.729	5.760	-1.516	3.825	5.760
C2	0.336	0.515	1.139	-1.091	0.786	2.027	-1.108	0.493	1.866	-0.991	0.572	1.865
S2	-0.281	0.203	0.488	-0.226	0.261	0.486	-0.012	0.363	0.498	0.042	0.356	0.498
Z3				0.360	0.104	0.447	-0.324	0.529	1.189	-0.317	0.513	1.137
Z2X				-0.087	0.096	0.203	-0.116	0.139	0.244	-0.096	0.146	0.242
Z2Y				0.442	0.247	0.727	-0.571	0.856	1.955	-0.637	0.876	2.041
ZC2				0.446	0.201	0.680	0.325	0.191	0.608	0.312	0.201	0.608
ZS2				-0.064	0.066	0.187	-0.137	0.091	0.277	-0.142	0.081	0.271
C3				-0.054	0.040	0.082	-0.014	0.036	0.070	-0.043	0.021	0.070
S3				0.034	0.031	0.070	-0.131	0.119	0.292	-0.124	0.111	0.266
Z4							0.058	0.036	0.112	0.057	0.035	0.108
Z3X							-0.010	0.020	0.039	-0.009	0.021	0.039
Z3Y							-0.104	0.060	0.218	-0.112	0.077	0.227
Z2C2							-0.027	0.027	0.071	-0.019	0.031	0.065
Z2S2							-0.004	0.013	0.025	-0.002	0.013	0.023
ZC3							-0.006	0.014	0.023	0.002	0.009	0.018
ZS3							0.058	0.037	0.099	0.060	0.041	0.101
C4							-0.017	0.008	0.024	0.003	0.018	0.025
S4							-0.001	0.005	0.008	0.001	0.005	0.008
ZC4										-6.3e-3	5.6e-3	1.14e-2
ZS4										-5.9e-4	5.2e-4	1.10e-3
C5										-4.8e-5	2.3e-4	3.77e-4
S5										-2.0e-5	3.7e-4	5.65e-4
ZC5										-3.1e-5	6.3e-5	1.22e-4
ZS5										-4.0e-5	1.0e-4	2.03e-4

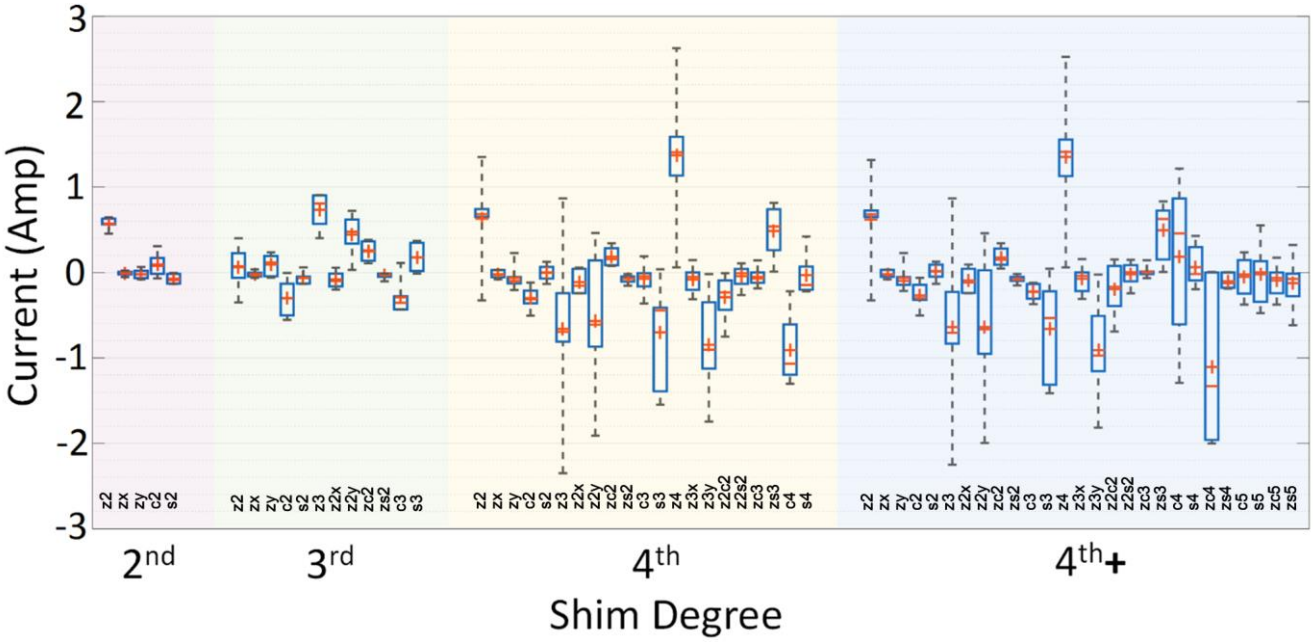

Supporting Figure S2 Applied shim currents (corresponding to the shim strengths in Table S2). The maximum available current strength for each channel is 10 A. None of the applied shim currents exceeded 2.5 A.

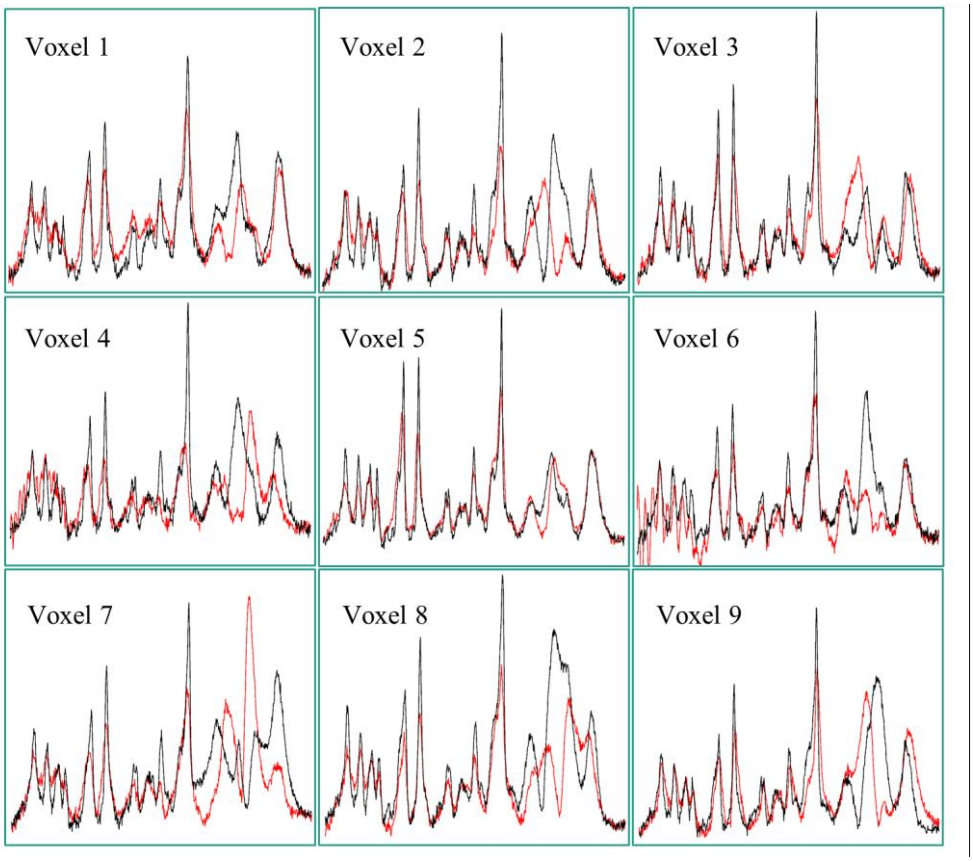

Supporting Figure S3 Effect of very high degree B_0 shimming on single-slice 1H FID MRSI. Sample spectra from 9 different voxels across the slice are shown from 0.5 to 4.2 ppm for 2^{nd} degree (red) and 4^{th}+ degree (black) B_0 shimming. The voxels are shown from the positions marked in Figure 8.

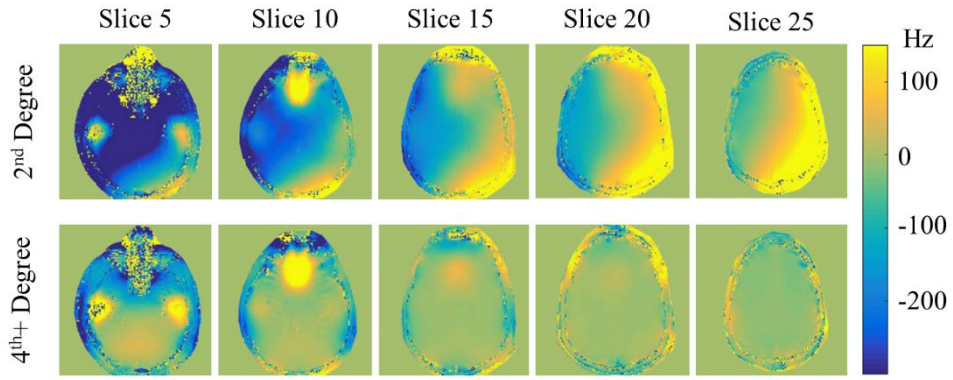

Supporting Figure S4 B_0 maps of the EPI data for 2nd degree and 4th+ degree whole-brain B_0 shimming.

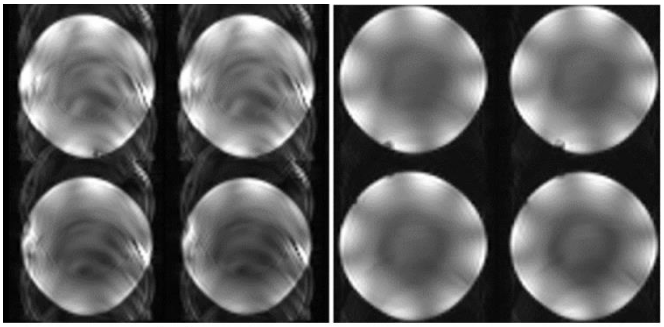

Supporting Figure S5 EPI of a spherical phantom with (a) and without (b) the insert shim in the scanner bore. The same sequence, parameters and shim values were used for both cases. Ghosting artifacts cause significant problems due to eddy currents generated in the shim coils.

Publication III

"Dynamic B_0 Shimming at Ultra High Fields for Proton Spectroscopic Imaging of the Human Brain"

P Chang*, S Nassirpour*, A Henning

[in preparation]

Dynamic B_0 Shimming at Ultra High Fields for Proton Spectroscopic Imaging of the Human Brain

Abstract

Purpose: To compare different B_0 shimming approaches at 9.4T and to evaluate their performance in the context of high resolution multi-slice metabolite mapping of the human brain.

Methods: Two different B_0 shimming approaches, namely, a very high degree spherical harmonic insert shim and a multi-coil system were used to perform B_0 shimming on the human brain at 9.4T. The performance of the different shim settings was compared in simulation for 5 different regions of interest. In-vivo B_0 shimming was performed using both systems. High degree static shimming was compared to both low and high degree dynamic slice-wise shimming. Dynamic shimming using spherical harmonics was also compared to multi-coil slice-wise shimming. High resolution metabolite maps were acquired from 3 slices for different B_0 shim settings.

Results: The simulations show that the combination of the 16-channel multi-coil with 2^{nd} degree spherical harmonics performs similarly to a 4^{th} degree spherical harmonic shim system in most shimming applications. In-vivo measurements confirmed these results and further highlighted the advantages of dynamic shim updating over static shimming. Better B_0 homogeneity achieved through dynamic shimming using either of the systems resulted in a more accurate quantification of spectra. Metabolite maps acquired using the 4^{th} degree spherical harmonic shim system were comparable to those acquired with the multi-coil setup.

Conclusion: Metabolite mapping at 9.4T benefits greatly from advanced B_0 shimming approaches. Dynamic shimming performed using a 4^{th} degree spherical harmonic shim system resulted in a similar quality of metabolite maps as a 16-channel multi-coil system combined with 2^{nd} degree spherical harmonic shims.

Introduction

The increased interest in ultra-high field MR imaging and spectroscopy applications has led to several efforts being made at further optimizing the static field homogeneity through improving the B_0 shimming process. Without a spatially homogenous magnetic field, the many advantages of ultra-high field strengths cannot be fully exploited. While the commercial MR scanners are usually equipped with up to 2^{nd} or sometimes 3^{rd} degree spherical harmonic shim coils, recent studies [1, 2, 3, 4, 5] have already shown that for higher field strengths ($\geq$7T) these shim coils will not be sufficient to correct for subject-induced, intensive, and localized B_0 field distortions that are inherent to these field strengths.

Two main hardware setups have been shown to be viable options for achieving better B_0 shim quality at higher field strengths: shim systems with higher degrees of spherical harmonics shim coils [3, 2], or multi-coil setups [6] with multiple dedicated and local shim coils. Depending on the application, performing dynamic B_0 shim updating [7] on the slice that is being imaged at each time will, needless to say, improve the quality of the images as the shim settings are optimized for the specific slice at hand rather than globally over the whole imaging volume (also known as static B_0 shimming). However, it is worth noting that performing dynamic B_0 shimming, regardless of which shimming approach is used, often requires additional hardware and software.

Several studies [2, 3, 4, 8, 9, 5] have previously reported advantages of each of these two main B_0 shimming methods (higher degree spherical harmonic and multi-coil) in the human brain compared to the standard 2^{nd} or 3^{rd} degree spherical harmonic B_0 shimming provided by the vendors. While the higher degree spherical harmonic shimming generally increases the homogeneity of the magnetic field over all, the multi coil setup can, depending on the design, produce local field patterns that more closely match the local inhomogeneities caused by the tissue susceptibility differences (e.g. close to the sinus air

cavities) [4]. Therefore, using higher degree spherical harmonics B_0 shimming systems likely provides more degrees of freedom for producing global field patterns that result in a more homogenous field distribution overall. On the other hand, the multi-coil approach is more suited to producing locally complicated patterns.

The question of which B_0 shimming setup is optimal when imaging different regions of the brain is still a point of discussion in the field and a thorough comparison of the two methods for shimming different regions of interest is missing. Given the differences between the two shim approaches, for each MRI imaging application (depending on the focus being on a small region of the brain versus on multiple slices), a certain B_0 shim setup might be more beneficial over the other approach. Additionally, each of these shimming methods can be applied in a static or dynamic manner. While it is known that performing dynamic shim updates improves the quality of the images compared to static shimming, for some imaging applications such as 3D sequences, dynamic shim updating is not possible. Then the question is whether or not using more shim coils for static shimming can ever come close to the same shim quality as dynamic shimming (with fewer coils).

Proton magnetic resonance spectroscopic imaging (^{1}H MRSI) for multi-slice metabolite mapping in the human brain at ultra-high fields is a good example of such challenging applications where the choice of the optimal B_0 shimming scheme becomes very important. ^{1}H MRSI is, in general, very susceptible to inhomogeneities in the magnetic field and can suffer from insufficient water suppression performance [10], or poor quality spectra with broadened linewidths and low signal to noise ratio (SNR) if insufficient B_0 shimming is performed. The poor quality of the spectra then directly affects the reliability of the fits for metabolite quantification and result in metabolite maps that do not fully reflect the underlying anatomy. Furthermore, B_0 inhomogeneities can affect the water suppression pulses and result in metabolites being suppressed rather than the water peak. Also, any spectrally selective pulses will also be effected by B_0 inhomogeneities. Depending on the slice position in the human brain, different field inhomogeneity patterns are observed and these patterns can be compensated best with one of the two main B_0 shimming approaches (i.e. higher degree shimming or multi-coil shimming). Additionally, if 3D sequences such as EPSI [11] are used for metabolite mapping, dynamic B_0 shim updating is not feasible and hence the only option is shimming the whole imaging volume globally.

Although, the advantages of very high degree spherical harmonics dynamic B_0 shimming for multi-slice ^{1}H MRSI have been studied in previous works [12, 3, 5], to the best of our knowledge, no previous study has directly compared the use of higher degree spherical harmonic B_0 shimming to the multi-coil approach for human brain metabolite mapping at ultra-high fields using dynamic shim updating.

Therefore, the aim of this paper is to systematically compare the quality of B_0 shimming that can be achieved in the human brain using the very high degree spherical harmonics shim system and with the multi-coil approach. The comparison is performed in several regions of interest of different sizes and positions. Afterwards *in vivo* B_0 shimming is performed using the very high degree spherical harmonic shim system as well as the multi-coil approach in the human brain. Multiple shimming approaches were performed including higher degree static shimming, low degree dynamic shimming, high degree dynamic shimming, and multi-coil dynamic shimming. These shim approaches were then used to perform multi-slice high resolution metabolite mapping at 9.4T. The effect of each B_0 shim setup on the resulting field homogeneity as well as the quality of the acquired spectra and the resulting metabolite maps are investigated. For the first time, high resolution metabolite maps of the human brain using very high degree spherical harmonic and a multi-coil B_0 dynamic B_0 shimming approach are presented.

Methods

Equipment

In this study, we investigated B_0 shimming in the human brain using two different sets of shim coils: very high-degree spherical harmonics (up to 4th-degree) shim coils and a 16 channel multi-coil shim

array. We also show an application of these B_0 shim methods for multi-slice high resolution metabolite mapping of the human brain.

All measurements were performed on a Siemens Magnetom 9.4T whole-body human scanner (Erlangen, Germany). For all experiments an in-house developed 18Tx/32Rx transceiver head RF coil [13] was used. An insert shim from Resonance Research Inc. (Billerica, MA) with complete 4^{th}-degree spherical harmonic shim coils and partial 5^{th}- and 6^{th}-degree shim coils was used for the very high-degree B_0 shimming. This insert shim system will be referred to as the VHOS (very high order shim) system and is shown in Figure 1a. A multi-coil shim array with 16 circular shim coils arranged in two rows, as shown in Figure 1b, was used for the localized multi-coil B_0 shimming. The local shim coils were 10 cm in diameter and had 20 turns. The multi-coil shim array was used in combination with the 1^{st} and 2^{nd}-order/degree spherical harmonic shim coils from the vendor. For a fair comparison, the partial 5^{th}- and 6^{th}-degree shim coils from the insert shim were not used, so that the total number of channels of VHOS system was also 16 channels. Therefore, both methods used up to 2^{nd}-order/degree shim coils and 16 additional coils.

The reference B_0 maps produced by each of the 16 local shim coils is shown in Figure 2. Reference field maps were also acquired for the VHOS system on a silicon oil spherical phantom. Each coil channel was driven with 0.5 A and the shim fields were measured using a dual echo GRE with the following parameters: in-plane resolution = 1.56 x 1.56 mm^2; number of slices = 50; slice thickness = 4 mm (0% distance factor); FOV = 200 x 200 mm^2; TE = 4.00/4.76 ms; TR = 1200 ms; read-out bandwidth = 1500 Hz/Px. The reference shim fields were then modelled using spherical harmonic decomposition based on the Legendre functions as described in [5].

Simulations

The performance of the multi-coil and VHOS shim were simulated for multiple regions-of-interest (ROIs):

1) a whole-brain region covering the entire cerebrum, cerebellum and brain stem denoted as whole-brain$^+$,
2) another global region consisting of the whole brain minus the medulla and the cervical spine denoted as whole-brain,
3) a single-slice positioned off-centre and going through the frontal sinus air cavity,
4) a single voxel (2x2x2 cm^3) located in the pre-frontal cortex and
5) another single voxel located in the visual cortex.

23 *in vivo* B_0 maps acquired at 9.4T using a 2D dual-echo GRE sequence with the same sequence parameters as described in the previous section were used for these comparisons. The shimmed B_0 maps were simulated using four different hardware setups:

- the multi-coil combined with only first degree spherical harmonic shim terms (MC16),
- the multi-coil combine with first and second degree spherical harmonic shim terms (MC16+SH2),
- the VHOS with up to third-order/degree shim terms (SH3), and
- the VHOS with up to fourth-order/degree shim terms (SH4).

The reference shim field maps and the VHOS spherical harmonic models (described in the previous subsection) were used in the simulations.

The mean standard deviations of the frequency shifts in the shimmed B_0 maps (σB_0) for all volunteers were used to evaluate the quality of the B_0 homogeneity. The shim terms were calculated using a constrained and regularized optimization algorithm (ConsTru) [14], that has been shown to give optimal shim currents for the given hardware constraints. All shim currents were constrained to a maximum of 1.5 A per channel for both the multi-coil and the VHOS shim systems.

In vivo B_0 Shimming

To compare the quality of each of the B_0 shim setups *in vivo*, 3 healthy volunteers were scanned at 9.4T. All volunteers gave their written consent prior to the scan according to the regulations of the local ethics committee. On each volunteer B_0 maps were acquired using the sequence and parameters mentioned in the previous subsection from a 5cm volume: 25 slices with 2 mm slice thickness. The middle slice was always placed above the *corpus callosum* with a transversal orientation. Different B_0 shimming approaches were implemented on the volunteers as described below.

For spherical harmonic B_0 shimming, we compared high degree static B_0 shimming to slice-wise dynamic B_0 shimming of both low and high degree spherical harmonics on all the volunteers. For static B_0 shimming, very high-order/degree shimming was done over the entire 5cm volume using up to 4^{th}-degree shim terms shimmed. Next, the slab was divided into 3 slices with 100% distance factor to perform dynamic B_0 shimming. Since the MRSI application used a slice thickness of 10 mm (described further in the following subsection), each ROI for the slice-wise shimming used 5 slices from the B_0 reference map. In other words, MRSI-slice 1 used B_0-slices 1 to 5, MRSI-slice 3 used B_0-slices 11 to 15 and MRSI-slice 5 used B_0-slices 20 to 25 for shimming. Next the MRSI-slices 1, 3 and 5 were slice-wise shimmed using 2^{nd}-degree shim terms and then again using up to 4^{th}-degree shim terms. The optimal shim currents were calculated using a custom written software that allowed us to accurately define the ROIs on the anatomical images. The ROIs were defined only for the cortex (the skull and subcutaneous fat were excluded). In summary, static and dynamic B_0 shimming were compared using: 4^{th}-degree static shimming (S4), 2^{nd}-degree dynamic (D2) and 4^{th}-degree dynamic shimming (D4) on MRSI-slices 1, 3 and 5.

B_0 shimming for the multi-coil was performed on the same 3 volunteers in a similar manner with a 25 slice reference B_0 map and slice-wise shimmed for the MRSI-slices 1, 3 and 5. The ROI was placed in the same position and the same transversal orientation. For the multi-coil comparison, the 2^{nd}-degree slice-wise shimmed (D2) B_0 maps were acquired and then the multi-coil (combined with the 2^{nd}-degree spherical harmonics) slice-wise shimmed (DMC) B_0 maps were acquired. The measurements using the multi-coil could not be used in the same session as the VHOS due to hardware incompatibility of the insert shim system and the multi-coil setup and so the D2 setting served as a benchmark for this comparison.

Spectroscopic Imaging

A slice-selective ultra-short TE ^{1}H FID MRSI [15, 16, 12] sequence was used to acquire the spectroscopic imaging data from all volunteers. No lipid suppression or outer volume suppression pulses were used, which allowed the repetition time (TR) to be short. The water suppression was comprised of three pulses. The flip angles and gradients of the water suppression were optimized for a range of B_1^+ values (between 50% and 150%) [10]. The sequence parameters were: FOV = 200 x 200 mm^2, acquisition delay = 1.56 ms; spectral bandwidth = 8 kHz, acquisition time = 128 ms; TR = 300ms, in-plane matrix size = 64 x 64; slice thickness = 10mm. The nominal voxel size was therefore 97µL. An R=4 GRAPPA [17] acceleration was used for all MRSI acquisitions. Non-water suppressed reference data were acquired using the same parameters (at 4 times lower spatial resolution) for eddy current and phase correction purposes.

The MRSI data reconstructed using a 2D GRAPPA operator method [18] and were coil-combined using singular value decomposition [19]. Automatic 0^{th} order phase and eddy current correction was performed using Klose eddy current correction [20] and linear back prediction was used to perform automatic 1^{st} order phase correction as described in [10]. LCModel [21] was used to fit the spectra and generate the metabolite maps.

The MRSI data were acquired from the three slices described above. That is, MRSI-slice 1 which corresponds to B0-slices 1 to 5 (denoted as the top slice), MRSI-slice 3 corresponding to B0-slices 10 to 15 (denoted as the centre slice) and MRSI-slice 5 corresponding to B0-slices 20 to 25 (denoted as the

bottom slice). Each slice was separated from the next one by 1cm, so that the 3 slices span over a 5cm volume). These data were acquired for each of the shim settings described in the previous section.

Results

Simulations

Figure 3 shows the boxplot of the shimming comparison results. Each box contains the results of all 23 volunteer datasets. The mean and standard deviation for each shim setting is also summarized in Table 1. The simulations showed that for the global shimming applications (whole-brain+ and whole-brain), the multi-coil setup when combined with 2nd degree spherical harmonic shim coils (MC15+SH2) performs similarly to 3rd degree spherical harmonic shims (SH3). The standard deviation of the 4th degree spherical harmonics are on average 7 Hz less than the combined multi-coil setup for both cases. For a single slice ROI, the combined multi-coil performs similarly to 4th degree spherical harmonics and they both perform better than the 3rd degree spherical harmonics by about 7 Hz on average. However, for single voxel applications both in the frontal and visual cortex the performance of the combined multi-coil is similar to the VHOS system. It is worth noting that, for a single voxel in the frontal cortex, the MC16 (without SH2) seems to do significantly worse than all the others.

In vivo B_0 Shimming

In the first comparison, we looked at the VHOS system and compared high degree static (S4) to both low (D2) and high (D4) degree dynamic B_0 shimming. Three slices with 10 mm slice thickness were evaluated. The slices were described as the MRSI-slices 1, 3 and 5 in the previous section, and will be referred to as the top, centre and bottom slices, respectively. The comparison between S4, D2 and D4 are shown for a representative volunteer in Figure 4 (left). All B_0 maps in the figure are shown between -80 and 80 Hz. Clearly, the B_0 maps resulting from D4 are much more homogeneous than D2 for all slices with a 2 Hz improvement on the top slice and a 10 Hz improvement on both the centre and bottom slices. The S4 also shows some improvement over D2, however the improvement is very little on the top slice. The figure also shows the histograms of the B_0 field distributions between -100 and 100 Hz. The histograms give a rough indication of the linewidth of the spectra acquired from the whole slice for each position and shim setting. Compared to D2, the S4 and D4 histograms have taller and thinner distributions.

In the next comparison, we looked at the difference between using a 2nd degree spherical harmonics dynamic B_0 shimming (D2) and the dynamic multi-coil combined with 2nd degree spherical harmonics shim setting (DMC) for shimming the different slices. The results of this study are also shown for a representative volunteer in Figure 4 (right) .The DMC proves to be superior to D2 on all slices. The D2 results for this volunteer are similar to the volunteer shown for the VHOS system on the left of the same Figure. However, the improvement over D2 for the bottom slice was slightly more for D4 than the DMC (10 Hz compared to 7 Hz). The histograms, once again, show narrower linewidths for DMC than D2.

Figure 5 shows the means and standard deviations of the B_0 maps averaged over all the volunteers for all shim settings. The improvement from D2 to D4 is comparable to the improvement seen from D2 to DMC, which is similar to what was shown in Figure 4. These averaged standard deviations of D2 vary between the two graphs due to different positioning of the heads mandated by the different hardware setups. Table 2 shows the actual means and standard deviations. Improvements can be seen on all slices for both D4 and DMC methods compared to D2. However, the improvement is always less for the top slices compared to the centre and bottom slices.

Comparison of static and dynamic shimming shows that on average 4th order static shimming outperforms 2nd order dynamic shimming for the centre and bottom slices. However, the improvement is traded off for the homogeneity of the top slice since the top slice of D2 is better than the top slice of

S4. Furthermore, the improvement of S4 for the centre and bottom slices is only about 4 or 5 Hz compared to the potential 8 to 9 Hz that could be achieved with D4.

Spectroscopic Imaging

Figure 6 shows the spectra for the different B_0 shimming settings acquired from the centre slice. Representative spectra are shown from a region in the left posterior hemisphere. The spectra are shown between 1.8 and 3.5 ppm for better visualization. Two different comparisons are represented: spectra acquired with D2 vs. D4 and once again D2 vs DMC. The respective anatomical reference image overlaid with the grid from which the spectra are chosen are also shown. As expected, the more homogeneous the B_0 field, the narrower the linewidths of the spectra. The peaks in the spectra resulting from the D2 shimmed slices are in general broader than for the D4 and DMC B_0 shims.

The resulting metabolite maps along with their respective Cramer-Rao lower bound (CRLB) maps for the VHOS comparisons are shown in Figure 7. The maps are shown for NAA, Glutamate and total Choline relative to the Creatine concentrations. The metabolite maps acquired from D2 shimming are different to the maps acquired from D4 shimming. For NAA on the bottom slice the signal dropout due to the residual B_0 inhomogenity from the nasal cavity is smaller when using D4 than when using D2. Also, in the CRLBs of NAA, more voxels could be reliably fit for the centre and bottom slices when D4 shimming was used. The effect of good shimming is more obvious for the Glutamate and total Choline metabolite maps. The Glutamate maps resemble the underlying anatomical structure much more closely for D4 than D2. This is evident in all the slices and is also reflected in the CRLB maps which have more voxels being reliably fit for the D4 case. A similar effect can be seen for total choline.

The resulting metabolite and CRLB maps for the MC comparisons are shown in Figure 8. Compared to the VHOS metabolite maps, the slice position was slightly higher due to different hardware setups and the effect of the nasal cavity is less observed. Since the position was slightly higher, the metabolite maps from D2 were already quite good for the centre slice. However, we still see very good improvement of the DMC over D2 (particularly for the bottom slice). Again, the metabolite maps resemble the underlying anatomical structure better for the DMC shimming, especially for Glutamate in the top and bottom slices, and for total Choline in all slices. The grey and white matter contrast is clearer in the total Choline maps for DMC. Furthermore, the improved fitting is also clearly reflected in the CRLB maps for the bottom slice and the total Choline in the top slice.

The average CRLB (of Cre) and SNR (absolute peak of NAA over the root mean square of the noise) are summarized in Table 2 for each B_0 shim setting.

Overall, it is evident that better B_0 homogeneity not only improves the reliability of the quantification process (i.e. more voxels can be reliably fit) but also with better B_0 shimming, the metabolite concentration maps are more reflective of the underlying anatomical structure.

Discussion

The goal of this work was to provide further insight into the benefits of two different B_0 shimming concepts, namely very high degree spherical harmonics and multi-coil, for performing B_0 shimming in the human brain at 9.4T. After theoretical comparisons, the two different shimming concepts were used in the context of multi-slice high resolution metabolite mapping in the human brain. To the best of the authors' knowledge, this is the first time that the multi-coil shim setup has been used in the context of MRSI applications.

For the simulation comparisons, different settings were considered, where the total number of shim coils were kept the same among different setups at an attempt to perform a fair comparison. This way the shim quality merely depends on the spatial distribution of the shim fields that these coils are generating and not on the number of degrees of freedom. We considered two different settings for a 16-coil B_0 shim system, namely our 16-channel multi-coil setup (MC) versus the 3rd degree spherical harmonic

shim system (SH3) and two different settings for a 25-coil B_0 shim setup, namely the combination of the multi-coil and 2nd degree spherical harmonics (MC+SH2) versus the 4th degree spherical harmonic shim system (SH4).

These simulations showed that for this particular multi-coil design, the performance of the 16-channel multi-coil system on its own is generally slightly worse than 3rd degree spherical harmonics shim system, except for shimming on a single-slice where it outperforms the 3rd degree shim system and on a single-voxel in the frontal cortex where it performs much worse. These results further confirm what has been reported in previous studies by Juchem et al [1] where they showed that their DYNAMITE multi-coil setup outperforms a 3rd degree spherical harmonic shim on a single slice of the brain in a position similar to the one chosen in this study. Truong et al [9] also showed that using a multi-coil design they can achieve good shimming performance for a similar slice position, reporting a σB_0 of 15.2Hz on 3T, which translates to 0.123 ppm compared to about 0.09 ppm that we achieve on 9.4T.

The combination of the multi-coil with 2nd degree spherical harmonic shim coils performs similarly to 3rd degree spherical harmonic shim system for global shimming applications and larger ROIs, however, for shimming smaller regions such as single-slice or single-voxel spectroscopy applications, its performance is similar to a 4th degree spherical harmonic shim system. So, unless a very large region needs to be shimmed globally, for other applications in the human brain the combination of this multi-coil design and the 2nd degree spherical harmonics performs similarly to a 4th degree spherical harmonics shim system.

The two best B_0 shim setups (judging by the results of the theoretical simulations), namely the combination of the multi-coil with the 2nd degree spherical harmonics and the 4th degree spherical harmonics were then compared *in vivo*. In addition, another aspect of B_0 shimming, namely, performing global shimming over the whole imaging volume (static shimming) versus updating the shim values for each slice that is currently being imaged (dynamic shim updating) was also included in the study: comparing a very high degree (4th degree) spherical harmonic global shimming versus dynamic shim updating. In all cases dynamic shim updating using 2nd degree spherical harmonic shims was taken as a benchmark. The results showed that including more degrees of spherical harmonic while performing static shimming improves the quality of the shim overall. On the bottom and middle slice position indeed including more spherical harmonics improves the shim quality compared to when 2nd degree dynamic shimming is performed. However, the 2nd degree dynamic shim updating proves to perform better on the top slice where the static shimming sacrifices the shim quality for better shimming on other slices. Overall, the results showed that when it is not possible to perform slice-wise dynamic B_0 shim updating (due to lack of driving hardware or software), one can still achieve reasonable shim quality by including higher degree spherical harmonics and performing global shimming over the whole slab.

Alternatively, the shim quality can be further improved by performing dynamic shim updates using 4th degree spherical harmonics or the multi coil in combination with 2nd degree spherical harmonics. This proves to always be consistently advantageous over 2nd degree dynamic shimming. The amount of improvement gained from going to higher degree spherical harmonics versus including a multi-coil design was comparable to each other for similar slice positions. The highest improvement was seen on inferior slice positions, where due to the susceptibility difference between the air in the nasal cavities and the tissue, severe B_0 inhomogeneities are present. This has also been confirmed before for the case of dynamic spherical harmonic shim updating by Boer et al [12] and Pan et al [3].

It is well known that the quality of B_0 shimming directly affects the quality of the acquired spectra in MRSI applications. This can be due to the fact that as a result of lower local B_0 inhomogeneity, the lines are sharper and the SNR is higher, which means that quantification is much more accurate. Additionally, the quality of water suppression is affected by B_0 inhomogeneity. In regions with high residual B_0 distortion, the water suppression will fail leaving a strong residual water peak that will distort the quantification of the metabolites of interest. High resolution metabolite maps acquired with the two improved B_0 shim setups of this study further highlights the advantages of these advanced shim setups

compared to 2nd degree slice-wise shim update. Qualitatively speaking the maps acquired with 4th degree spherical harmonic shim system are similar to those acquired with the multi-coil combined with 2nd degree spherical harmonic shims. In all cases however, the maps look much more accurate than only performing 2nd degree dynamic shimming as they reflect the underlying anatomy much better. The white/gray matter contrasts are much clearer and the confidence in fits are higher as a result of improved B_0 shimming.

It should be noted that even though the results of this study show that for multi-slice imaging in the brain at 9.4T, both the multi-coil plus 2nd degree spherical harmonics setup and the 4th degree spherical harmonics setup perform comparably well, the manufacturing of the local shim coils are in practice much easier than the higher degree spherical harmonics. The requirements on manufacturing shim coils to generate spherical harmonic functions over a large spatial region are much more demanding than building local shim coils. Furthermore, spherical harmonic shim coils are more prone to eddy currents [5], while the local shim coils are smaller and have much less eddy currents due to gradient or shim switching [1]. Using spherical harmonic shim coils for dynamic B_0 shim updating often requires pre-emphasis and calibration of the system [4, 12] while the multi-coil does not.

Conclusion

In this study, we compared the performance of a high degree spherical harmonic B_0 shim system to a 16-channel multi-coil setup for B_0 shimming of the human brain at 9.4T. Simulations on 5 different B_0 shimming applications showed that the multi-coil setup combined with the 2nd degree spherical harmonics performs similarly to 4th degree spherical harmonic shimming for almost all shimming applications. The results were confirmed by applying the two different B_0 shimming approaches *in vivo* for a dynamically shim updated multi-slice MRSI application. High resolution metabolite maps were acquired from three slices across the human brain using each of the B_0 shimming methods. Both methods showed advantages over low degree (up to 2nd) spherical harmonic dynamic shimming. The results emphasize the importance of slice-wise B_0 shimming for metabolite mapping at ultra-high fields and suggest that either of the two B_0 shimming approaches can be used to achieve similar results.

Bibliography

[1] C. Juchem, S. U. Rudrapatna, T. W. Nixon and R. A. de Graaf, "Dynamic multi-coil technique (DYNAMITE) shimming for echo-planar imaging of the human brain at 7 Tesla," *Neuroimage,* vol. 105, pp. 462-472, 2015.

[2] V. O. Boer, M. P. Luttje, P. R. Luijten and D. W. Klomp, "Requirements for static and dynamic higher order B0 shimming of the human breast at 7 T," *NMR in Biomedicine,* vol. 27, no. 6, pp. 625-631, 2014.

[3] J. W. Pan, K.-M. Lo and H. P. Hetherington, "Role of very high order and degree B0 shimming for spectroscopic imaging of the human brain at 7 tesla," *Magnetic Resonance in Medicine,* vol. 68, no. 4, pp. 1007-1017, 2012.

[4] C. Juchem, T. W. Nixon, S. McIntyre, V. O. Boer, D. D. Rothman and R. A. de Graaf, "Dynamic multi-coil shimming of the human brain at 7T," *Journal of magnetic resonance,* vol. 212, no. 2, pp. 280-288, 2011.

[5] P. Chang, S. Nassirpour and A. Henning, "Modeling real shim fields for very high degree (and order) B0 shimming of the human brain at 9.4 T," *Magnetic Resonance in Medicine,* 2017.

[6] C. Juchem, T. W. Nixon, S. McIntyre, D. L. Rothman and R. A. de Graaf, "Magnetic field homogenization of the human prefrontal cortex with a set of localized electrical coils," *Magnetic resonance in medicine,* vol. 63, no. 1, pp. 171-180, 2010.

[7] A. M. Blamire, D. L. Rothman and T. Nixon, "Dynamic shim updating: a new approach towards optimized whole brain shimming," *Magnetic resonance in medicine,* vol. 36, no. 1, pp. 159-165, 1996.

[8] J. P. Stockmann, T. Witzel, B. Keil, J. R. Polimeni, A. Mareyam, C. LaPierre, K. Stesompop and L. L. Wald, "A 32-channel combined RF and B0 shim array for 3T brain imaging," *Magnetic resonance in medicine,* vol. 75, no. 1, pp. 441-451, 2016.

[9] T.-K. Truong, D. Darnell and A. W. Song, "Integrated RF/shim coil array for parallel reception and localized B0 shimming in the human brain," *NeuroImage ,* vol. 103, pp. 235-240, 2014.

[10] S. Nassirpour, P. Chang and A. Henning, "High and ultra-high resolution metabolite mapping of the human brain using 1 H FID MRSI at 9.4 T," *NeuroImage,* 2016.

[11] A. A. Maudsley, C. Domenig, V. Govind, A. Darkazanli, C. Studholme, K. Arheart and C. Bloomer, "Mapping of brain metabolite distributions by volumetric proton MR spectroscopic imaging (MRSI)," *Magnetic resonance in medicine,* vol. 61, no. 3, pp. 548-559, 2009.

[12] V. O. Boer, D. D. Klomp, C. Juchem, P. R. Luitjen and R. A. de Graaf, "Multislice 1H MRSI of the human brain at 7 T using dynamic B0 and B1 shimming," *Magnetic resonance in medicine,* vol. 68, no. 3, pp. 662-670, 2012.

[13] N. Avdievitch, I. A. Giapitzakis and A. Henning, "Combined Surface Loop/"Vertical" Loop Element Improve Receive Performance of a Human Head Transceiver Array at 9.4T: an Alternative to Surface Loop/Dipole Antenna Combination," *NMR in Biomedicine,* 2017.

[14] S. Nassirpour, P. Chang and A. Henning, "A comparison of optimization algorithms for localized in vivo B0 shimming," *Magnetic Resonance in Medicine,* 2017.

[15] A. Henning, A. Fuchs, J. B. Murdoch and P. Boesinger, "Slice-selective FID acquisition, localized by outer volume suppression (FIDLOVS) for 1H-MRSI of the human brain at 7 T with minimal signal loss," *NMR in Biomedicine,* vol. 22, no. 7, pp. 683-696, 2009.

[16] W. Bogner, S. Gruber, S. Trattnig and M. Chmelik, "High-resolution mapping of human brain metabolites by free induction decay 1H MRSI at 7 T," *NMR in Biomedicine,* vol. 25, no. 6, pp. 873-882, 2012.

[17] M. A. Griswold, P. M. Jakob, R. M. Heidemann, M. Nittka, V. Jellus, J. Wang, B. Kiefer and A. Haase, "Generalized autocalibrating partially parallel acquisitions (GRAPPA)," *Magnetic resonance in medicine,* vol. 47, no. 6, pp. 1202-1210, 2002.

[18] M. Blaimer, F. A. Breuer, M. Mueller, N. Sieberlich, D. Ebel, R. M. Heidemann, M. A. Griswold and P. M. Jakob, "2D-GRAPPA-operator for faster 3D parallel MRI," *Magnetic resonance in medicine,* vol. 56, no. 6, pp. 1359-1364, 2006.

[19] M. Bydder, G. Hamilton, T. Yokoo and C. B. Sirlin, "Optimal phased-array combination for spectroscopy," *Magnetic resonance imaging,* vol. 26, no. 6, pp. 847-850, 2008.

[20] U. Klose, "In vivo proton spectroscopy in presence of eddy currents.," *Magnetic Resonance in Medicine,* vol. 14, no. 1, pp. 26-30, 1990.

[21] S. W. Provencher, "Estimation of metabolite concentrations from localized in vivo proton NMR spectra," *Magnetic resonance in medicine,* vol. 30, no. 6, pp. 672-679, 1993.

[22] M. Blaimer, F. A. Breuer, M. Mueller, N. Seiberlich, D. Ebel, R. M. Heidemann, M. A. Griswold and P. M. Jakob, "2D-GRAPPA-operator for faster 3D parallel MRI," *Magnetic resonance in medicine,* vol. 56, no. 6, pp. 1359-1364, 2006.

[23] P. Chang, S. Nassirpour and A. Henning.

[24] "Modeling real shim fields for very high degree (and order) B0 shimming of the human brain at 9.4 T," *Magnetic Resonance in Medicine,* 2017.

[25] "Combined Surface Loop/"Vertical" Loop Element Improve Receive Performance of a Human Head Transceiver Array at 9.4T: an Alternative to Surface Loop/Dipole Antenna Combination," *NMR in Biomedicine,* 2017.

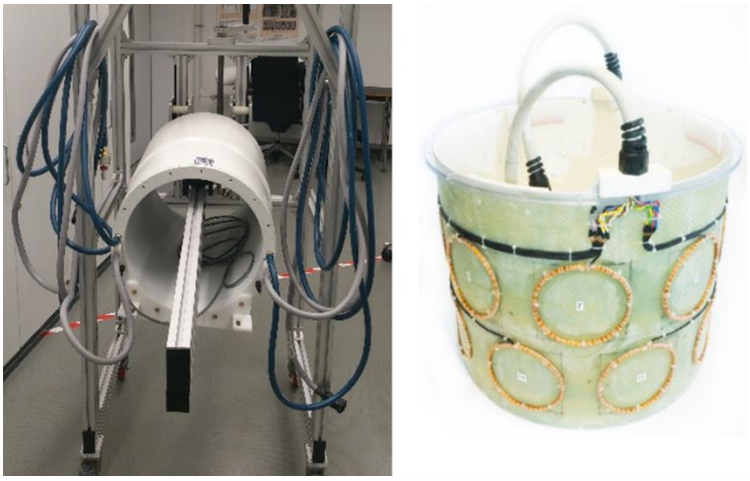

Figure 1 – (Left) Insert shim system with very high order B_0 shim (VHOS) and (right) multi-coil array of localized shim coils.

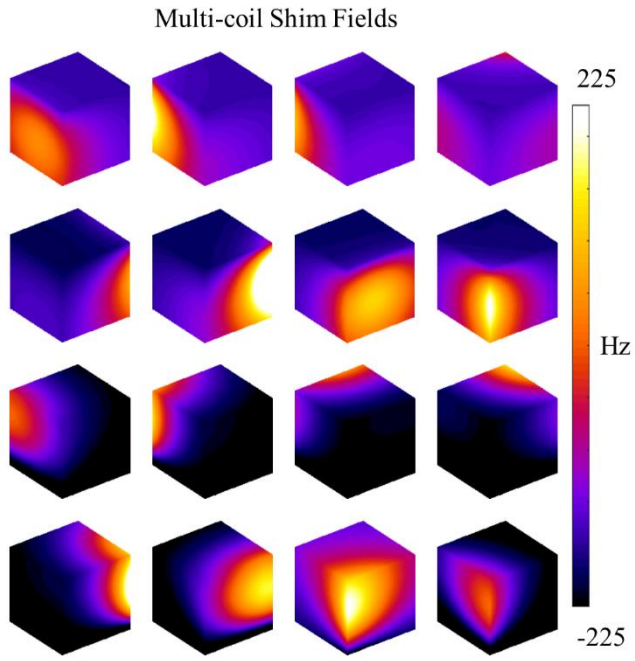

Figure 2 – Shim fields generated by each coil element of the multi-coil array for 1 A.

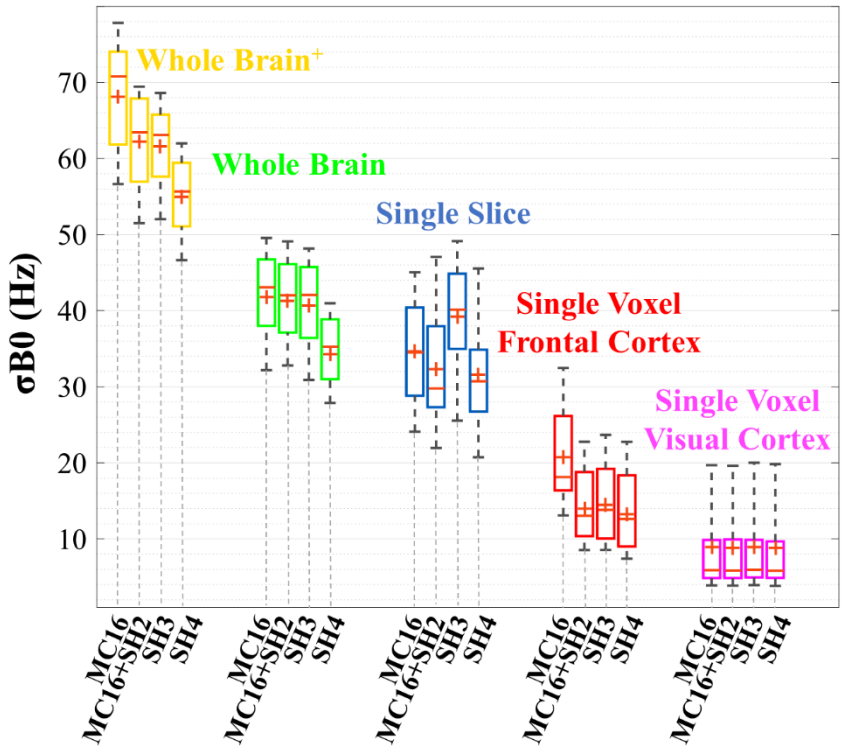

Figure 3 – Mean residual standard deviations after B_0 shimming for different regions of interest on 23 *in vivo* datasets for four different setups: the 16-channel multi-coil (MC16), the 16-channel multi-coil combined with 2nd degree spherical harmonics (MC16+SH2), up to 3rd degree (SH3) and 4th degree (SH4) spherical harmonics.

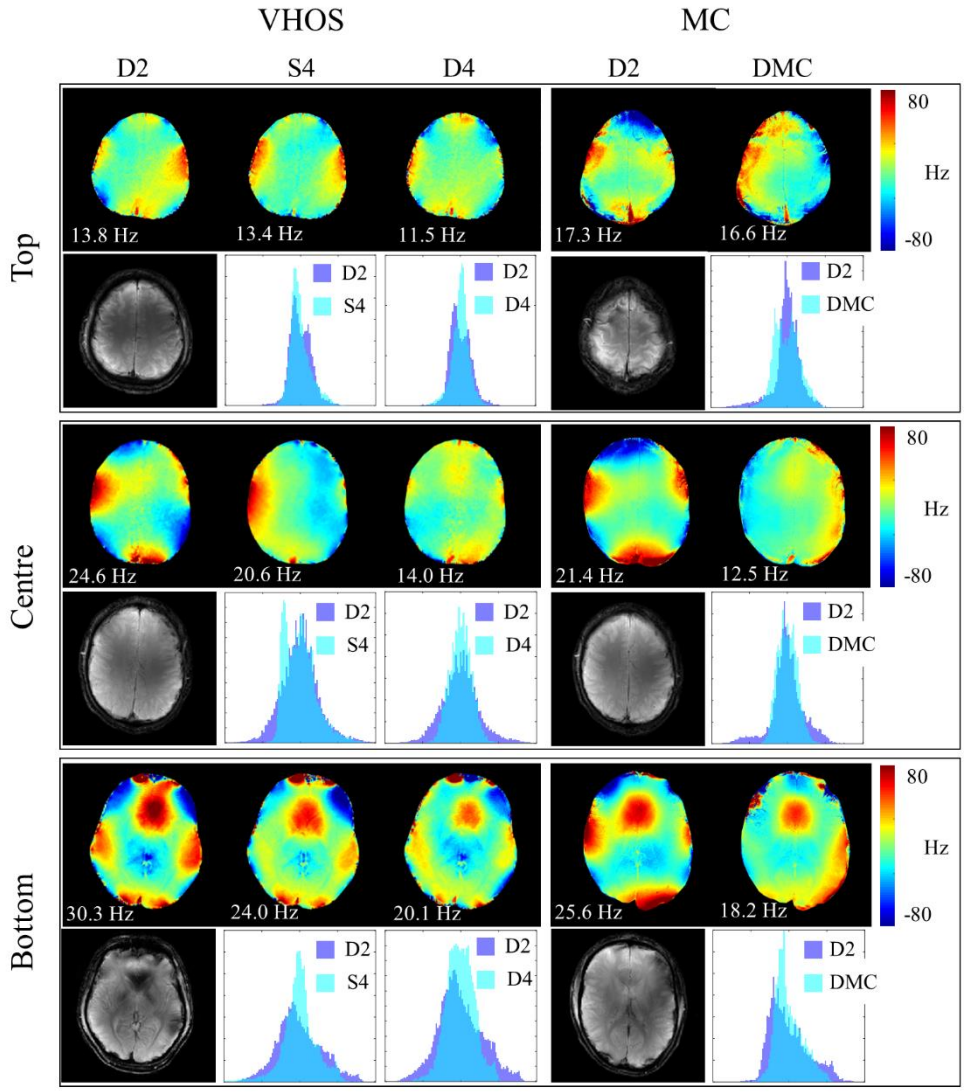

Figure 4 – B_0 maps of top, centre and bottom slices using VHOS B_0 shimming and multi-coil (MC) B_0 shimming. The 2nd degree dynamic slice-wise updated B_0 shimmed maps (D2) are shown as references for each volunteer. Dynamic slice-wise updated shimmed maps are shown for the 4th degree VHOS (D4) and MC system (DMC). The statically shimmed 4th degree shimmed B_0 maps are also shown for the VHOS system (S4). Corresponding histograms are shown beneath the respective B_0 maps.

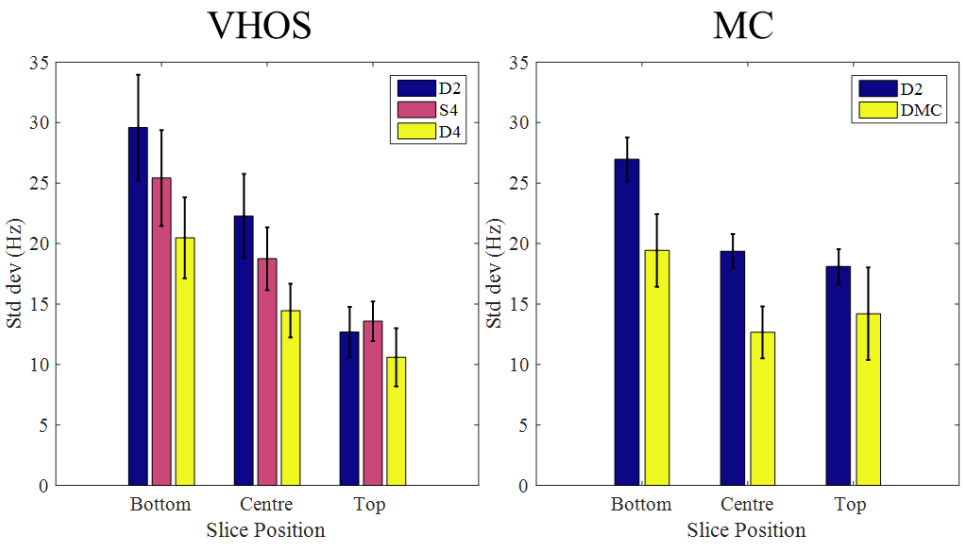

Figure 5 – Standard deviations of shimmed B_0 maps for 3 slice positions averaged across all volunteers. The 2nd degree dynamic slice-wise B_0 maps are shown as a reference (D2). The results for the dynamic slice-wise 4th degree (D4) and multi-coil (DMC) are shown along with the statically shimmed 4th degree (S4).

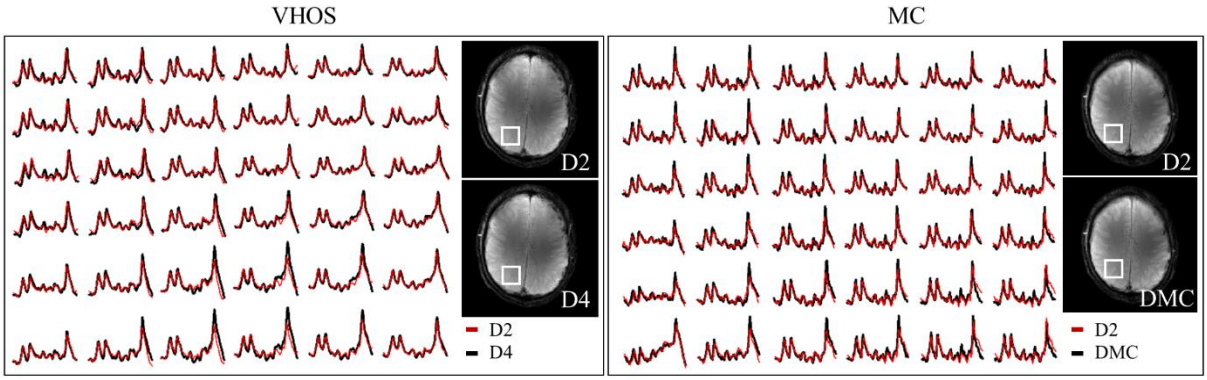

Figure 6 – Representative spectra from the acquired MRSI data for the centre slice using different B_0 shim systems: the VHOS and the MC system. The 2nd degree B_0 shimmed spectra are shown as a reference in red. All spectra are shown between 1.8 to 3.5 ppm.

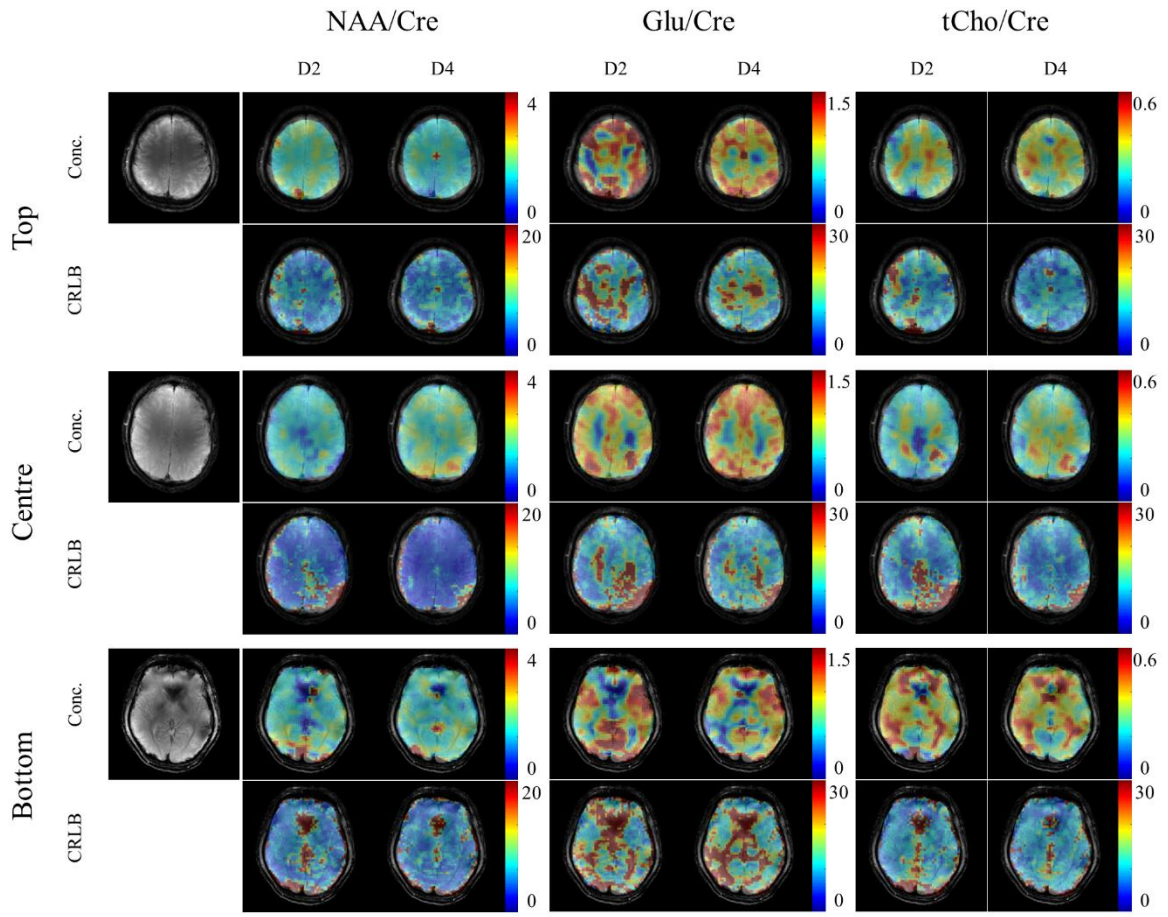

Figure 7 – Metabolite maps for top, centre and bottom slices in the human brain using the VHOS system for B_0 shimming. The maps for 2nd degree (D2) and 4th degree (D4) dynamic slice-wise updated shim are shown. The metabolite ratios are shown (with respect to creatine) along with the CRLBs.

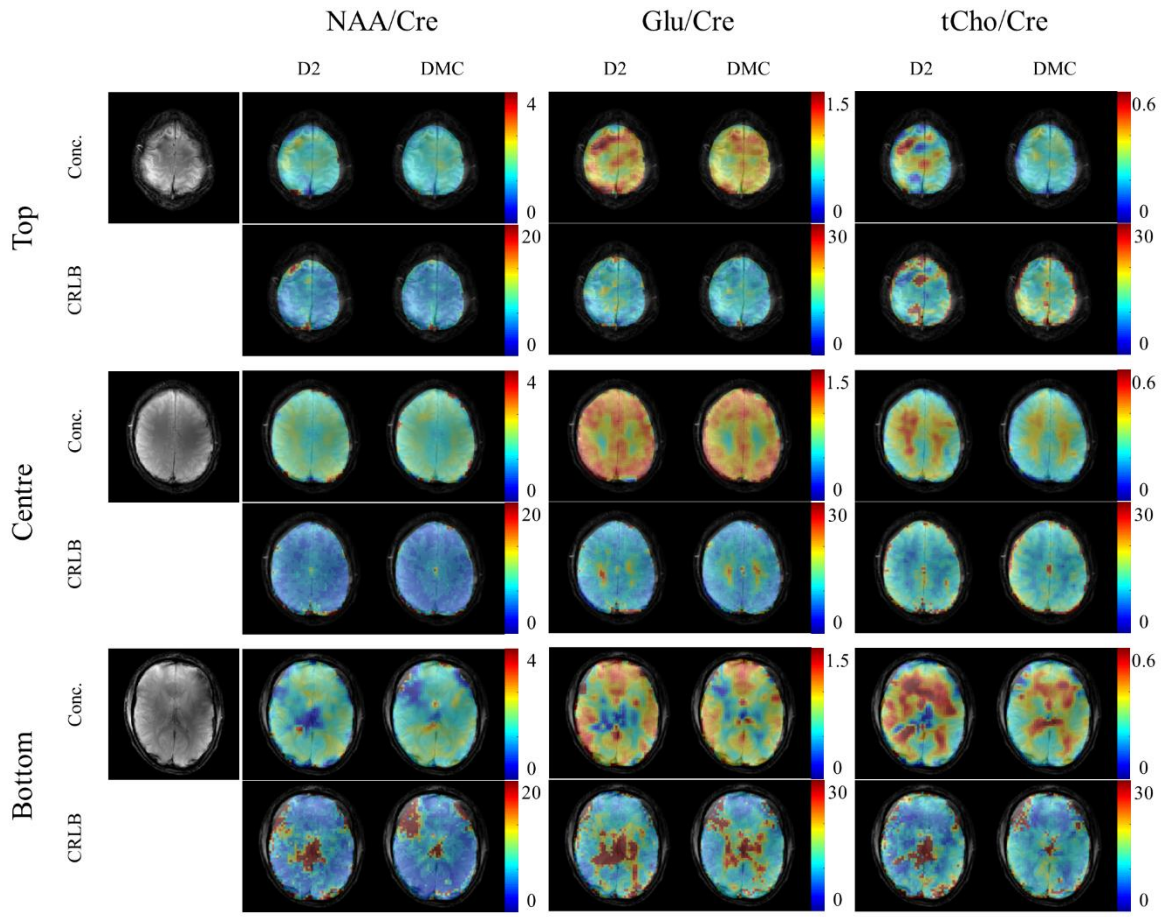

Figure 8 – Metabolite maps for top, centre and bottom slices in the human brain using the multi-coil (MC) system for B_0 shimming. The maps for 2nd degree (D2) and multi-coil (DMC) dynamic slice-wise updated shim are shown. The metabolite ratios are shown (with respect to creatine) along with the CRLBs.

Table 1 – Standard deviations of 23 *in vivo* datasets using the VHOS and MC shim coil systems for different regions of interest in the brain.

	MC		VHOS	
δB_0 (Hz)	**MC16**	**MC16+SH2**	**SH3**	**SH4**
Whole-Brain$^+$	68.16 ± 7.99	62.25 ± 6.41	61.59 ± 6.01	54.96 ± 5.90
Whole-Brain	41.83 ± 6.48	41.30 ± 6.87	40.67 ± 6.55	34.34 ± 5.67
Single-Slice	34.60 ± 8.65	32.35 ± 9.07	39.21 ± 8.15	31.61 ± 9.06
Single-Voxel (frontal cortex)	20.76 ± 7.56	14.04 ± 5.31	14.50 ± 5.61	13.27 ± 5.48
Single-Voxel (visual cortex)	8.94 ± 7.16	8.87 ± 7.08	8.99 ± 7.09	8.83 ± 7.04

Table 2 – Standard deviations of the B_0 maps for the top, centre and bottom slices using the VHOS and MC dynamic slice-wise shimming. The CRLB of creatine and the SNRs of the MRSI spectral data are also shown for the two shim settings.

	VHOS			MC	
δB_0 (Hz)	**D2**	**S4**	**D4**	**D2**	**DMC**
Top	12.7 ± 2.1	13.6 ± 1.6	10.6 ± 2.4	18.1 ± 1.4	14.2 ± 3.8
Centre	22.3 ± 3.5	18.7 ± 2.6	14.5 ± 2.2	19.4 ± 1.4	12.7 ± 2.1
Bottom	29.6 ± 4.4	25.4 ± 4.0	20.5 ± 3.3	27.0 ± 1.8	19.4 ± 3.0
CRLB (Cre)					
Top	11 ± 1.5	-	10 ± 1	8 ± 1	8 ± 0.5
Centre	8 ± 1.5	-	8 ± 1	8 ± 1	7 ± 0.5
Bottom	10 ± 2		8 ± 1.5	9 ± 1.5	8 ± 1.5
SNR					
Top	34 ± 9	-	39 ± 11	41 ± 10	43 ± 10
Centre	42 ± 10	-	49 ± 12	51 ± 15	60 ± 16
Bottom	27 ± 11	-	34 ± 10	36 ± 14	40 ± 13

Publication IV

"Constrained Optimisation for Position Calibration of a NMR Field Camera"

P Chang, S Nassirpour, M Eschelbach, K Scheffler, A Henning

Magnetic Resonance in Medicine, 2017, doi:10.1002/mrm.27010

FULL PAPER

Magnetic Resonance in Medicine 00:00–00 (2017)

Constrained Optimization for Position Calibration of an NMR Field Camera

Paul Chang,[1,2]* Sahar Nassirpour,[1,2] Martin Eschelbach,[1,3] Klaus Scheffler,[1,4] and Anke Henning[1,5]

Purpose: Knowledge of the positions of field probes in an NMR field camera is necessary for monitoring the B_0 field. The typical method of estimating these positions is by switching the gradients with known strengths and calculating the positions using the phases of the FIDs. We investigated improving the accuracy of estimating the probe positions and analyzed the effect of inaccurate estimations on field monitoring.
Methods: The field probe positions were estimated by 1) assuming ideal gradient fields, 2) using measured gradient fields (including nonlinearities), and 3) using measured gradient fields with relative position constraints.
The fields measured with the NMR field camera were compared to fields acquired using a dual-echo gradient recalled echo B_0 mapping sequence. Comparisons were done for shim fields from second- to fourth-order shim terms.
Results: The position estimation was the most accurate when relative position constraints were used in conjunction with measured (nonlinear) gradient fields. The effect of more accurate position estimates was seen when compared to fields measured using a B_0 mapping sequence (up to 10%–15% more accurate for some shim fields).
The models acquired from the field camera are sensitive to noise due to the low number of spatial sample points.
Conclusion: Position estimation of field probes in an NMR camera can be improved using relative position constraints and nonlinear gradient fields. **Magn Reson Med 000:000–000, 2017. © 2017 International Society for Magnetic Resonance in Medicine.**

Key words: Field monitoring; NMR field camera; NMR field probes; position calibration; high order B_0 shim.

INTRODUCTION

Spatiotemporal monitoring of the B_0 field can be used to measure the dynamics of the MR systems and has a variety of applications. The dynamics can be used to perform preemphasis for correcting eddy currents (1–3), frequency stabilization (4), and field stabilization with online control of the B_0 shim fields (5–7). Spatiotemporal monitoring of the B_0 field requires fast measurements of the B_0 field without compromising the spatial accuracy.

For this purpose, projection-based B_0 mapping methods such as FASTMAP (8,9) and FASTMAP (10) can be used. These methods can also be integrated into the sequence to perform real-time B_0 shimming (5,11). Alternatively, spatiotemporal monitoring can be done using very low-resolution B_0 maps or B_0 shim navigators (6,12,13). All of the above-mentioned methods need to be included in the pulse sequence, which increases the complexity of implementation and also the scan duration.

Alternative to these sequence-based techniques, one can use NMR field probes (henceforth referred to as field probes) for spatiotemporal monitoring (14,15). A field probe can measure the B_0 magnetic field at a single spatial point at a very high temporal resolution. An array of field probes (often called a field camera) can be used to measure the B_0 at many spatial points simultaneously (16,17). A field camera can be used independently of the MRI scanner and thus requires no additional scan time. The positions of the field probes need to be estimated before monitoring. One disadvantage of using the field camera is that it requires additional hardware.

A comparison of the different B_0 field measurement methods shows that there is a tradeoff between the spatial and temporal resolution of monitoring the B_0 field (Fig. 1). For applications in which high spatial resolution is required (e.g., calibrating shim systems), an entire B_0 map should be acquired. For applications in which high temporal resolution is required, the projection-based or low-resolution B_0 mapping methods should be employed. If even faster dynamics of the B_0 field need to be measured, use of a field camera can be appropriate. However, field cameras usually only have up to 16 field probes and thus have very low spatial resolution. Due to the low spatial resolution of the field camera, the B_0 field cannot be completely determined using a few sample points. Instead, the sample points are used to derive an approximation of the B_0 field using spherical harmonic decomposition (18,19). Spherical harmonic decomposition approximates arbitrary B_0 fields using a set of orthogonal basis functions (the Legendre polynomials). This is a common method of approximating and modeling B_0 fields (8,9,16,20).

Field probes and field cameras have been extensively used in (15–17) for dynamic field monitoring and in (4,7) for real-time feedback. In this study, we show that we can improve the spatial accuracy of the field camera by introducing prior knowledge about the field camera structure and about the gradient nonlinearities into the

[1]Max Planck Institute for Biological Cybernetics, Tuebingen, Germany.
[2]IMPRS for Cognitive and Systems Neuroscience, Eberhard-Karls University of Tuebingen, Germany.
[3]Department of Physics, Eberhard-Karls University of Tuebingen, Germany.
[4]Department of Biomedical Magnetic Resonance, Eberhard-Karls University of Tuebingen, Germany.
[5]Department of Physics, University of Greifswald, Greifswald, Germany.
*Correspondence to: Paul Chang, Max Planck Institute for Biological Cybernetics, Max-Planck-Ring 11, 72076 Tübingen, Germany.
E-mail: paul.chang@tuebingen.mpg.de.

Received 22 June 2017; revised 23 October 2017; accepted 25 October 2017
DOI 10.1002/mrm.27010
Published online 00 Month 2017 in Wiley Online Library (wileyonlinelibrary.com).

© 2017 International Society for Magnetic Resonance in Medicine

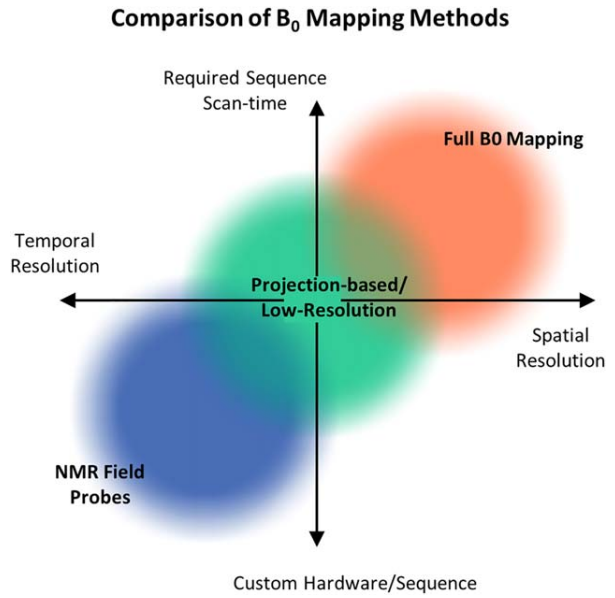

FIG. 1. Qualitative comparison of different B_0 mapping methods show a clear tradeoff between the spatial and temporal resolution. Although field probes require more special hardware, they can be used independently of the MRI scanner and thus do not increase the scan duration.

position calibration. We then extensively compare B_0 maps measured with a large number of field probes to static B_0 maps acquired using a full B_0 mapping sequence. We show that small perturbations in the measurements can result in spatial measurement inaccuracies despite the large number of field probes used in this study.

THEORY

The physics of field probes goes back to the very basics of MR. A field probe is a small sample of water (or fluorine (4,7) or ^{2}H (21) for in vivo measurements) that is excited using a small RF coil to generate a FID. It is well-known that the frequency of the FID (which can be calculated from the phase) is related to the magnetic field strength through the gyromagnetic ratio. Because the water or fluorine sample in the field probes is small, the magnetic field strength of this small volume at this position can be measured:

$$f = {}^{d\varphi}/_{dt} = \gamma B, \qquad [1]$$

where f is the frequency, γ is the gyromagnetic ratio, and B is the magnetic field strength. The gyromagnetic ratio of proton is approximately 42.576 Hz/uT.

Usually, several field probes are used to measure many spatial locations of the field simultaneously. These measurements are then modeled by spherical harmonic decomposition using Legendre polynomials to measure the spatiotemporal field dynamics. Legendre polynomials are used because they provide a number of benefits, such as orthogonality, coverage of a 3D space, and ease of use.

In order to decompose the B_0 field using spherical harmonics, the positions of the field probes (relative to the scanner) need to be determined prior to the measurements. In the case of field cameras, despite the field probes being mounted in fixed positions, accurately obtaining their positions relative to the scanner can be complicated. Even in the construction of the field camera, the field probes may be slightly misplaced. Furthermore, because the field probes are often encapsulated inside an epoxy mold (14), this may cause even more inaccuracies in the construction and prevent accurate relative position calibration based on optical methods.

Currently, the method of estimating the positions of the field probes is to use the scanner gradients. Known gradient strengths are applied in each of the x-, y-, and z-directions, and positions can be estimated from the measured frequencies of the field probes (16) using the following equation:

$$f = \gamma \cdot B = \gamma \cdot G_x \cdot x - f_{off\_res}, \qquad [2]$$

where f_{off_res} is the off-resonance calculated from FID without any gradients applied (as the reference); G_x is the gradient strength in the x-direction; and x is the x-position. Because the applied gradient strength is known and the frequency can be measured, the x-position can be estimated. Similarly, applying a gradient in the y- and z-directions gives us the y- and z-positions, respectively.

The problem with this method is that it relies on the assumption of the gradient fields being perfectly spatially linear. Unfortunately, deviations in the linearity of the gradient may introduce an error in the position estimate of the field probes. Note that this is not a problem if we only want to monitor first-order B_0 terms because the nonlinearities cancel each other out; however, for higher order spherical harmonic terms, the accuracy of the decomposition is heavily dependent on the accuracy of the position estimates.

Gradient spatial nonlinearities can be modeled using the following nonlinear equation:

$$f = \gamma \cdot G_x(x) - f_{off\_res}. \qquad [3]$$

This is simply a generalization of Equation (2).

METHODS

All the measurements were performed on a 9.4T Siemens human whole-body MR scanner (Erlangen, Germany). B_0 monitoring using full B_0 mapping was compared to B_0 monitoring using a field camera. The B_0 fields were generated from shim fields produced by a Resonance Research Inc. 28-channel insert shim (Billerica, MA) that has zero-, second-, third-, and fourth-order spherical harmonics and partial fifth- and sixth-order terms. For this investigation, only the shim terms up to the fourth order were used.

Each of the shim fields were measured using a high-resolution 2D dual-echo (gradient recalled echo (GRE)) B_0 mapping sequence. The reference field maps were acquired on a 170-mm diameter silicon oil spherical phantom with an eight-channel transceiver coil array (22). The sequence parameters were: resolution $= 1.56 \times 1.56\,mm^2$; FOV $= 200 \times 200\,mm^2$; slice thickness $= 3$ mm; slices $= 40$ (distance

Table 1
Shim Terms and Insert Shim Coil Sensitivities

Shim Term	Spherical Harmonic Function	Sensitivity (Hz/cm^n/A)
Z0	1	6058
Z2	z^2-1/2*(x^2+y^2)	6.942
ZX	zx	24.15
ZY	zy	24.15
C2	x^2-y^2	3.64
S2	2xy	3.64
Z3	z(z^2-3/2*(x^2+y^2))	0.4923
Z2X	x(z^2-1/4*(x^2+y^2))	1.0
Z2Y	y(z^2-1/4*(x^2+y^2))	1.0
ZC2	z(x^2-y^2)	1.77
ZS2	2zxy	1.77
C3	x(x^2-3y^2)	0.188
S3	y(3x^2-y^2)	0.188
Z4	z^4-3z^2(x^2+y^2)+3/8*(x^2+y^2)	0.04206
Z3X	zx(z^2-3/4*(x^2+y^2))	0.123
Z3Y	zy(z^2-3/4*(x^2+y^2))	0.123
Z2C2	z(x^2-y^2)(z^2-1/6*(x^2+y^2))	0.093
Z2S2	2z(xy)(z^2-1/6*(x^2+y^2))	0.093
ZC3	x(x^2-3y^2)(z^2-1/8*(x^2+y^2))	0.121
ZS3	x(x^2-3y^2) (z^2-1/8*(x^2+y^2))	0.121
C4	x^4-6x^2y^2+y^4	0.0187
S4	4xy(x^2-y^2)	0.0187

factor = 20%); TR = 1,200 ms; TE = 4.00/4.76 ms; and readout bandwidth = 1,500 Hz/px. B_0 maps were acquired for each of the shim channels of the Resonance Research Inc. insert shim (up to and including the fourth-order terms) by applying a current of 1.0 A. The sensitivities of the shim coils are given in Table 1.

These reference field maps were used as the benchmark B_0 fields and compared to the B_0 fields measured using a field camera. No gradient distortion correction was applied by the scanner in the image reconstruction.

A field camera consisting of 12 ^{1}H field probes was constructed (Fig. 2). The field probes were positioned on three layers at spacings of 56.25 mm. Each layer had four field probes, with equidistant spacings of 82.5 mm between adjacent field probes. To reduce the T_1 relaxation time of the field probes, the field probes were doped with $CuSO_4.5H_2O$ (16). However, due to the higher magnetic field strength, a lower doping concentration was recalculated based on (23) to be 3.0 g/L. The ^{1}H samples were contained inside a 10-mm glass capillary tube with an inner diameter of 0.8 mm. The field probes were encapsulated using doped epoxy to minimize magnetic susceptibility and homogenize the field within the field probe (24). The field probe samples were tilted at 45 degrees relative to the B_0 direction, which decreases the SNR. However, the SNRs of the field probes were sufficiently high (1,200–4,200) for the 12 probes of the field camera. The SNR was taken as the maximum amplitude of the water signal over the SD of the noise region. The field probes were also decoupled with cable traps tuned to the proton Larmor frequency (Fig. 2). An in-house splitter and transceiver chain were used to acquire the FIDs of the field probes using the MR scanner. A FID pulse sequence with the following parameters was used to acquire the FIDs: rectangular pulse excitation with 0.5 ms duration, 5 V; sampling rate = 100 kHz; vector size = 2,048; TR = 25 ms.

Before using the field camera to measure the B_0 fields of the insert shim, different position calibration methods were investigated to improve the position estimates of the field probes of the field camera.

Position Calibration

The actual positions of the field probes of the field camera with respect to each other needed to be measured for the position calibration study. However, the epoxy encapsulation of the field probes made the accurate measuring of the actual positions of the field probes difficult. To locate the actual positions of the field probes within the epoxy molds, a CT scan of the field camera was acquired. A CT scanner was chosen to circumvent the image distortions of the MR modality (due to the gradient nonlinearities or B_0 inhomogeneity). The resolution of the scan was: [1, 1, 0.6386] mm in the respective x-, *y*-, and z-directions.

The positions were marked and calculated from the CT scan and were then used as the reference positions. These positions could then be compared to the positions estimated using the MRI scanner.

Three different methods were used to estimate the positions of the field probes using the MRI scanner. The first method (denoted as *lin*) uses Equation [2] and assumes that the gradient fields are spatially linear (16,17). The second method (denoted as *nonlin*) considers the gradient field spatial nonlinearities by using Equation [3] for each field probe of the field camera. The last method uses the gradient nonlinearities in combination with the CT scan positions. Thus, the positions of all the field probes are optimized simultaneously by incorporating relative position constraints obtained from the CT scan positions. This method is denoted as *connonlin* (constrained nonlinear estimation).

For the nonlinear methods that use Equation [3], the $G_r(r)$ for $r \in [x, y, z]$ needs to be known for each gradient

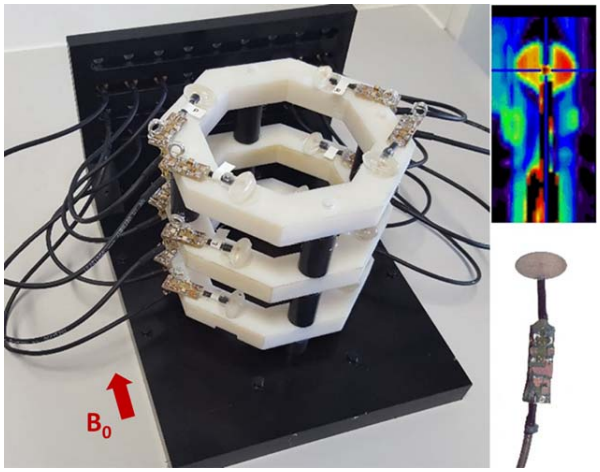

FIG. 2. The field camera (left) consists of 12 field probes (bottom-right). The direction of the B_0 field is also indicated. The CT scan of the field probe (top-right) shows that the sample within the epoxy mold can be easily identified.

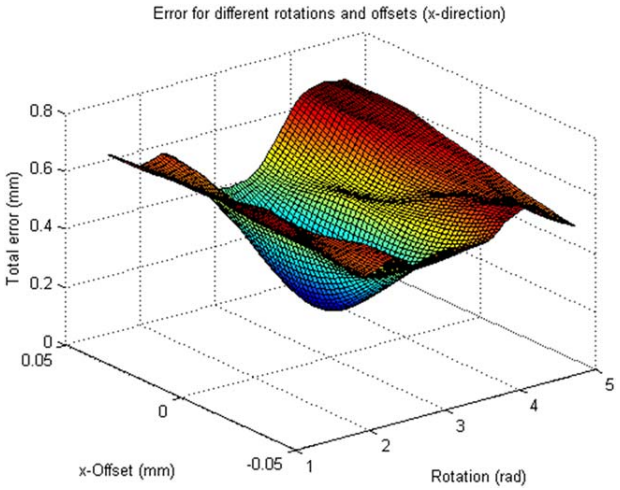

FIG. 3. The objective function for the position optimization for two of the parameters (*x*-position and θ-rotation). The objective function is the norm of the difference between the measured and predicted frequencies calculated from the gradient field models.

direction. Once we have a model for $\boldsymbol{G}(\boldsymbol{r}) = [G_x(\boldsymbol{r}), G_y(\boldsymbol{r}), G_z(\boldsymbol{r})]$, the frequencies measured at any position r can be estimated using Equation [2]. Therefore, we can find the optimal position (in the linear least squares sense) by solving the following minimization problem:

$$\min_{\boldsymbol{r}} ||\boldsymbol{f}_{\boldsymbol{meas}} - \gamma \boldsymbol{G}(\boldsymbol{r})||^2. \quad [4]$$

In this equation, $\boldsymbol{G}(\boldsymbol{r})$ is the spatial model of the gradient fields and $\boldsymbol{f}_{\boldsymbol{meas}}$ are the frequencies measured for each corresponding gradient. To acquire the spatial model $\boldsymbol{G}(\boldsymbol{r})$, the gradient fields needed to be measured in a manner that is independent of the MR scanner to avoid biased estimates in the MR hardware and image reconstruction. Therefore, gradient fields were measured by using a single field probe and moving it to different positions on a fixed 3D grid. The dimensions of the sampling grid were $9 \times 4 \times 9$ (in the *x*–*y*–*z* dimensions), with a spacing of $32 \times 30 \times 32$ mm between each sample. The frequencies (and thus magnetic field strength) at each of these positions were measured for each of the gradients. These data were then used to model the nonlinearities of the gradient fields by decomposing them using up to fourth-order spherical harmonic functions:

$$\boldsymbol{G}(\boldsymbol{r}) = \sum_{l=0}^{N} \sum_{m=-l}^{l} k_l^m S_l^m(\boldsymbol{r}), \quad [5]$$

where k_l^m is the coefficient corresponding to the spherical harmonic function S_l^m, and where N is the maximum order of the decomposition; l is the degree; and m is the order. Note, that if the gradients are perfectly linear, this reduces to $\boldsymbol{G}(\boldsymbol{r}) = \boldsymbol{G} \cdot \boldsymbol{r}$, which is the same as Equation [2].

A Newton optimization algorithm can be used to calculate the position of a single field probe. This algorithm is known for its quadratic convergence rate but is usually problematic because the Hessian matrix needs to be calculated at every step, and also because it does not always converge if a poor starting point is chosen. In this case, these are not significant problems because the function $\boldsymbol{G}(\boldsymbol{r})$ is a sum of polynomials (Eq. [5]) and thus the Hessian is relatively easy to calculate from the Jacobian. Additionally, if the starting point is chosen by assuming perfectly linear gradient fields, this should be a relatively good approximation of the optimal point, and thus initializing the starting point should not be a problem. This means that an optimization method with quadratic convergence speed can be used and the algorithm was found to typically converge in one step; the threshold for convergence was 1e-6. The *nonlin* method thus used this algorithm to calculate the positions for each of the field probes. The calculations for the Jacobian and Hessian are given in more detail in the Appendix (available online).

For the *connonlin* method, the positions of the field probes are fixed (relative to each other) and can thus be considered a rigid body. Therefore, only three translation and three rotation parameters $\tau = [x, y, z, \theta, \varphi, \rho]$ need to be

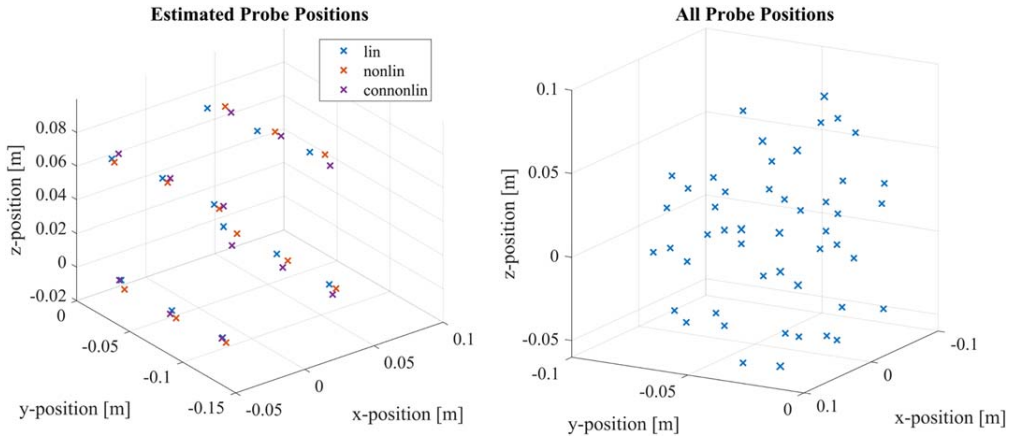

FIG. 4. The positions of the field probes (for one position of the field camera) using each of the three-position optimization methods (left). The differences are quite significant and can sometimes be more than 10 mm. All the field probe positions resulting from several field camera positions, limited to a 100-mm radius from the isocentre, are also shown (right).

found to find the optimal positions of all the field probes. The optimization problem from Equation (3) then becomes:

$$\min_{\tau=[x,y,z,\theta,\varphi,\rho]} \sum_{p=1}^{N_p} ||\boldsymbol{f}_{\boldsymbol{meas}} - \gamma \boldsymbol{G}(\boldsymbol{r}(\boldsymbol{\tau}))||^2. \quad [6]$$

As an example, Figure 3 shows the optimization objective function for two of the parameters (*x*-coordinate and θ-rotation). The optimization was performed with a Newton optimization algorithm (implemented in C++) using the Jacobian and Hessian matrices with respect to the variable $\boldsymbol{\tau}$ (details are given in the Appendix, available online). The initial position and rotation parameters were calculated by using the *lin* method and registering the estimated positions to the relative positions of the field camera acquired from the CT scan.

B_0 Mapping Validation

As previously mentioned, field cameras use spherical harmonic decomposition to describe B_0 fields. Therefore, the number of measured sample points need to be greater than (or equal to) the number of spherical harmonic coefficients. Also, the sample positions are also important and need to be sufficiently well distributed for the matrix S in Equation [5] to be well conditioned (25). Because we used shim terms up to and including fourth-order spherical harmonics, each shim field was decomposed using up to fourth-order spherical harmonic functions. This resulted in a total of 25 coefficients that needed to be determined for each shim field. To acquire enough points, the field camera was placed in eight different positions to measure the shim fields. Eight positions and 12 field probes on the field camera gave 96 sample points of each shim field. However, all points outside of a 100-mm radius (from the isocenter) were discarded to be consistent with the FOV of the B_0 mapping.

A current of 1.0 A was applied to each of the shim channels for the measurements. Note, that when measuring the shim fields, the shim channels were switched on for several seconds (at least 5 s) before acquiring the FIDs using the field camera. This was to allow most eddy currents to settle before acquisition.

The field camera was calibrated using three different position estimation methods (*lin, nonlin*, and *connonlin*), and thus each calibration gave a different set of spherical harmonics coefficients. We determined which set of coefficients was more accurate by comparing them to the reference shim maps (acquired using a full B_0 mapping sequence). To compare these fields to the reference maps, the coefficients were used to reconstruct the field on a $200 \times 200 \times 200\,\text{mm}^3$ FOV. The errors between these reconstructed fields and the reference maps were compared using the SDs, as well as the Pearson product moment to compare the similarity between the reconstructed fields (26). The Pearson product-moment coefficient is defined as:

$$\rho_{X,Y} = \frac{cov(X, Y)}{\sigma_X \sigma_Y}. \quad [7]$$

This coefficient is a measure of the similarity between the two signals, which results in a value between −1 and 1, for which 1 indicates that the signals are identical and 0 indicates that there is no correlation between the signals.

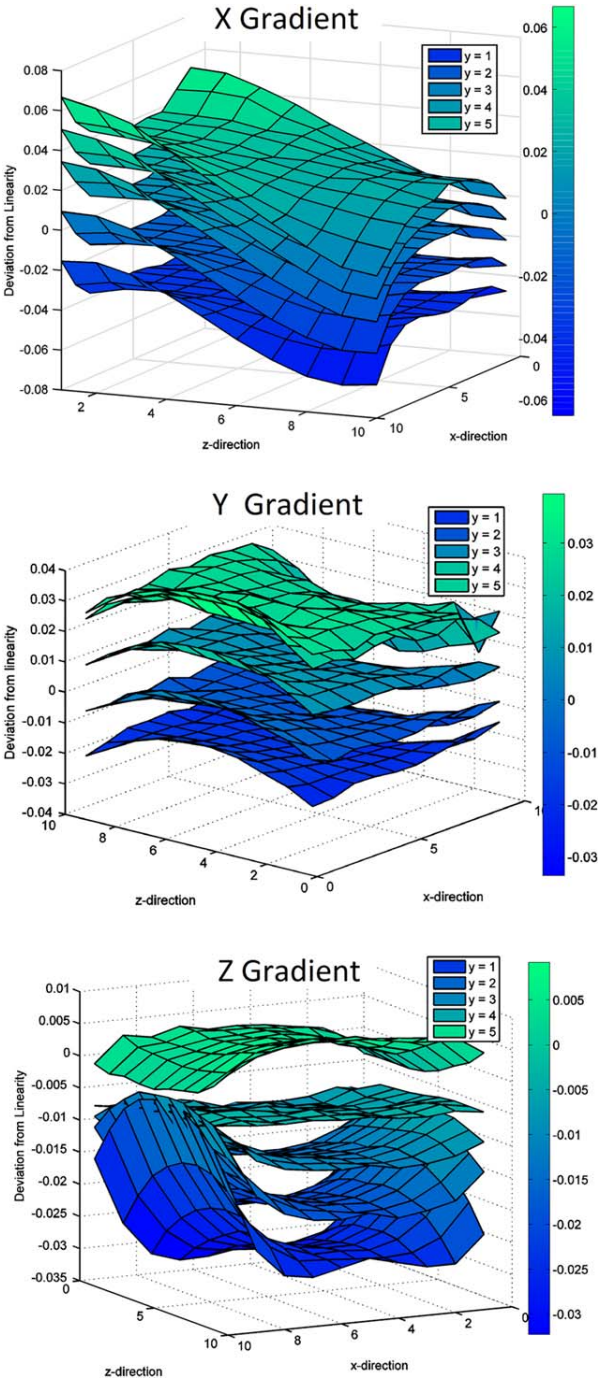

FIG. 5. The normalized gradient field deviation for 1 mT/m from spatial linearity are shown for five slices (y = 1…5), that is, if the gradient fields were perfectly linear, then each plane would be flat. The deviations are shown in percentage (of the gradient field strength).

Any error between the reconstructed and reference maps is a combination of the error in the position estimation and the error due to downsampling the B_0 field by acquiring only a few sample points with the field camera. We isolated and investigated the effect of downsampling by decomposing the fully sampled reference

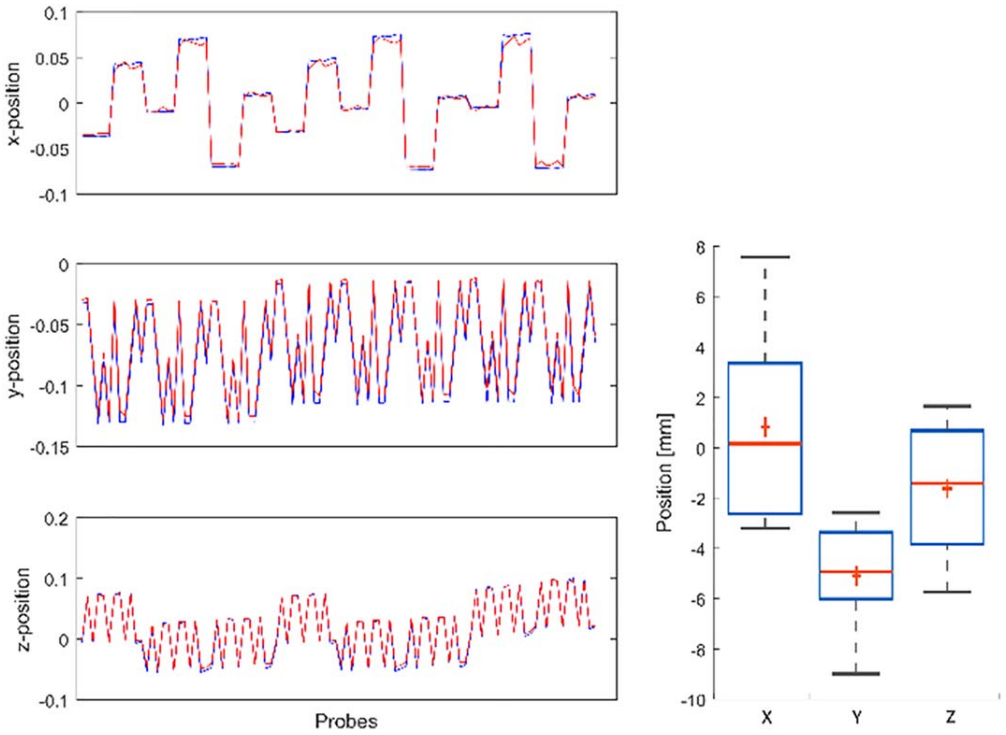

FIG. 6. (Left) The normalized gradient field frequencies for 1 mT/m for 96 field probes (blue) are compared to the frequencies measured from the reference field map using a B_0 mapping sequence (red). The figure shows good agreement between the two measuring techniques. (Right) The normalized mean differences between the frequencies shown on the left.

maps using only the sample points given by the constrained field camera positions. This is theoretically the most accurate B_0 field that we can acquire using a field camera (with the same number of sample points).

These decomposition coefficients were then compared to the original reference maps. Any resulting error is thus only due to downsampling.

Simulations

We performed simulations to investigate the possible factors causing differences between the position calibration methods. The simulations were performed as follows:

1. The field probe positions measured from CT scanner were used as the actual positions.
2. The frequencies at these positions for the *x*-, *y*-, and *z*-gradients were simulated using the fourth-order gradient models.
3. These frequencies were used to calculate the positions using the *lin, nonlin*, and *connonlin* methods.
4. The positions were used to decompose:
    a. The ideal theoretical shim fields; and
    b. The ideal theoretical shim fields with added random white Gaussian noise.
5. The decomposed models were then compared by reconstructing the field on a $100 \times 100 \times 100\,\text{mm}^3$ FOV (as described above).

A range of noise levels were simulated: 0.5%, 1%, 2%, and 5% of the shim coil strength.

RESULTS

Position Calibration

The positions of the field probes measured using the CT scanner can be seen in Figure 4 (see *connonlin*; this method uses the CT scanner data). The deviation of the distance between the *connonlin* and the *nonlin* is on average 5.0 ± 1.4 mm, with a maximum error of 7.0 mm. Similarly, the deviation of the distance between the *connonlin* and the *lin* method is on average 8.8 ± 4.0 mm, with a maximum error of 14.5 mm. As a reminder, the *lin* is the current method (in the literature) used to calculate the positions of the field probes, where the gradient fields are assumed to be spatially linear.

As mentioned earlier, the field camera was moved to multiple positions for the measurements to increase the number of spatial points (an effective total of 49 field probes). The distribution of the field probe positions calculated using the *connonlin* method are shown in Figure 4.

These positions were estimated based on measured gradient fields. The gradient field measurements showed that the fields were spatially relatively linear. The deviations from the ideal linear case are shown in Figure 5 (i.e., if the fields were perfectly linear, then each plane in the figure would be flat). The figure shows that there are still slight deviations from linearity. These gradient field measurements were modeled using up to fourth-order spherical harmonic coefficients. It was previously shown that the accuracy of the model saturates after approximately the sixth or seventh order (27). We thus further compared modeling the gradient fields using

sixth- and fourth-order decomposition. The Pearson product-moment coefficients were 0.9912, 0.9968, and 0.9945 for the *x*-, *y*-, and *z*-gradient fields, respectively (comparing fields reconstructed on a $200 \times 200 \times 200$ mm FOV). Because the coefficients were very close to 1.0, this showed that the difference between the fourth-order and sixth-order models was insignificant.

B_0 Mapping Validation

Firstly, we compared the field probe measurements to the B_0 mapping measurements of the gradient fields. Figure 6 shows the normalized frequencies of the gradient field reference maps compared to the field probes. The figure shows that, for the gradient fields, the frequencies measured from the field camera are very similar to the frequencies of the reference maps (acquired from the B_0 mapping sequence). Figure 6 shows that the mean error between the frequencies was 0.0008 mT/m, −0.0051 mT/m, and −0.0016 mT/m for the *x*-, *y*- and *z*-gradients, respectively (with gradient strength 1 mT/m). For spatially linear gradients, this translates into a position error of 0.8 mm, −5.1 mm, and −1.6 mm in the *x*-, *y*- and *z*-directions, respectively. Note that the slightly higher position error in the *y*-direction may be due to the distribution of the field probes covering mostly only the lower *y*-positions (with respect to the isocenter) (Fig. 6). If the field probes were more centered in the *y*-direction, then this error would most likely reduce (because gradients are more nonlinear further from the isocenter). The Pearson product-moment coefficients were 0.9990, 0.9968, and 0.9945 for the *x*-, *y*-, and *z*-gradients, respectively. This metric indicates that the modeled-and-measured gradient fields were very similar.

After the gradient fields, we analyzed the shim fields of the insert shim. The reconstructed maps (using the field probes) were compared to the reference shim field maps (acquired using a B_0 mapping sequence). A comparison of the reconstructed fields is shown in Figure 7 (only second-order terms are shown for illustration purposes). The fields were reconstructed for the B_0 mapping and for the field-probe measurements with two different field-camera calibrations, using the linear estimation and the constrained optimization method.

The root-mean-squared error (RMSE) for each shim field was calculated, and respective results are shown in Figure 8a. There was no single position calibration method that was the most accurate for every shim field. However, the *connonlin* method gave more consistent results. For example, shim terms ZX and Z3 were poorly estimated using the *lin* and *nonlin* methods, whereas the *connonlin* method was able to drastically improve the accuracy of measuring the B_0 map. However, the *nonlin* method gave slightly better accuracy than the *lin* method for most shim fields. Therefore, if the relative positions of the probes are unknown, using the gradient fields for estimating the positions still improves the accuracy of the position estimates.

Also shown on Figure 8a is the RMSE between the reference map and the downsampled reference map. As mentioned in the previous section, the reference map was spatially downsampled using the field probe positions. This value indicates the intrinsic error of spatial downsampling; in other words, this would be the error if the position calibration was perfect. The ZX, Z3, Z4, and ZC3 shim fields deviate the most and the largest improvements from the *connonlin* method is seen for the ZX, Z3, ZC2, ZS2, and ZC3 terms.

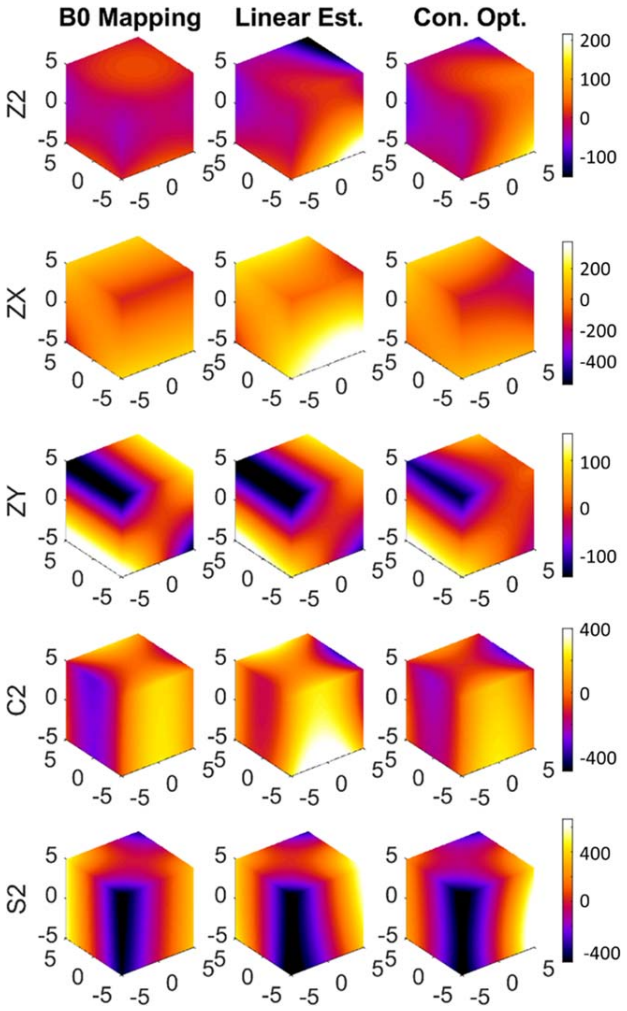

FIG. 7. Shim fields for the second-order terms measured using B_0 mapping (original reference maps) and measured using the field camera (with linear estimation and constrained optimization for position calibration). The fields are shown in Hz (for 1.0 A).

The RMSE for each shim field was also calculated for the simulated results without noise (Fig. 8b). The level of error of only downsampling is similar to the measured data. As expected, the *connonlin* method reaches the same level of error as the downsampling case.

Simulations

Figure 9 shows the simulated fields (resulting only from downsampling) with different levels of noise: 0.5%, 1%, 2%, and 5%. The trend of the deviations between the theoretical fields and the reconstructed fields from simulations is similar to the deviations in the measured data in Figure 8a.

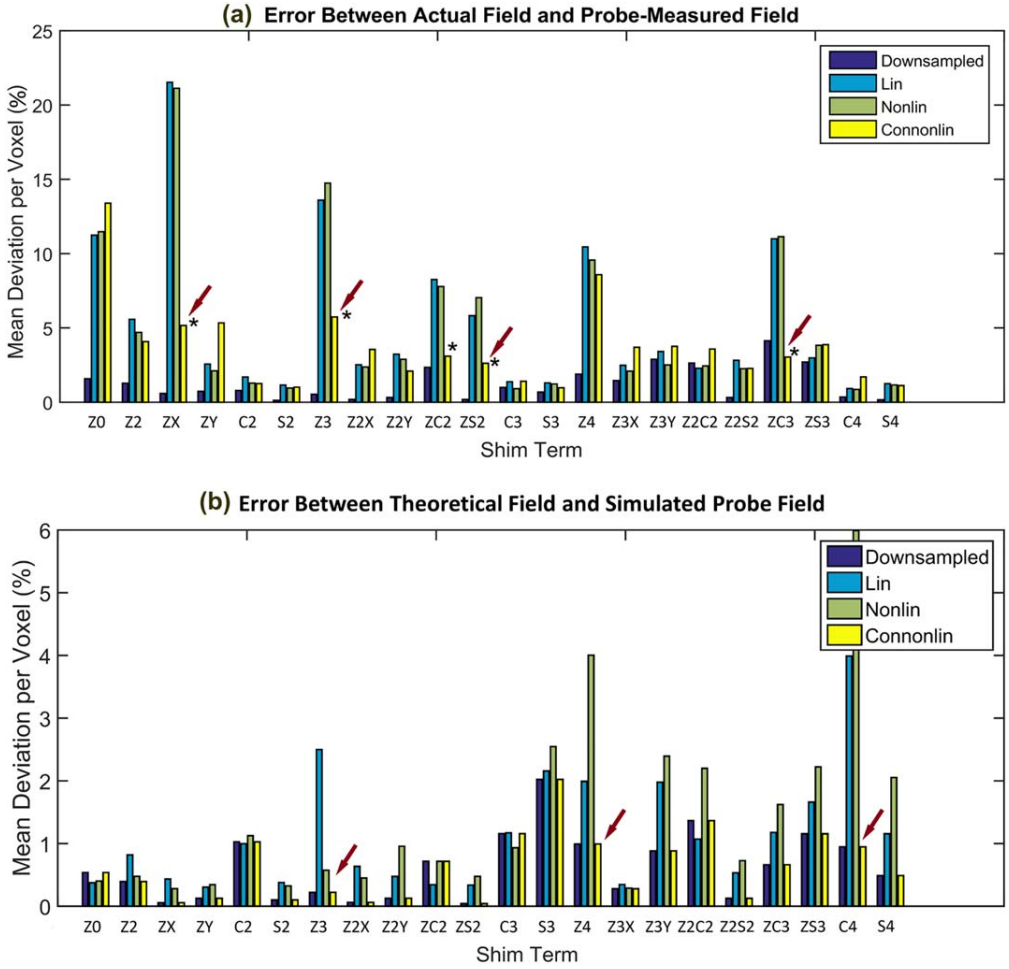

FIG. 8. Mean deviation between the reference shim field maps and the field probes measurements (top). The significant improvements of the *connonlin* method are shown (*). Also shown are the RMSEs of the theoretical fields and the simulated fields from the field probes calculated from simulations (bottom). In both cases, although the *connonlin* position optimization does not always perform better, it is more consistent and can improve the accuracy of most B_0 fields. RMSE, root-mean-square error.

DISCUSSION

Position Calibration

Three different calibration methods for calculating the positions of the field probes in a field camera were investigated. In the current literature, only the linear estimation has previously been used. However, our investigation showed that this is not sufficient for accurate B_0 monitoring. Instead, a constrained nonlinear optimization should be used. This requires that the relative field probe positions be measured (which we did using a CT scan), and also requires that the gradient field

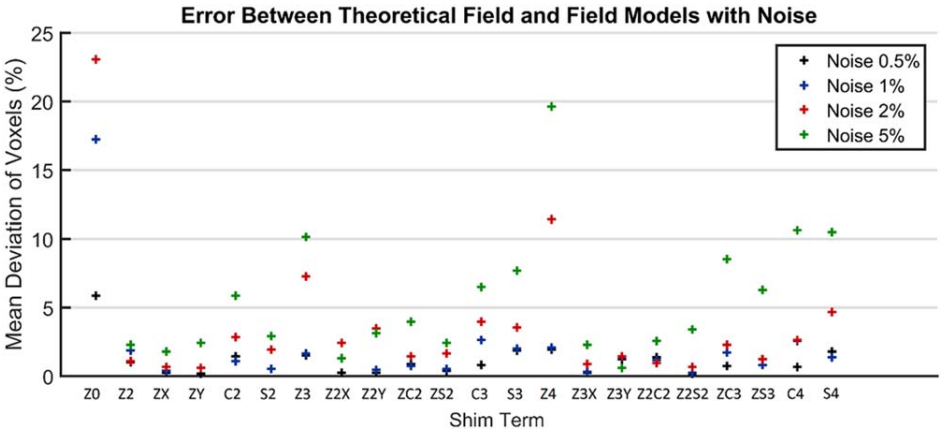

FIG. 9. Mean deviation between the theoretical shim fields and the downsampled field probe fields calculated from simulations. Different levels of noise were applied to the simulated shim fields, and the reconstructed fields were compared. The trend of the deviations is similar to the results from the measured field probe data.

nonlinearities be measured and modeled. The *connonlin* method gave the best consistency of monitoring the B_0 field.

As shown previously in the results section, the gradient fields could be sufficiently modeled using a fourth-order decomposition. Increasing the modeling order to six resulted in very similar coefficients. This is because the gradient fields only have small imperfections. Another limiting factor on spherical harmonic decomposition is the fact that it inherently is radially symmetric, which means that local asymmetric inhomogeneities of the field cannot be properly modeled. The caveat is that, as we have seen, small differences in the field probe positions result in the B_0 field models differing significantly. Therefore, the position of the field probes should be determined as accurately as possible. To overcome slight modeling errors in the gradient fields, a constrained position calibration optimization is recommended.

Intuitively, the constrained optimization should yield the most accurate result because it considers the fixed positions of the field probes and also considers the gradient nonlinearities. The results of the position calibration of the 12-probe field camera showed that consideration of the gradient field nonlinearities significantly affected the estimated positions of the field probes; that is, the difference could be more than 10.0 mm, which in turn will affect the spherical harmonic decomposition. Furthermore, the *nonlin* optimization showed very similar results to the *connonlin* optimization for the gradient fields, indicating that the gradient fields were relatively well modeled in this region and that the two methods are in agreement. Although this implied that the *nonlin* optimization could be used for position calibration, the *connonlin* approach was still used because it was more robust in measuring the B_0 fields.

B_0 Mapping Validation

The reference shim field maps were used as the benchmark fields because the spatial resolution that can be achieved by using the mapping sequence is much greater and thus gives more spatial fidelity. Although the mapping sequence is susceptible to imaging artifacts induced by, for example, gradient nonlinearities and geometric distortion, the artifacts should be minimal because the phantom's spatial coverage was within the gradient fields' linear range and the high readout bandwidth minimized the geometric distortion (27). However, it should be noted that the magnetic susceptibility of the material used for the B_0 mapping setup and the field camera setup were different and could thus result in slight inconsistencies between the two methods.

The results show that the low spatial sampling of the field camera (compared to the B_0 mapping sequence) is an important factor in the accuracy of the field model. Even when the positions of the field probes are perfectly calibrated, the field model still deviates significantly from the mapping sequence model. This is shown by the error of the downsampled field (Fig. 7). There are two contributing factors for the error between the downsampled field and the field maps: 1) the lower spatial resolution, and 2) the field models were calculated using up to fourth-order spherical harmonic terms. Therefore, the higher spatial frequency information (and field imperfections) cannot be accurately modeled with fourth-order terms. This is also consistent with the level of error shown in the simulations compared to the measured data (Fig. 8). It was also shown in (27) that there is a significant loss of accuracy when the fields are modeled using up to fourth-order terms instead of using up to sixth-order terms. Andersen et al. (25) also found that using 16 field probes is not sufficient to model the field using up to third-order decomposition.

The field comparison was performed by reconstructing the fields from the spherical harmonic coefficients and comparing the difference between them. The field coefficients were not directly used as a comparison because they are difficult to interpret. Firstly, the coefficients depend on the units of measurement that they are decomposed with. For example, decomposing using meters will result in the coefficients increasing exponentially with the order of the spherical harmonic function, whereas decomposing using centimeters results in the coefficients an exponential decrease with the order. This makes it difficult to compare B_0 fields using only coefficients due to the different orders of magnitudes of the coefficients. Secondly, coefficients are difficult to compare because two similar fields can have widely varying coefficients, especially if the measurements are noisy. Thus, the fields were reconstructed from the coefficients to better perform the comparison of the models.

The results showed that comparing the RMSE between the models (in Hz) using the *connonlin* optimization was the most similar to the downsampled model from the mapping sequence. The remaining difference between the downsampled model and *connonlin* model can be explained by the noise in the B_0 maps or field-probe measurements (because the signals dephase in strong applied fields). The models acquired from the field camera are sensitive to noise due to the low number of spatial sample points. The noise level is similar to the simulated noise levels for approximately 1% to 2% noise. This noise can be result from measurement noise or any inconsistencies between the B_0 mapping setup with the phantom and the field camera setup. A limitation of this study is that the magnetic susceptibility effects of the field camera mount material were not matched to the field probe. Therefore, the measured magnetic fields could deviate between the two setups. Although for position calibration purposes this would be minimized because of the relative position constraints, the effect of the magnetic susceptibility could explain the residual inconsistencies between the two field measurement methods.

The difference between the RMSEs showed that the linear optimization of the position calibration can lead to significant errors in the modeled B_0 fields. Although using *connonlin* optimization can reduce the errors, for some shim channels they could not be reduced any further.

CONCLUSION

In this study, we compared position calibration methods for the field probes. We introduced a method that used information about the gradient field spatial nonlinearities

and relative field probe positions to estimate the probe positions.

Furthermore, we compared the spatial fidelity of the field camera to B_0 mapping sequences. We showed that a limited number of field probes (thus reduced number of sample points) resulted in a loss of spatial accuracy. Furthermore, a constrained optimization calibration yielded the best results for the shim fields. However, for some shim fields, all calibration methods performed similarly.

The low spatial sampling of the field camera results in an unavoidable loss of spatial accuracy. The linear position calibration method that is currently used is more inaccurate than a constrained optimization method that uses prior knowledge about gradient nonlinearities and relative field probe positions. A more accurate probe position estimate means that field monitoring will be more accurate, especially for higherorder terms. Therefore, B_0 shimming with the field camera will be more accurate.

APPENDIX

The Jacobian and Hessian for the optimisation functions from Equations [4] and [5] can be calculated as follows. For the cost function:

$$\boldsymbol{F} = ||\boldsymbol{K}(\boldsymbol{r}) - \boldsymbol{f}_{\boldsymbol{meas}}||2$$

where $\boldsymbol{K}(\boldsymbol{r})$ is defined as $\gamma\boldsymbol{G}(\boldsymbol{r})$, and $\boldsymbol{G}(\boldsymbol{r})$ is defined by Equation [5], the Jacobian is:

$$\nabla\boldsymbol{F} = (\boldsymbol{K}(\boldsymbol{r}) - \boldsymbol{f}_{\boldsymbol{meas}})^T \cdot \nabla\boldsymbol{K}(\boldsymbol{r})$$

and the Hessian is:

$$\nabla^2\boldsymbol{F} = \nabla\boldsymbol{K}(\boldsymbol{r})^T \cdot \nabla\boldsymbol{K}(\boldsymbol{r}) + (\boldsymbol{K}(\boldsymbol{r}) - \boldsymbol{f}_{\boldsymbol{meas}})^T \cdot \nabla^2\boldsymbol{K}(\boldsymbol{r})$$

Since $\boldsymbol{K}(\boldsymbol{r})$ is a linear combination of Legendre polynomials (Eq. [5]), the partial derivatives are given by:

$$\begin{aligned}
\frac{\partial \boldsymbol{K}}{\partial x} &= k_1^1 S_0^0 + k_2^1 S_1^0 + \left(2k_2^2 - k_2^0\right) S_1^1 + k_2^{-2} S_1^{-1} + k_3^1 S_2^0 \\
&\quad + \left(2k_3^2 - 3k_3^0\right) S_2^1 + k_3^{-2} S_2^{-1} + \left(3k_3^3 - \frac{1}{4}k_3^1\right) S_2^2 \\
&\quad + \left(6k_3^{-3} - \frac{1}{2}k_3^{-1}\right) S_2^{-2} + k_4^1 S_3^0 + \left(2k_4^2 - 6k_4^0\right) S_3^1 \\
&\quad + k_4^{-2} S_3^{-1} + \left(3k_4^3 - \frac{3}{4}k_4^1\right) S_3^2 + \left(6k_4^{-3} - \frac{3}{2}k_4^{-1}\right) S_3^{-2} \\
&\quad + \left(4k_4^4 - \frac{1}{6}k_4^2\right) S_3^3 + \left(k_4^{-4} - \frac{1}{12}k_4^{-2}\right) S_3^{-3} \\
\frac{\partial \boldsymbol{K}}{\partial y} &= k_1^{-1} S_0^0 + k_2^{-1} S_1^0 + k_2^{-2} S_1^1 + \left(-2k_2^2 - k_2^0\right) S_1^{-1} + k_3^{-1} S_2^0 \\
&\quad + k_3^{-2} S_2^1 + \left(-2k_3^2 - 3k_3^0\right) S_2^{-1} + \left(3k_3^{-3} - \frac{1}{4}k_3^{-1}\right) S_2^2 \\
&\quad + \left(-6k_3^3 - \frac{1}{2}k_3^1\right) S_2^{-2} + k_4^{-1} S_3^0 + k_4^{-2} S_3^1 \\
&\quad + \left(-2k_4^2 - 6k_4^0\right) S_3^{-1} + \left(3k_4^{-3} - \frac{3}{4}k_4^{-1}\right) S_3^2 \\
&\quad + \left(-6k_4^3 - \frac{3}{2}k_4^1\right) S_3^{-2} + \left(k_4^{-4} + \frac{1}{12}k_4^{-2}\right) S_3^3 \\
&\quad + \left(-4k_4^4 - \frac{1}{6}k_4^2\right) S_3^{-3} \\
\frac{\partial \boldsymbol{K}}{\partial z} &= k_1^0 S_1^0 + 2k_2^0 S_1^0 + k_2^1 S_1^1 + k_2^{-1} S_1^{-1} + 3k_3^0 S_2^0 + 2k_3^1 S_2^1 \\
&\quad + 2k_3^{-1} S_2^{-1} + k_3^2 S_2^2 + k_3^{-2} S_2^{-2} + 4k_4^0 S_3^0 + 3k_4^1 S_3^1 \\
&\quad + 3k_4^{-1} S_3^{-1} + 2k_4^2 S_3^2 + 2k_4^{-2} S_3^{-2} + k_4^3 S_3^3 + k_4^{-3} S_3^{-3}
\end{aligned}$$

If there are multiple positions $\boldsymbol{r}_1, \ldots, \boldsymbol{r}_n$ and the positions are constrained relative to each other (as in the case of the constrained optimisation), then the positions can be a function of a rigid transformation (a rotation and a translation) defined by parameters $\boldsymbol{\tau} = [x_0, y_0, z_0, \theta, \varphi, \rho]$:

$$\boldsymbol{r_i} = \begin{bmatrix} \cos\varphi\cos\rho & \cos\rho\sin\theta\sin\varphi - \cos\theta\sin\rho & \cos\theta\cos\rho\sin\varphi \\ \cos\varphi\sin\rho & \cos\theta\cos\rho + \sin\theta\sin\varphi\sin\rho & -\cos\rho\sin\theta + \cos\theta\sin\varphi\sin\rho \\ -\sin\varphi & \cos\varphi\sin\theta & \cos\theta\cos\varphi \end{bmatrix} \cdot \boldsymbol{r}_{i,0} + \begin{bmatrix} x_0 \\ y_0 \\ z_0 \end{bmatrix}$$

The function $\nabla\boldsymbol{K}(\boldsymbol{r}(\boldsymbol{\tau}))$ can now be calculated with respect to $\boldsymbol{\tau}$, where $\boldsymbol{r}_{i,0}$ is the initial position of position $\boldsymbol{r_i}$. So the Jacobian (for Eq. [6]) is then:

$$\nabla\boldsymbol{F} = (\boldsymbol{K}(\boldsymbol{r}(\boldsymbol{\tau})) - \boldsymbol{f}_{\boldsymbol{meas}})^T \cdot \nabla\boldsymbol{K}(\boldsymbol{r}(\boldsymbol{\tau})) \cdot \nabla\boldsymbol{r}(\boldsymbol{\tau})$$

and the Hessian can be similarly calculated.

REFERENCES

1. Boesch C, Gruetter R, Martin E. Temporal and spatial analysis of fields generated by eddy currents in superconducting magnets: optimization of corrections and quantitative characterization of magnet/gradient systems. Magn Reson Med 1991;20:268–284.
2. Papadakis NG, Martin KM, Pickard JD, Hall LD, Carpenter TA, Huang CL, Gradient preemphasis calibration in diffusion-weighted echo-planar imaging. Magn Reson Med 2000;44:616–624.
3. Fillmer A, Vannesjo SJ, Pavan M, Scheidegger M, Pruessmann KP, Henning A. Fast iterative pre-emphasis calibration method enabling third-order dynamic shim updated fMRI. Magn Reson Med 2016;75:1119–1131.
4. Boer VO, van Vliet G, Luijten PR, Klomp DW. Direct B0 field monitoring and real-time B0 field updating in the human breast at 7 Tesla. Magn Reson Med 2012;67:586–591.
5. Keating B, Ernst T. Real-time dynamic frequency and shim correction for single-voxel magnetic resonance spectroscopy. Magn Reson Med 2012;68:339–1345.
6. Hess AT, Tisdall MD, Andronesi OC, Meintjes EM, van der Kouwe AW. Real-time motion and B0 corrected single voxel spectroscopy using volumetric navigators. Magn Reson Med 2011;66:314–323.
7. Wilm BJ, Duerst Y, Dietrich BE, Wyss M, Vannesjo SJ, Schmid T, Brunner DO, Barmet C, Pruessmann KP. Feedback field control improves linewidths in in vivo magnetic resonance spectroscopy. Magn Reson Med 2014;71:1657–1662.
8. Gruetter R, Boesch C. Fast, noniterative shimming of spatially localized signals. In vivo analysis of the magnetic field along axes. J Magn Reson 1992;96:323–334.
9. Gruetter R. Automatic, localized in vivo adjustment of all first- and second-order shim coils. Magn Reson Med 1993;2:804–811.

10. Shen J, Rycyna RE, Rothman DL. Improvements on an in vivo automatic shimming method (FASTERMAP). Magn Reson Med 1997;38:834–839.
11. Ward HA, Riederer SJ, Jack CR. Real-time autoshimming for echo planar timecourse imaging. Magn Reson Med 2002;48:771–780.
12. Bogner W, Hess AT, Gagoski B, Tisdall MD, van der Kouwe AW, Trattnig S, Rosen B, Andronesi OC. Real-time motion- and B0-correction for LASER-localized spiral-accelerated 3D-MRSI of the brain at 3T. Neuroimage 2014;88:22–31.
13. Saleh MG, Alhamud A, Near J, van der Kouwe AW, Meintjes EM. Volumetric navigated MEGA-SPECIAL for real-time motion and shim corrected GABA editing. NMR Biomed 2016;29:248–255.
14. Barmet C, De Zanche N, Wilm BJ, Pruessmann KP. A transmit/receive system for magnetic field monitoring of in vivo MRI. Magn Reson Med 2009;62:269–276.
15. De Zanche N, Barmet C, Nordmeyer-Massner JA, Pruessmann KP. NMR probes for measuring magnetic fields and field dynamics in MR systems. Magn Reson Med 2008;60:176–186.
16. Barmet C, De Zanche N, Pruessmann KP. Spatiotemporal magnetic field monitoring for MR. Magn Reson Med 2008;60:187–197.
17. Vannesjo SJ, Haeberlin M, Kasper L, Pavan M, Wilm BJ, Barmet C, Pruessmann KP. Gradient system characterization by impulse response measurements with a dynamic field camera. Magn Reson Med 2013;69:583–593.
18. Romeo F, Hoult DI. Magnetic field profiling: analysis and correcting coil design. Magn Reson Med 1984;1:44–65.
19. Ashburner J, Friston KJ. Nonlinear spatial normalization using basis functions. Hum Brain Mapp 1999;7:254–256.
20. MackKenzie IS, Robinson EM, Wells AN, Wood B. A simple field map for shimming. Magn Reson Med 1987;5:262–268.
21. Sipila P, Greding S, Wachutka G, Wiesinger F. 2H transmit–receive NMR probes for magnetic field monitoring in MRI. Magn Reson Med 2011;65:1498–1506.
22. Avdievich NI. Transceiver-phased arrays for human brain studies at 7T. Appl Magn Reson 2011;41:483–506.
23. Tofts PS. Quality assurance, accuracy, precision and phantoms. In: Tofts PS ed. Quantitative MRI of the Brain: Measuring Changes Caused by Disease. Chichester, UK: John Wiley & Sons; 2003.
24. McClurg G. Magnetic field distributions for a sphere and for an ellipsoid. Am J Phys 1956;24:496–499.
25. Andersen M, Hanson LG, Madsen KH, Wezel J, Boer VO, van der Velden T, van Osch MP, Klomp D, Webb AG, Maarten JV. Measuring motion-induced B0-fluctuations in the brain using field probes. Magn Reson Med 2016;75:2020–2030.
26. Juchem C, Muller-Bierl B, Schick F, Logothetis NK, Pfeuffer J. Combined passive and active shimming for in vivo MR spectroscopy at high magnetic fields. J Magn Reson 2006;183:278–289.
27. Chang P, Nassirpour S, Henning A. Modeling real shim fields for very high degree (and order) B0 shimming of the human brain at 9.4T. Magn Reson Med 2017. doi: 10.1002/mrm.26658.

Publication V

"Controller Design for Feedback of B_0 Shim Systems"

P Chang, S Nassirpour, A Henning

[submitted]

Controller Design for Feedback of B_0 Shim Systems

Abstract

Magnetic resonance imaging (MRI) is dependent on a static magnetic B_0 field. This field needs to be as homogeneous as possible because an inhomogeneous B_0 field can result in poor quality data and artifacts. Additional "shim" coils typically used to homogenize the field. However, the need for more sophisticated methods of B_0 shimming is increasing because the inhomogeneity of B_0 increases at higher field strengths.

Although spatial homogeneity of the B_0 field needs to be maintained, in reality disturbances cause temporal fluctuations in the field. One way that the B_0 homogeneity can be improved is using feedback. This would allow the B_0 field to be corrected for temporal fluctuations caused by sources such as eddy currents and physiological disturbances during a scan. Shim systems are large multivariable systems because the number of shim coils define the number of inputs of the system.

In this study, a NMR field camera was used to measure the dynamics of the B_0 shim system at a 9.4T human MRI scanner. Custom-built hardware and software was used to actuate the currents of the shim coils at an update rate of 1ms. For this multivariable system, three different decoupling strategies were investigated: a static decoupling, Vaes optimal static decoupling and dynamic decoupling. Optimal PI controllers were designed for the effective decoupled systems. The performance and robustness of the closed-loop systems were analysed.

We showed a decoupling method for designing a feedback control of a multivariable B_0 shim system. For large multivariable system that are near-diagonal, static decoupling proved to be more robust than dynamic decoupling. Decoupling control and optimal PI controller design were used to demonstrate the potential and limitations of real-time feedback in a B_0 shimming application.

Introduction

Magnetic resonance imaging relies on a main static magnetic B_0 field to acquire signals for imaging and spectroscopy. MRI scanners for humans are moving towards higher magnetic field strengths of 7T and 9.4T. This is driven by a need for higher signal-to-noise ratio (SNR) resulting in higher resolution imaging in a shorter time. As the strength of the B_0 field increases, the field becomes more inhomogeneous [1, 2]. As a result, the problem of B_0 homogeneity is becoming a greater concern for the ultra-high field MRI community since an inhomogeneous B_0 field can compromise data quality and introduce multiple artifacts into the images such as image distortions and signal dropout [3, 4].

The magnetic field homogeneity is usually maintained using an extra set of "shim" coils that drive DC currents to generate magnetic fields that correct for inhomogeneities. However, the switching of strong gradient fields can couple with these coil elements and generate eddy currents that result in artifacts [5, 6, 7]. Furthermore, for dynamic slice-wise B_0 shimming, switching shim currents can also cross-couple and generate eddy currents [8, 9]. To compensate for eddy currents, the B_0 shim coils can be dynamically decoupled using pre-emphasis in an open-loop setup. Pre-emphasis is typically done for the gradient coils [10, 11]. However, pre-emphasis of shim coils has only been done in recent years [8, 9, 12]. This has been performed on spherical harmonic systems using a multiple-input multiple-output (MIMO) model and designing a filter based on the inverse of the model [12].

However, a feedback (or closed-loop) system is useful for maintaining a constantly homogeneous B_0 field since the magnetic field is susceptible to fluctuations during a MRI scan [13]. Any unmodeled disturbance such as physiological disturbances from breathing and motion or drift of the magnet and thermal changes of the equipment can be prospectively corrected for using feedback. For physiological fluctuations of the B_0 field, closed-loop control has been used to keep the magnetic field homogeneous [14, 13]. In [13], a feedback system was used to correct for slow-varying fluctuations using single-input single-output (SISO) proportional-integral-derivative (PID) controllers which were tuned with the Ziegler-Nichols method. This method, while still used in industry, is outdated and is well-known to have

problems with robustness [15]. The update rate in [13] was 100 ms which is sufficient for slow-varying fluctuations but cannot correct for faster variations such as eddy current effects, for example, for fast-changing gradient currents in fast sequences. Even though for slow update rates, using pre-emphasis and SISO PID controllers is sufficient, if the update rates are faster than the spatiotemporal dynamics of the shim system, alternative methods for controller design need to be investigated. So far, a controller design strategy for real-time feedback of shim systems for fast sampling times has not been shown.

Furthermore, in the case of [13], cross-coupling interactions between higher order shim coils were not considered. Different approaches can be used for this purpose. Dynamic decoupling (or pre-emphasis [9, 12]) can decouple the system over a larger range of frequencies, however, this requires an accurate model of the system and is difficult to implement. Static decoupling is much easier to implement but only decouples the system for a small frequency range.

In this work, we measure the dynamics of a shim system using B_0 mapping and a field camera for comparison and then use these measurements to model the system using a parametric model. This model is then used to show the feasibility of designing a pre-emphasis MIMO filter (as previously done in [12]). We then also show, for the first time in B_0 shimming, a design for a closed-loop feedback controller that can help correct for slow time-varying changes (eddy currents and physiological fluctuations) and faster transient dynamics of the system. We also introduce metrics for analyzing control systems in the context of B_0 shimming.

Theory

Linear Time-invariant Control Systems

Linear time-invariant (LTI) systems can be fully characterized by their impulse response function as described in [16, 17, 18]. Therefore, a LTI system can be represented as a transfer function, which means that any nth-order ordinary differential equation:

$$a_n\left(\frac{d}{dt}\right)^n \cdot y(t) + \cdots + a_1\frac{d}{dt}\cdot y(t) + a_0 \cdot y(t) = b_m\left(\frac{d}{dt}\right)^m \cdot u(t) + \cdots + b_1\frac{d}{dt}\cdot u(t) + b_0 \cdot u(t) \quad (1)$$

Can be written as:

$$\begin{gathered} a_n s^n Y(s) + \cdots + a_1 sY(s) + a_0 Y(s) = b_m s^m U(s) + \cdots + b_1 sU(s) + b_0 U(s) \\ (a_n s^n + \cdots + a_1 s + a_0)\cdot Y(s) = (b_m s^m + \cdots + b_1 s + b_0)\cdot U(s) \\ G(s) = \frac{Y(s)}{U(s)} = \frac{b_m s^m + \cdots + b_1 s + b_0}{a_n s^n + \cdots + a_1 s + a_0} \end{gathered} \quad (2)$$

Where u(t) and y(t) are the input and output signal of the system, respectively; U(s) and Y(s) are the Laplace transforms of the corresponding signals and zero initial conditions are assumed. It should also be noted that *s* is complex and the equivalent, more commonly used frequency domain transfer function [16, 12] is obtained by setting the real part to zero, that is: $s = j\omega$. Hence, $G(s)$ is the impulse response function of the system in the Laplace domain (also known as the s-domain).

The system $G(s)$ can be corrected for by simply using a filter $K(s)$ in series with the system, where $K(s) \approx G^{-1}(s)$. For all physical processes, the system $G(s)$ is strictly proper, which mean that $m < n$. Therefore, implementing $K(s) \approx U(s)/Y(s)$ in a physical system is not feasible, and thus a propering filter $F(s)$ is typically used such that $K(s) = U(s)/(Y(s) * F(s))$ where the degree of $F(s)$ is larger than $(m - n)$. Filters that implement an inversion of the system are also known as pre-emphasis or pre-compensation filters and have previously been used to improve the performance of gradient and shim systems [9, 12]. A control system without any feedback (such as the one described above) is also known as an open-loop controller (Figure 1a).

However, if a feedback system is implemented (Figure 1b) such that the loop is closed, the design of $K(s)$ is not as intuitive. A commonly used structure of $K(s)$ in industry is the proportional-integral-differential (PID) controller, which has the following structure:

$$K(s) = K_P + {K_I}/{s} + s \cdot K_D \quad (3)$$

Another commonly used controller implement only the first two terms and are referred to as PI controllers. These controllers are an industry standard because they are easy to implement in practice. However, the tuning of PI/D controllers is still commonly done by rule-of-thumb or heuristically (such as the Ziegler-Nichols tuning method [19, 13]) and is often not optimal [15]. This is mainly because of two factors: firstly, the objectives to be optimized are often not clear since there is a trade-off between performance and robustness, and secondly, it is still unclear what measures should be used to evaluate the performance of such controllers and the objectives are often nonlinear, which make the calculation of optimal parameters complex and time-consuming [20, 21].

Evaluation of the performance of transfer functions can be done by looking at the closed-loop transfer function, calculated from *y(s)* with respect to the *r(s)* signal (from Figure 1b). Typical performance criteria use the response time, settling time, or absolute-integral-error (IAE) of the *y(s)* signal [22]. On the other hand, robustness can be evaluated from *y(s)* with respect to the *v(s)* or *d(s)* signals, referred to as the input and output disturbance signals, respectively. The transfer function $\frac{Y(s)}{D(s)} = \frac{1}{1+K(s)\cdot G(s)}$ is known as the sensitivity function [22, 23].

Decoupling Control

The theory presented in the previous section only dealt with SISO LTI systems. This can easily be extended to MIMO systems using transfer functions. A MIMO system can be represented using a matrix of transfer functions as described in [12, 24]. Theoretically, an input on one channel of the system can result in outputs on all the output channels. If the system is weakly coupled then the off-diagonal terms are approximately zero. Figure 2a depicts a model of a MIMO system for two inputs and two outputs.

Again, if pre-emphasis is used, then we simply design a filter that is approximately the inverse of the matrix of transfer functions. However, the design of closed-loop controllers becomes more complicated. Although there are methods to design MIMO systems, many of these methods are not scalable to larger systems. If a MIMO system is large and nearly diagonal, arguably the easiest approach would be to decouple the system (*T(s)* in Figure 2b) so that the off-diagonal terms become negligible and we are left with an array of SISO systems, and therefore the design process of the controller becomes much simpler.

There are multiple options for decoupling a MIMO system. Firstly, we can use pre-emphasis and dynamically decouple the system over a large frequency range; secondly, we can statically decouple the system by inverting the steady-state gain of the system [25]. Alternatively, instead of using only the steady-state information (that is, at 0 Hz), one can optimize static decoupling matrices T_u and T_y (as shown in Figure 2c) to decouple the system over a range of frequencies [26, 27].

A decoupled (or decentralized) system should have as many degrees of freedom as possible, such that the performance and robustness of the resulting SISO systems are not restricted by the process of decoupling [28, 29]. A good measure for evaluating decoupling is the μ-interaction measure which can be directly related to the stability of the decentralized controller [29]. The μ-interaction is defined as the singular value of the relative error matrix, where the relative error matrix is:

$$E_{P_d}(\omega) = \left(P_d(\omega) - diag\{P_{d,ii}(\omega)\}\right) \cdot \left(diag\{P_{d,ii}(\omega)\}\right)^{-1} \quad (4)$$

And

$$P_d(\omega) = T_y P(\omega) T_u \quad (5)$$

where T_u and T_y are the decoupling matrices and $P(\omega)$ is the measured frequency response function (FRF) matrix. The complementary sensitivities of the decoupled SISO loops are limited by the inverse of the μ-interaction measure. Thus, an optimal decentralized controller can be found by minimizing the μ-interaction (maximum singular value of $E_{P_d}(\omega)$) over the frequency range of interest.

Once the system has been sufficiently decoupled and we are left with the effective SISO systems, the cross-coupling effects can be considered as output disturbance signals (as shown in Figure 2a), and individual controllers can be designed for each SISO system ($C_1, \dots, C_P$ are the controllers in Figure 2c)

Methods

Hardware

A B_0 insert shim system from Resonance Research Inc. (RRI) (Billerica, MA) was used (Figure 3). The shim coils were designed using the spherical harmonic functions as basis functions. 28 shim coils were available and included full zeroth, second, third and fourth degree spherical harmonic shim terms. The scanner was a Siemens 9.4T human whole-body Magnetom (Erlangen, Germany).

The B_0 shim system is multivariable in nature since there are multiple shim coils and these interact with each other due to eddy currents. Furthermore, the construction of the shim coils is not perfect and thus the magnetic field generated by the coil is not the spatial spherical harmonic function that it was designed to be [30].

Proton field probes were constructed using a small capillary tube filled with doped water and encapsulated within epoxy as described in [31, 32, 33]. NMR field probes are useful for measuring the spatiotemporal dynamics of the magnetic field. The sample in the probe can be excited to generate a free induction decay (FID) signal within the MRI scanner. The magnetic field strength is calculated from the phase φ of the FID signal as follows:

$$B_0 = \frac{1}{\gamma} \cdot \frac{d\varphi}{dt} \tag{6}$$

For proton, the gyromagnetic ratio is 42.577 MHz/T.

An array of NMR field probes is usually referred to as a field camera. In this study, a ^{1}H 12-probe field camera (Figure 3) was built for measuring the dynamics of the B_0 field [33, 34].

The shim amplifiers were driven and controlled by custom hardware. A commercial off-the-shelf microcontroller (Raspberry Pi 2 B) with a 900 MHz quad-core ARM Cortex-A7 CPU running a Debian distribution of Linux was used (Figure 4a). Synchronization with the MRI scanner was performed using a transistor-transistor logic (TTL) trigger as an input into one of the general purpose input/output (GPIO) pins of the microcontroller. Low level control of the device was performed using the WiringPi library written in C. The controller was connected to a digital-to-analog converter (DAC) board (AD5360 from Analog Devices), and communicated through a serial peripheral interface (SPI) protocol (Figure 4a). The clock rate of the SPI was 5 MHz and required 32-bits to update a single channel. The DAC board had 16 channels, and therefore two boards were required for a sufficient number of channels to drive the insert shim amplifiers. However, in this application only 16 channels were used (up to full 3rd degree shim terms) could be controlled. Updating 16 channels required approximately 100 us for the SPI communication. All software implementation on the microcontroller were done in C.

The DAC was then connected to two banks of single-to-differential amplifiers. Each bank had 16 amplifiers and had a separate power supply. An ADC driver from Texas Instruments (AN-1812) was used for this purpose. The board schematic is shown in Figure 4b. Each board could provide a voltage of ±5V rail-to-rail and a current of 0.5A. The outputs from the amplifiers were then connected to the shim amplifier.

Data Acquisition

The B_0 shim system was characterized using two different methods of measuring the spatiotemporal dynamics of the magnetic field. Firstly, a low resolution B_0 mapping sequence was used to acquire fast B_0 maps. A 3D dual-echo GRE sequence with the following parameters was used: matrix size of 32x32x4; FOV of 200x200x80 mm; ΔTE = 1 ms; TR = 400 ms. The maps were acquired with a temporal

resolution of 600 ms for a total duration of 10 seconds. A shim current of 1.0A was applied to one of the channels during the acquisition. This was then done for each of the channels of the insert shim.

Secondly, the resulting changes in the magnetic field were also measured using the field camera. The field camera measurements were decomposed using the spherical harmonic functions and hence, the magnetic field was characterized by the corresponding coefficients. These coefficients were converted into current using Equation 6 and the coil design sensitivities. The coil sensitivities are given in the supporting material (Table S1). For system identification of the gradient (1st degree) terms, a step input of 1 mT/m was applied to each of the gradient coils. The spherical harmonic coefficients of the 1st degree terms were converted to mT/m. Therefore, the units of 1st degree terms are in mT/m and all other degrees are in Amperes.

The field camera measurements were decomposed using the Legendre polynomials. As mentioned in [34], the magnetic field can be decomposed if the positions of the field probes are known. This is calculated by solving the system of linear equations:

$$B(\boldsymbol{r}) = \sum_{l=0}^{N} \sum_{m=-l}^{l} k_l^m \, S_l^m(\boldsymbol{r}) \tag{7}$$

where S_l^m is the spherical harmonic function of degree l and order m and k_l^m is the corresponding coefficient, r is the position (x,y,z) and B is the magnetic field strength at position r. Thus, the units of the k_l^m coefficients are Tesla.

The positions of the field probes are calculated with a constrained optimization method using the gradient fields of the MRI scanner. Prior knowledge of the spatial positions of the field probes (relative to each other) were used to constrain the probe positions. The position of the field camera within the MRI scanner was optimized for nonlinearities in the gradient fields [33]. A disadvantage of the field camera is that the limited number of field probes means that the magnetic field cannot be measured with high spatial resolution. The number of spatial measurements was increased by moving the field camera to multiple positions and repeating the measurements for each position. The field camera measurements were then combined across all measurements. Only spatial points within the volume of interest (VOI) were retained; this resulted in a total of 50 spatial points measured by the field probes.

The field probes were repeatedly excited at intervals of 25 ms to produce the FID signals during the measurements. The excitation pulses were rectangular RF pulses with a duration of 100 us. The FIDs were measured at a sampling rate of 10 kHz. The phase signals calculated from the FIDs were then downsampled to 1 kHz (i.e. samples were averaged over every 1 ms) to reduce the noise in the raw phase signals.

Finally, the spatial accuracy of the two measurement approaches (B_0 mapping versus field camera measurements) were compared by reconstructing the spatial distribution of the fields using the field camera coefficients (k_l^m).

System Identification and Pre-emphasis

In this study, a simple unit step was used as input for system characterization (or identification). The measurements from the field camera were used for system identification since the temporal resolution was much higher than the temporal resolution of the B_0 mapping sequences.

For the full 4th degree system, we decomposed each of the field measurements up to 4th degree spherical harmonic terms. Therefore, the system had a total of 25 input channels and a total of 25 output channels (coefficients of the spherical harmonic decomposition or k_m^l from Equation 7). The system matrix of transfer functions was then:

$$\boldsymbol{G}(s) = \begin{bmatrix} G_{1,1}(s) & \cdots & G_{1,25}(s) \\ \vdots & \ddots & \vdots \\ G_{25,1}(s) & \cdots & G_{25,25}(s) \end{bmatrix} \tag{8}$$

Where each transfer function $G_{j,k}(s)$ can be determined from $Y_k(s)/U_j(s)$ where $Y_k(s)$ is the Laplace transform of the k[th] output channel time domain signal of the open-loop system, and $U_j(s)$ is the Laplace transform of the j[th] input channel time domain signal of the open-loop system, and $1 \leq j, k \leq 25$.

One method for characterizing the system $G_{j,k}(s)$ is to predefine the order of the system and find the parameters that best fit the model to the data. In other words, suppose we use a first order system:

$$g_{model}(s) = \frac{b_0}{a_1 s + a_0} \tag{9}$$

Then an optimization is performed to find parameters $[b_0, a_0, a_1]$ that best fit the data. The initial values of the parameters can be well estimated by using the time response of the system, which is approximately $T_{response} \approx a_1/a_0$, and the gain of the system which is b_0/a_0.

For the transfer functions of the system $\boldsymbol{G}(s)$, third order models were used to fit each element of the matrix. Most of the cross-coupling effects (i.e. off-diagonal terms) are due to eddy current effects. Furthermore, eddy current effects can be well-modeled using exponentially decaying functions in the time domain (which are first order systems) [35].

For pre-emphasis, due to the hardware limitations mentioned previously, only up to 3[rd] degree shim terms were considered. Therefore, the system identification process are repeated using only up to 3[rd] degree shim terms and decomposition. Therefore, the system had a total of 16 inputs and 16 outputs. Pre-emphasis was performed by inverting the system $\boldsymbol{G}(s)$ and a propering filter $\boldsymbol{F}(s)$ where all off-diagonal elements were zero and the diagonal transfer functions were $F_{k,k}(s) = (200/s + 200)$ for $1 \leq k \leq 16$. The resulting matrix filter was then: $\boldsymbol{K}(s) = \boldsymbol{G}^{-1}(s) \cdot \boldsymbol{F}(s)$. However, this filter needed to be implemented on a microcontroller and therefore needed to be converted to discrete time. If the sampling/update rate T of the system is constant, then a continuous filter $\boldsymbol{K}(s)$ can be converted to discrete time by going to the z-domain $\boldsymbol{K}(z)$ where $s = \frac{1}{T}\ln z$. This is normally accompanied by a zero-order hold so that the output is step-wise invariant. Therefore the digital filter was implemented as:

$$\boldsymbol{K}(z) = \mathbb{Z}\{\boldsymbol{G}^{-1}(s) \cdot \boldsymbol{F}(s) \cdot diag\left(\frac{1 - e^{-sT}}{sT}\right)\} \tag{10}$$

Where $\mathbb{Z}$ is the z-transform. Even though the DACs could be updated at a rate of 100 us, since the microcontroller did not run a real-time operating system and had latencies, we used a more conservative sampling/update rate of 2 kHz.

Closed-loop Feedback

Using the μ-interaction measure, we can determine how well the system was decoupled and compare different decoupling methods. Three decoupling strategies were simulated on the B_0 shim system: static decoupling, static decoupling using the Vaes method [36], and dynamic decoupling.

Firstly, the static decoupling was performed by calculating the steady-state of the system and inverting this matrix (to find the T_u decoupling matrix). The T_y decoupling matrix was set to the identity matrix. Secondly, the Vaes method was used to calculate both static decoupling matrices. This method uses the μ-interaction measure as a cost function for an optimization problem. The optimization parameters are the elements of the matrices T_u and T_y. The optimization problem is then [36]:

$$\min_{\alpha_{1,1} \ldots \alpha_{n,n}, \beta_{1,1} \ldots \beta_{n,n}} (\max_{\omega} \mu_{\Delta}(E_{P_d}(\omega) \cdot \mathrm{W}(\omega))) \tag{11}$$

where μ_{Δ} is the μ-interaction measure for decentralized controller Δ, $\alpha_{1,1}, \ldots \alpha_{n,n}$ are the elements of T_u, $\beta_{1,1} \ldots \beta_{n,n}$ are the elements of T_y, and $W(\omega)$ is a weighting vector.

Since the optimization problem is nonlinear, a constrained conjugate gradient descent algorithm with the interior-point method (25), was used. The T_u and T_y matrices were constrained to have singular values between (0.1 and 10) to ensure that they are well-conditioned. The solution found by the

algorithm is also dependent on the initial starting point because the problem has local minima. Vaes [27] suggested using the Owen's method to find the initial starting point. However, since the B_0 shim system was nearly-diagonal, the static decoupling matrices (described previously) were used as the starting point. Since we were interested in decoupling low-frequency dynamics (between 0 and 1Hz), the weighting vector was defined as:

$$W(\omega) = \begin{cases} 1 & 0 \leq \omega \leq 0.01 \cdot 2\pi \\ \frac{1}{\omega} & 0.01 \cdot 2\pi < \omega \end{cases} \quad (12)$$

Lastly, a dynamic decoupling compensator, which was the same as the pre-emphasis filter described in the previous section, was used.

The decoupled system was used to design controllers for the effective SISO systems. To simplify the implementation of the controller, PI controllers were designed for this application. An optimization problem was formed to find the optimal controller for each effective SISO system An integral-absolute error (IAE) constraint was used to ensure that the performance of each closed-loop system had a sufficiently fast settling time (within a few milliseconds). Another constraint was used to ensure that the input current used to drive the amplifiers were not too large. The maximum control effort (the signal that the amplifiers must drive or *u(s)* from Figure 1b) was restricted to three times the maximum of the desired set-point signal *r(t)*. The goal was to optimize the closed-loop robustness, so the objective function was to maximize the open-loop phase-margin. Therefore, the optimization problem was written as:

$$\begin{aligned} &\max_{K_P, K_I} PM(G(s) \cdot (K_P + {K_I}/{s})) \\ s.t. \quad &\int_{t=0}^{\infty} |y(t)| \cdot dt < E \\ &\max |u(t)| < 2.5 * \max |r(t)| \end{aligned} \quad (13)$$

where G(s) is the plant system of the SISO loop, *y(t)* is the output signal of the SISO system and E is a constant (= 0.005). The constant E was chosen empirically such that the average closed loop response time was approximately 4 ms. The constraint on the control effort *u(t)* ensures that input signal to the amplifiers is not too large. For example, in this case, if a current of 1.0 A is required then the amplifiers will not use more than 2.5 A.

The complete closed-loop system was simulated for discrete-time controller with a sampling rate of 2 kHz to be consistent with the sampling rate of the pre-emphasis filter (in the previous section) and the shim system was simulated in the continuous time domain. The closed-loop system was hence a mixed signal system.

Results

System Identification and Pre-emphasis

The spatiotemporal dynamics of the shim system were measured using a B_0 mapping sequence as well as a field camera for comparison. Figure 5 shows the comparison between the fields measured using the two methods for some of the shim terms. The spatial distributions of the fields are similar between the two methods, however, the field camera measurements clearly have some deviations from the B_0 mapping sequence. Although, the B_0 mapping sequence had a higher spatial resolution than the field camera, the field camera has higher temporal resolution. The temporal sampling rate of the B_0 mapping sequence was 600 ms while the (effective) temporal resolution of the field camera was 1 ms.

All the self-terms up to 4th degree shim terms are shown in Figure 6 in the time domain. Both the measured data and modeled responses are shown in the figure. It can be seen that the Z3 and Z4 terms deviate quite substantially from the ideal case. Also, for C3 and some of the higher 4th degree terms the steady-state values are not close to 1.0. The fit accuracy for most of the self-terms is very high (above 85% for all terms excluding Z4 that could not be accurately modeled using spherical harmonics). Some

of the more significant cross-terms are also shown in the figure. The accuracy of the model for the cross terms is generally lower than the self-terms because the magnitude of the cross terms are usually smaller and hence noisier in comparison.

Figure 7 shows the steady state amplitudes given by the 3rd degree system that was modeled for pre-emphasis. Using the measured data for modelling a system, a pre-emphasis compensation filter was designed. The resulting pre-emphasis step input responses are shown for some of the shim terms in Figure 7. Only up to 3rd degree shim terms could be corrected for because of the limited number of channels of the DAC. It can be seen from the figure that the transients caused by eddy currents were corrected by the pre-emphasis filter and the responses are much closer to the intended step input. Note that the uncorrected responses differ from Figure 6 (which is decomposed up to 4th degree) since the pre-emphasis model only used up to 3rd degree decomposition.

Closed-loop Feedback

Firstly, we analyze the performance of the decoupling using the μ-interaction measure. The lower the maximum singular value, the better decoupled the system. In Figure 8, the μ-interactions are shown for a dynamically decoupled system (using pre-emphasis) and two static decoupling methods between a frequency range of 1e-4 to 1e5 Hz. The dynamically decoupled system has much lower μ-interaction for the entire frequency range, which is expected. The statically decoupled system (that only decouples on the 0 Hz frequency) is well decoupled for the low frequencies but quickly increases and is worse than the original system for frequencies higher than 0.5 Hz. Finally, the optimal statically decoupled system (using the Vaes method) again shows good decoupling for low frequencies but is able to better decouple the system for a wider range of frequencies. It performs better than the original system over a wide bandwidth.

The performance and robustness of the closed-loop systems were analyzed. The step responses of the closed-loop self-terms are shown in Figure 9 for all 3rd degree self-terms. The step response of statically decoupled and Vaes decoupled systems were similar. Both dynamically and statically decoupled systems have similar settling times. However, the dynamically decoupled system has more overshoot and thus is less robust. The sensitivity functions are also shown for each channel. The lower the values, the more robust the system is. This, again, shows that the dynamically decoupled system is less robust. The performance of the statically and Vaes decoupled systems are similar for some terms like Z3, Z2X and S3. However, the Vaes system performs slightly better (faster settling time) for some terms such as X, ZX and ZC2 and furthermore, from the sensitivity plots, the robustness is also better for the Vaes system.

Finally, Figure 10 shows the control effort required to achieve this performance. That is, it shows the *u(t)* signal for a step input *r(t)* (refer to Figure 1b). The dynamically decoupled system has higher amplitude and more oscillation than the two statically decoupled systems. This also explains why the dynamically decoupled case is less robust. For static/Vaes decoupling, the required control effort remains below five times the *r(t)* set-point current. However, for higher 3rd degree terms the required current to drive the amplifiers is less than 2.5 times *r(t)*.

Discussion

In this study, we modeled a B_0 shim system up to 3rd degree spherical harmonic terms. A digital pre-emphasis filter was used to compensate for coupling between the shim terms and this was implemented on a commercial-off-the-shelf microcontroller and DACs using custom software. We proposed a method for designing closed-loop controllers for fast update rates using decoupling control. To the best of our knowledge, decoupling design methods for feedback control of B_0 shim system has not been shown in previous studies.

System Identification and Pre-emphasis

We showed that system identification can be performed using a simple step input. However, since the power of the input signal decreases with frequency, the higher frequency dynamics are dominated by noise. In comparison to [16] which used chirp signals as inputs (constant power for a wideband frequency range) using a step input is less accurate for the high frequency components. Nevertheless, for slower dynamics such as eddy currents a step input is sufficient.

Furthermore, in modeling the system, we used a parametric time domain method. The resulting models are therefore simple and easier to work with analytically. Again, compared to [12] which used a non-parametric method in the frequency domain to characterize the system, our method is less accurate as it is unable to model the high frequency components and resonances [37]. Furthermore, since the method presented in the paper is parametric, it makes an assumption about the structure of the dynamic system and is less flexible than a non-parametric method. However, our method still gave reasonably good accuracy. In addition, when designing closed-loop controllers it is usually understood that the model of the system is usually an approximation and that uncertainty in the model needs to be accounted for, which is why controllers are designed to be robust against a margin of uncertainty.

We showed that despite the lower input signal power at high frequencies and the less accurate model of the system, using this model for pre-emphasis was still sufficient to obtain good compensation of the eddy currents. It should be noted that since [12] modelled the system in the frequency domain, a filter was required for the pre-emphasis to be realized in practice and in this case a time domain Gaussian filter was used. However, in this work, due to the nature of the transfer functions in the s-domain, a first order filter is equivalent to a decaying exponential filter in the time domain.

Closed-loop Feedback

The μ-interactions of the three decoupling schemes showed that the dynamic decoupling results in better decoupling, followed by the Vaes decoupling and static decoupling methods. Although, dynamic decoupling provides decoupling for a large frequency range, the closed-loop responses showed that since the decoupling system was designed in the continuous-time domain, it had frequencies higher than the sample rate which results in ringing due to discretization; this could explain the oscillation in the control effort. This occurs when there are poles (roots of the denominator of the transfer function) that lie on the negative real axis of the z-transform. Another factor is that a dynamically decoupled system cancels poles and zeros (roots of the numerator of the transfer function) of the open-loop system and this can result in internal instability, that is, a closed-loop system less robust to input disturbances.

The Vaes decoupled system was able to provide better performance and robustness for some of the channels indicating that there are more degrees of freedom for designing controllers than for the statically decoupled case. The better the system is decoupled, the more design flexibility there is for better feedback controllers. However, it should also be noted that the control effort for the Vaes system seemed to be slightly more oscillatory than the statically decoupled system. The full controller system required up to 5 times the desired set-point current which was much higher than the constraints of 2.5 times the set-point. This is due to the decoupling matrices used for the controller.

The decoupling approach to MIMO systems is only applicable if the system is weakly coupled. If the shim system is strongly coupled then alternative MIMO controller design methods need to be employed, such as H_∞ [38], linear quadratic optimization [39] or μ-synthesis [40].

Conclusion

Eddy currents and cross-coupling in gradient and shim coils can cause problems in MRI. For accurate correction and compensation of these effects, the spatiotemporal dynamics of the gradient/shim system need to be measured. In this work, we compared using a B_0 mapping sequence to using a field camera for monitoring the system. Thereafter, we modeled the system using a time-domain parametric model for the MIMO system. The model was then used to perform pre-emphasis up to 3rd degree shim terms. Finally, closed-loop responses of the system were simulated for optimized PI controllers using different

decoupling strategies. We showed that good performance and robustness for feedback control can be achieved using static decoupling.

References

[1] X. Hu and D. G. Norris, "Advances in high-field magnetic resonance imaging," *Annual Reviews in Biomed. Eng.,* vol. 6, pp. 157-184, 2004.

[2] K. M. Koch, D. L. Rothman and R. A. de Graaf, "Optimization of static magnetic field homogeneity in the human and animal brain in vivo," *Nucl. Magn. Resonan. Spectrosc.,* vol. 54, no. 2, pp. 69-96, 2009.

[3] L. N. Baldwin, K. Wachowicz, S. D. Thomas, R. Rivest and B. G. Fallone, "Characterization, prediction, and correction of geometric distortion in 3T MR images," *Med. Phys.,* vol. 34, pp. 388-399, 2007.

[4] X. Hong, X. V. To, I. Teh, J. R. Soh and K.-H. Chuang, "Evaluation of EPI distortion correction methods for quantitative MRI of the brain at high magnetic field," *Magn. Reson. Imaging,* vol. 33, pp. 1098-1105, 2015.

[5] T. W. Nixon, S. McIntyre, D. L. Rothman and R. A. de Graaf, "Compensation of gradient-induced magnetic field perturbations," *Journal of Magnetic Resonance,* vol. 192, pp. 209-217, 2008.

[6] J. J. van Vaals and A. H. Bergman, "Optimization of Eddy-current Compensation," *Journal of Magn. Reson.,* vol. 90, pp. 52-70, 1990.

[7] A. M. El Sharkawy, M. Schar, P. A. Bottomley and E. Atalar, "Monitoring and correcting spatio-temporal variations of the MR scanner's static magnetic field," *Magn. Reson. Mater. Phy.,* vol. 19, pp. 223-236, 2006.

[8] C. Juchem, T. X. Nixon, P. Diduch, D. L. Rothman, P. Starewicz and R. A. de Graaf, "Dynamic shimming of the human brain at 7 Tesla," *Concepts Magn. Reson. Part B Magn. Reson. Eng.,* vol. 37B, no. 3, pp. 116-128, 2010.

[9] A. Fillmer, S. J. Vannesjo, M. Pavan, M. Scheidegger, K. P. Pruessmann and A. Henning, "Fast Iterative Pre-Emphasis Calibration Method Enabling Third-Order Dynamic Shim Updated fMRI," *Magn. Reson. Med.,* vol. 75, no. 3, pp. 1119-1131, 2016.

[10] D. J. Jensen, W. W. Brey, J. L. Delayre and P. A. Narayana, "Reduction of pulsed gradient settling time in the superconducting magnet of a magnetic resonance instrument," *Med. Phys.,* vol. 14, no. 5, pp. 859-862, 1987.

[11] T. W. Nixon, S. McIntyre, D. L. Rothman and R. A. de Graaf, "Compensation of gradient-induced magnetic field perturbations," *Journal of Magn. Reson.,* vol. 192, pp. 209-217, 2008.

[12] S. J. Vannesjo, Y. Duerst, L. Vionnet, B. E. Dietrich, M. Pavan, S. Gross, C. Barmet and K. P. Pruessmann, "Gradient and Shim Pre-Emphasis by Inversion of a Linear Time-Invariant System Model," *Magn. Reson. Med.,* vol. 78, pp. 1607-1622, 2017.

[13] Y. Duerst, B. J. Wilm, B. E. Dietrich, S. J. Vannesjo, C. Barmet, T. Schmid, D. O. Brunner and K. P. Pruessmann, "Real-Time Feedback for Spatiotemporal Field Stabilization in MR Systems," *Magn. Reson. in Medicine,* vol. 73, pp. 884-893, 2015.

[14] B. J. Wilm, Y. Duerst, B. E. Dietrich, M. Wyss, S. J. Vannesjo, T. Schmid, D. O. Brunner, C. Barmet and K. P. Pruessmann, "Feedback Field Control Improves Linewidths in In Vivo Magnetic Resonance Spectroscopy," *Magn. Reson. Med.,* vol. 71, pp. 1657-1662, 2014.

[15] K. J. Astrom and T. Hagglund, "Revisiting the Ziegler–Nichols step response method for PID control," *Journal of Process Control,* vol. 14, pp. 635-650, 2004.

[16] S. J. Vannesjo, B. E. Dietrich, M. Pavan, D. O. Brunner, B. J. Wilm, C. Barmet and K. P. Pruessmann, "Field Camera Measurements of Gradient and Shim Impulse Responses Using Frequency Sweeps," *Magn. Reson. Med.,* vol. 72, pp. 570-583, 2014.

[17] F. G. Goora, B. G. Colpitts and B. J. Balcom, "Arbitrary magnetic field gradient waveform correction using an impulse response based pre-equalization technique," *Journal of Magn. Reson.,* vol. 238, pp. 70-76, 2014.

[18] S. J. Vannesjo, M. Haeberlin, L. Kasper, M. Pavan, B. J. Wilm, C. Barmet and K. P. Pruessmann, "Gradient System Characterization by Impulse Response Measurements with a Dynamic Field Camera," *Magn. Rseon. Med,* vol. 69, pp. 583-593, 2013.

[19] J. G. Ziegler and N. B. Nichols, "Optimum settings for automatic controllers," *Trans. American Soc. Mech. Eng.,* vol. 64, pp. 759-765, 1942.

[20] R. A. Krohling and J. P. Rey, "Design of Optimal Disturbance Rejection PID Controllers Using Genetic Algorithms," *IEEE Trans. Evolutionary Computation,* vol. 5, no. 1, pp. 78-82, 2001.

[21] A. Herreros, E. Baeyens and J. R. Peran, "Design of PID-type controllers using multiobjective genetic algorithms," *ISA Transactions,* vol. 41, pp. 457-472, 2002.

[22] D. E. Rivera, M. Morari and S. Skogestad, "Internal Model Control: PID Controller Design," *Ind. Eng. Chem. Process Des. Dev.,* vol. 25, pp. 252-265, 1986.

[23] J. C. Doyle and G. Stein, "Multivariable feedback design: Concepts for a classical/modern synthesis," *IEEE Trans. on Automatic Control,* vol. 26, no. 1, pp. 4-16, 1981.

[24] H. H. Rosenbrock, "Proceedings Institution of Electrical Engineers," *Design of multivariable control systems using hte inverse Nyquist array,* vol. 116, no. 11, pp. 1929-1936, 1969.

[25] K. J. Atrom, K. H. Johansson and Q. G. Wang, "Design of decoupled PID controllers for MIMO systems," *Proc. of American Control Conference,* vol. 3, pp. 2015-2020, 2001.

[26] C. Ding, M. Gajdusek, A. H. Damen and P. J. van den Bosch, "Optimal Static Decoupling for the Decentralized Control: an Experimental Study," in *Proc. of 18th IFAC World Congress*, Milan, 2011.

[27] D. Vaes, W. Souverijns, J. De Cuyper, J. Swevers and P. Sas, "Optimal decoupling for improve multivariable controller design, applied on an automotive vibration test rig," *Proc. of American Control Conference,* vol. 1, pp. 785-790, 2003.

[28] E. Bristol, "On a new measure of interaction for multivariable process control," *IEEE Trans. Auto. Control,* vol. 11, no. 1, pp. 133-134, 1966.

[29] P. Grosdidier and M. Morari, "Interaction measures for systems under decentralized control," *Automatica,* vol. 22, no. 3, pp. 209-319, 1986.

[30] P. Chang, S. Nassirpour and A. Henning, "Modeling Real Shim Fields for Very High Degree (and Order) B0 Shimming of the Human Brain at 9.4T," *Magn. Reson. Med.,* 2017.

[31] N. De Zanche, C. Barmet, J. A. Nordmeyer-Massner and K. P. Pruessmann, "NMR probes for measuring magnetic fields and field dynamics in MR systems," *Magnetic Resonance in Medicine,* vol. 60, pp. 176-186, 2008.

[32] C. Barmet, N. De Zanche, B. J. Wilm and K. P. Pruessmann, "A transmit/receive system for magnetic field monitoring of in vivo MRI," *Magnetic Resonance in Medicine,* vol. 62, pp. 269-276, 2009.

[33] P. Chang, S. Nassirpour, M. Eschelbach, K. Scheffler and A. Henning, "Constrained Optimization for Position Calibration of an NMR Field Camera," *Magn. Reson. Med.,* 2017.

[34] C. Barmet, N. De Zanche and K. P. Pruessmann, "Spatiotemporal magnetic field monitoring for MR," *Magnetic Resonance in Medicine,* vol. 60, pp. 187-197, 2008.

[35] P. Jehenson, M. Westphal and N. Schuff, "Analytical method for the compensatio of eddy-current effects induced by pulsed magnetic field gradient in NMR systems," *Journal of Magn. Reson.,* vol. 90, pp. 264-278, 1990.

[36] D. Vaes, J. Swevers and P. Sas, "Optimal decoupling for MIMO-controller design with robust performance," *Proc. of American Control Conference,* vol. 5, pp. 4601-4606, 2004.

[37] S. J. Vannesjo, Y. shi, K. P. Pruessmann, A. Dewdney, K. L. Miller and S. Clare, "Comparison of preemphasis based on a broadband filter vs. a standard exponential model for higher-order dynamic shimming," in *Proc. of ISMRM*, Singapore, 2016.

[38] J. C. Doyle, K. Glover, P. Khargonekar and B. Francis, "State-space solutions to standard H2 and H-inf control problems," *IEEE Trans. Auto. Ctrl,* vol. 34, no. 8, pp. 831-847, 1989.

[39] B. D. Anderson and J. B. Moore, Optimal Control: Linear Quadratic Methods., Mineola, 2007.

[40] G. J. Balas and J. C. Doyle, "Robust control of flexible modes in the controller crossover region," *AIAA Journal of Guidance, Dynamics and Control,* vol. 17, no. 2, pp. 370-377, 1994.

Figure Legends

Figure 1 – (a) Open-loop controller where *G(s)* is the system, *K(s)* is the controller (or filter), *r(s)* is the set-point signal, *u(s)* is the input signal and *y(s)* is the output signal. **(b)** Closed-loop control system where *e(s)* is the error signal, *v(s)* is the input disturbance, and *d(s)* is the output disturbance.

Figure 2 – (a) Multivariable system with two inputs and two outputs and corresponding self-term transfer functions $G_{1,1}(s)$ and $G_{2,2}(s)$, and cross-term transfer functions $G_{1,2}(s)$ and $G_{2,1}(s)$. The red box shows how self-terms of the multivariable system can be considered a SISO system with the cross-coupling effect as a output disturbance signal $d(s)$. **(b)** Closed-loop control system with decoupling filter $T(s)$. (c) Closed-loop control system with static decoupling matrices T_u and T_y and an array of SISO controllers $C_1 \ldots C_P$.

Figure 3 – Hardware setup of the feedback system with corresponding shim coils, shim amplifiers and field camera.

Figure 4 – (a) Custom made control system using a Raspberry Pi microcontroller and DAC board and a bank of single-to-differential driver boards as preamplifiers. **(b)** Schematic of the single-to-differential driver boards.

Figure 5 – B_0 maps acquired using a low resolution B_0 mapping sequence and field camera. The B_0 maps are shown for a few of the terms from the 2nd, 3rd and 4th degree shim terms for illustration.

Figure 6 – Measured outputs (gray) and system modelled outputs (blue) for the full 4th degree system. Self-terms are shown on the top and example cross-terms are shown on the bottom. Input signals were step functions with 1.0 A.

Figure 7 – Cross-coupling matrix for the steady-state of the full 3rd degree system. Field camera measurements for a step input of 1.0 A without (black) and with (red) pre-emphasis filter.

Figure 8 – μ-interaction measure for the original system G(s), the dynamically decoupled, the statically decoupled and the Vaes statically decoupled systems. The plots are on a log-log scale between 1e-4 and 1e4 Hz.

Figure 9 – Step response functions for the self-terms of the closed-loop systems using different decoupling strategies: dynamically decoupled (red), statically decoupled (black), and Vaes decoupled (blue). Corresponding sensitivity functions are also shown in the frequency domain between 10e-2 and 10e3 Hz on a log-log scale.

Figure 10 – Control effort for the self-terms to achieve the step responses shown in Figure 9. The plots show the required input signal u(t) for the shim amplifiers using different decoupling strategies: dynamically decoupled (red), statically decoupled (black), and Vaes decoupled (blue).

Supporting Table S1. Shim terms and insert shim coil sensitivities

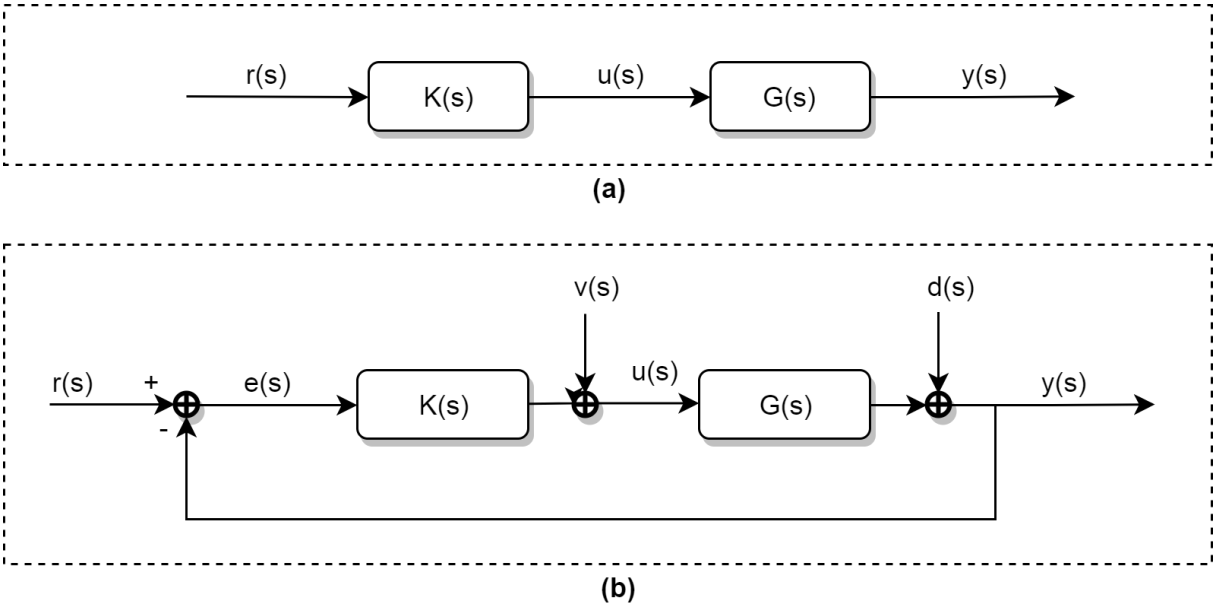

Figure 1 – (a) Open-loop controller where *G(s)* is the system, *K(s)* is the controller (or filter), *r(s)* is the set-point signal, *u(s)* is the input signal and *y(s)* is the output signal. **(b)** Closed-loop control system where *e(s)* is the error signal, *v(s)* is the input disturbance, and *d(s)* is the output disturbance.

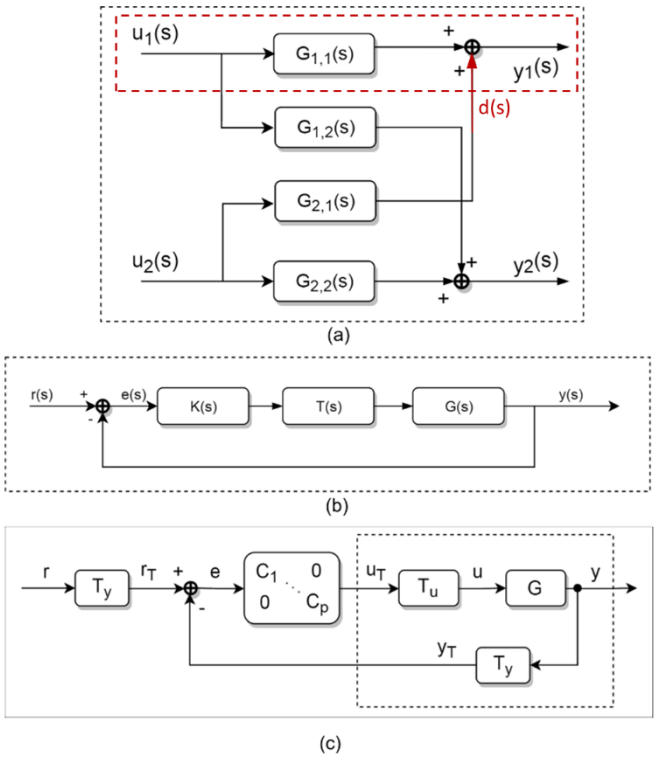

Figure 2 – (a) Multivariable system with two inputs and two outputs and corresponding self-term transfer functions $G_{1,1}(s)$ and $G_{2,2}(s)$, and cross-term transfer functions $G_{1,2}(s)$ and $G_{2,1}(s)$. The red box shows how self-terms of the multivariable system can be considered a SISO system with the cross-coupling effect considered as a output disturbance signal *d(s)*. **(b)** Closed-loop control system with decoupling filter *T(s)*. (c) Closed-loop control system with static decoupling matrices T_u and T_y and an array of SISO controllers $C_1 \ldots C_P$.

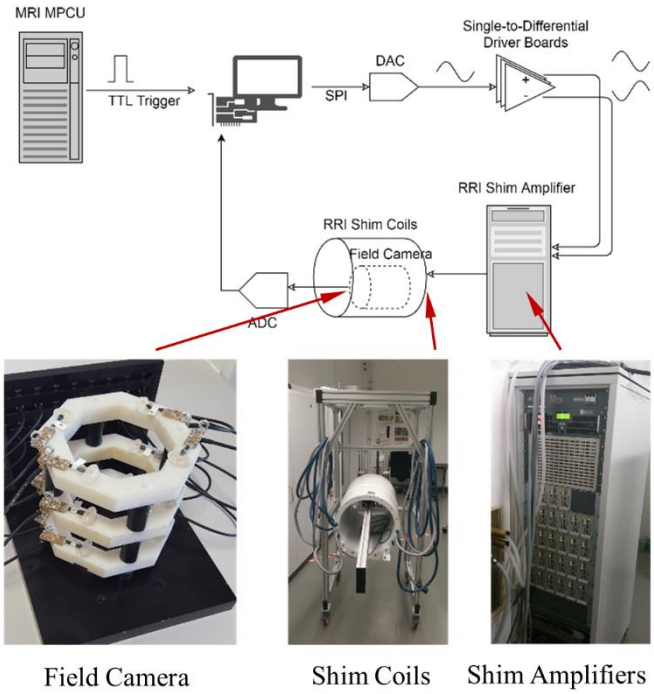

Figure 3 – Hardware setup of the feedback system with corresponding shim coils, shim amplifiers and field camera.

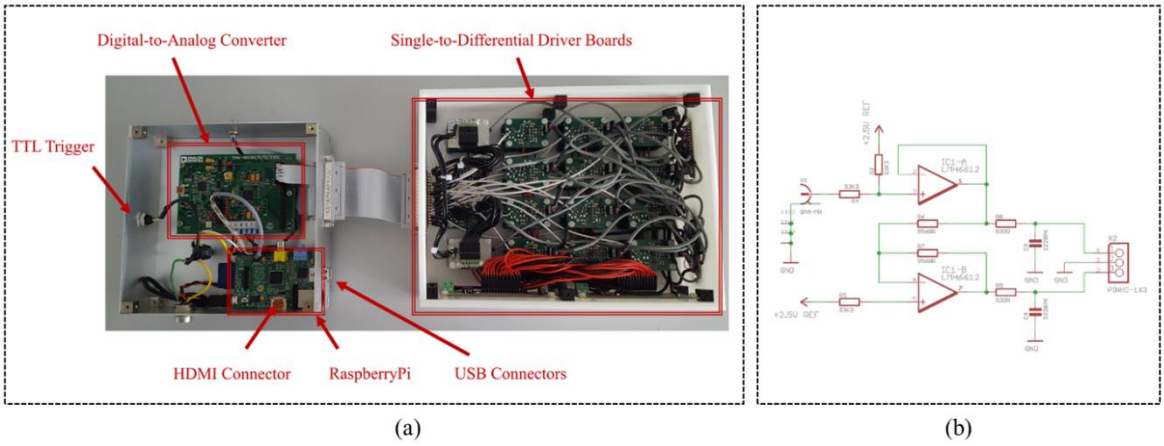

Figure 4 – (a) Custom made control system using a Raspberry Pi microcontroller,DAC board, and a bank of single-to-differential driver boards as preamplifiers. **(b)** Schematic of the single-to-differential driver boards.

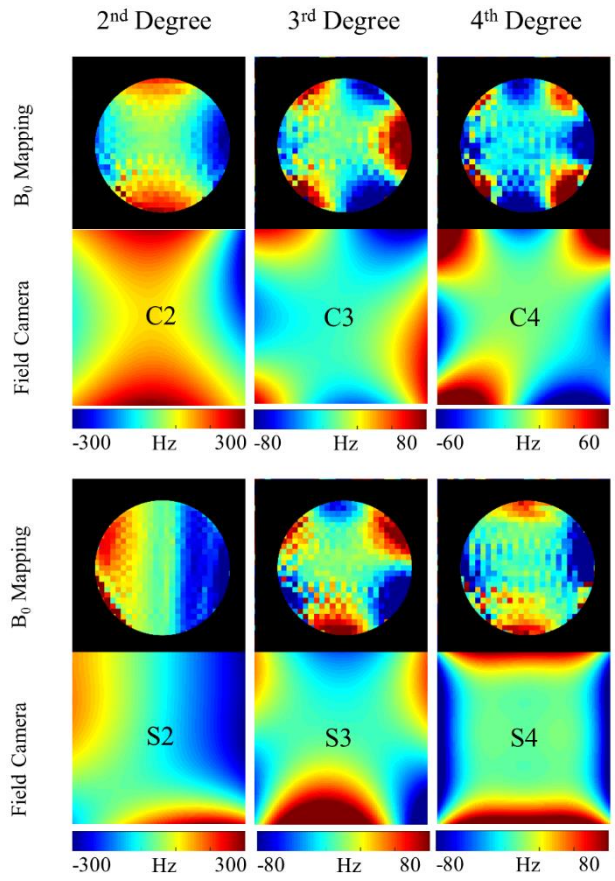

Figure 5 – B_0 maps acquired using a low resolution B_0 mapping sequence and field camera. The B_0 maps are shown for a few of the terms from the 2nd, 3rd and 4th degree shim terms for illustration.

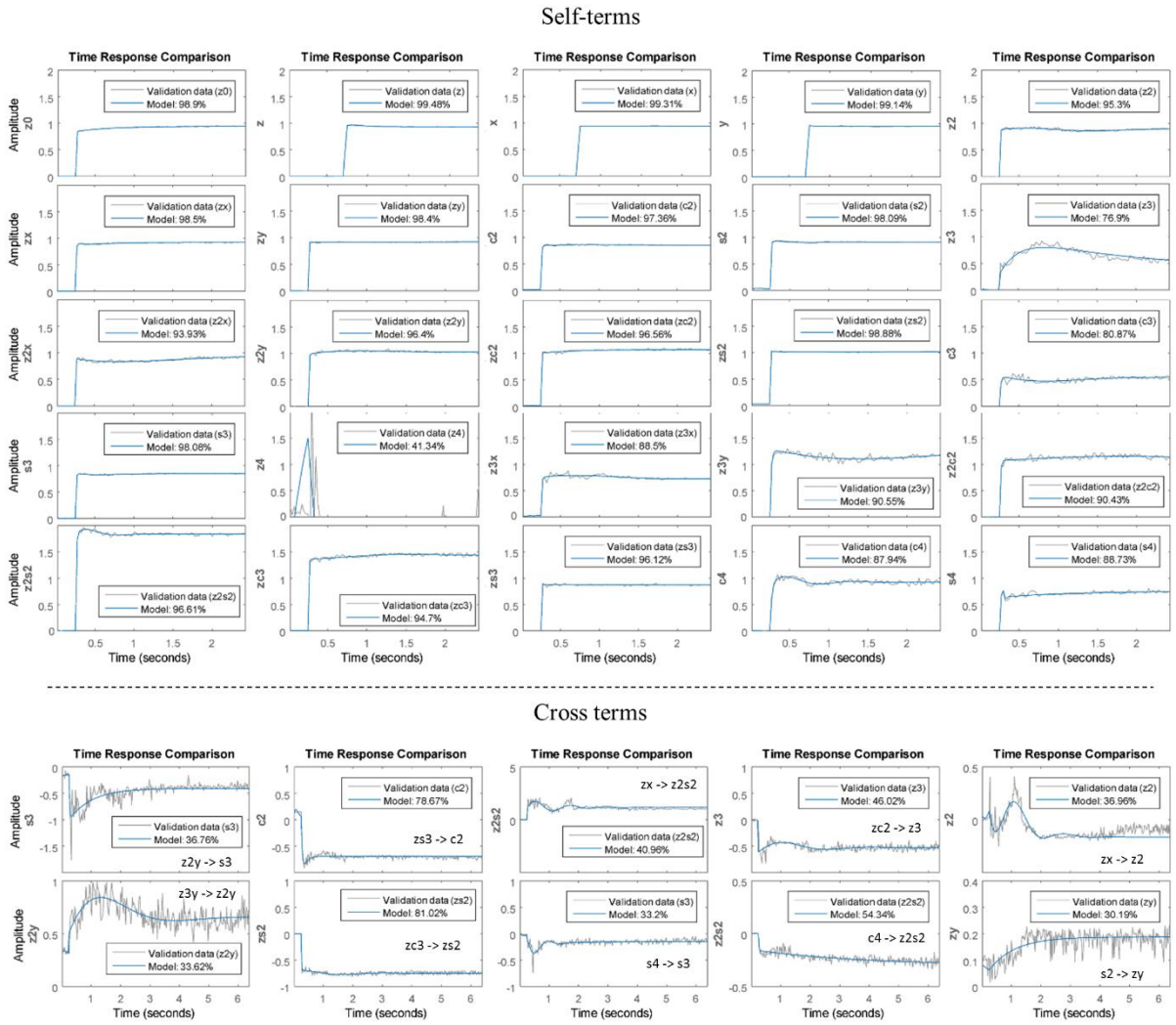

Figure 6 – Measured outputs (gray) and system modelled outputs (blue) for the full 4th degree system. Self-terms are shown on the top and example cross-terms are shown on the bottom. Input signals were step functions with 1.0 A.

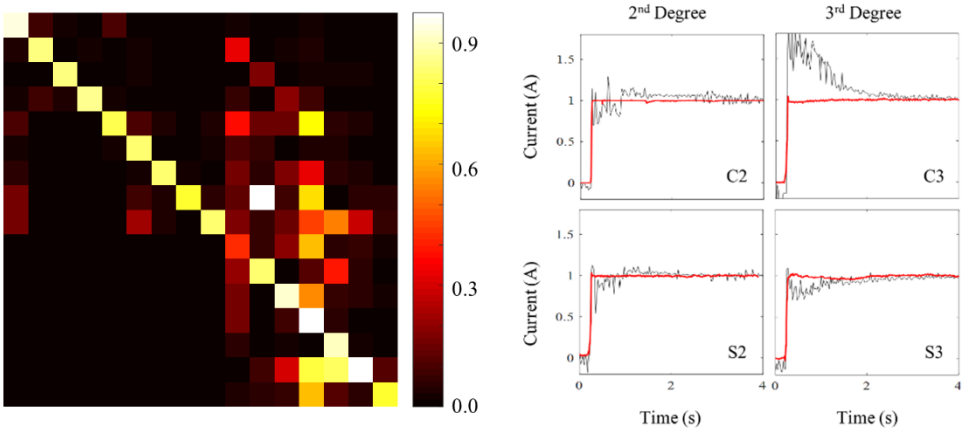

Figure 7 – Cross-coupling matrix for the steady-state of the full 3rd degree system. Field camera measurements for a step input of 1.0 A without (black) and with (red) pre-emphasis filter.

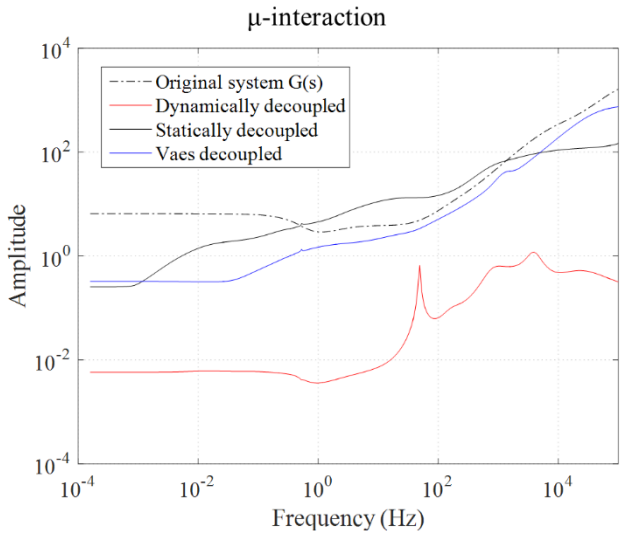

Figure 8 – μ-interaction measure for the original system G(s), the dynamically decoupled, the statically decoupled and the Vaes statically decoupled systems. The plots are on a log-log scale between 1e-4 and 1e4 Hz.

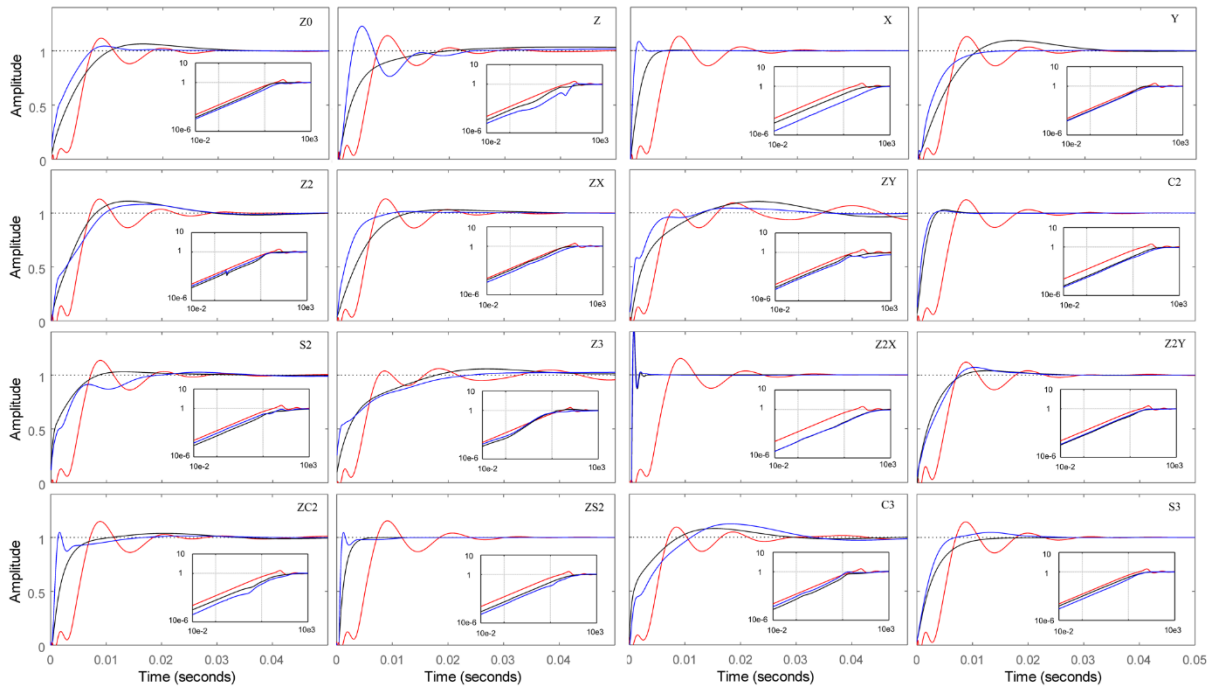

Figure 9 – Step response functions for the self-terms of the closed-loop systems using different decoupling strategies: dynamically decoupled (red), statically decoupled (black), and Vaes decoupled (blue). Corresponding sensitivity functions are also shown in the frequency domain between 10e-2 and 10e3 Hz on a log-log scale.

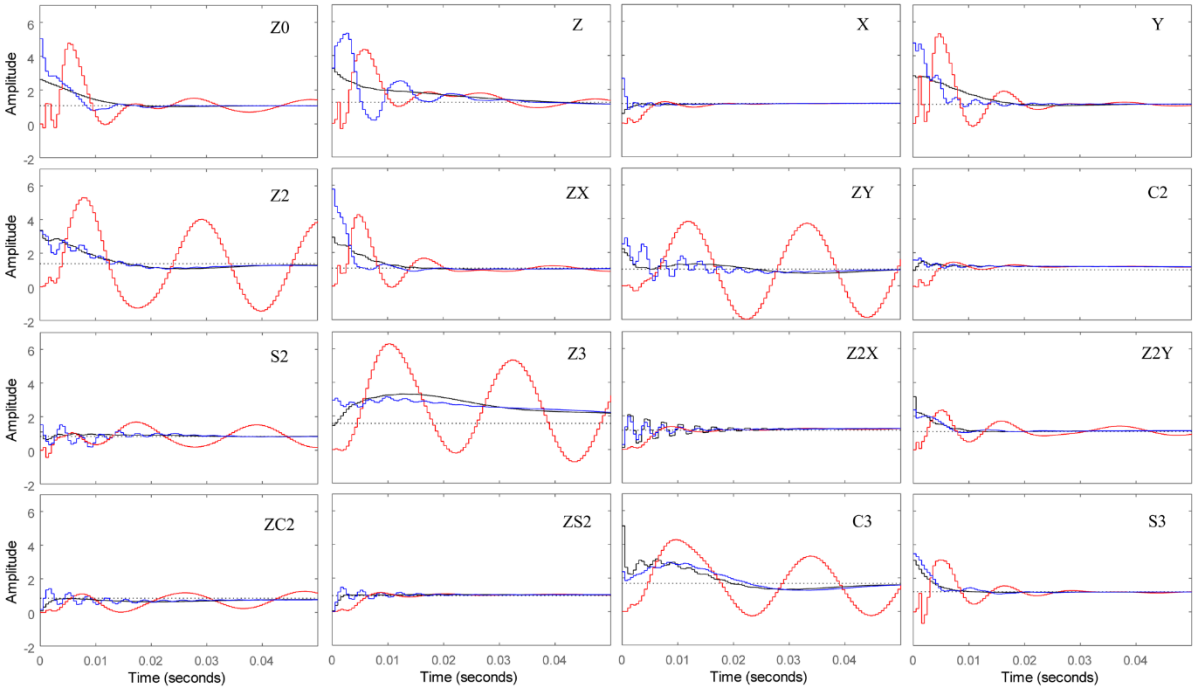

Figure 10 – Control effort for the self-terms to achieve the step responses shown in Figure 9. The plots show the required input signal u(t) for the shim amplifiers using different decoupling strategies: dynamically decoupled (red), statically decoupled (black), and Vaes decoupled (blue).

Supporting Table S1. Shim terms and insert shim coil sensitivities

Shim Term	**Spherical Harmonic Function**	**Sensitivity (Hz/cm^n/A)**
Z0	1	6058
Z2	$z^2-1/2*(x^2+y^2)$	6.942
ZX	zx	24.15
ZY	zy	24.15
C2	x^2-y^2	3.64
S2	2xy	3.64
Z3	$z(z^2-3/2*(x^2+y^2))$	0.4923
Z2X	$x(z^2-1/4*(x^2+y^2))$	1.0
Z2Y	$y(z^2-1/4*(x^2+y^2))$	1.0
ZC2	$z(x^2-y^2)$	1.77
ZS2	2zxy	1.77
C3	$x(x^2-3y^2)$	0.188
S3	$y(3x^2-y^2)$	0.188
Z4	$z^4-3z^2(x^2+y^2)+3/8*(x^2+y^2)$	0.04206
Z3X	$zx(z^2-3/4*(x^2+y^2))$	0.123
Z3Y	$zy(z^2-3/4*(x^2+y^2))$	0.123
Z2C2	$z(x^2-y^2)(z^2-1/6*(x^2+y^2))$	0.093
Z2S2	$2z(xy)(z^2-1/6*(x^2+y^2))$	0.093
ZC3	$x(x^2-3y^2)(z^2-1/8*(x^2+y^2))$	0.121
ZS3	$x(x^2-3y^2)\ (z^2-1/8*(x^2+y^2))$	0.121
C4	$x^4-6x^2y^2+y^4$	0.0187

S4	$4xy(x^2-y^2)$	0.0187

Publication VI

"System Identification and Signal Processing for PID Control of B_0 Shim Systems in Ultra-High Field Magnetic Resonance Applications"

P Chang, N Avdievitch, A Henning

Proc. of 19th World Congress of the International Federation of Automatic Control, 47(3), pp. 7517-7522, 2014.

System Identification and Signal Processing for PID Control of B0 Shim Systems in Ultra-High Field Magnetic Resonance Applications

Yu-Chun Chang* Nikolai Avdievich Anke Henning*****

**Max Planck Institute for Biological Cybernetics, Tübingen, Germany.*
Graduate School of Neural & Behavioural Sciences, University of Tübingen, Tübingen, Germany
(e-mail: paul.chang@tuebingen.mpg.de).

***Max Planck Institute for Biological Cybernetics, Tübingen, Germany. (e-mail: nikolai.avdievitch@tuebingen.mpg.de)*

****Max Planck Institute for Biological Cybernetics, Tübingen, Germany*
Institute for Biomedical Engineering, University and ETH Zurich, Switzerland (e-mail: anke.henning@tuebingen.mpg.de)

Abstract: Magnetic resonance (MR) scanners are important tools in medical diagnostics and in many areas of neuroscience. MR technology is moving towards ultra-high field (UHF) 7T and 9.4T scanners which provide more signal intensity. However they also suffer from inhomogeneity of the static (B0) magnetic field which can lead to artifacts and uninterpretable data. B0 shimming is a technique used to reduce inhomogeneities but most MR scanners use static shim settings for the duration of the experiment. Dynamic shim updating (DSU) updates the shim in real-time while the scan is in process and can hence reduce any fluctuations in B0 field which may arise due to patient breathing, mechanical vibrations and soforth. However DSU is currently very slow and if we intend to increase the update rate then control theory needs to be applied. This paper presents an application of basic system identification and signal processing in the context of MR systems for DSU. Although system identification of these systems has been done before, they are non-parametric frequency domain approaches. These systems can be modelled as linear multivariable systems.

Keywords: Medical systems; gyromagnetic ratios; process identification; parameter optimization; smoothing filters; phase-locked loop; Hurwitz criterion; PID controllers.

1. INTRODUCTION

Magnetic resonance (MR) scanners are widely used in both clinical and research environments with a large range of applications, from medical diagnosis to research in psychological neuroscience. In MR imaging (MRI), higher magnetic field strength of the static magnetic field (referred to as the B0 field) results in higher signal intensity and therefore a higher spatial resolution and a decrease in scan time (Takahashi, 2003). This is particularly beneficial in functional MRI where time resolution is important. Furthermore in MR spectroscopy (MRS), higher fields result in higher frequency separation between spectral resonances and also allow the detection of smaller concentrations of metabolites (Xu and Vigneron 2011). These benefits have led to the development of higher magnetic fields from 1.5T and 3T scanners to ultra-high field (UHF) 7T and 9.4T scanners.

Naturally, certain disadvantages also come with the benefits of high fields. UHF systems have higher specific absorption rates (SAR) which relates to how much RF energy is absorbed by the patient. The homogeneity of the static B0 field is also an issue at all field strengths but especially at UHF and is particularly important in MR spectroscopy (De Graaf, 2003). There are many more advantages and disadvantages of UHF but only the problem of B0 inhomogeneity shall be discussed in this paper.

1.1 B0 Shimming

Shimming is the processes of adjusting the static magnetic field to make it more homogeneous. There are two types of shimming: passive and active (De Graaf, 2007). Passive shimming uses pieces of ferromagnetic material to optimise the homogeneity. Once this optimisation has been done, it cannot be changed. Active shimming uses coils to generate the optimum magnetic field adjustments by driving them with the appropriate current.

Active shimming can be either static or dynamic. For static shimming, the optimal adjustments are made before the scan and remain the same for the duration of the scan. Most MR systems that have shimming functionality use static shimming. On the other hand, dynamic shimming automatically updates the shim during the scan. Dynamic shim updating (DSU) is a field of study that has only recently attracted the attention of the MR community.

DSU has been used to correct for fluctuations in the field due to breathing (see Boer et al., 2012 and Wilm et al., 2013). Since breathing is relatively slow, the shim update rate is slow and also much slower than the shim system. The feedback loops typically use digital proportional-integrator (PI) controllers (Wilm et al., 2013). Furthermore stability is not an issue because the open-loop system is stable and settles in less than

one time sample thus the PI controller does not have to be designed based on the open-loop system.

Certain applications would benefit from a high time resolution closed-loop control of the shim system. For example, dynamically updating the shim settings for every slice or volume of interest during an image acquisition sequence (Koch et al., 2006; Juchem et al., 2010) and updating shim settings for a moving volume of interest (Schär et al., 2004). These fast switching currents generate eddy currents which need to be compensated for. Thus if the system is to be controlled at a much smaller time scale such that the update rate is faster than the open-loop system then controllers based on the open-loop system need to be designed. Controller design based on a system model with a fast update rate is proposed in this paper.

1.2 System Identification of Shim Systems

To identify the system we need to measure the response of the static magnetic field. Jezzard and Balaban (1995) show that the B0 field can be determined from phase maps. However, obtaining phase maps is too slow and cannot capture the dynamics of the system. A more effective method for measuring the B0 field is to use nuclear MR (NMR) field probes (Barmet et al., 2008; and Handwerker et al., 2013).

1.3 Outline

Section 2 describes the hardware that was available and the process of manufacturing the sensors and instrumentation. This section also includes the signal processing methods that were used and proposes a hybrid filter for reducing noisy measurements. Section 3 presents the method used for system identification. An example of how PID controllers can be designed is shown in section 4 and their simulated results also included. Finally section 5 draws the conclusions and makes further recommendations for improving B0 shimming.

2. INSTRUMENTATION AND SIGNAL PROCESSING

2.1 Hardware and Sensors

The experiments were performed on a whole-body 9.4T Siemens Magnetom MR scammer (Erlangen, Germany).

A custom built 9.4T field camera consisting of sixteen 1H field probes was used to monitor the field (fig. 1). De Zanche et al. (2008) describes the process for producing NMR probes. The probes were constructed using water samples doped with $CuSO_4$ at a ratio of 3.7g/ℓ to decrease the T_1 relaxation time to approximately 80ms. Each coils consisted of six turns around a 1.0mm outer diameter and 0.8mm inner diameter glass tube where the tube was a length on 10mm. Each probe was encapsulated in epoxy and doped with $Dy(III)(NO_3)_3.5H_2O$ at a ratio of 2.75mg per 5g of epoxy for susceptibility matching to the copper wire. The probes were arranged on a spherical mount with a diameter of 250mm.

Each of the probes were tuned to the appropriate frequency of 399.72MHz (given by $\omega = \gamma \times B0$ where γ is the gyromagnetic ratio). The probes were matched to 50Ω and decoupled using cable traps with an isolation of more than 42dB between any two probes. The probes were operated in transmit/receive mode using a custom-build 16 channel interface (-50dB isolation, 0.2dB insertion loss per channel). A rectangular RF excitation pulse of 0.5ms duration was used and the signals were sampled at 300kHz.

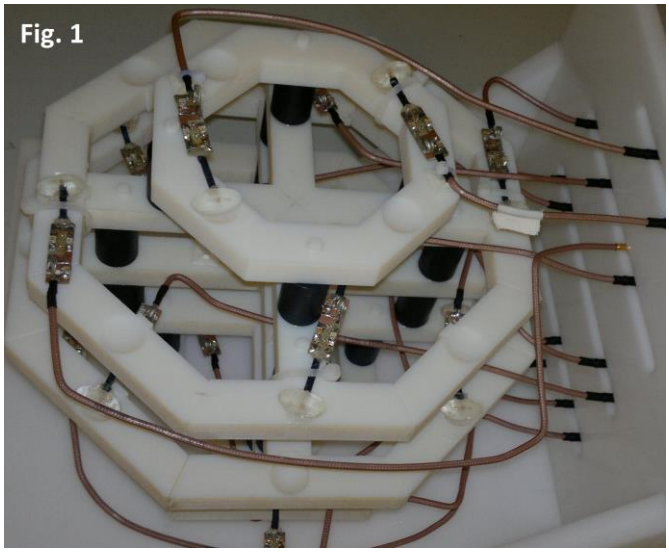

Fig. 1. Magnetic field camera with 16 NMR probes for spatio-temporal monitoring of the B0 field.

2.2 Input and Output Signals

The input signals to the system were the current signals used to drive the shim coils. The output of the system is the B0 field, which can be described using a set of basis functions as

$$|\boldsymbol{B}(\boldsymbol{r},t)| = \sum_{i=0}^{N_L-1} c_i(t) f_i(\boldsymbol{r}) + B_{ref}(\boldsymbol{r})$$

where $\boldsymbol{r}$ is the position in space, $f_i(\boldsymbol{r})$ is the set of basis functions, $c_i(t)$ are the field coefficients, N_L is the number of basis functions and $B_{ref}(\boldsymbol{r})$ is the reference field some initial time t_0 (see Barmet et al., 2008). Spherical harmonic (SH) functions are used as the basis functions because the shim coils are designed to generate the SH components of the field (Clare et al., 2006). Molecules subject to a magnetic field B(r,t) and a gyromagnetic ratio γ accrue a phase given by $\varphi(t) = \gamma \int_0^t B(t')dt'$. Therefore the field coefficients that characterise the B0 field are related to the phase coefficients by

$$c_i(t) = \frac{1}{\gamma} \cdot \frac{dk_i(t)}{dt} \qquad i = 0, \dots, N_L - 1$$

where $k_i(t)$ are given by fitting basis functions to the phase maps (Vannesjo et al., 2013).

The NMR probes measure the free-induction decay (FID) of the molecules (Handwerker, 2013). The FID phase of a probe at position $\boldsymbol{r}$ is the phase $\varphi(\boldsymbol{r},t)$. The field coefficients $c_i(t)$ can then be calculated using SH basis functions as described by Barmet et al. (2008).

2.3 Hybrid Filter

The probes are small for high spatial resolution and specificity but this results in noisy FIDs. Furthermore since the field

coefficients are dependent on the derivative of the phase signals, phase jitter makes the field measurements noisier.

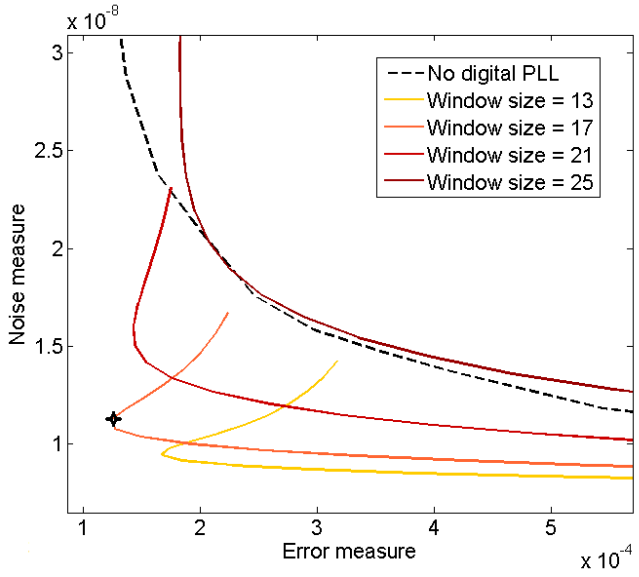

Fig. 2. Comparison of the digital PLL with a moving-average filter. PLL filters with bandwidths ranging from 200 to 800 times greater than the bandwidth of the gradient system. The performance of a moving-average is shown as a reference (window sizes from 3 to 41 samples).

Phase locked-loop (PLL) filters can be used to reduce phase jitter. A second-order digital PLL was used and the closed-loop transfer function in the z-domain is

$$H(z) = \frac{\gamma((1+\rho)z - 1)}{z^2 + (\gamma + \gamma\rho - 2)z + (1-\gamma)}$$

where γ and ρ are the design parameters (Shayan and Le-Ngoc, 1989). The filter poles were constrained to be real and equal.

The input signal was a gradient in the x-direction switched on and off to produce a triangular wave-form. The gradient amplitude was 5mT/m and the slew rate was 40mT/m/ms.

Two objectives were considered when filtering: minimizing noise and preserving the underlying signal (i.e. avoid over-smoothing). A moving-average filter was able to outperform the PLL in both objectives. The noise measure is the square sum of the error signal when the output signal is in steady-state. The preservation measure is the square sum of the difference between the filtered signal and the predicted response. The predicted response was found using a basic system identification method (as described in section 3).

A hybrid filter using the PLL and moving-average filters was investigated. A range of moving-average window sizes, varying from 3 to 41 samples, was use. The closed-loop response of the PLL needs to be much faster than the system. A range of PLL filters were tested where γ was 200 to 800 times faster than the system response time. Fig. 2 shows the performance of the different combinations of γ and the window size. Hence we can find optimal parameters for reduce noise and preserve the actual signal. The cross in fig. 2 was chosen as the optimal point its performance is shown in fig. 3. Fig. 3 shows a comparison of the time domain signals for the PLL filter, moving-average, and the hybrid filter.

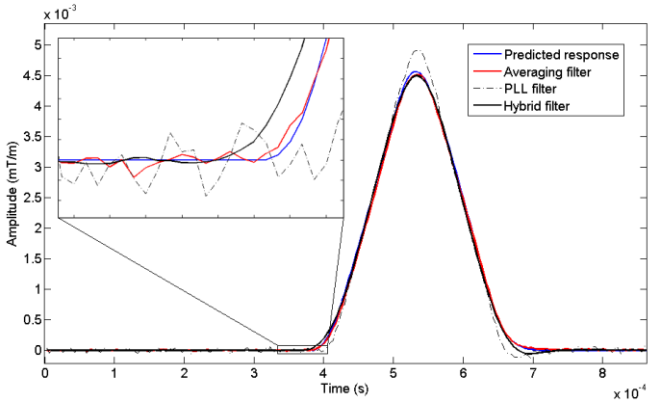

Fig.3. Time domain plots of the derivatives of the phase signals after being processed with different filters. The moving-average filter window size is 13. The PLL filter bandwidth is 360 times greater than the gradient system. The hybrid filter is the same as the PLL but with a moving-average with window size 17 (optimal point as shown in fig. 2).

3. SYSTEM IDENTIFICATION

Until this point, shim systems have been exclusively mentioned. However, notice that the gradient system are the set of linear shim terms. The integrated shim system of the scanner could not be changed during an experiment and therefore only gradient coils were used and so there are three inputs: x-, y- and z-gradients. The output signals were the field coefficients. The zero to second-order SH functions can be calculated from the 16 probes which gives a total of nine output functions.

Each transfer function is assumed to be at most a second-order system and with no dead-time, so the transfer functions in the s-domain are:

$$g(s) = \frac{A\omega}{s^2+2as+(a^2+\omega^2)} \text{ or } g(s) = \frac{A}{s+a}$$

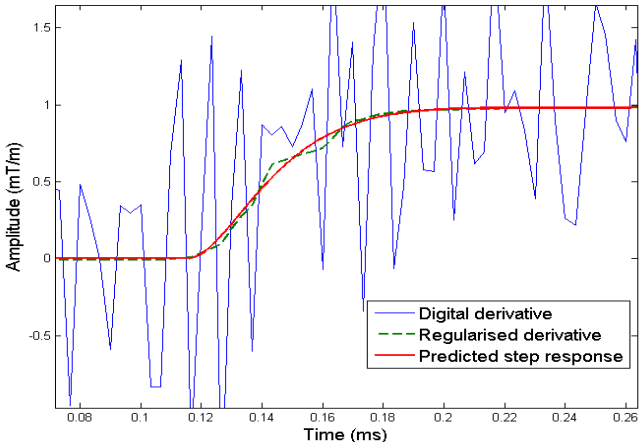

Fig. 4. Derivative of the field coefficient during the gradient ramp period of the x-gradient (slew rate 43.5mT/m/ms). The gradient was started at 0.12ms. The digital finite difference derivative.

Due to hardware limitations, step inputs could not be applied to obtain the step responses. Instead, ramp inputs were used

and the derivative of the output signal gave the step response. To calculate the derivative of the output signals (to find the step response from the ramp response), the finite difference derivative was found to be too noisy. Therefore a total regularisation derivative method proposed by Chartrand (2011) was used to calculate a smooth derivative. The difference between the digital derivative and the regularised derivative is shown in fig. 4. A regularisation factor of $\alpha = 5e^{-6}$ was used.

Table I: System model

Input	Output	A	a	ω
Gx	F0	5.23e3	31.4e3	-
Gx	**X**	133.3e3	54.4e3	27.2e3
Gx	XY	-1.99e3	33.4e3	-
Gx	Z2	-2.67e3	36.6e3	-
Gx	X2+Y2	4.06e3	0	34.5e3
Gy	F0	-1.78	27.8e3	-
Gy	**Y**	86.98e3	42.8e3	35.8e3
Gy	XY	3.95e3	29.2e3	-
Gz	**Z**	86.31e3	42.4e3	34.2e3
Gz	YZ	-0.737e3	19.4e3	-
Gz	XZ	3.21e3	28.4e3	-

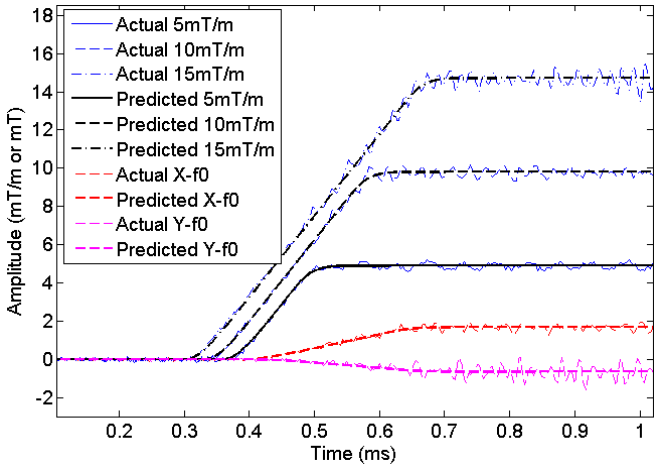

Fig. 5. Predicted and actual response of the x-gradient for different amplitudes. The cross-terms of the x- and y- gradients (10mT/m) to the zero-order term (mT) are also shown.

Using the derivative as the step response, the transfer function could be fit to the data. The slew rate was set to 43.5mT/m/ms and this corresponds to the amplitude of the step input. The system model was fit to the data and the optimal values (in the least-squares sense) for the parameters A, a and ω were found. The step response of the fitted transfer function is shown in fig. 4. The complete system is given in table I; transfer functions where the ω is omitted refer to first-order systems.

To verify the results, the predicted output from the applied input (10mT/m with 43.5mT/m/ms slew rate) was compared to the actual output. This was also done for gradient input amplitudes of 5mT/m and 15mT/m for each of the gradient inputs. Fig. 5 shows the time domain responses of the x-gradient input.

4. CLOSED-LOOP SIMULATION

4.1 PID Controller Design

Only the first-order shim coils (input) – called the gradient coils – and first-order SH terms (output) were considered. This results in three independent single-input single-output (SISO) systems which is unsurprising as the gradients are coils are decoupled and shielded from each other.

The gradient system is controlled with an inner closed-loop circuit that controls the current. Our goal is to control the slower outer loop to make it robust against noise and disturbances and not necessarily improve the speed of the system. The setpoint signal for the inner current control loop is a digital signal and hence the aim is to design digital controllers for the outer loop. PID controllers were designed for each of the three systems to test for feasibility of the digital controllers. PID controllers are well-known and the transfer function can be defined as

$$K_{PID}(s) = K_P + {K_I}/{s} + {K_D s}/{(1 + T_F s)}$$

where the design parameters are $\theta = [K_P, K_I, K_D, T_F]$. The PID controllers were designed using a multi-objective optimisation approach. The optimal points are defined using the Pareto dominance condition. Suppose there are two fitness functions $F(\theta) = [F_1(\theta), F_2(\theta)]$ where θ is the domain variable (in this case, the design parameter vector), then θ_1 Pareto dominates θ_2 if

$$[F_1(\theta_1) < F_1(\theta_2)\ and\ F_2(\theta_1) \leq F_2(\theta_2)] \text{ or}$$
$$[F_1(\theta_1) \leq F_1(\theta_2)\ and\ F_2(\theta_1) < F_2(\theta_2)]$$

where we suppose that we want to minimise F. This can be extended to more fitness functions. A formal description of Pareto optimality is given in Hajiloo et al. (2008).

Firstly the fitness functions need to be defined. Hajiloo et al. (2008) use Pareto optimum design to find a set of robust PI and PID controllers. Popov et al. (2005) analyse the trade-off between the controller performance (integral squared error) and the controller effort, while Sabahi et al. (2008) consider the trade-off between performance (settling time) and the robustness (over/undershoot). Considering these previous fitness functions, three objectives were chosen: the performance, the robustness and the control effort. The performance was measured using the settling time, the control effort was measured using the infinity-norm on the control signal and the robustness was measured using the infinity norm of the sensitivity and complementary sensitivity (Garcia et al., 2007). These fitness functions were to be minimised

1. Settling time: $\left|\frac{y_\infty - y(t)}{y_\infty}\right| < 0.05 \quad t > t_0$
2. Sensitivity: $\left\|\frac{1}{1+gk}\right\|_\infty$

3. Complementary sensitivity: $\left\|\frac{gk}{1+gk}\right\|_\infty$

4. Control effort: $\left\|\frac{k}{1+gk}\right\|_\infty$

Given that the plant and controller are both second-order system, the closed-loop system is fourth -order and the characteristic equation is given by

$$\varphi(s) = T_F \cdot s^4 + (1 + 2aT_F)s^3 + (2a + T_F(a^2 + \omega^2) + T_F K_P A\omega)s^2 + \big((a^2 + \omega^2) + (K_P + T_F K_I + K_D)A\omega\big)s + K_I A\omega$$

Constraints for the parameters were then obtained from the Hurwitz stability criteria. The domain space for θ was defined by considering the Routh-Hurwitz stability criteria and by requiring firstly, that the closed-loop system cannot be much slower than the open-loop system (settling time with 20% of the open-loop), and secondly, requiring the noise to be sufficiently reduced the filter time constant T_F was chosen to be between 1e-5 and 1e-3 and lastly, requiring the K_P cannot exceed some upper bound (chosen as 1.0).

Table II. Chosen Optimal PID Controller Parameters

	K_P	K_I	K_D	T_F
x-Grad	0.051	14.06e3	-0.197	20e-5
y-Grad	0.213	19.10e3	-0.073	2.11e-5
z-Grad	0.538	23.51e3	-0.243	2.23e-5

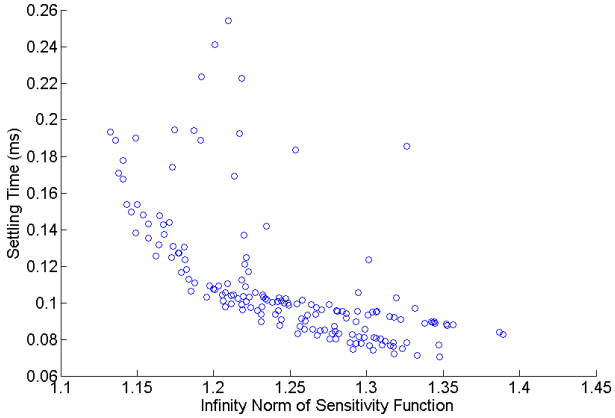

Fig. 6. Trade-off between the closed-loop performance (measured with the settling time) and robustness (measured with the sensitivity function) of PID controllers for the z-gradient system.

Since the domain space was defined to be relatively small, a brute-force search method was used to find the Pareto-optimal points. The infinity-norm complementary sensitivity of the Pareto-optimal points were found to be very similar (close to 1.0) thus providing little additional information and so was discarded as a fitness function. This left three fitness functions which was easier to visualise. The trade-off between the sensitivity and settling time (for the z-gradient system) is shown in fig. 6. The optimum point was chosen to be the minimum sensitivity where the closed-loop and open-loop settling times are equal. The corresponding PID parameters θ can then be found from this point. The PID controllers for the x-, y- and z-gradients were all designed in this manner. The chosen PID parameters are shown in table II.

4.2 Closed-Loop Simulation

The closed-loop systems of each gradient was simulated to verify the results of the PID controllers. These simulations were also used to obtain hardware specifications for implementation of these controllers digitally.

The time domain simulations show that the systems have good disturbance rejection and low sensitivity to noise. Fig. 7 shows these results for the z-gradient however the x- and y-systems were very similar. Furthermore, the figure shows that the closed-loop system is as fast as the open-loop system (as given by the design criteria). The analogue PID controllers were converted to digital controllers using a bilinear transformation (Tustin's method) without pre-warping (see Al-Alaoui, 2007). The sampling rate shown in fig. 7 is 20kHz. As the sampling rate decreases, the system starts to oscillate more until the sampling rate is so low that the system becomes unstable. Therefore for digital controller implementation it is recommended that the sampling rate (or rather update rate) is at least 20kHz. For fast and effective closed-loop control of the gradient system with a digital controller, an embedded system is recommended rather than a microcontroller since most off-the-shelf microcontrollers are generally not fast enough.

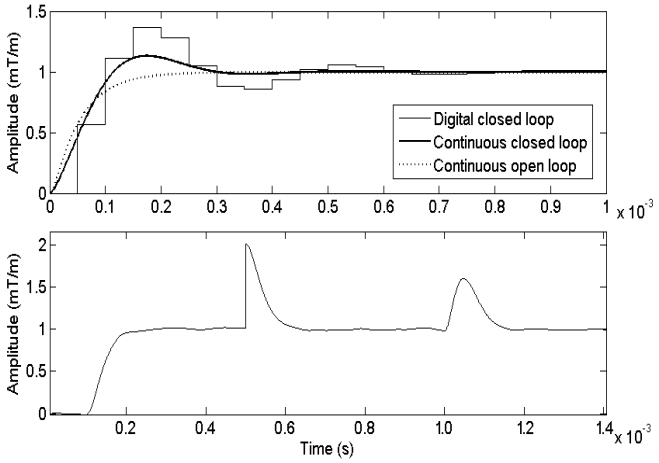

Fig. 7. Time domain simulation of the continuous open-loop plant, the continuous closed-loop system and the digital closed-loop system for the z-gradient system (top). Time domain plot of the continuous closed-loop system for the z-gradient with a step input at t=0.1ms, an output disturbance (1mT/m) at t=0.5ms and an input disturbance (1mT/m) at t=1.0ms and white measurement noise from -2 to 2mT/m (bottom).

5. CONCLUSION

A field camera consisting of 16 NMR probes was built to measure the B0 magnetic field. Filters for processing the phase signals measured by the probes were investigated and a hybrid filter utilising a moving average and a phase locked-loop filter was proposed. System identification was performed on a 9.4T MR gradient system using standard first- and second-order parametric models. PID controllers were designed for the system and the closed-loop responses were simulated.

With the current field camera, the system model can be easily extended to identify a multivariable shim system of up to second-order SH. Unlike the linear SH terms where the systems are independent, gradients also affect higher order terms (see also Vannesjo et al., 2013). Juchem et al. (2010) also show that higher order shim coils can affect other SH terms. Therefore controller design for shim systems require multivariable control techniques.

Analogue PID controllers were designed and the results were simulated. The analogue controllers were used to evaluate the required update rate for implementation of digital controllers. It is recommended that the update rate needs to be at least 20kHz to ensure stability.

ACKNOWLEDGEMENTS

The authors would like to thank Martin Eschelbach at the Max Planck Institute for Biological Cybernetics for his contributions on providing information about the process for the manufacturing of the NMR probes.

REFERENCES

Al-Alaoui, M.A. (2007). Novel approach to analog-to-digital transforms. *IEEE Transactions on Circuits and Systems-I: Regular Papers*, 54(2), 338-350.

Barmet, C., De Zanche, N., and Pruessmann, K.P. (2008). Spatiotemporal magnetic field monitoring for MR. *Magnetic Resonance in Medicine*, 60, 187-197.

Boer, V.O., van Vliet, G., Liujten P.R., and Klomp D.W. (2012). Direct B0 field monitoring and real-time B0 field updating in the human breast. *Magnetic Resonance in Medicine*, 67, 586-591.

Chartrand, R. (2011). Numerical differentiation of noisy, non-smooth data. *ISRN Applied Mathematics*, 2011.

Clare, S., Evans, J., and Jezzard, P. (2006). Requirements for room temperature shimming of the human brain. *Magnetic Resonance in Medicine*, 55, 210-214.

De Graaf, R.A., Brown, P.B., McIntyre, S., Rothman, D.L. (2003). Dynamic shim updating (DSU) for multislice signal acquisition. *Magnetic Resonance in Medicine*, 49, 409-416.

De Graaf, R.A. (2007). *In Vivo NMR Spectroscopy: Principles and Techniques (2nd ed.)*, ch. 10: Hardware. John Wiley&Sons Ltd. England.

De Zanche, N., Barmet, C., Nordmeyer-Massner, J.A., and Pruessman, K.P. (2008). NMR probes for measuring magnetic fields and field dynamics in MR systems. *Magnetic Resonance in Medicine*, 60, 176-186.

Garcia, D., Karimi, A., and Longchamp, R. (2007). Robust proportional integral derivative controller tuning with specifications on the infinity-norm of sensitivity functions. IET Control Theory Applications, 1(1), 263-272.

Hajiloo, A., Nariman-zadeh, N., and Moeini, A. (2008). Pareto optimum design of robust controllers for systems with parametric uncertainties. P. Pecherkova, M Flidr and J Dunik (ed.), *Robotics, Automation and Control*, ch. 12, 205-226. Vienna, Austria.

Handwerker, J., Ortmanns, M., Anders, J., Eschelbach, M., Chang, P., and Scheffler, K. (2013). An active TX/RX NMR probe for real-time monitoring of MRI field imperfections. *Proceedings of IEEE Biomedical Circuits and Systems Conference*. Netherlands, Oct 2013.

Jezzard, P., and Balaban, R.S. (1995). Correction for geometric distortion in echo planar images from B0 field variations. *Magnetic Resonance in Medicine*, 34 (1), 65-73.

Juchem, C., Nixon, T.W., Diduch, P., Rothman, D.L., Starewicz, P., and de Graaf, R.A. (2010). Dynamic shimming of the human brain at 7T. *Concepts in Magnetic Resonance B*, 37(3), 116-128.

Koch, K.M., McIntyre, S., Nixon, T.W., Rothman, D.L., and de Graaf, R.A. (2006). Dynamic shim updating on the human brain. *Journal of Magnetic Resonance*, 180, 286-296.

Popov, A., Farag, A., and Werner, H. (2005). Tuning of a PID controller using a multi-objective optimization technique applied to a neutralization plant. *Proc. of the 44th IEEE Conference on Decision and Control*. Spain, Dec 2005.

Sabahi, K., Sharifi, A., Aliyari Sh., M., Teshnehlab, M., and Aliasghary, M. (2008). Load frequency control in interconnected power system using multi-objective PID controller. *Journal of Applied Sciences*, 8(20), 3676-3682.

Schär, M., Kozerke, S., and Boesiger, P. (2004) Navigator gating and volume tracking for double-triggered cardiac proton spectroscopy at 3 Tesla. *Magnetic Resonance in Medicine*, 51, 1091-1095.

Shayan, Y.R., and Le-Ngoc, T. (1989). All digital phase-locked loop: concepts, design and applications. IEE Proceedings F, 136(1), 53-56, Feb 1989.

Takahashi, M., Uematsu H., and Hatabu, H. (2003). MR imaging at high magnetic fields. *European Journal of Radiology*, 46, 45-52.

Vannesjo, S.J., Haeberlin, M., Kasper, L., Pavan, M., Wilm, B.J., Barmet, C., and Pruessman, K.P. (2013). Gradient system characterization by impulse response measurements with a dynamic field camera. *Magnetic Resonance in Medicine*, 69, 583-593.

Wilm, B.J., Duerst Y., Dietrich B.E., Wyss, M., Vannesjo, S.J., Schmid, T., Brunner, D.O., Barmet, C., and Pruessmann, K.P. (2013). Feedback field control improves linewidths in *in vivo* magnetic resonance spectroscopy. *Magnetic Resonance in Medicine*, doi: 10.1002/mrm.24836.

Xu, D., and Vigneron, D.B. (2011). High field MR spectroscopy: Investigating human metabolite levels at high spectral and spatial resolution. J. Hennig and O. Speck (ed.), *High-Field MR Imaging*, 215-228. Springer, Berlin Heidelberg.